Development and Optimisation of Incremental Sheet Forming of Titanium Grade 2: Process Mapping

by
Emad Harari A. Uheida

Dissertation presented for the degree of
Doctor of Philosophy in Engineering at
Stellenbosch University

Supervisor: Dr Gert Adriaan Oosthuizen
Co-supervisor: Prof Dimiter Dimitrov

Faculty of Engineering
March 2017

DECLARATION

By submitting this dissertation electronically, I declare that the entirety of the work contained therein is my own, original work, that I am the sole author thereof (save to the extent explicitly otherwise stated), that reproduction and publication thereof by Stellenbosch University will not infringe any third party rights and that I have not previously in its entirety or in part submitted it for obtaining any qualification.

December 2016

ABSTRACT

Manufacturing products ensure value creation from natural resources. The change in manufacturing systems to a greater emphasis on personalisation, increase the need for customised products. Manufacturing challenges are presented by the increasing instability in global markets, shorter innovation cycles, input cost pressures and generally expensive resources.

Ever since the industrial revolution, the transformations in manufacturing from mass production and product variety and vice versa, were driven by market and societal transformations and the development of new enabling technologies. Single point incremental forming is a promising rapid prototyping technology for sheet metal applications.

Titanium alloys are an attractive material for numerous applications, but its use has been mainly restricted by its material and manufacturing costs. Titanium alloys are also used in a variety of engineering applications, due to its high-strength to weight ratio, corrosion resistance and biocompatibility. The alloy's mechanical characteristics make it possible to reduce the application's structural weight and increase its performance with thin-wall designs.

Incremental sheet forming is characterised by its highly localised deformation ability without drawing in material from a surrounding area. In this truly die-less configuration the sheet is shaped only by the action of a forming tool that has a single point of contact with the blank. Significant cost reductions can be realised from these flexible technologies devoted to reduce the buy-to-fly ratio and enlarge the scope of applications to small series titanium products.

Although single point incremental sheet forming (SPIF) is an active research area, the process demands and limitations for forming of CP Grade 2 titanium alloy sheets are not clearly understood. Understanding the effects of these process variables to develop resource-efficient forming process chains of CP Grade 2 titanium sheets will make a significant contribution to manufacturing knowledge. In this dissertation, an efficient two-stage process mapping approach is developed and validated.

In order to characterise the SPIF conceptual processing space and to identify the key design factors, a systematic quantitative literature review has been undertaken analysing results from relevant publications. The design of experiments (DoE) and one factor at a time test (OFAT) experiments have been methodically implemented to verify the developed conceptual framework. The ultimate goal is to design a process suitable for incremental forming of CP Grade 2 sheets that can consistently deliver a product that meets the required quality attributes.

The established approach involves mapping the SPIF of the CP Grade 2 in terms of the five key process variables. Once the behaviour of the SPIF process has been mapped, a thorough study of the role of a secondary process variable can be accomplished to evaluate its effect on the process across the full five-key-variables working window. The influence of SPIF factors on the formability of CP Grade 2 were investigated based on the forming forces, the forming temperature and the process productivity. The approach yields insight into the

theory of the SPIF process, which deepens the understanding of the dependence of the process outcomes on different variables.

The region of the SPIF process variable space, where successful forming of the CP Grade 2 titanium can be anticipated is identified throughout this process mapping approach. The processed data have been presented in a practical two-dimensional process map. The developed working window can be used as a design tool to understand the process demands and limitations for forming of CP Grade 2 titanium alloy sheets. This understanding of the effects of these process variables will enable the development of resource-efficient forming process chains for the CP Grade 2 titanium sheets. The approach as such, however, can be implemented for the establishing of process characteristics for other titanium alloys too.

OPSOMMING

Vervaardiging van produkte verseker die toevoeging van waarde tot natuurlike hulpbronne. Die verandering in vervaardiging stelsels om vir individue voorsiening te maak, verhoog die behoefte vir meer persoonlike produkte. Die uitdagings in vervaardiging word veroorsaak deur die toenemende variasie in wêreldmarkte, korter innovasie siklusse, toenemende insetkostes en duur hulpbronne.

Sedert die Industriële Revolusie was die transformasie in vervaardiging van massaproduksie na produk verskeidenheid en omgekeerd, gedryf deur die mark, sosiale veranderinge en die ontwikkeling van nuwe tegnologie. Enkel punt inkrementele vervorming is 'n belowende snel vervaardiging tegnologie vir plaatmetaal toepassings.

Titaan allooie is 'n gesogte materiaal vir talle toepassings, maar die gebruik daarvan is hoofsaaklik beperk deur die materiaal en vervaardigingskoste. Titaan allooie word ook gebruik in 'n verskeidenheid ingenieurstoepassings, as gevolg van sy hoë sterkte-tot-gewig verhouding, korrosie weerstand en biomediese aanvaarbaarheid. Die meganiese eienskappe van die allooie maak dit moontlik om die strukturele gewig van toepoasssings te verminder en hul prestasie met 'n dun-muur ontwerpe te verhoog.

Inkrementele plaat vervorming word gekenmerk deur die hoogs gesentraliseerde vervorming vermoë, sonder om die nabye materiaal te betrek. In die werklike vormlose opstelling word die plaat gevorm slegs deur die beweging van die beitel wat 'n enkele kontakpunt met die plaat het. Beduidende kostes kan deur hierdie vervormings tegnologie gespaar word. Terselfdertyd kan die koop-tot-vlieg verhouding met titaan allooie verminder word en die toepoassings van klein reeks titanium produkte vermeerder.

Hoewel enkele punt inkrementele plaat vervorming (SPIF) 'n aktiewe navorsing gebied is, is die proses vereistes en beperkings vir die vorming van CP Graad 2 titaan allooi plaatmateriaal nie duidelik bekend nie. Die verstaan van die gevolge van hierdie proses veranderlikes om hulpbrondoeltreffend vervorming proses kettings van CP Graad 2 titaan plate te ontwikkel, sal 'n belangrike bydrae tot vervaardiging kennis maak. In hierdie tesis word 'n doeltreffende twee fase proses kaart benadering ontwikkel en bevestig.

Die SPIF konseptuele verwerking ruimte kon slegs ontwikkel word deur die sleutel ontwerp faktore te identifiseer. 'n Stelselmatige kwantitatiewe literatuuroorsig was onderneem om die resultate van relevante publikasies te ontleed. Die ontwerp van eksperimente (DOE) en een faktor op 'n tyd toets (OFAT) eksperimente was wetenskaplik geïmplementeer om die ontwikkelde konseptuele raamwerk te bevestig. Die doel is om 'n proses kaart vir die vervorming van CP Graad 2 plate te ontwikkel wat ‘n konstante kwaliteit produk kan verseker.

Die benadering behels die kartering van die SPIF van die CP Graad 2 titaan allooi in terme van die vyf mees belangrikste prosesveranderlikes. Sodra die gedrag van die SPIF proses gekarteer is, kan 'n deeglike studie van die rol van 'n sekondêre proses veranderlike tot stand gebring word om die uitwerking daarvan op die proses oor die volle vyf sleutel-veranderlikes werk venster te evalueer. Die invloed van SPIF faktore op die vormbaarheid van CP Graad 2 titaan allooi is ondersoek en baseer op die vervorming kragte, die vervorming

temperatuur en die produktiwiteit van die proses. Die benadering lewer insig in die teorie van die SPIF proses op, wat die begrip van die afhanklikheid van die proses uitsette op verskillende veranderlikes verdiep.

Die area waar die SPIF proses veranderlikes suksesvolle vervorming van die CP Graad 2 titaan kan verwag word geïdentifiseer deur hierdie proses kartering benadering. Die verwerkte data is aangebied in 'n praktiese tweedimensionele proses kaart. Die ontwikkelde werk venster kan gebruik word as 'n ontwerp instrument om die proses vereistes en vervorming beperkings van CP Graad 2 titaan allooi plate te verstaan. Hierdie begrip van die gedrag van hierdie proses veranderlikes sal die ontwikkeling van die hulpbron-doeltreffende vervorming proses kettings vir CP Graad 2 titanium plate moontlik maak. Die benadering kan ook geïmplementeer word vir ander titaan allooie.

ACKNOWLEDGEMENTS

"I'm thankful for so many things, but mostly God, without him I'd have nothing else to be thankful for"

It would not have been possible to write this doctoral dissertation without the help and support of kind people around me, to only some of whom it is possible to give particular mention here.

My deep gratitude goes first to my principle supervisor, Dr Gert Adriaan Oosthuizen. Not to mention, his friendship, generosity and financial support during my difficult times, has been invaluable on both an academic and personal level, for which I am extremely grateful.

My sincere appreciation extends to my second supervisor, Prof Dimiter Dimitrov, for his enlightening guidance and advices. My deepest appreciation for his profound contribution in providing financial assistance for me. I am also grateful for the precious time he spent to revise my dissertation, papers, and the suggestions on how to improve them.

To my amazing daughter, Sarah, you always chipping in with curious questions and proofreading my writing. You helped me more than you will ever know, and for this, I am truly thankful.

I would also like to express thanks to Mr. Mike Saxer and his team at the Stellenbosch Technology Centre, for their professional work, and technical assistance.

Special thanks to Mr P. Hugo, Mr M. Bezuidenhout, Dr P. Conradie, Mr D. Hagedorn-Hansen, thanks for your friendship, support, and advice over the years.

And to my all colleagues, at the STC-LAM research group, thank you for always being creative, enthusiastic, and the joy you added to our weekly meetings.

My sincere appreciation goes to the staff and the assistance of the Industrial Engineering Department, especially to K. Smith, M. Rust and A. Henning, thank you for always being there for us.

To my many great friends in Stellenbosch: Dr W. Hadasha, Dr A. Rugbani, Dr F. Saud, and Dr R. Fleet. I appreciate the deep and special friendship we share, which has over the years bestowed many good moments upon us. You should also know that your care was worth more than I can express on paper.

Above ground, I am indebted to my family, to my parents whose value to me only grows with age. I appreciate their understanding, and endless love. Especially, to my wife, Eman, for the support and for sacrificing her time, to allow me the time I needed to complete my study. Finally, to my three daughters, Sarah, Tasnem, and Ream, you are precious in every way, with you all, life is better. God has truly blessed me.

TABLE OF CONTENTS

LIST OF FIGURES

LIST OF TABLES

NOMENCLATURE

Symbol	Description	Unit
F_x, F_y, F_z	force components; along the x, y and z axes	N
t_{ref}	reference cycle time	s
F_r	force component in radial direction	N
F_t	force component in tangential direction	N
F_{zp}	peak point of axial force	N
F_{zs}	steady-state of axial force	N
L_{max}	sheet contact ribbon	mm
L_{oh}	length of tool overhang	mm
R_a	arithmetic roughness	μm
R_t	total roughness	μm
R_z	mean roughness	μm
T_{ref}	reference temperature	℃
d_s	tool-shank diameter	mm
d_t	tool-tip diameter	mm
f_t	tool centre speed	mm/min
h_{max}	maximum forming depth	mm
h_{ref}	reference depth at 9 mm	mm
t_f	final thickness of formed sheet	mm
t_0	initial blank thickness	mm
β_s	scallop angle	radians
ε_t	strain through thickness	mm/mm
ε_θ	strain in tangential direction	mm/mm
ε_φ	strain in longitudinal direction	mm/mm
θ_{max}	maximum forming angle	degrees
σ_u	ultimate tensile stress	MPa

σ_y	yield stress	MPa
ω_t	tool rotational speed	rpm
Δh	scallop height	mm
Δw	theoretical scallop width	mm
Δz	vertical step-down of the tool path	mm
D	diameter of a circle	mm
F	force	N
G	shear modulus	MPa
I	moment of inertia	mm^4
L *or* l	length	mm
M	moment of force	Nm
O	point of origin	-
R	generatrix radius	mm
d	symbol for diameter	mm
h	depth, often cross-sectional	mm
m	mass	kg
t	current thickness of sheet	mm
ℓ	half-side length of pyramid top	mm
A	area, often cross-sectional	mm2
E	modulus of elasticity	MPa
α	contour half-apex angle	degrees
δ	elongation	mm
ε	plastic strain	mm/mm
θ	inclination angle of the formed part	degrees
μ	coefficient of friction	non
ρ	radial distance	mm
σ	normal stress	MPa

GLOSSARY

Abbrev.	**Expansion**
2D	two-dimensional
2FI	two-factor interaction
3D	three-dimensional
ANOVA	analysis of variances
C&E	cause and effect
CAD	computer-aided design
CAM	computer-aided manufacturing
CFRP	carbon fibre reinforced plastic
CL	cutter location
CNC	computer numerically control
CP	commercial pure
CT	computer tomography
CTE	coefficient of thermal expansion
DDF	digitised die forming
DoE	statistical design of experiments
FLC	forming limit curve
FLD	forming limit diagram
HRC	Rockwell number of hardness
HSS	high speed steel
ID	identification number of test run
ISF	incremental sheet forming
ISMF	incremental sheet metal forming
LSD	least significant difference
MMCs	metal matrix composites
MRI	magnetic resonance imaging
OFAT	one factor at a time test
REML	restricted maximum likelihood
SPIF	single point incremental forming
UTS	material ultimate tensile strength
VWACF	varying wall angle conical frustum
VWAPF	varying wall angle pyramidal frustum
WJ	water jet
WJSMF	water jet sheet metal forming

CHAPTER 1 INTRODUCTION

1.1 Growing demands for titanium alloys

In all branches of engineering in which moving masses are produced, there is a clear advantage to form thin-walled components from lightweight materials. There is ever-growing demand for lighter, more fuel efficient and environmentally compliant materials. Mass reduction is necessary to reduce fuel consumption and carbon emissions, and to improve functionality (Jeswiet *et al.*, 2008; Ambrogio, Filice and Gagliardi, 2012). In a variety of engineering applications, particularly in aerospace and automotive industries, high-strength and thin-wall from titanium alloys are of crucial importance and are a preferred design option for structural weight reduction and increased performance.

The aerospace industry is the second-largest user (over 50% of titanium products in both USA and Europe) after chemical industry in global market of titanium (Boyer, 2010). This is due to the high strength-to-weight ratio of titanium (density being 60% that of steel), good strength at elevated and cryogenic temperatures and excellent corrosion resistance. Commercially pure titanium and titanium alloys (hereinafter referred to as titanium) are largely used for airframe and engine components (Inagaki, 2014). Despite aluminium representing nearly half (47%) of total material demand by weight in aerospace material market, titanium is recognised as the largest material by market value in 2015. Titanium comprises a significant value at $ 3.4 billion, compared to $ 3.1 billion for aluminium and $ 2.6 billion for composites, being the third largest category (Zimm, 2015). Figure 1-1 (a) is an illustration of aircraft raw material demand by material type by weight for 2015.

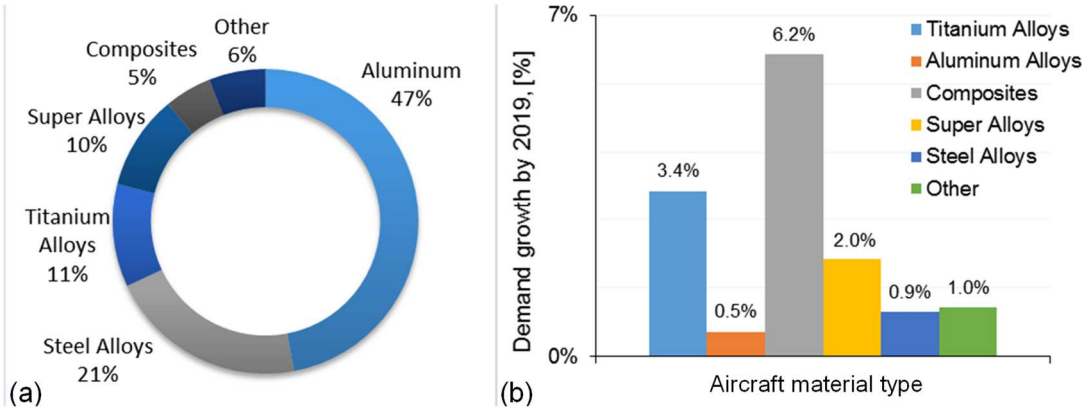

Figure 1-1: Material demand in the aerospace market : (a) Aircraft raw material demand by material type (by percentage of the weight applies to 2015). (b) The foreseen growth demand from 2014 – 2019, adapted from Zimm (2015).

The global demand for aluminium, titanium and composites for aerospace will remain stable. In 2019 the growth in the demand for titanium alloys and composites (see Figure 1-1, (b)) are expected to be the fastest growing material categories, at a rate of 3.4% and 6.2% respectively (Inagaki, 2014; Zimm, 2015). Table 1-1, summarises a few examples of common applications of titanium in aircrafts.

Table 1-1: Examples of applications of titanium alloys in aircraft (Inagaki, 2014; Zimm, 2015)

Titanium material	**Broad characteristics**	**Example of applications**
Commercially pure CP Grade2	Several grades categorised by strength. Excellent corrosion resistance, Cold workable. Grade 2 strength (yield ~300MPa, tensile 390-540 MPa)	Non-structural, high corrosive applications: water supply and sanitary ducts and piping
Ti-6Al-4V	Good balances of strength, ductility, fracture toughness, up to 300℃. Strength (yield 825 MPa, tensile 895 MPa), elongation 10%	In frames, cockpit window frame, wing box, bolts and seat rails. Engine fan cases
Ti-6Al-2Sn-4Zr-2Mo	Good heat and oxidation resistant up to 500°C. Has less β − phase than the Ti-6Al-4V. Strength (yield is 860 MPa, tensile 930 MPa), elongation 10%	Exhaust, Tail cone Compressor discs
Ti-8Al-1Mo-1V	Heat resistant up to 400℃. Strength (yield 930 MPa, tensile 1000 MPa), elongation 10%	Compressor blades
Ti-10v-2Fe-3Al*	Excellent hardenability, high yield strength 1105 MPa, tensile strength 1249 MPa, low elongation 4%	Landing gear

*Using this alloy in landing gear of the Boeing 777 resulted in a weight saving of over 580 kg (Boyer, 2010).

Expansion in the demand for titanium is attributed to the building of more economical and environmentally friendly jetliners, with a high application ratio of CFRP (carbon fibre-reinforced plastic) to their airframe and engine components. The CFRP is typically 20 percent lighter than aluminium with additional strength and a longer lifespan. In different forms of metal matrix composites (MMCs), titanium is more compatible than aluminium in two respects:

- High galvanic potential between aluminium and graphite in the composite fibres. In presence of moisture, aluminium can corrode easily (Boyer, 2010; Sherif *et al.*, 2011).

- The low coefficient of thermal expansion (CTE) for titanium, which is much higher than those in fibres, but lower than that of aluminium (Ti, $8.6 \times 10^{-6}/K$; Al, $24 \times 10^{-6}/K$), makes titanium more favoured as a composite-interface material. Bearing in mind the variation in operating temperature extremes of fuselage (-60°C at cruising to +50°C on a hot day), the difference in the CTE using aluminium attached to the composites, can result in severe loading which becomes worse for longer components. This can be avoided by using titanium structures, as titanium is compatible with CFRP with respect to corrosiveness and low thermal expansion (Fei, 1995; Boyer, 2010; Inagaki, 2014).

The best example of the expanded titanium use (percent by weight) can be seen in commercial airplanes produced by the two biggest aircraft manufacturers. For instance, the efficient airplane A350XWB from Airbus has up to 25% lower fuel consumption compared to its current aluminium long-range competitors. Owing to the largest amount of CFRP (53%) in its frame, it has more than twice the amount of titanium as used in

conventional aircraft. Another example is the Boeing 787 Dreamliner, which is often described as a composite aircraft. Titanium represents 15% of its total weight. As shown in Figure 1-2 (b), titanium makes up the biggest share after composites (50%) and aluminium (20%). The percentages in the figure correspond directly to the large proportion of composite components used in the construction of a Boeing 787 (Wagner and Norris, 2009).

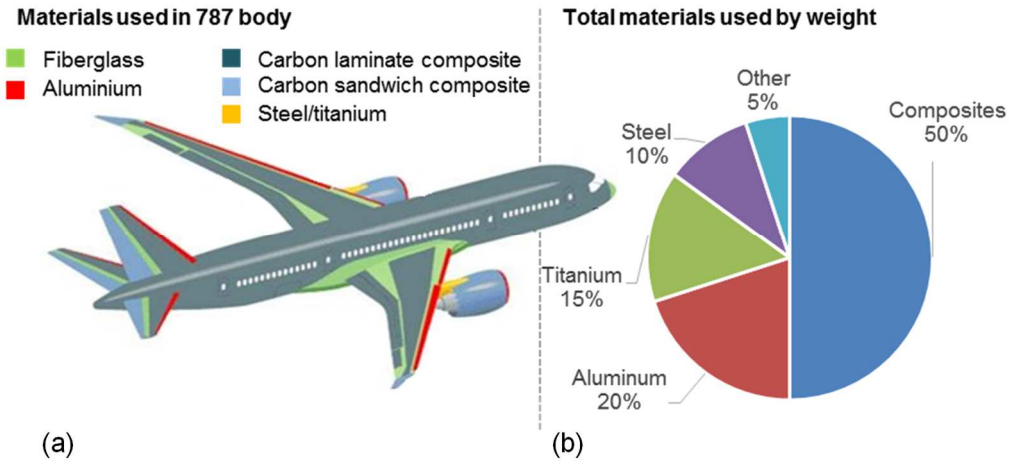

Figure 1-2: Latest materials used for airplane manufacturing. Data correspond to Boeing 787 Dreamliner: (a) material type (b) by percentage weight (Hale, 2006).

Unlike in the aerospace industry, titanium has not found widespread application as major structural material in the automotive sector. Despite the same beneficial requirements for strong lightweight material being applicable, the automobile consumer market is more cost-sensitive, which limits the amount of titanium that can be used. Until recently, the use of titanium in passenger vehicles was restricted to *prototype-stage,* racing cars and special purpose cars. The fact that lightweight alloys can reduce vehicle mass, which in turn improves fuel consumption and enhance performance, has resulted in increasing acceptance and use of titanium in the automotive industry. Titanium currently maintains a good share of total automotive engineering.

Potential applications have been found in internal combustion engine, where titanium is deployed in components such as valves, valve springs and retainers, and connecting rods. Further applications such as brake systems, suspension springs, exhaust pipes and mufflers are now common and these components are mass-produced. Table 1-2 gives a brief list of high-end automobile components made from titanium alloys.

In armour, its excellent strength/weight ratio, low ferromagnetism and compatibility with composites have made titanium a desirable material for upgrading military ground compact vehicles. Examples are the Bradley Infantry Fighting Vehicle and Abrams Main Battle Tank, in which the high cost of titanium has been overcome using plates made by low price techniques (Boyer, 2010).

Table 1-2: Summary of standard auto components made of titanium (Faller and Froes, 2001).

Year	Component	Material*	Manufacturer	Model
1992	Connecting rods	Ti-3Al-2V-rare earth	Honda	Acura NSX
1994	Connecting rods	Ti-6Al-4V	Ferrari	All 12-cyl.
1996	Wheel rim screws	Ti-6Al-4V	Porsche	Sport wheel option
1998	Brake pad guide pins	CP Grade2	Daimler	S-Class
1998	Brake sealing washers	Ti grade 1s	Volkswagen	All
1998	Gearshift knob	Ti grade 1	Honda	S2000 Roadster
1999	Connecting rods	Ti-6Al-4V	Porsche	GT3
1999	Valves	Ti-6Al-4V & PM-Ti	Toyota	Altezza 6-cyl
1999	Turbo charger wheel	Ti-6AL-4V	Daimler	Truck diesel
2000	Suspension springs	TIMETAL LCB	Volkswagen	Lupo FSI
2000	Wheel rim screws	Ti-6Al-4V	BMW	M-Techn. Option
2000	Valves spring retainers	β-titanium alloys	Mitsubishi	All 1.8 l – 4-cyl
2000	Turbo charger wheel	γ −Tail	Mitsubishi	Lancer
2001	Exhaust system	Ti grade 2	General Motor	Corvette Z06
2001	Wheel rim screws	Ti-6Al-4V	Volkswagen	Sport package GTI
2002	Valves	Ti-6Al-4V & PM-TI	Nissan	Infiniti Q45
2003	Suspension springs	TIMETAL LCB	Ferrari	360 Stradale

**PM: powder metallurgy titanium alloy; LCB: low-cost beta titanium alloy*

The expansion of titanium sheet applications to replace steel panels (costing 50–100 times more), is not expected in the near future. At its present high cost, titanium is only justified for niche design applications in the auto industry. In conclusion, titanium has established a foothold in the mass-market of the automotive industry, with an obvious potential for further expansion; the only challenge to overcome is the material price.

The biological compatibility of titanium is very attractive in medical applications. It offers an excellent set of properties (Table 1-3,), including immunity to corrosion, a relatively low modulus and density, an absence of tendency to create thrombi upon contact with blood (Bauer *et al.*, 2013).

Table 1-3: Requirements for biomedical material (Bauer *et al.*, 2013).

Property	Desirability
Biocompatibility	Non-inflammatory, non-toxic, non-carcinogenic, blood compatible, non-pyrogenic, non-allergic
Sterilizability	Not destroyed by typical sterilizing techniques like autoclaving, dry heat, ethylene oxide, radiation
Physical characteristics	Strength, elasticity, durability, thermal expansion
Manufacturability	Machin-able, formable, mouldable

Among all the alloplastic materials available, titanium continues to be the mainstream material used, due to the abovementioned attributes (Table 1-3). It has a nonreactive property (nontoxic, no-allergenic, and fully biocompatible) as an implant material and ability to join with bone and other tissue that naturally matches the requirements for implantation in the human body (Adamus, 2007). Surgical instruments, orthopaedic implants, and dental implants made from titanium are widely encountered. As the focus is on the use of titanium sheets, custom-made cranial, jaw and face prostheses are relevant examples.

Advances in medical imaging include CAT (computerized axial tomography) and MRI (magnetic resonance imaging), and enabled construction of 3D models of anatomical structures for several medical needs. By combining imaging techniques with CAD/CAM technologies, fabricating more apt and stable implants from titanium sheets will be more feasible. Consequently, a reduction in surgery time and better aesthetic results with high degree of customisation, is becoming viable at low cost (Saldarriaga and Vélez, 2011; Rocha *et al.*, 2013).

The work in this dissertation signifies a part of broader research project conducted in the Industrial Engineering Department at Stellenbosch University. As illustrated in Figure 1-3, the research project is directed to developing of resource-efficient manufacturing process chains for medical applications. Single point incremental forming process (SPIF) has been selected to be evaluated as a cost effective manufacturing alternative to the production of patient-specific knee replacements.

CP grade 2 based sheets, characterise moderate ductility and workability at ambient temperatures. Therefore, they have been as chosen to search the potential of the SPIF in fabricating of customised unicondylar knee arthroplasty and for developing of process map for the SPIF of this biocompatible material.

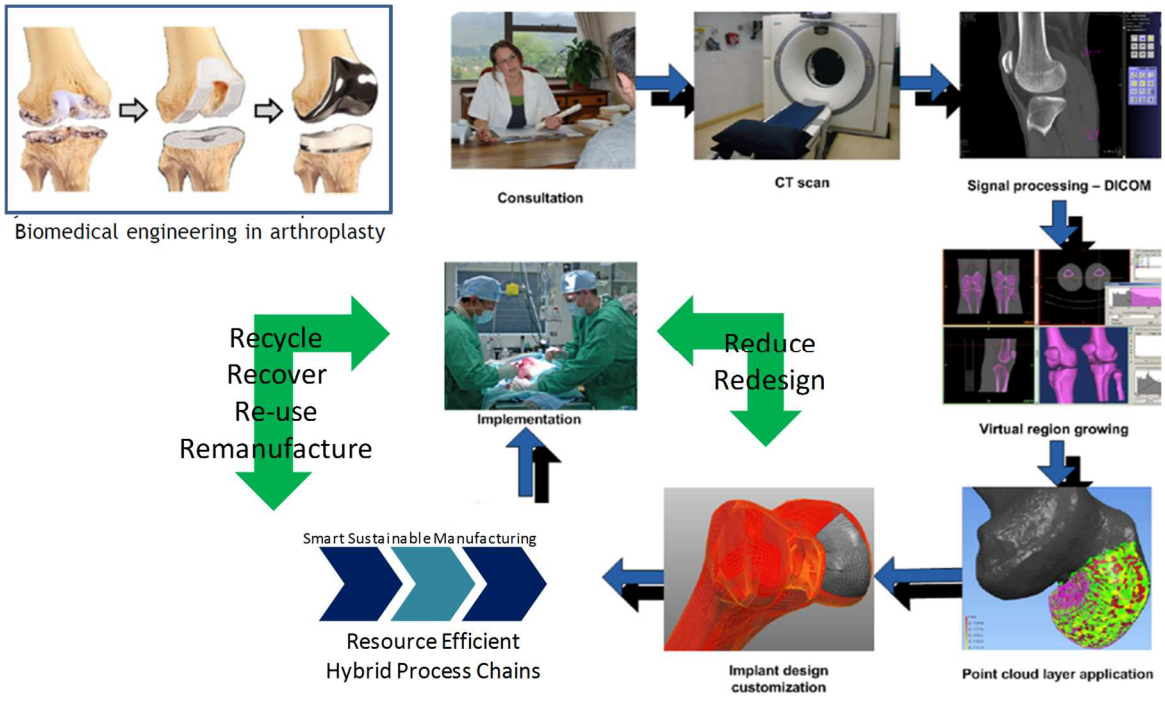

Figure 1-3: Framework for efficient SPIF process chain for a customised unicondylar knee arthroplasty from titanium grade 2 sheets (Oosthuizen 2017).

1.2 Novel process technologies to meet global challenges

In manufacturing, titanium and its alloys are characterised by their poor formability at room temperature, strong microstructural sensitivity to processing, low thermal conductivity and a strong affinity towards gases when hot formed. Chemical composition and microstructure are responsible for their properties, and the reduced workability of titanium alloys is attributed to their hexagonal, close-packed crystal structure. Depending on influence of alloying elements on beta–transus temperature, titanium alloys are classified according to the predominant phase into alpha, alpha-plus-beta and beta. The focus in this dissertation is on the single-phase alpha titanium, namely the commercially pure titanium (CP Grade 2).

The low alloy CP Grade 2, exhibits a good balance of strength and ductility. The material is very corrosion resistant and sheets can readily be shaped at ambient temperatures. CP Grade 2 sheets can be drawn, stamped, or spun, using techniques and equipment similar to that applied for steel. However, particular attention must be paid to ensure its trouble-free cold fabrication; low ductility at room temperature, high springback as result of a lower modulus of elasticity, and its tendency to gall against forming tools (calls for the use of effective lubricant), must be considered.

In manufacturing, today, challenges are presented by increasing instability in global markets, short innovation cycles, cost pressures and generally expensive resources. At the same time, these challenges have opened new business opportunities for manufacturers, who are able to adapt to the market dynamics. Adaptability to achieve sustainable competitiveness is attained by resolving the dichotomies between scale and scope, and between plan and value orientation (see Figure 1-6); this relates to offering flexible manufacturing options, having a minimum carbon footprint, being able to produce customer-specific products at mass production costs, and optimising the use of resources (Brecher and Özdemir, 2015).

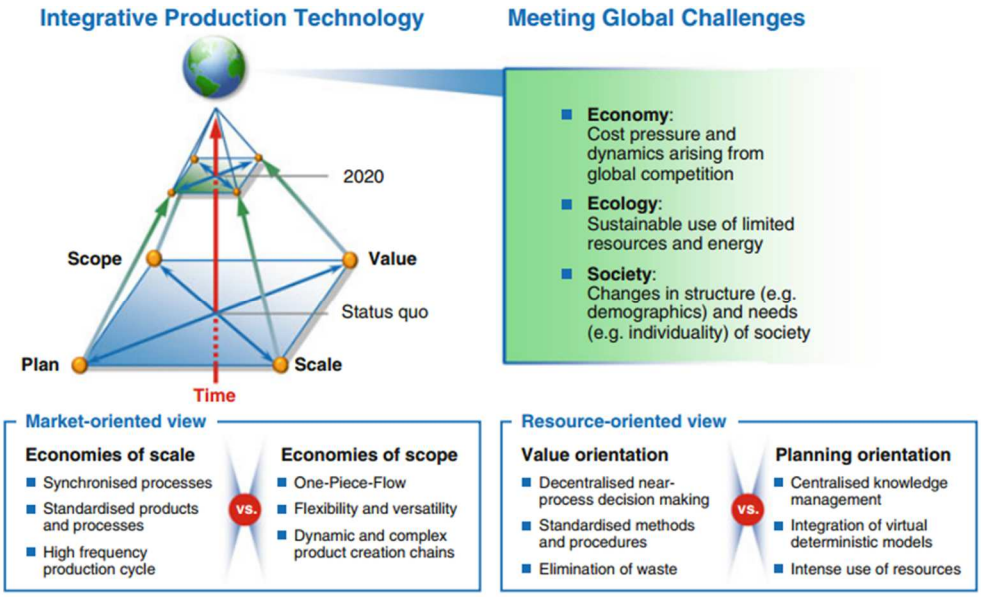

Figure 1-4: Integrative production for meeting manufacture challenges in economic, ecological and social environments (Brecher & Özdemir, 2015).

In the field of sheet metal forming, a number of novel techniques have emerged over the past decade. They are oriented mainly to applications where speed and low costs are preconditions for time-to-market reduction and global competitiveness. These techniques attempt to confirm agile sheet metal forming principles by eliminating the need for matching dies, reducing the number of forming steps, increasing the degree of freedom of a process, and allowing for late-stage product differentiation (Jeswiet *et al.*, 2005; Daehn, 2007).

Among these new processes, incremental sheet forming (ISF) is attractive for producing complex, high cost components for aerospace and other industries. For small batch sheet forming, ISF incurs minimal initial costs when compared to conventional sheet forming processes such as stamping and deep drawing. ISF allows the forming of sheet metal parts with minimal preparation time and manual processing, using conventional computer numerical control (CNC) machines, resulting in high flexibility and low tooling costs.

The simplest configuration of ISF, also known as single point incremental forming (SPIF), is a truly die-less, and is based on a layered manufacturing principle. By proper tool path planning, it is possible to produce very complex shapes of thin-walled components, without the need for a die. The applicability of the SPIF process has a wide range of applications in the field of rapid prototyping, and is used in aerospace and automotive industries, for manufacture of medical implants, as well as in architectural engineering (Rocha et al., 2013; Fan and Gao, 2014).

In the SPIF process, input factors that affect performance can be classified into freely-selectable or controllable process parameters, for example tool-tip diameter and features of the tool path. Other parameters, which are dependent on the geometry of the formed component, are the nominal final slope component, the radiuses of curvature, as well as the type and thickness of material to be formed. Figure 1-8, illustrates the steps commonly involved in the planning of an ISF process.

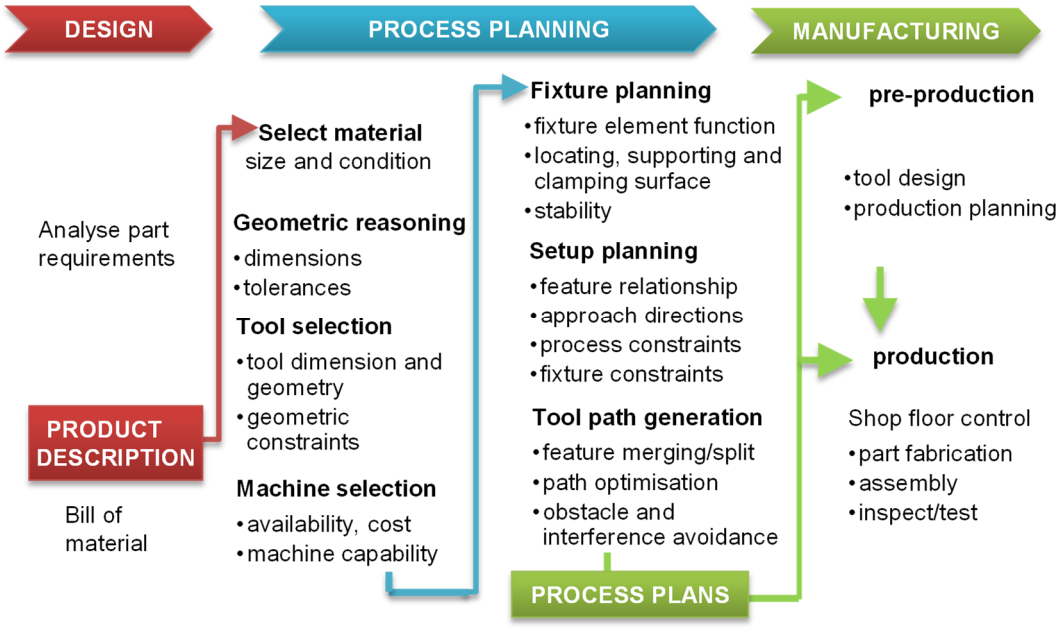

Figure 1-5: Steps/ activities involved in planning the ISF process. Adapted from Rajput (2007)

During the forming operation, the sheet thickness is reduced due to the local pressure. The minimum thickness specified for a model, together with the highest wall slope, is essential in selecting the initial thickness of the blank sheet. The definition of sine, known from shear spinning, is a good approximation to determine the final shaped wall thickness depending on the local draw angle and blank initial thickness (Meier, Magnus and Smukala, 2011).

The mechanical properties of the specified material, in particular its ultimate tensile stress (UTS), provides a first indication of the magnitude of the forces that will be generated during deformation. Under standard ISF conditions, there is a simple proportion between the UTS and the force needed to create plastic deformation in the material of the workpiece; this can be useful in designing the tooling and selecting the appropriate equipment for the ISF operation. Thus, the fixture supporting the workpiece, the forming tool and the CNC machine can all be examined in terms of rigidity of the set-up.

Users of ISF usually need to design and manufacture their own forming tools, as they are not yet commercially available. The first step of the tool design process is to take account of the smallest features (radii) to be formed, considering the target geometrical profile of the CAD model. After determining the approximate values of the forming loads, the initial blank thickness, and the applicable tool-tip size, the next stage of the design process can be initiated, if the required machine capacity is available. The machine characteristics entail such factors as stiffness, maximum vertical stroke, speeds and rate of increment.

In planning ISF operations (see Figure 1-5), the model and tool data must be entered into a CAM package, suitable (spiral/contour) finishing tool paths must be generated, vertical and horizontal steps must be set, and spindle speeds need to be specified. Furthermore, attention should be paid to cutter compensation, which is achieved by offsetting the tool-tip by its radius, as well as to the determination of subsequent terms. To control elastic recovery of the sheet, small incremental deviations in keeping with the component size, must be implemented over form. The CAM software enables description of the best tool trajectory in the cutter location (CL) file, facilitates simulation runs, and allows evaluation and adjustments when necessary. Once all gears work probably and all clatters have been eliminated, the CAM postprocessor can convert the CL file into data, which is executable on the CNC machine.

Upon complying with all the preceding steps, the stage is reached where ISF of a particular item can be performed. The initial production provides feedback, allowing assessment of the quality of the item produced, as well as the forming process, which can be optimised by making adjustments as necessary.

1.3 Problem statement

Since the initial development of ISF, a lot of research on this process has been carried out in both academia and industry. So far, various studies have been conducted on the topic of ISF, leading to numerous publications. In these works, several process aspects have been explored in depth. The research was mostly based on experimental work, some numerical modelling, and a few analytical studies; it resulted in a large amount of information and important findings. The overall conclusion of these studies deliberates ISF as a potentially

viable and economically affordable approach to fabricating functional sheet components in small-scale production runs.

ISF limitations are often recognised as restricting the range of its industrial application. These limitations are excessive sheet thinning; low geometric accuracy associated with a high springback effect; long processing time, and the dearth of a reliable tool for virtual process planning.

Another impediment that delayed widespread commercialisation of ISF in industry may be linked to the process being a hybrid combination of two different technologies. It has to be stated that the ISF traces its origin back to metal spinning and incremental deformation by a black-smith's hammer (Dixit, 2013). In another way, ISF has been industrialised through modification (deboning) of the typical sheet forming operation by elimination of the concept of matching dies, and incorporation of CNC equipment.

The integration of the high speed and accuracy of CNC with related CAM programming and its application to the sheet forming process, leads to greater flexibility, potential for individualisation and reduced resource consumption. Even it might seem that effectively sheet metal work and machining are not very different. In practice there are several requirements which are very dissimilar between the two processes and these differences need to be well thought through when considering a hybrid process (Date, 2013; Brecher and Özdemir, 2015):

Firstly, the domain of sheet metal forming is very different from that of machining, which demands a different class of knowledge, processes, tools and machines to be industrialised. As outlined in Figure 1-6 the distinctions in process chain between machining and sheet forming start early, when material attributes are tested and a suitable material is selected, and extend through to process design, product design, tool design, CNC programing, inspection, quality control and assembly (Date, 2013).

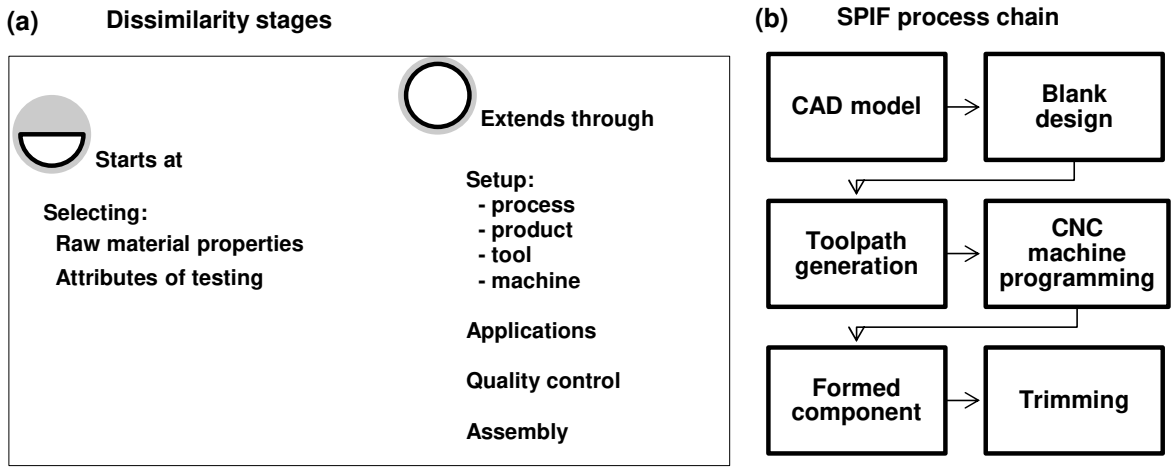

Figure 1-6: The dissimilarity between machining and sheet forming; (a) the stages of dissimilarities in process chains between machining and forming; (b) a SPIF process chain

The steps in SPIF process chain are given in Tables 1-4(a)–(c), as coming from both the sheet work and machining chains. The arrows in the tables indicate the dominant affinity.

Table 1-4: Affinity of ISF parts to forming / machining process chain (a) in the setup stage

Point of comparison	**Machined parts**	**ISF parts**	**Sheet metal parts**
Rigidity of parts	Non-compliant parts	⇨	Compliant parts
Designing and dimensioning	Orthogonal datum planes (reference)	⇨	Special features (holes) not shift/get deform. Edges/ boundaries go into trim
Fixture design	**3-2-1** principle used for location in fixture	⇨	**N-2-1** principle (N > 3), Very sensitive to sequences of clamping
Tool materials	Machinability is associated with tool life i.e. tool material	⇨	Tool geometry and formed sheet properties determine formability
Machine tools major considerations	Complex tool paths accuracy, cutter compensation, collision checks, low forces	⇦	Built to deliver large forces and stiffness

The differences extend through the application stage, where ISF is more relevant compared to milling operations in terms of tooling cost, forming zone and diversity of shapes produced with single tool.

Table 1-4: Affinity of ISF parts to forming / machining process chain (b) in the applications stage

Point of comparison	**Machined components**	**ISF parts**	**Sheet metal parts**
Standardisation of tool geometry and control parameters	Easy; tool angles, geometries, single and multipoint are widely available	⇦	Impractical, only guidelines are feasible. Classification of components based on similar features
Cost of tooling	Much lower. Single tool for many shapes Smaller lead-time in procuring tools.	⇦	Expensive (not mass produced) Change of tool expensive and difficult. Large lead time
Generation of the desired shape	Movement of one tool (different shapes)	⇦	Linear tool movement + tool design (dedicated)
Diversity of shapes	Any shape with suitable tool-path	⇦	Needs large diversity of tool designs and control variables
Zone of metal affected at a given time	Deformation zone is localised to current tool position	⇦	The entire sheet blank gets deformed
Shape of the zone of deformation	Relatively unchanged (steady-state process)	⇨	Shape and size of deformation evolves continuously

ISF characterises the quality issues in sheet forming operations, which include more variables than that in machining. Material thinning, uniformity in thickness, flatness of the flange, surface blemishes, burring, springback, are basic characteristics in sheet forming.

Table 1-4: Affinity of ISF parts to forming /machining process chain (c) in the quality control and assembly

Point of comparison	**Machined components**	**ISF parts**	**Sheet metal parts**
Dimensional gradients/ deviations	Unintended gradients can be avoided	⇨	Unintended gradient due to thinning, springback are part and parcel of process
Tolerances achievable	Close tolerances (microns/ nanometres)	⇨	Non-achievable— springback, part complaints and variables not under complete control.
Surface finish and integrity	Several stages of finishing operation are applicable	⇨	Limited extent, no finishing operation. Useable after trimming
Rework and ease of rework	Out of tolerance parts can be salvaged	⇨	Salvaging out-of-tolerance parts is not possible
Springback and residual stresses	Very small, machining relieves surface residual stresses	⇨	Unreleased because part shape and processing history
In-process stability of shape	Stable shape throughout inner as well as external surface	⇨	Determined by interplay between residual stress, separating operations, trimming & punching
Inspection and assembly	Dimensional errors can be inspected. Assembly occurs by selective assembly	⇨	Only at well-defined critical points. Out-of-tolerance parts need to be assembled within tolerances

Secondly, standardisation of processing variables is difficult in sheet metal working; forming conditions tend to be specific to material, product design and tool design. Establishing design guidelines, which are relatively independent of these variables, is the feasible option when designing the sheet forming processes.

Thirdly, the impressive experiences and knowledge previously accumulated and documented by the researchers, are spread over a wide range of topics, publications, and periods, and a general model for process design has not yet been developed. Interchange of this information, knowledge, and of the skills, involves a high level of cooperation and integration among the various parties. Although this is a common phenomenon in the research space, it is not always the case in the industrial environment. Thus, little transfer of process knowledge has occurred across the two trades of metal forming and machining. Yet, the reliable definition of the ISF parameters has been forthcoming from expenditures on trial-and-error approaches forming part of extensive experimental programmes. An accurate process design is not possible at this stage due to a lack of knowledge and the inadequacy of current simulation tools. Thus, the potential benefits in reducing turnaround time using this flexible technology have yet not been realised due to time, complexity, and costs constraints on planning and programming.

Fourthly, and most notably, the applications of SPIF are mainly accessible in technical literature where the focus is on aluminium and steel. There is very little information on materials which are hard to form, such as titanium sheet alloys which are more relevant to high-value, small-batch and customised components (Fan *et al.*, 2009; Lu, Ou, *et al.*, 2014).

From the brief discussion above the following benefits of SPIF applied to titanium are apparent:

- Titanium is an attractive material for numerous applications, but its use has been mainly restricted by material and manufacturing costs.
- Significant cost reductions can be realised from technologies devoted to reduce the buy-to-fly ratio and enlarge the application scope of titanium alloys to small series products.
- There is a growing need for customised products, and for rapid prototyping technologies in forming of sheet components.
- Regarding the needs mentioned in the previous bullet point, SPIF is a promising approach, and an active research topic, which can fulfil these aforementioned. However, several process issues still need to be industrialised.

The following research questions are therefore formed to guide this study:

- What is the process demand of SPIF as a flexible forming technique?
- What are the process limitations for SPIF of CP Grade 2 sheets?
- How can the process variables of SPIF, as applied to CP Grade 2 sheets, be manipulated to create resource-efficient process chains?

1.4 Research aim and objectives

Process mapping is an approach that represents process outcomes in terms of process variables. The development of a processing map which presents relationships between key SPIF variables and the formability of titanium Grade 2, is viable and a worthwhile avenue of research. Once identified, it will create a knowledge base that will increase understanding, and uncover opportunities to expand the process applications. The aim of this study is twofold: firstly, to provide a better understanding of SPIF process, and secondly, to develop a processing-map for CP Grade 2 sheets. As with any typical engineering approach, the aim is to seek simplicity and efficiency. To achieve that, the following steps have been undertaken:

1) In order to broaden the understanding of the demands of ISF, a systematic quantitative literature review of state-of-the-art ISF was conducted on data from previously accomplished research efforts; this data has been classified and documented.

2) The documented data and knowledge were then deployed as references when identifying key design process variables. Wherever possible, these variables and their effects on ISF have been visually presented in the form of charts and tables, with related deductions and conclusions provided in the adjoining text.

3) A test platform for experimental work was designed and created. It included the design and manufacture of a dedicated fixture and forming tools, the development of a test benchmark, and setting up and connecting a data acquisition system to the testing platform.

4) The design of experiment (DoE) and one factor at a time (OFAT) approaches were implemented to develop a qualitative correlation that describes the cause-and-effect relationship between SPIF process control parameters and modelling the process limitations formability, temperature and force.

5) The process mapping approach was undertaken. It consists of experimentally tracking five process variables that are critical to the SPIF process, as well as process outcomes such as formability and product quality. The five process variables are sheet thickness, tool-tip size, vertical step, tool feed and rotational speed.

1.5 Research methodology

The research in this dissertation was a mixed-methods study conducted in three phases as follows:

Phase I: A systematic quantitative literature review has been conducted. Hereby-significant process data on SPIF key operating parameters and forming conditions, from more than 100 relevant research articles and studies, were analysed and documented. The information and statistical data extracted from empirical work reported in these articles were drawn on as references when the crucial design factors, the presumed relationship among them and their variable extremities, were characterised. A conceptual framework of SPIF was developed, based on this critical and evaluative review.

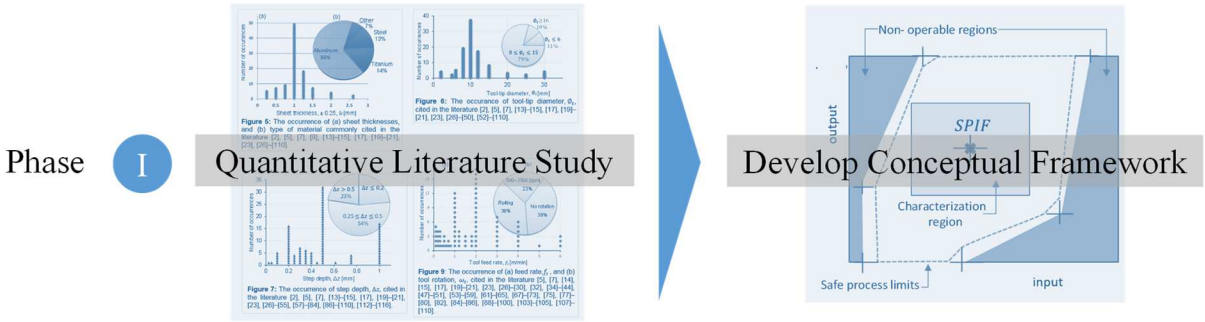

Figure 1-7: Research methodology Phase I, results met in Research Steps 1 and 2

Phase II: An experimental study was carried out to understand the SPIF process limits as applied to titanium Grade 2. The DoE approach was implemented to characterise both the main and the interactive effect of the SPIF key factors on the process outcomes. Process characteristics in terms of formability, thermal and mechanical limits for the selected material, were established.

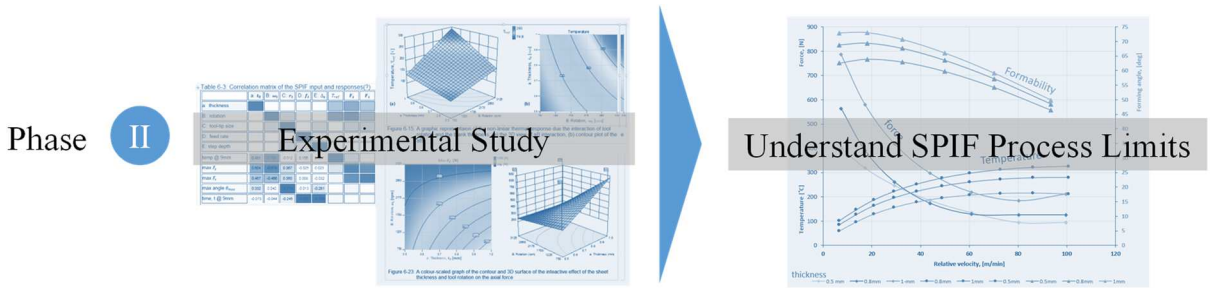

Figure 1-8: Research methodology Phase II , results met in Research Step 3 and 4

Phase III: Sequence of OFAT experimental campaigns were conducted to validate the process limits and revisit the developed conceptual framework. Based on the process data and knowledge accumulated, a correlation matrix of the cause and effect in SPIF and a final framework (process map) for the SPIF of titanium Grade 2 as a function of the five key process variables were produced.

Figure 1-9: Research methodology Phase III , results met in Research Step 5

1.6 Dissertation outline

In broad outline, the content of this dissertation can be divided as follows:

- The document begins with overview of the current flexible sheet forming technologies including the simple-pass and the incremental forming approaches. The goal is not to provide a detailed analysis of these technologies, but to allocate and justify selecting SPIF as a cost-effective manufacturing process for a one-off component and small production lots. A selection of existing flexible forming processes for sheet metal forming are compared and results presented in Chapter 2.

- The mechanics of the ISF process was not treated at an advanced level in this dissertation, given the availability of the many more-specific reference texts. Even so, the abridged presentation of this study provides significant insight into the mechanical and thermal demands of SPIF. Instead of a deep analysis of the process mechanisms, several forming aspects are broadly discussed. An equitable study of the current understanding of the mechanical and thermal loads during SPIF, that assist in characterising the broad limits of the process, is deliberated in Chapter 3.

- In Chapter 4 the results and analysis of the process data from the systematic quantitative literature review, were reported. The goal is to identify the key process factors, the interaction between them and their explicit influences on forming. At the end of this chapter, a conceptual process framework is set out. The layout of this dissertation is illustrated in Figure 1-10.

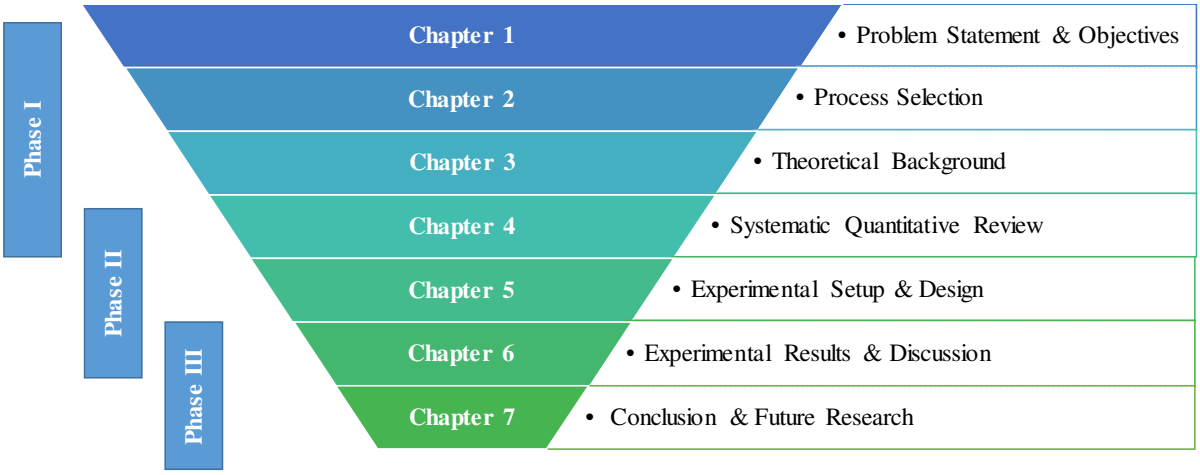

Figure 1-10: Research layout and document roadmap

- In Chapter 5 an overview of the equipment used, and the procedures and methodology followed, are given. Details of the material and data acquisition apparatus applied are reported. Information on layout of the experiment treatments for both the DoE and OFAT campaigns is provided.

- In Chapter 6 an analysis and discussion of the obtained experimental results are given. Relationships (with relative strengths) between the SPIF variables and responses are presented. Process limitation in terms of formability, thermal and mechanical demands as related to the design factors, are established.

- Finally, in Chapter 7, conclusion of the study and recommendation for future research are given.

CHAPTER 2 OVERVIEW OF FLEXIBLE FORMING PROCESSES

The flexible forming technologies currently available in the field of sheet metal forming may broadly be grouped under two headings, as illustrated in Figure 2-1; the simple-pass approach and the incremental forming approach.

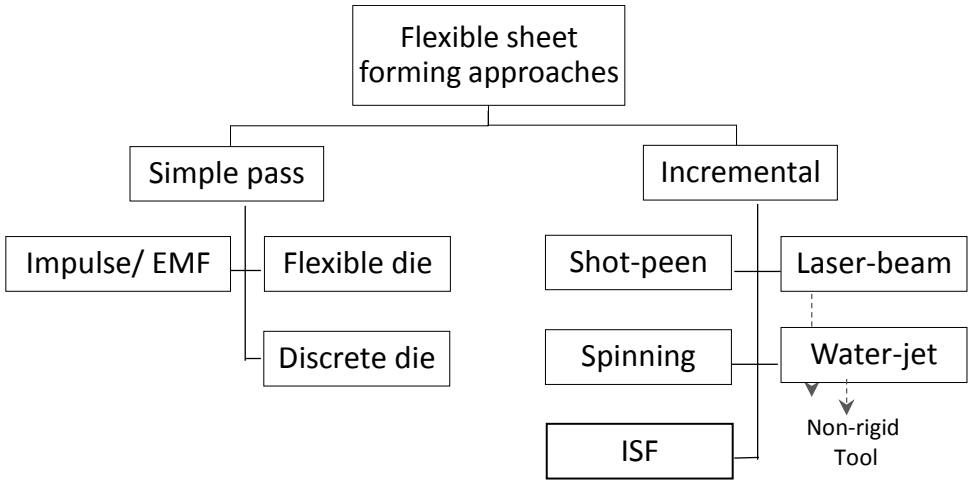

Figure 2-1: Broder classification of flexible sheet forming approaches

2.1 The simple pass approach

This approach groups all the process variations in which the final product is shaped by a simple tool trajectory. Impulse forming, flexible (media- based) die methods and forming with discrete dies are some technologies currently used in rapid sheet forming.

2.1.1 Impulse forming

High velocity, also known as impulse forming, includes all processes that convert stored energy to form workpiece in a very short cycle. Forces from explosive, electrical discharges, or electromagnetic fields are applied to accelerate the workpiece to a high speed (> 100 m/s), against a single-sided forming die. Lately, forming with the high-impulse electromagnetic force (EMF) technique has been the subject of considerable interest, mainly in the automotive industry. Reasons for this include the demand for the production of high-strength sheet components, and the engineering development attained in high-performance voltage equipment (Daehn, 2007; Carson *et al.*, 2010).

EMF is based on the utilisation of current driven electromagnetic forces (Lorentz forces) acting on workpiece such as sheets or tubes. A capacitor bank is charged to store a significant amount of energy (1–100 kJ) at a high voltage (up to 20 kV). This energy is then rapidly discharged through a specifically designed ‘coil’ or ‘actuator’. Figure 2-2, is a schematic diagram of the high-velocity EMF process, it combines EMF for both sheet forming and cutting operations.

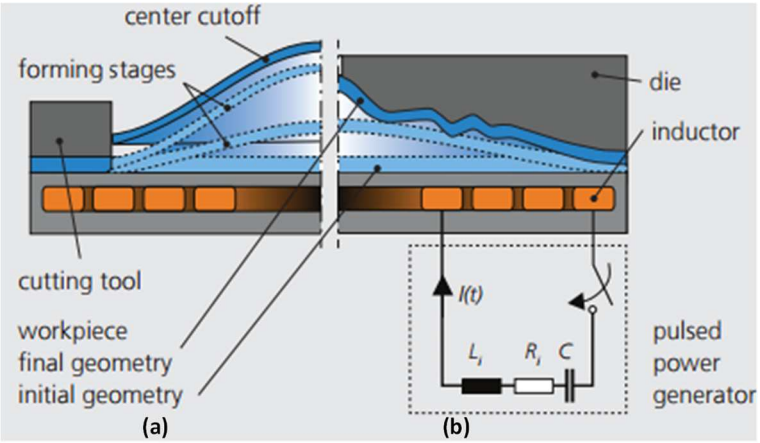

Figure 2-2: Principle of the impulse forming process : (a) In sheet cutting operation, (b) In sheet forming operation (IWU, 2016).

The primary current creates a magnetic field and induces currents that run in opposite directions in the nearby workpiece. This provides a high electromagnetic repulsion between the actuator and workpiece, generating a high magnetic pressure (> 250 MPa), that persists only over a short period (< 30 µs). The pressure is sufficient to stress the workpiece beyond its yield strength and high strain rates (up to 10^4/s), resulting in permanent deformation (Daehn, 2007).

EMF processes have the following advantages:

- High process repeatability due to a high-level controllability of the forming pressure generated
- Only single-sided dies and light tooling sets are applied due to low static forces
- High forming rates; material reaches a velocity of 100 m/s within < 0.1 µs.

Process limitations of EMF are:

- Non-conductive materials need a conductive drive attached to the workpiece
- Unsuitable for deep drawing operations; the very short period of deformation reduces the ability of the material to stretch (Davis and Hryn, 2008)
- The short lifespan equipment (coils, capacitor banks, and fast-acting switches)

The design concepts and manufacture of customised coils for specific applications represent critical factors; moreover, the knowledge and information pertaining to these concepts are based on the experience of the suppliers of these components – this information is unavailable in the market.

2.1.2 Media-based forming

In flexible-die forming, one of the die in a set (punch/die) is replaced with a flexible material, such as a rubber pad, polyurethane, or a pressurised fluid. The **rubber pad** is used to produce components from sheet metal over a positive forming die. The sheet blank is placed on the form-block (metal die) and formed to the desired shape under continuous pressure during a complete stroke of the press. The flexible (rubber) material applies nearly equal pressure over the entire workpiece surfaces as it is pressed around the form block (Kalpakjian and

Schmid, 2008). The **Sheet hydroforming** uses a hydraulic fluid in flexible bladder or diaphragm to shape sheet material against a single tool. The main two types (fluid cell and deep draw) of sheet hydroforming are briefly discussed below:

The fluid cell forming is a cost effective sheet metal forming process designed for both lower volume parts production and prototyping. In the fluid cell, the part is formed over a single tool using the force of the diaphragm. The basic principle of the fluid cell process corresponds to pure stretch forming, i.e. the surface extension required for shaping is generated only from the sheet metal thickness. No material after-flow occurs due to the exterior lock-bead. As shown in Figure 2-3, the process uses a soft diaphragm sits under the blank and seals the lower die volume, which is filled with highly pressurised ((100–140 MPa) hydraulic oil, to press the sheet blanks uniformly into and around a rigid, shape-defining tool (Campbell, 2011).

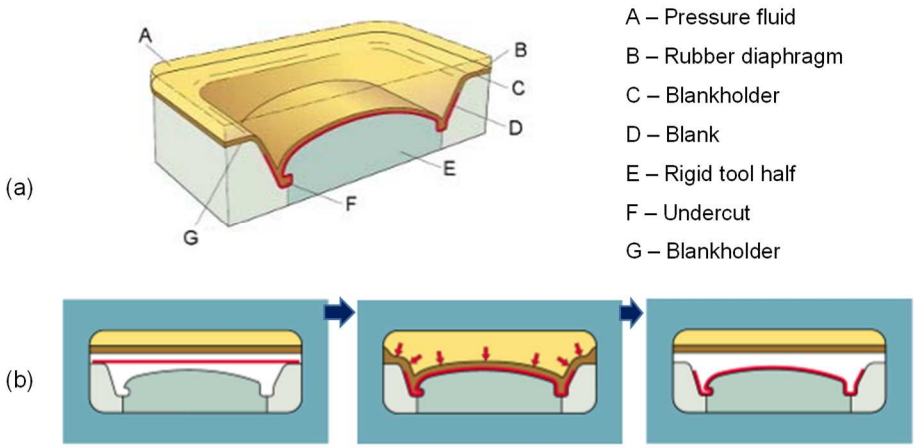

Figure 2-3: Principle of the fluid cell forming: (a) components of the fluid cell system, (b) forming stages ((Yadav, 2008).

Fluid cell represents high-performance alternative to traditional rubber-pad presses. As the later (rubber-pad) typically has limitations on a maximum pressure (10 MPa). The fluid cell capable of exerting much higher pressure (up to 70 MPa) on the formed sheet thus helps provide an even pressure on the sheet, results in reduced material wrinkling, increased definition and less manual hand-finish.

Specific presses, so-called fluid cell presses, are required for applying the fluid cell technology. These presses differ from conventional presses in so far that they do not comprise a press ram. The ram is substituted by a specific membrane (fluid cell unit) to which internal pressure can be applied. Thus, the fluid cell unit undertakes the function of the forming punch that is generally required. By applying this method, an entire cost-intensive element of plastic deformation of the forming tool can be saved.

In the deep draw sheet hydroforming, the parts are formed using the same diaphragm principle in Fluid cell forming. However, the rigid tool (Figure 2-4) is attached to a moveable cylinder (works as punch) which extends up into the diaphragm during forming. Parts that require a controlled flow of the material, such as cans, boxes or those with curved flanges, which have a greater tendency to wrinkle, benefit greatly from the deep drawing action.

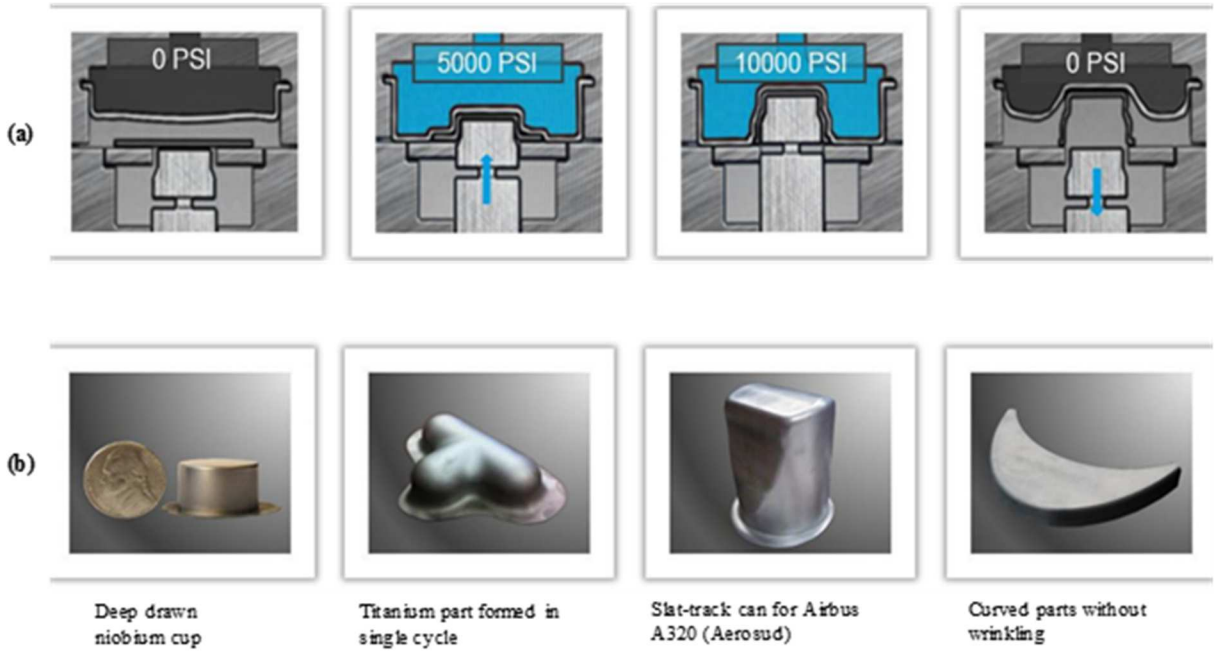

Figure 2-4: Deep draw hydroforming process: (a) Schematic of forming steps and (b) examples of applications. Source (Triform, 2012)

The uniform application of very high pressure forces the metal evenly into intricate shapes, including undercuts. Besides uncertainties related to variation in material thickness, properties and lubrication usually rise in traditional metal forming, hydroforming processes can also exploit actuation of fluid pressure or volume flow. Online sensing of strain, strain rate, temperature and fluid pressure increases opportunity to add more value through metal forming and to tailor product properties more precisely. However, the sensing approach is more constrained in hydroforming operations, as the fluid must be fully contained and this has led to increased interest in off-line closed-loop control (Allwood *et al.*, 2016). Recently, important progress has been made with the fluid cell process due to the development of high-pressure sealing techniques, and the advanced level of high-pressure computer control systems.

Advantages of media-based forming can be as follows:

- Saving in tooling costs compared to stamping presses
- Decrease forming operations and reduce scrap
- Higher and uniform strain distribution over the entire sheet surface.
- High accuracy, good surface finish, lower springback and uniform thickness are obtained.

Limitations of media-based forming are:

- Very high pressures may be required to form components with small fillet radii.
- Slightly high material consumption and the preparation and finishing steps (generally require laser cutting operations) which increase the total forming cost.

2.1.3 Discrete die forming

Discrete element-based tooling systems are relatively new members of the rapid, low-cost production tooling family (Koc and Thangaswamy, 2011). In discrete die sheet metal forming or digitised die forming (Figure 2-5), both the forming die components are an assemblage of discrete elements (punches), as opposed to of a solid piece. The discrete nature of tools makes them reconfigurable to meet design changes. Different tool configurations can be achieved by changing the pin locations relative to each other, which eliminates the need for multiple tools. The height of each punch is computer controlled and the matrix of punches is approximated to a continuous working surface of the die (Chen et al., 2005). Such a tool can help reducing the cost and time required for designing and fabricating dies for variants of existing products.

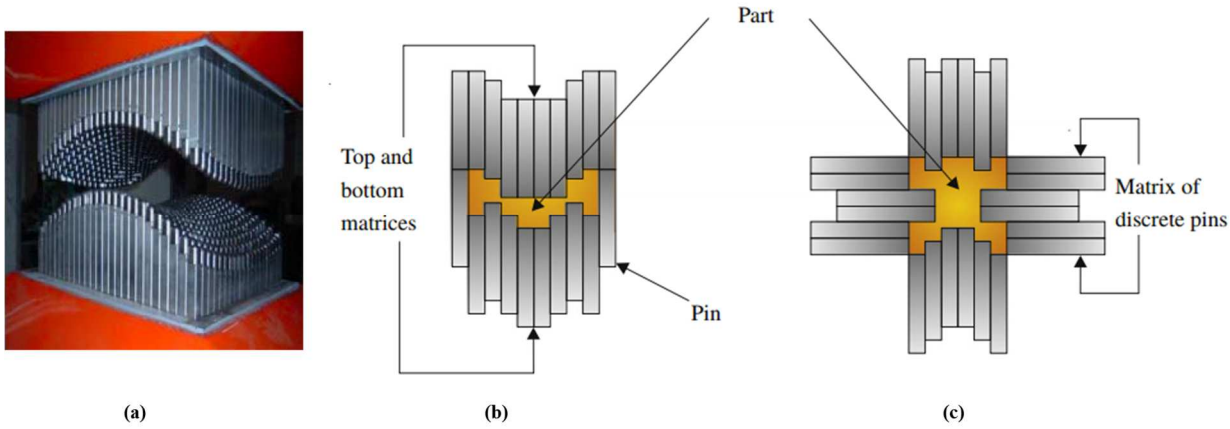

Figure 2-5: Concept of discrete-die forming: (a) Depiction of the apparatus. Li (2007), cross-sectional of the closed reconfigurable die: (b) 2-matrix setup and (c) 6-matrix setup, Koc and Thangaswamy (2011)

Advantages forming with discrete dies:

- High flexibility and short lead time (eliminates the need to design and produce dies)
- Improved sheet formability.

The following difficulties are facing the technology:

- Mechanical defects such as bulking and dimpling occur due to difficulties associated with the positioning of forming punches (Li, Cai and Liu, 2007).
- The process requires expensive equipment and a complicated control system.

2.2 The incremental approaches

The forming processes discussed in this section are described as incremental sheet metal forming (ISMF, or simply ISF), implying that a small zone of the workpiece is deformed at any instant, but the location of the deformation is relocated around the workpiece under computer control. This ISF approach leads to various advantages, for example: reduced tooling, since either no die or only a single die is needed; lower forming forces permit the die to be made of inexpensive material; and the size of the formed products is only limited by the available hardware (Allwood and Utsunomiya, 2006). Examples of the ISF process developed are:

2.2.1 Shot peen forming

This incremental process (Figure 2-6) applies steel balls as forming media. They are accelerated by compressed air to a specific velocity and directed at the form sheets.

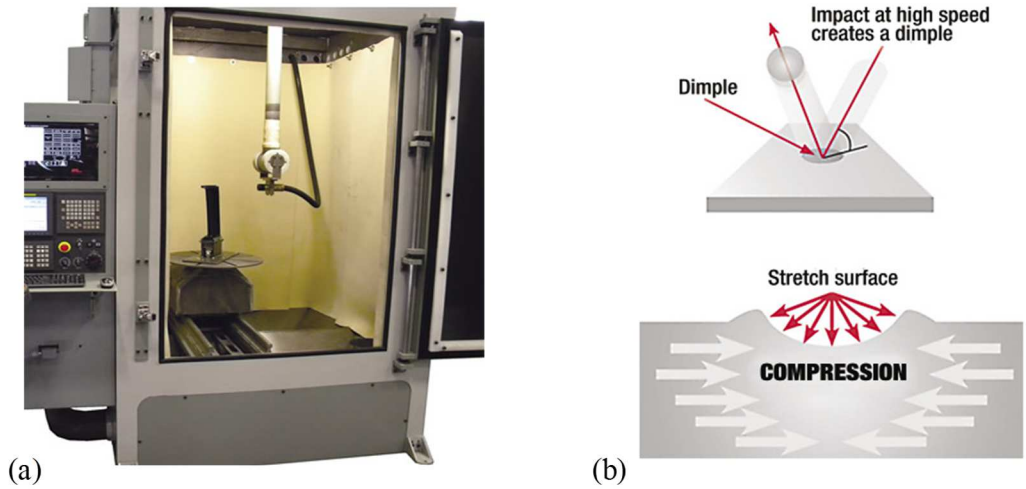

Figure 2-6: Shot peen forming process : (a) CNC shot peening machine, (b) Principle of the shot peen forming. Kip Hanson (2015).

A large number of statistically distributed tiny steel balls (shot) are blasted through a computer numerical control (CNC) nozzle, onto the workpiece surface. During impact, shot imparts kinetic energy to the workpiece. This creates plastic deformation of the material (Figure 2-6), stretching the upper surface and producing compressive stresses below the surface. This trigger the material to generate a compound curvature on the peened side. The curvature radius and direction can be adjusted by altering process parameters like shot velocity, mass flow and shot coverage. Low shot velocity produces convex surfaces, while high kinetic energy will form a concave curvature (Vieira, Almeida and Martins, 2010).

Advantages of using the shot peen in sheet metal forming:

- Die-less forming process with good flexibility and independent of the sheet size.
- Formed parts exhibit increased fatigue stress and resistance to corrosion cracking.
- Reduced material allowance from trimming

Limitation of the shot peen in sheet forming

- Only suitable for forming shallow contours with large panel shapes and large radii bends
- On-line process control is complicated, and equipment cost can be high
- Mostly a trial-and-error process, which largely depends on the operator's experience.

Current applications of the shot peen in metal forming:

The process is applied mainly for forming large-sized sheets from steel, aluminium and titanium, with sheet thicknesses of up to 6 mm (Vieira, Almeida and Martins, 2010). It is used to form aeroplane wings, fuselages, segments for space rockets, as well as various large components in the shipbuilding industry.

2.2.2 Laser beam forming

For several years, the industrial laser market has had a robust revenue growth, and it is anticipated to grow further. Figure 2-7(a) shows the industrial laser revenue from a 2015 annual economic review. There are clear indications on increased role of the laser technology in current industry, mainly, in material processing, 3D printing, flow cytometry, sensing and molecular research (Overton, Belforte and Nogee, 2015)..

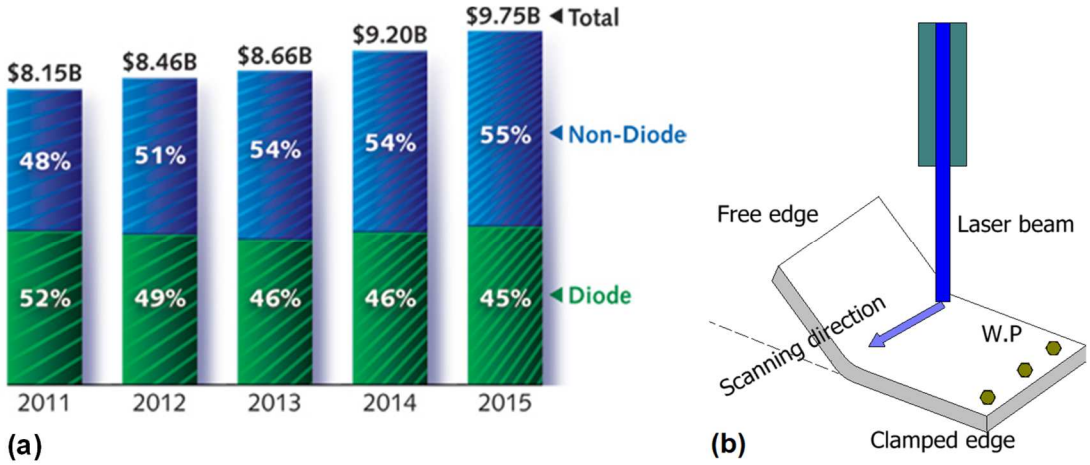

Figure 2-7: Laser beam forming (a) industrial lasers revenue, source (Overton et al. 2015), (b) schematic diagram of sheet forming with laser beam

The technology is extensively used in cutting, drilling, micromachining, marking, welding, sintering, heat treatment, and more recently in 3D printing. However, expanding laser applications into sheet forming is a relatively new and potentially promising field (Paunoiu *et al.*, 2008).

Laser beam forming (LBF) is initiated by directing a laser source onto the workpiece surface, thereby introducing thermal stresses. These thermal stresses induce plastic strain, resulting in bending or buckling of the sheet blank (Figure 2-7(b)).

The process has three forming mechanisms: a buckling mechanism, an upsetting mechanism, and a temperature gradient mechanism. The latter is the mechanism mostly used in the laser forming process. The temperature mechanism is governed by the temperature field, which in turn is influenced by three major variables: the material parameters, the laser parameters and the geometric parameters of the formed part. The material parameters are typically the thermal conductivity, coefficient of thermal expansion, density, elastic and plastic mechanical parameters, and the rate of laser absorption. The laser parameters include laser power, feed rate, beam spot diameter and wavelength of the beam, which depends on the type of laser. While the geometric variables are generally sheet length, width, and thickness (Akinlabi E, Shukla and Akinlabi S, 2012).

The available laser machines typically differ in terms of the laser sources they use. Table 2-1 presents a comparison between these laser types (Belforte, 2012; Trotec, 2016).

Table 2-1: Comparison between common laser types : CO_2, fibre and crystal (Trotec, 2016b)

Laser Type	Characteristics	Applications
CO_2 (gas) lasers	10.6 µm wavelength; most widely used laser type; based on CO_2 gas mixture; high efficiency and a good beam quality.	Non-metallic, wood, glass and plastics
Fibre (solid) lasers	1.06 µm wavelength; extremely small focal diameter; intensity is able to 100 times higher than that for the CO_2 lasers with the same emitted average power; long service life of over 25000 laser working hours.	Metals, coated metals and high contrast plastics
Crystal (solid) lasers (Nd:YAG/Nd:YVO)[*1]	1.06 µm wavelength; solid-state laser, includes expensive and wearing pump diodes; 8 000 –15 000 laser working hours; applied crystal has service life shorter than that of fibre laser.	Metals, coated metals and plastics

Advantages of using laser technology in metal forming:

- High process flexibility, with no hard tool or mechanical contact
- Applicable to the formation of objects with constant and varying thickness, and objects made of brittle or high hardness materials
- Very good potential for accuracy and controllability of forming.

The following difficulties restrain commercial application of laser technology in metal forming applications (Roohi, Gollo and Naeini, 2012; Nadeem and Na, 2013; Shidid *et al.*, 2013)

- High energy consumption due to the low energy conversion factor of laser sources
- High investment due to the expensive forming stand and safety protection equipment required
- To enhance surface absorption, pre-coating is required for many metals
- Warped deformation occurs because of the dissymmetry of laser irradiations
- Limited to small bending angles
- Proper insulation is required in LBF of titanium alloys; oxide film formation can lead to low leaser absorption and the promotion of crack propagation

The LBF process is still in its development stage. Further efforts in the areas of control and measurement systems need to be undertaken to fully exploit its industrial potential. Recently, LBF has been applied for correcting the distortions of automotive parts from previous welding operations. It has, also been used in micro-fabrication for precision adjustment of components (Narendra B. Dahotre, 2008).

[1] Nd:YAG (neodymium-doped yttrium aluminium garnet) and Nd:YVO (neodymium-doped yttrium ortho-vanadate),

2.2.3 Water jet forming

Instead of using rigid tools, this novel process applies the kinetic energy of a high velocity and high-pressure water jet to form sheet components. When water jet (WJ) pressure exceeds the yield limit of the blank sheet, local plastic deformation occurs. Based on the planned trajectory, the water jet, under CNC completes the forming layer by layer (Kai *et al.*, 2011).

In the water jet sheet metal forming (WJSMF) process, the extent of plastic deformation on the formed material is subjected to the WJ characteristics and the properties of the workpiece itself. Figure 2-8 presents the most relevant process parameters in the case of sheet forming by water jet.

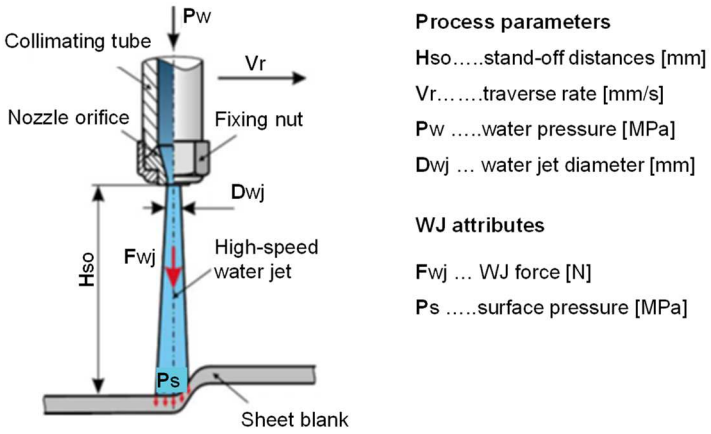

Figure 2-8: Relevant WJSMF process parameters (Jurisevic, 2006).

These parameters differ when compared to the cutting applications of the same technology. To prevent erosion of workpiece surface, the water pressure is (~30 MPa) ten times lower than that used in cutting (normally 400 MPa) applications with the same technology. In order to generate a sufficient deformation force, water flow needs to be increased ten times (from 0.2 to 2 mm) by increasing the nozzle diameter (Jurisevic et al., 2007).

WJSMF processes have the following advantages:

- Low friction between the water jet and sheet eliminates the need for lubricant
- Well distributed forces act on the workpiece interface surface
- From an environmental point of view, WJSMF is considered as green manufacturing process due to the absence of lubrication, and low noise (Kai *et al.*, 2011).

Process limitations include:

- The absence of a solid punch however, requires a mould for defining the final shape; a requirement that does not satisfy the flexibility attributes.
- Compared with incremental sheet forming with a rigid tool, the WJSMF is characterised by low accuracy, a long cycling time and high energy consumption (Petek *et al.*, 2009).
- The WJSMF process is still in its infancy and it requires extensive research to establish its possibilities

2.2.4 Metal spinning

The spinning process for forming components is based on appropriately modified lathe technology. Adding a hydraulic copying device or, more recently, CNC equipment, allows for producing a wide range of axisymmetric hollow-parts at a relatively low cost. The process variations include conventional, tube and shear spinning operations (Music and Allwood, 2011).

In conventional spinning (Figure 2-9(a)), a circular blank of sheet metal is held against a form block (mandrel) and rotated, while a rigid tool is used to deform and shape the workpiece over the form block. Tools may be operated manually or by a hydraulic mechanism.

Shear (power) spinning is quite like the conventional spinning; the difference is the forming action, which involves material stretching rather than bending. In power spinning, the shape is generated by keeping the diameter of the workpiece constant (Figure 2-9(b)), that is, keeping it the same as that of the blank. This fact has a significant influence on the blank thickness variation along the wall (Kalpakjian and Schmid, 2008). The cone angle (α) and initial thickness of the blank (t_0) are interdependent, and the final thickness (t_0) of the produced component is approximated using the formula of sine of the cone angle. further discussion of this relationship is presented in Section 3.1.

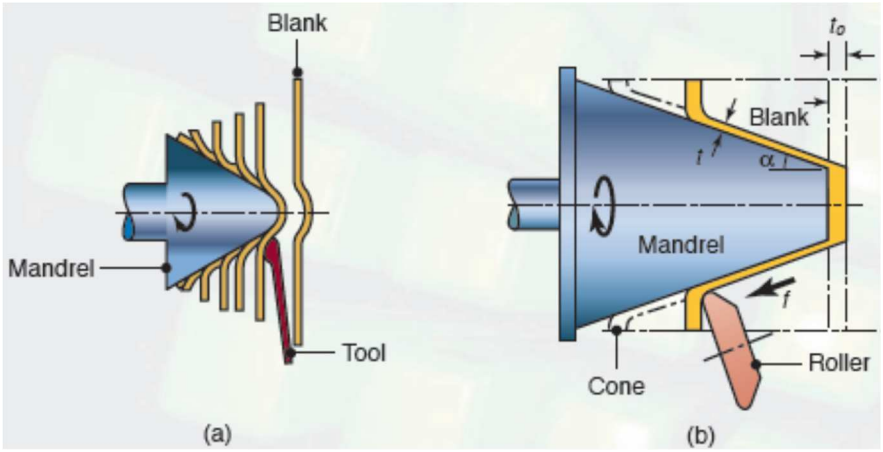

Figure 2-9: Metal spinning process: (a) Conventional spinning, (b) Shear spinning (Kalpakjian & Schmid 2008).

Advantages of metal spinning operations are:

- The tooling costs and investment in capital equipment are relatively small
- A short set-up time
- Design changes can be made at relatively low cost.

Drawback of the process as follows:

- The process is limited to axisymmetric shapes only.
- The need for full size and shape mandrels reduces its flexibility.
- The process typically requires long cycle times, and operation by highly skilled operators.

2.2.5 Asymmetric incremental forming

The asymmetric incremental sheet forming AISF or simply ISF has recently emerged as a forming process. ISF is characterised by its highly localised deformation ability without drawing in material from a surrounding area, attributes to the use of a fully clamped blank. During forming, the model is split into sequences of two-dimensional layers, and plastic deformation is accomplished layer-by-layer through the progressive movements of a CNC-guided forming tool. On completion of each layer, the forming tool moves down a small step depth (Δz) along the component z-axis and continues to form the subsequent layer, until all required layers are processed (Echrif and Hrairi, 2011). Based on the number of points of contact, ISF is categorized into two major groups as follows:

2.2.5.1 Single point incremental forming

In this truly die-less configuration the sheet is shaped only by the action of a forming tool-tip that has a single point of contact with the workpiece as shown in Figure 2-10(a). In some cases, a custom faceplate (beneath the blank) is employed to support the sheet and to create well-defined edges on the formed product.

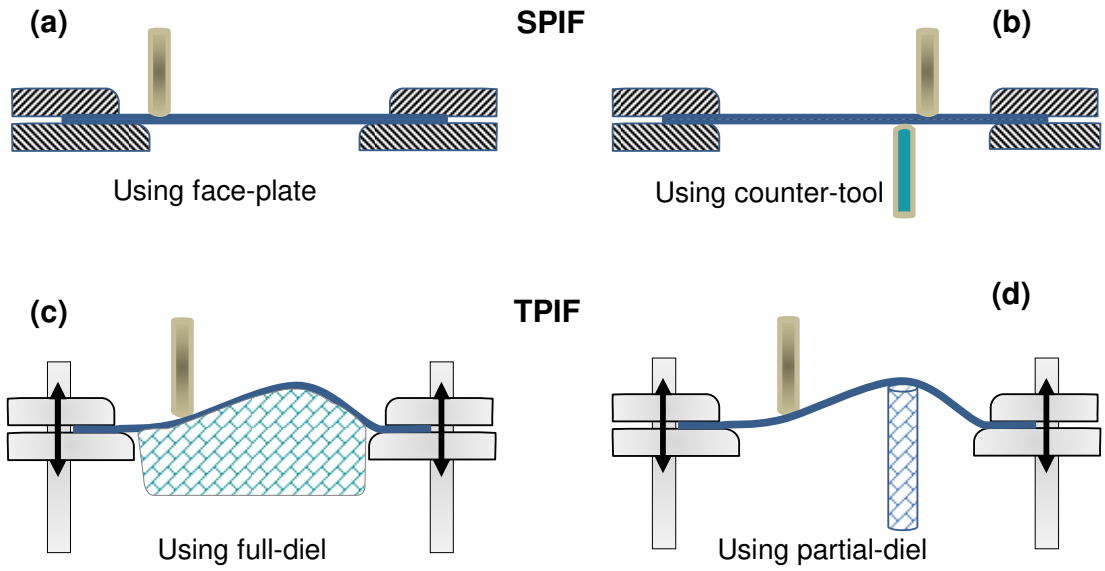

Figure 2-10: Configurations ISF process

2.2.5.2 Double-sided incremental forming

This setup variation (Figure 2-10(b)) applies two robots or kinematic machines to drive two tools, one on either side of the workpiece. During forming, the support tool holds the back face of the sheet and moves in unison with the main forming tool. Thus, enables maintaining process flexibility, and increasing forming accuracy.

2.2.5.3 Two-point incremental forming

TPIF utilises a partial or full die (Figure 2-10 (c) and (d)) to support a critical region of the part during forming and to decrease unwanted deviations from the target geometry. When the die is positive, the sheet blank is clamped in a moveable blank holder that descends over the die, and is progressively formed against the die.

2.2.5.4 Hybrid ISF

To overcome certain process limitations and extend the material spectrum, new ISF hyper-variations, known as heat assisted approaches have been explored. They attempt to fabricate hard-to-form materials such as magnesium, high-strength steel and titanium alloys, which are characterised by poor cold formability. Table 2-2 gives a brief description of two hybrid variations cited in literature: the laser heat-assisted and the electric heat-assisted ISF methods.

Table 2-2: Characteristics of heat-assisted ISF approaches

Heating approach	**● advantages / ○ drawbacks**
Laser heat-assisted ISF 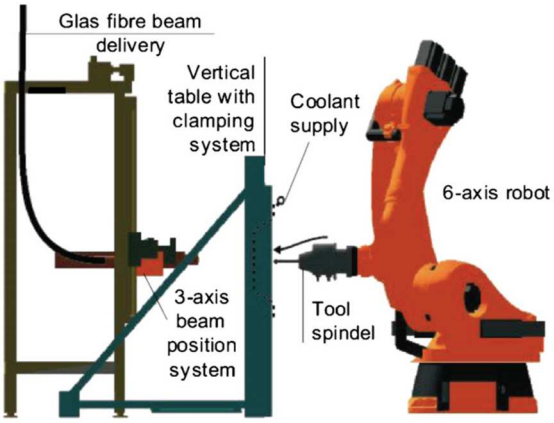	Applies heat from a laser beam on the reverse side of the sheet, causing thermal softening of the plastic zone under the forming tool. • Improves sheet formability and reduces springback ○ High setup cost (laser source and accessories) ○ Complex equipment as opposed to the low cost and simplicity of the ISF process. Palumbo & Brandizzi (2012).
=	
Electric heat-assisted ISF 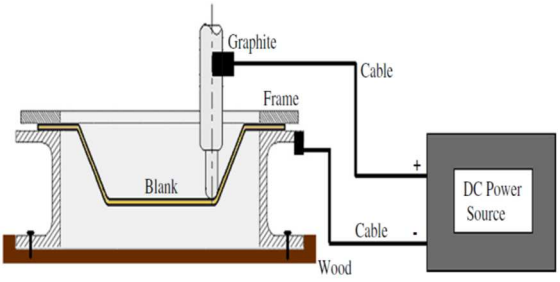	Utilises DC current to heat the workpiece material per Joule's law. • Improves material deformation level and reduces springback • Involves the use of relatively simple and cheap equipment Ambrogio (2012) ○ Reduces process flexibility.

2.2.5.5 ISF process equipment

In principle, any CNC machine that allows for 3D or more movement of a forming tool in space can be applied to perform the ISF process. To date, conventional CNC milling machines, purpose built machines, industrial serial robots, hexapods or parallel kinematics, and, recently, a Verne hybrid machine have been used. Maximum payload, stiffness, speed, tool path flexibility, working volume, availability, and costs are the key factors considered when deciding on the equipment type to be used (Marabuto et al., 2011; Altan and Tekkaya, 2012). Table 2-3, summarises advantages and limitations using these different equipment for ISF operations.

Table 2-3: Comparison between different types of ISF equipment

Applied equipment	**Characteristics: ● advantages / ○ drawbacks**
CNC milling machine 	• Widely available in different designs, capacities, and prices • Can be easily adapted to the requirements of ISF with low additional costs • Existence of well-developed CAD/CAM interfaces ○ Limited loads capacity in a vertical plane (the axis of the tool) ○ Suitable for low sheet thickness or milder materials
Serial robot 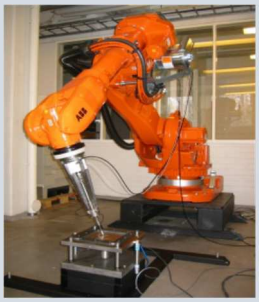	• Moderate prices, large work-space to robot size • High flexibility (mobility in six degrees), allowing ISF in the most convenient position Due to low stiffness and serial structure: ○ Manipulating a relatively low effective load; ○ Reactional forces acting on the tool lead to its deviation; ○ Positioning errors accumulating from link to link, leading to large final geometrical deviations.
Parallel kinematic machine 	• A parallel kinematics machine (PKM) has compact structure, therefore, high stiffness, and lower moving inertia • High load-to-weight ratio, high dynamic performance, and good accuracy potential ○ Compared to serial robots, a PKM has a more intricate construction, limited working area, and quite a complex control mechanism ○ Relatively expensive, with a very limited market supply.
AMINO ISF machine 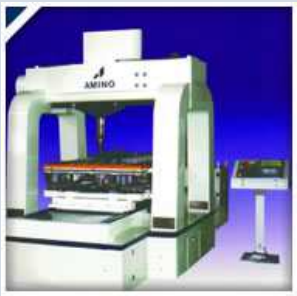	• Stiff solid structure, high feed rates (30 m/min), medium-sized working volumes • Equipped with a controlled, movable blank holder • Can perform sheet trimming, bending and hemming • Wide variety of materials can be formed with thickness ranging from 0.1 mm to 4.0 mm ○ Low machine flexibility and extra cost (single purpose machines).
Verne 5-axis machine 	• Combines a serial module, a tilting table, and a parallel module • Structure stiffness is adequate for carrying out milling and implementing ISF applications (Rauch *et al.*, 2009) ○ High machine cost and programming complexity.

2.2.5.6 Advantages of ISF process

- Parts can be directly produced from their CAD data, allowing design changes fast and very effective
- Low forming cost; reduction up to 80% of dedicated tooling costs can be realised with lead time for new production can be reduced by 90%
- It can be performed on most standard CNC machines.
- The significantly high level of strains achievable leads to the following:
    - Increases material utilisation (buy-to-fly ratio) by more than 20% over conventional stamping (also due to elimination of draw beads, thereby reducing scrap from trimming).
    - Increase the ability to form materials with low cold-formability economically.
    - The ability to produce components with a controlled thickness (in aerospace applications, particularly, this can lead to large savings in fuel consumption and carbon emissions).

2.2.5.7 Limitations of ISF process

- In ISF, sheet thinning follows the so-called definition of the sine law. Consequently:
    - this can lead to an inhomogeneous thickness distribution in the final product
- Limitation on the maximum wall angle achieved in a single forming stage
- There are deviations from the target CAD model due to a high level of springback
- The process is slow; forming time depends on the part size and selected tool path

2.2.5.8 Application areas

ISF has found numerous engineering applications, for example (Jeswiet *et al.*, 2008):

- In automotive engineering: body-panels prototyping, small production runs (e.g. in motor sport, and after-sales service)
- Housings and fairings for aerospace applications
- In medicine: forming medical prosthetics, such as customised cranial implants, ankle supports and custom-made dental crowns
- In architecture: in all areas where sheets need to be formed in small production runs

2.3 Summary of existing flexible forming processes

Despite all the recent developments in process flexibility, particularly in machining operations, sheet metal forming technologies are still lagging; they still rely on rigid tooling for the forming of each specific component. In this chapter, several emerging sheet metals forming techniques are presented. The focus is mainly on their applications where the speed and low cost are preconditions for time-to-market improvement (reduction) and global competitiveness. Attempts directed at, for example, eliminating the die on one side, minimising forming forces, reducing process steps, increasing the degree of freedom, and allowing for late-stage product adjustments, have been discussed.

One of the aims of this dissertation is to show that potentially SPIF is probably the answer to the challenge of increasing flexibility in the field of sheet metal forming. Table 2-4 illustrates a symbolic comparison of the various forming approaches, considering three main criteria: the selection of the evaluation criteria for consideration is based on what has been discussed thus far.

Table 2-4: A comparison between flexible sheet metal forming processes, based on selected criteria

Criteria / Process	Cost saving in equipment		Process time		Final product characteristics		
	Machine	Tool	Setup	Forming	Complexity	Size variation	Accuracy
EMF							
Fluid cell							
Discrete-die							
Shot-peen							
Laser-beam							
Water-jet							
Spinning							
SPIF							

Legend

Very good Good Medium Poor Very poor

For the author the main area of interest is the SPIF of titanium alloys sheets, with a specific research interest focused on the formation of customized biomedical implants from CP grade 2. It can be concluded that each developed sheet forming approach has its own strengths and weaknesses. They cannot interchangeably be applied to all applications.

CHAPTER 3 THEORETICAL BACKGROUND OF SPIF PROCESS

3.1 Formability mechanisms

Sheet metal forming processes are limited by (necking) instability, created when the applied tension stresses are excessive; sheet failure results with localised deformation over a small area (neck), while the adjoining area of the sheet stops deforming and any further stress creates a strain that exceeds the capacity of the material. The analysis of deformation in sheet metal forming is often based on two principle membrane strains, ε_1 and ε_2. Usually the maximum plane (major) strain ε_1 is positive for the forming operation. The definitions of positive and negative strains are respectively illustrated in Figure 3-1(a). In the sheet industry the graphic representation of the in-plane strain states is known as a forming limit diagram (FLD); the forming limit curves (FLCs) depicted on such diagrams are widely used to assess material formability and part manufacturability (Emmens, van der Weijde and van den Boogaard, 2009).

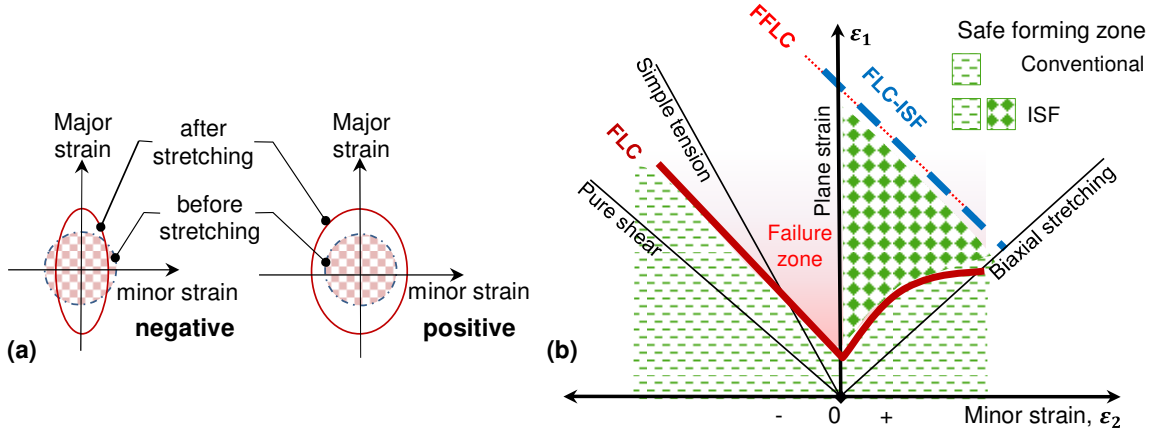

Figure 3-1: Principal strain space in sheet metal forming showing:(a) the definition of positive and negative strains, Kalpak Jian and Schmid (2008); (b) a forming limit diagram (FLD) with the necking limit (FLC), and the fracture forming limit curve (FFLC),

The FLC in Figure 3-1(b) forms the boundary between the safe forming zone and the material plastic instability zone above the curve. Hence, the state of strain in sheet metal forming must be such that it falls below the curve for particular combination of material strains (Kalpakjian and Schmid, 2008). Practically, FLDs and FLCs are valid, subject to certain restrictions. These restrictions are amongst others: a straight strain path (proportional loading); the situation of plane stress; the absence of bending; and the absence of through-thickness shear (Emmens and van den Boogaard, 2009; Hasan, Kinsey and Tsukrov, 2011).

For ISF, the relationship between strain limits plots as a straight line, falling from left to right (with negative slope), in the zone where the minor strain, $\varepsilon_2 > 0$. As shown in Figure 3-1(b), when $\varepsilon_2 > 0$, the FLC for ISF (blue dashed line which coincides with the fracture forming limit curve, FFLC) is significantly larger than the typical corresponding limit predicted for FLC as applicable to conventional sheet forming operation performed on presses, and close to material fracture limit (Emmens & van den Boogaard, 2009; Filice et al., 2002).

Previous studies on the morphology of the cracks and analyses of the thickness variation of components made by ISF revealed that material deforms by uniform thinning until fracture, without the development of necking. It has been postulated that the extremely small deformation region as compared to the sheet size, leads to a plastic zone always surrounded by elastic material that effects the development of necking (Fang et al., 2014; Silva et al., 2011). Furthermore, a combination of special forming conditions that lead to stabile deformation and the suppression of sheet necking, have been proposed. These special forming conditions are: serrated strain paths arising from cyclical, local loading; dynamic bending and unbending under tension; stretching; and through-thickness shear (Emmens & van den Boogaard, 2009; Malhotra et al., 2012).

All the above-mentioned forming conditions for generating an FLD are understood to be violated by ISF. Consequently, FLCs on standard FLDs for sheet metal work, which presume necking as the failure mode, are inapplicable to assess the instability and describe failure in an ISF process. Instead, formability limits by fracture and fracture forming limit curves (FFLCs) are suggested as characteristic of process formability and predicting material failure (Silva *et al.*, 2009; Isik *et al.*, 2014).

The attainable high levels of strain before fracture as mentioned above, are environmentally very beneficial and effect cost saving. The extended formability of ISF requires the use of less sheet material for the manufacture of one component, making ISF more attractive for processing high cost lightweight alloys. This favourably affects the buy-to-fly ratio, which is the relationship between the money invested in the resources for a certain product and the price of the final product (Cao et al., 2012; Zettler & Papadopoulos, 2011).

Maximum drawing angle of sheet before its fracture is a common practice to index the ISF formability. The manufacture of components with truncated, conical or pyramidal profiles (see Figure 3-2), is state-of-the-art in ISF and is regarded as the process benchmark. These profiles are constantly the subject of experimental work and analysis in research of late, and they are considered as benchmark during experiments in this dissertation.

Depending on the features to be evaluated: a varying wall angle conical frustum (VWACF), represents a homogeneous geometry with a symmetric section, and is eminently suitable for the evaluation of sheet formability. On the other hand, a varying wall angle pyramidal frustum (VWAPF) which is characterised by points of rigidity between areas which are less rigidly supported, is preferred when evaluating component roughness and the forming force (Ambrogio *et al.*, 2007; Hussain, Hayat and Lin, 2012). For the both the profiles mentioned the main shape-defining parameters that can affect deformation and the forming force during ISF, are identified as:

- the wall angle, θ;
- the depth of forming, h;
- the generatrix radius, R;
- the size of initial horizontal plane, defined by radius of curvature, ρ_i in conical profiles, or a half-side length, l_i in pyramidal shape

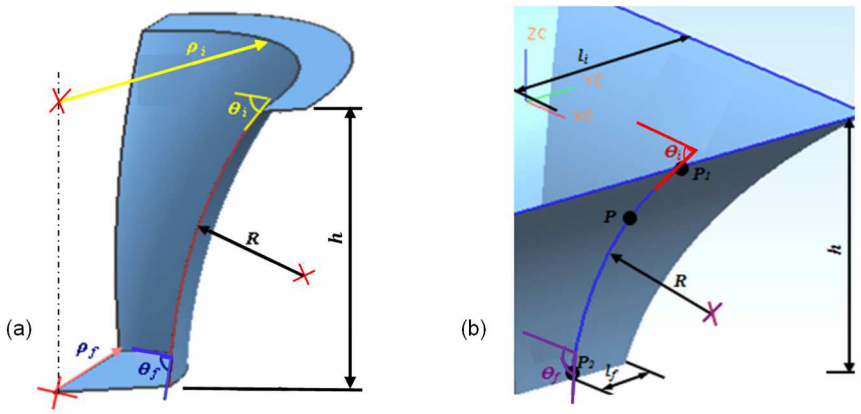

Figure 3-2: ISF benchmark test geometries (a) frustum of a cone; (b) frustum of a pyramid (adapted from Hussain et al., 2012)

Relevant studies on process mechanics revealed that the actual forming mechanism in ISF is the result of a combined deformation due to bending, stretching and through-thickness shearing. In axisymmetric components, if corners with a small radius of curvature are excluded, the material is plastically deformed mainly by plane strain stretching and small-scale bending — this is illustrated in Figure 3-3.

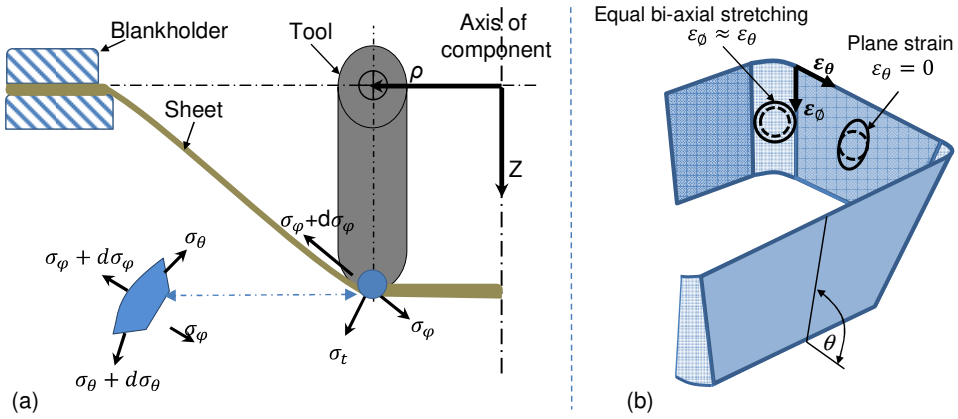

Figure 3-3: Illustration of stress and strain in SPIF: (a) ρ-Z view principle stress; (b) variation of strain with $\boldsymbol{\rho_i}$. Adapted from (Bhattacharya *et al.*, 2011)

In ISF operation, volume constancy is assumed and throughout the forming process; no material is added or removed. Therefore, any increase in sheet surface area is only offset by a reduction in its thickness. Thus, formability in terms of the occurrence of sheet thinning and fracture, are largely dependent on the component depth and the angle of forming. In the case of planar strain, which excludes zones having a small radius of curvature, only two kinds of in-plane strains exist. The first one is the major strain, (ε_φ), which is measured in the meridian direction, while the second one is the minor strain measured in the tangential direction (ε_θ) and it is relatively small enough to be considered negligible (Fang *et al.*, 2014). State of stress and strain in localised plane strain conditions are listed in Table 3-1. Considering that the volume is assumed to remain constant, the sum of the in-plane strains is equal zero, and therefore any change in area as a result of the major strain, is compensated for by the thickness strain (ε_t) or reduction in the component thickness (Ji and Park, 2008; Fang *et al.*, 2014).

Table 3-1: State of stress and strain in localised plane strain conditions (Silva *et al.*, 2009)

State of strain	$\boldsymbol{\varepsilon_{\emptyset}} = -\boldsymbol{\varepsilon_t},\ \varepsilon_t < 0$	(3-1)
State of stress	$\sigma_{\varphi} = \dfrac{\sigma_y}{(1 + t/r_t)} > 0$	(3-2)
	$\sigma_{\theta} = \dfrac{1}{2}(\sigma_{\varphi} + \sigma_t)$	(3-3)
	$\sigma_t = -\sigma_y \dfrac{t}{(r_t + t)} < 0$	(3-4)

whereas: r_t is tool-tip radius; $\sigma_{\varphi}, \sigma_{\theta}$, and σ_t are respectively the stress components in the meridian, circumferential and thickness directions.

An axial cross-section of a shear-formed component is illustrated in Figure 3-4, and shows the wall slope, θ, the vertical axis, Z and the radius of curvature, ρ, together with the initial sheet thickness and the deformed sheet thickness.

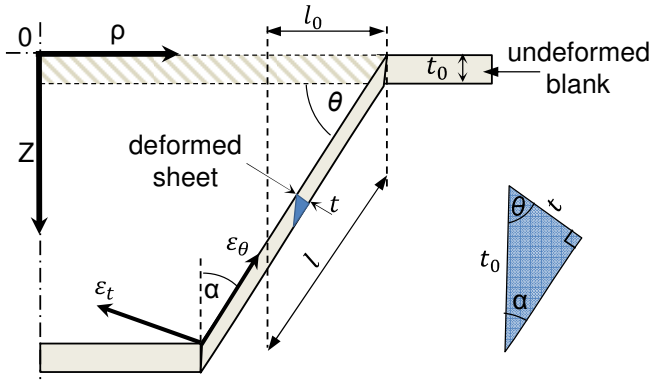

Figure 3-4: Axial cross-section of shear forming component

In the abovementioned shear spinning condition, when forming conical profiles, the relationship between wall thickness of starting blank, t_0 and the post-forming thickness, t, is a function of the half-apex angle of the formed cone , α, and the so-called 'thinning' of t_0 to t, as related by the sine of the angle α (Hagan & Jeswiet, 2002). The relationship for shear spinning is driven (Kegg, 1961; Sortais, S.Kobayashi and G, 1963) usually known as a sin low[2] of thickness and given by Equation 3-5,

$$t = t_0 * \sin\alpha = t_0 * \sin\left(\frac{\pi}{2} - \theta\right) \tag{3-5}$$

Note that in the ISF process the actual measurement of the formed sheet thickness for a constant wall angle is not uniform because it is affected by several process variables. For example using small ratio of step depth, Δz to tool-tip diameter $\Delta z/d_t$, some parts of sheet material is deformed repeatedly due to overlap (Bhattacharya *et al.*, 2011) and this leads to an over-reduction of sheet thickness. Despite this deviation, the sine relationship is still useful in ISF for predicting the approximate deformed wall thickness away from transient zones like for instance close to the part opening (Strano, 2005; Hussain, Hayat and Gao, 2008).

[2] Nonetheless, it is based on a simple definition of sine of the angle, in literature, it is often confused as a sin low

As can be seen in Figure 3-4, in shear spinning α is the half angle of the cone formed and it is measured off a line that is parallel to the spinning tool axis. While in the ISF, wall angle is measured from original plane of the blank sheet. The forming angle θ represents a significant design factor and the detrimental effects of a vertical slope on sheet thinning and fracture are well established. In practice, nominal thickness strains, ε_t are measured in regions with a larger slope (Strano, 2005), as indicated in Equation 3-6.

$$\varepsilon_t = ln\frac{t}{t_0} = ln(cos\,\theta) \tag{3-6}$$

For a particular sheet thickness used in the ISF process, each material has a characteristic maximum wall angle (θ_{max}) that can be achieved during in a single forming pass, without sheet fracture. The maximum wall inclination is stipulated because of the aforementioned material thinning. Even if the initial thickness is increased, a sheet cannot be formed beyond a certain depth due to the decreased thickness leaving limited material for stretching (Bhattacharya et al., 2011). To ensure that a formed part will not exceed the maximum permissible material strain, material formability is typically specified in accordance with the θ_{max} value that a sheet can endure without cracking.

The maximum wall angle can be determined directly by forming cone-hyperboloid profile as detailed by Hossain and Gao (2007), and depicted in Figure 3-2. The wall angle of the hyperbolic cone increases in relation to its depth, and is potentially suitable for predicting θ_{max} with a minimum number of experiments.

Although the maximum wall angle is a material and thickness dependent criterion, it can also be affected by other process factors. For instance, the tool-tip diameter and the depth of step can cause up to 5% variability in the applied wall inclination angle. As will be shown in the subsequent chapter, an increase in either the tool-tip diameter d_t or the depth of step Δz will result in a variation of θ_{max}. Additionally, the radius of curvature to be formed, affects formability and can result in a variation of the deformed wall inclination of up to 6° (Adams & Jeswiet, 2014a; Hussain et al., 2013). As shown in the diagram of the tool/sheet interface in Figure 3-5, throughout forming only a fraction of the tool-tip is in direct contact with the sheet surface.

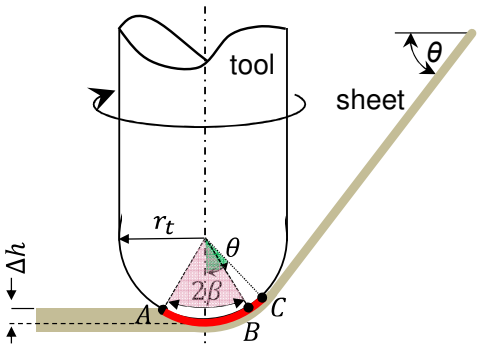

Figure 3-5: Enlarged diagram of tool/sheet interface in SPIF

The tool/sheet interface area can be simplified as a ribbon of constant width (Aerens *et al.*, 2009). The length of the ribbon l_c equals the arc length, $\widehat{ABC}$ which is function of two angles in the meridian direction: the wall angle, θ ; the half-angle (arc) of groove β also known as scallop:

$$\beta = \cos^{-1}(1 - \Delta z/r_t) \tag{3-7}$$

As focus in the following paragraphs is on the effect of geometrical factors and the tool/sheet interface on the deformation mode, it is seen that the contact length l_c increases with increasing of wall angle θ:

$$l_c = r_t \cdot (\theta + \beta) \tag{3-8}$$

whereas the arcs θ *and* β are in radians

An increase in the tool/sheet interface equates to more material being involved in the deformation process, and consequently this requires a bigger forming force (Aerens *et al.*, 2009; Asghar *et al.*, 2013). Variation of the stress mode at tool/sheet contact zone along longitudinal or hoop direction, is affected by the ratio between radius of curvature ρ of the geometry being formed and tool-tip diameter d_t.

On flat surfaces or surfaces having a large value of ρ/d_t and when using a small tool-tip, only longitudinal contact occurs and near plane (uniaxial) strain develops parallel to the tool path. This type of contact is associated with material failure by fracture together with the suppression of necking and an increased formability.

With small value of ρ/d_t and using a large tool-tip diameter, both longitudinal and hoop type of interfacial contact can occur, and material failure occurs by fracture, preceded by necking similar to conventional deep drawing and stamping processes (Silva *et al.*, 2011; Madeira *et al.*, 2015).

Table 3-2: States of strain and stress under equal biaxial conditions at small-radius bends (Silva, 2009)

State of strain	$\varepsilon_\varphi = \varepsilon_\theta$, and $\varepsilon_t < 0$	(3-9)
State of stress	$\sigma_\varphi = \sigma_\theta = \dfrac{\sigma_y}{(1 + 2t/r_t)} > 0$	(3-10)
	$\sigma_t = -2\sigma_y \dfrac{t}{(r_t + 2t)} < 0$	(3-11)

Typically, longitudinal and hoop contact develops at the corners of a formed component (refer to Figure 3-3(b)), where strain develops into a near-equal biaxial strain. Due to the large amount of strain, and depending on initial forming angle imposed, sheet cracks occur mostly at the corners of components. Therefore, a minimum flange size in comparison to the tool-tip diameter is desirable to meet the requirements for shear forming.

In contrast to small ratio ρ/d_t, large radii of curvatures or large half–side lengths in comparison to the tool-tip diameter, do not pose a risk of failure during forming, though there are several complex effects on product accuracy. These effects can be attributed to variations in workpiece stiffness and will lead to large rigid body movements of the unsupported material during the application of the forming forces — the resulting elastic

recovery from these movements will result in increased deviations from the target design (Silva *et al.*, 2011; Hussain, Hayat and Lin, 2012; Hussain, 2013; Isik *et al.*, 2014).

Finally, variations in two other geometrical parameters that control component profile, namely the forming depth, h, and radius of generatrix, R, have a lesser influence on formability and the acting forces; this conclusion is based on the results of a fair number of studies in which the effects of these two parameters were investigated (Hussain *et al.*, 2007).

All the deformations associated with the ISF process are confined to the proximity of the contact area. Individually the last two parameters, do not materially affect the outcome, if the other factors are controlled to operate at their optimal forming setting. The deformation behaviour and maximum formability in ISF are strongly influenced by the applied forces. These forces are in turn a function of several factors associated with the geometry of the component to be formed and the applied operative parameters.

3.2 Forming forces

In metal forming, a sufficient level of pressure is required to overcome yield strength of the workpiece material and create permanent deformation. The forming forces in ISF are not high and are far below those applied in conventional forming technologies such as stamping, and deep drawing. Nonetheless, depending on the material type and the blank thickness, significant forces can occur and they are of central importance when planning the forming process. For the most part, SPIF, the amount of local plastic deformation is solely dependent on the magnitude of the force at tool/sheet interface; any increased load can lead to a global effect on the unsupported sheet, rather than constraining the deformation to a local zone (Duflou *et al.*, 2007; Ren *et al.*, 2015).

The accurate prediction of forming forces is essential in the selection of optimal process variables and the choice of appropriate forming equipment. Excessive forming loads can have a detrimental effect on performance of inadequately stiffened tooling, fixtures, and machinery employed. This becomes even more important knowing that the typical platform used, whether it be a CNC milling machine or an industrial robot, is not meant for this type of work. Most CNC milling centres can be adapted to deliver an SPIF operation; the main constraint on this type of operation relates to the limited axial load that machine can provide.

In a mild overload situation, high forces can cause elastic bending deflections of the tooling system, resulting in deviations from the designed tool paths. In the worst-case scenarios, overloading can cause plastic bending or shattering failure of tooling system, deterioration of spindle, overloading of the machine table, and damage to the spindle or machine bearings. Hence, forming loads need to be carefully monitored and maintained within their design limits.

A visual presentation of the conceptual forming space is given in Figure 3-6. The applied force should be higher than yield strength of the material as indicated by the lower threshold in the figure. The upper threshold of the applied force is, limited by the stiffness of the machine.

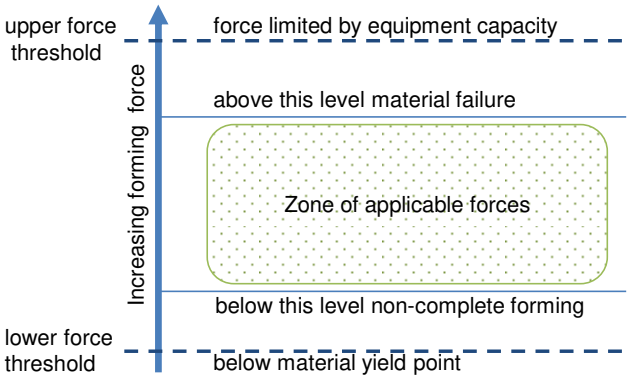

Figure 3-6: Applicable limits of forming force in SPIF

Unlike in traditional forming technologies, the forming forces in SPIF operations are not preselected by the designer or the operator. Instead, forces are generated as a reaction to the forming operation. These loads are determined to a large extent by the applied forming strategy, the process kinematics and the tool/sheet interaction (Ambrogio, Filice and Micari, 2006; Aerens *et al.*, 2009; Li, Liu, Lu, *et al.*, 2014).

Typically, forming forces in SPIF are measured consistent with the orthogonal Cartesian coordinate system; the in-plane components, parallel to initial sheet F_x and F_y, are the two components of the in-plane reactional force F_{xy} which is the subsequent of the tangential force, F_t, and the radial force, F_r.

The axial component acts along the tool-axis F_z. As depicted in Figure 3-7, the axial force, F_z, has a higher order of magnitude than either of the in-plane components and thus requires more attention during monitoring of the forces (Aerens *et al.*, 2009).

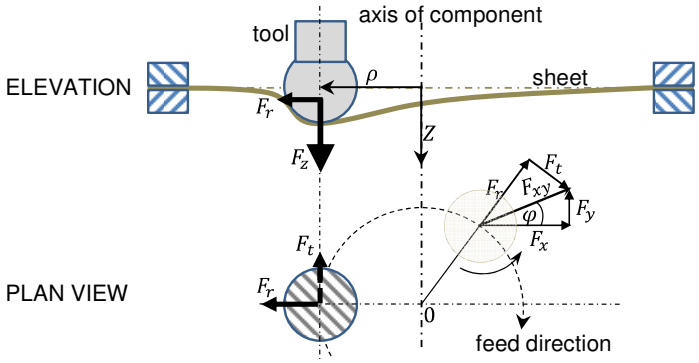

Figure 3-7: Diagram of the forming forces in SPIF

The tangential component or the force in tool-feed direction F_t, is relatively small and nearly constant during steady-state deformation. On the other hand, the radial component, F_r or the force normal to tool-axis and perpendicular to F_t, starts with positive or negative value close to zero when the wall angle, θ is small, and becomes positive as the forming proceeds and the angle increases. The phenomenon of negative F_r is related to the formation of a contact grove in the bottom of ISF component. For small wall angles, the inside part of the groove perceptibly exerts a larger radial reactional force in the outward direction, than does the outer part of the groove in the inward direction, which means that the tool is pushed outwards (Eyckens, Bael and Aerens,

2008; Aerens *et al.*, 2009). The radial force is the second most important force that has to be monitored in the SPIF process. Knowing that everything bends, an increased F_r acting on the tool-tip, generates a moment causing the tool to bend inwards and this deviation from its trajectory, results in the formation of contours shorter than required by target design; this reduces component accuracy.

There is a mathematical relationship between the three component forces acting on the tool-tip; by measuring F_z, and considering the slope of the formed component at a particular point in the process, the values of both the in-plane components, F_r and F_t, can be assessed. In Figure 3-8, a graphical presentation of the force components during SPIF of conical profiles, versus the cone generatrix line, R is given.

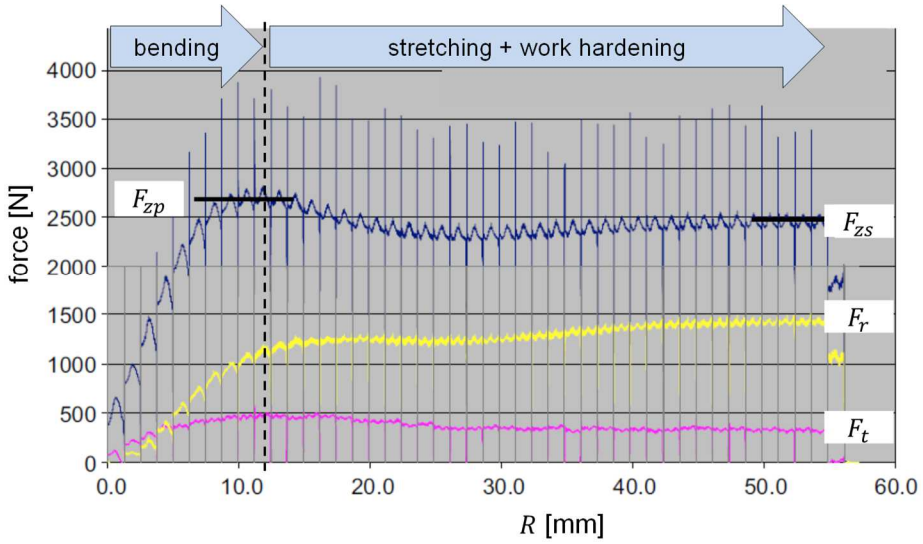

Figure 3-8: Trends of the SPIF forces F_z, F_t and F_r Versus the generating line of a typical formed cone – the material is DC01, t_0 = 1.15 mm, d_t = 25 mm, Δz = 1.06 mm, $\theta = 60°$ (adapted from Aerens et al., 2009).

As depicted in Figure 3-8 during forming, the magnitude of the axial force goes through a transient stage where it increases rapidly from zero to its maximum level or peak force (F_{zp}); thereafter it levels out, tending to become constant for the rest of the process. There are a number of reasons for this force build-up behaviour of F_z (Duflou *et al.*, 2007; Aerens *et al.*, 2009) :

- Firstly, it is in line with the material stress-strain curve and initial development of plastic deformation, where most of forces are created due to an unavoidable bending mechanism caused by the proximity of the supporting backing-plate at the component opening, rather than by a stretching effect.

- Secondly, the build-up of tool/sheet interface area increases the force required to deform the blank, and additionally stretching and shear deformation modes are activated;

- Finally, the material develops work- or strain-hardening and any further deformation results in an increase of force.

Before reaching the virtual steady-state stage where the force is practically constant at F_{zs}, the force falls from F_{zp} to a value slightly lower than F_{zs}. At the steady-state stage, the typical stretching mechanics dominates and deformation of the workpiece material is determined by dynamic equilibrium being achieved between two opposing effects; these effects are namely strain hardening, which increases the required forces, and thinning of the sheet, which tends to decrease the forces. This steady-state behaviour is usually observed when the imposed wall inclination is small and kept below the maximum forming angle, θ_{max} of the formed material (Li, Liu, Lu, *et al.*, 2014). The steady-state stage is maintained because material thinning is compensated by the concurrent strain hardening, up to a point where a monotonically downward trend of the force appears (not shown on Figure 3-8). At this level, a drop in the force occurs because of the influence of sheet thinning is much larger, negating the counter-effect of material strain hardening, thus ending the equilibrium condition. The monotonic drop of axial force is often observed in cases where sheet fracture occurs; this is either due to θ_{max} having been reached in the forming process, or because the strain limit of sheet material has been exceeded (Filice, Ambrogio and Micari, 2006; Lu, Ou, *et al.*, 2014).

It is well established that the forming forces and their influence are very much dependent upon the material type and thickness, the profile being formed, and the process conditions, particularly the tool-tip diameter and step depth.

3.3 Thermal aspects

Elevated temperatures are an enhancing factor in the thermomechanical processes of metal forming. Heat helps soften the workpiece material, reduce the required loads, and minimise springback. In different conventional metal forming operations, particularly, when forming of lightweight alloys, thermal energies from external sources is usually integrated with mechanical loads in at least one stage (before, during or after) the forming process, to increase formability and relieve residual stresses.

ISF is no exception, researchers have developed a few hybrid versions of the ISF process and they are referred to as heat-assisted incremental forming. In this heat-assisted process, localised dynamic thermal energy from an external source is applied and integrated into the forming zone. The energy can be from a high-ampere DC current running through the forming tool onto the sheet, so-called electrically-assisted forming. Alternatively, the energy is from a directed laser beam, and is referred to as laser-assisted forming. Applying external energy to the forming zone leads to significant benefits in terms of increased formability and a decrease in the forces required. There is an increase in both the process complexity and the cost. The scope of this dissertation is limited to studying of process demands of SPIF at room temperature.

Titanium Grade 2 is typically selected for its outstanding corrosion resistance, particularly in applications where high strength is not critical (given that its tensile strength is < 340 MPa). Forming temperature is a decisive factor affecting the processing of titanium alloys and is responsible for its microstructure phase changing. In SPIF, a localized temperature gradient and deformation cause microstructural changes along the forming path of the workpiece. As result, non-uniform material properties can be produced over the workpiece, which in turn impacts the quality and performance of the produced component (Mishra, De and Kumar, 2014).

For instance, dimensional accuracy and surface finish are vitally important properties to achieve the net required shape during forming production, and thermal distortion is among the factors by which these properties are influenced.

Considering the temperature gradient, errors or defects in a hot-formed component are more likely to be attributed to an accumulation of the thermal distortion due to a non-uniform temperature distribution on the material and the subsequent cooling to room temperature of the material (Yang *et al.*, 2011). If applicable, a titanium workpiece needs to be formed at a constant temperature (isothermal process[3]) and a low strain rate. This will decrease the deformation resistance, while increasing the plasticity and deformation homogeneity of the material, and thus the forming accuracy and microstructure homogeneity will be significantly improved. Thus the temperature variation during the SPIF of CP Grade 2 must be carefully supervised (Ambrogio et al., 2013; Fan & Gao, 2014). The development of isothermal SPIF for larger and more complex titanium components however, is beyond the capability of current technology.

In a thermomechanical metal process, the workpiece is pre-heated with the aim of reducing forces and so reducing the process energy consumption. In cold SPIF operations the workpiece to be formed is at ambient temperature at the start of forming and heat generation is accomplished mostly through friction (Durante *et al.*, 2009). Too much heat due to friction could lead to negative effects on the forming tool or workpiece surface, at the contact zone. Oxidation of the formed surface, tool failure due to deflection, severe wear of the tool, and breakdown of the lubricant, are all the major concerns. As illustrated in Figure 3-9, in SPIF the thermal load to be considered will only be the heat generated due to tool/sheet interaction and the plastic deformation.

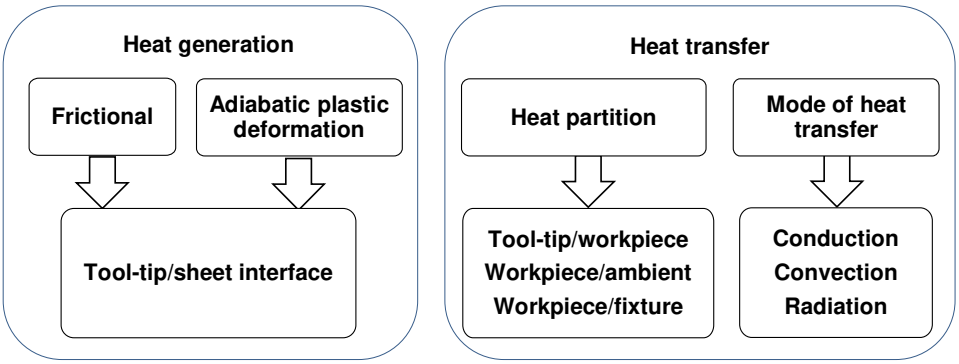

Figure 3-9: The nature of heat generation and utilisation in ISF. Mishra et al., (2014)

The sections following, highlight the primarily sources of heat generation in SPIF, which result from the friction between the tool-tip and sheet surfaces, and the heat generated due to the plastic deformation in the bulk of the workpiece material. The initial workpiece temperature, the heat transfers between the workpiece and tools, and between workpiece and environment— all these factors need to be considered.

[3] If a forming process is carried out at a temperature less than the re-crystallization temperature and at a slow rate, such a case may be taken as an isothermal process, i.e. the effect of temperature change during the process may be neglected and considering only the effect of strain hardening.

The average instantaneous temperature in the deformed workpiece T_A can be estimated from Equation 3-12.

$$T_A = T_w + T_D + T_F - (T_t + T_R + T_C) \tag{3-12}$$

where: T_w is the workpiece initial temperature; T_D is the temperature increase due the plastic deformation; T_F is temperature increase due to the friction; ($T_{t,}$, T_R *and* T_C) are respectively the drop in temperature; due to heat transfer to the tool, and to the environment; by radiation and convection.

Temperature increase due the deformation T_D, and friction T_F in a time interval Δt, can be estimated using the equations in Table 3-3.

Table 3-3: Formulae to calculate the increase in temperature during metal forming operations (Altan, Ngaile and Shen, 2005)

deformation	$\Delta T_D = \frac{A\,\bar{\sigma}\dot{\varepsilon}\Delta t}{\rho C}\beta$	(3-13)
friction	$\Delta T_F = \frac{Af\bar{\sigma}\,\mathrm{v}\,\mathrm{F}\Delta\mathrm{F}}{\rho C V_a}$	(3-14)

Where;

Symbol	*Description*
$\bar{\sigma}$	workpiece flow stress
$\dot{\varepsilon}$	effective strain rate
Δt	time interval
A	conversion factor between mechanical and thermal energy
C	Specific heat of the workpiece
ρ	workpiece specific weight
β	fraction of deformation energy converted into heat ($0 \leq \beta \leq 1$); usually $\beta = 0.95$
F	friction factor at tool/sheet interface (such that frictional shear stress $\tau = f\bar{\sigma}$)
V	velocity (at tool/sheet interface) of deformation
V_a	volume of material subjected to temperature increase

3.3.1 Heat generation from frictional heating

Tribology—the science of friction, wear and lubrication—is of great importance for all technical applications where moving bodies are in contact (Hölscher, Schirmeisen and Schwarz, 2008). The friction between metals arises mainly due to interfacial adhesion between asperities (surface irregularities on the metals) on the contact surfaces and the microscopic plastic deformation due to relative motion of the contact surfaces. It is through frictional processes that velocity differences at the contact interferences between the bodies are accommodated. The friction energy dissipated during the deformation is entirely converted (at least 95 %) into heat energy, which causes the temperature of the sliding bodies to increase (Bhushan and Kennedy, 2001; Mishra, De and Kumar, 2014).

Frictional heating and generated temperature at the interface can have a major role on the behaviour of failure of sliding bodies. Changes in the friction and wear behaviour at the interface, lubricant present in the contact, can significantly altered. Structure properties of sliding materials, oxidation of the surfaces, and melting of the contact solids are some possible consequences of increased frictional heating.

In SPIF, the tool-tip is considered non-deformed and microscopic deformation occurs mainly on workpiece surface. Considering Coulomb's law of friction, the friction force (F) is related to the normal pressure (P) by:

$$F = \mu P \tag{3-15}$$

where; μ is the coefficient of static/dynamic friction, which is a function of material formed and shear stress.

The shear stress between tool and workpiece can be calculated from measured machine spindle torque and surface area of the tool-tip/sheet interface, and the factor P is found from vertical force component.

In standard SPIF operations, tool and sheet do not have contact temperatures that close to their melting points, though, the forming temperature can still have a major influence on their tribological performance. Contact pressure in presence of thermal stresses is sufficient to create galling or sizing of titanium at the interface. Localised temperature gradient in vicinity of interface is responsible for softening and shear-failure of the near-surface layer of deformed titanium (Bhushan and Kennedy, 2001).

Different maps of wear mechanisms have been developed to characterise the transactions of sliding wear of metals. Transaction between mild oxidational wear, sever oxidation wear, and melt wear are strongly affected by the contact temperature. The ability of predict and measure of the contact temperature is significant to avoid failure of titanium workpiece and forming tool used.

Figure 3-10 schematics the three geometric and temporal conditions under which the interface temperature occur. The peak temperatures T_C can be very high (over 1000℃) happen at very small (10 μm diameter) contact spots of surface roughness (asperities) on the sliding metals and last (less than 10 μ s) as only as the aspirates are in contact.

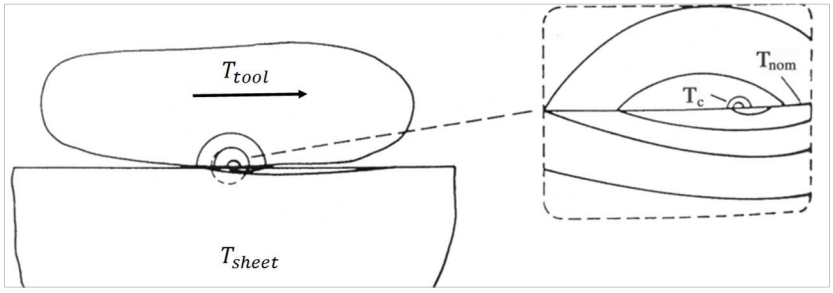

Figure 3-10: Temperature distribution around tool/sheet interface, adapted from (Bhushan, Kennedy, 2001)

At any instant, there are several short-duration flash temperature rises (ΔT_f) at various asperity contact spots with a nominal contact patch. The integrated average of in space and time of temperature forms the nominal contact temperature T_{nom}. For sever sliding conditions such as in breaks, the mean or nominal temperature can reach 500 ℃ . Temperature decrease (less than 100 ℃) to modest bulk volumetric temperature T_b at several mm as one moves away from the contact patch. The total contact temperature is given by the three contributions: $T_c = T_b + \Delta T_{nom} + \Delta T_f$.

Min factors affect the frictional heating in SPIF processes are discussed in the sections that follows:

3.3.1.1 Contact area

It is known that solid friction and related frictional heating are concentrated within the real region of contact between the two sliding bodies, where temperature is highest. Contact surfaces at interference have an apparent area which dependent on the geometry of tool-tip and blank and an actual contact area, which is several orders of magnitudes less than that apparent area. It is defined by sum microscopic contacts between surfaces. The aspect of the actual contact can be further illustrated with the help of Figure 3-11. It is difficult to measure the actual contact area because this area is dependent on the topological properties of the two surfaces making up the tool/sheet contact area. It is instructive to know characteristics of contact surfaces, such as roughness, lubrication, and loading condition (Hölscher, Schirmeisen and Schwarz, 2008; Samuel, 2010)

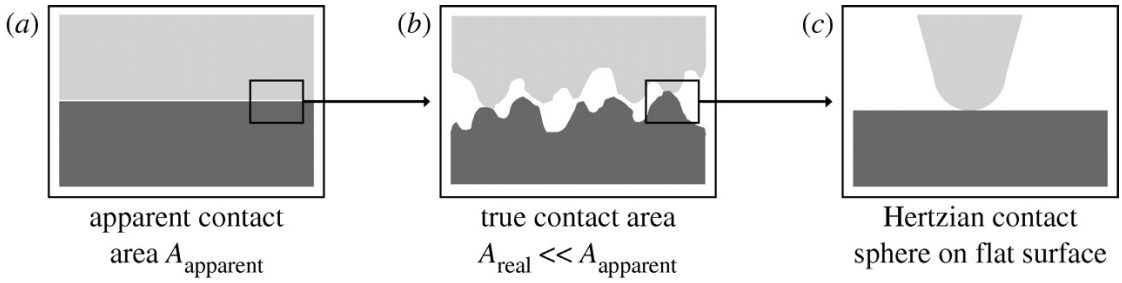

Figure 3-11: Microscopic contact area between two sliding bodies (Hölscher, 2008)

From an operational point of view, an SPIF run can be alienated into three sub-phases: Normal indentation, rotation, and traverse.

As shown in Figure 3-12, friction initially evolves from normal indentation; indentation plus rotation when tool first indents the sheet and creates step down, into sliding plus the first two friction effects due to traverse motion of the tool along forming contour. The latter phase is dominant, presents for the duration of forming and will be decided by process variables, mostly spindle speed, feed rate, wall angle and size of step depth.

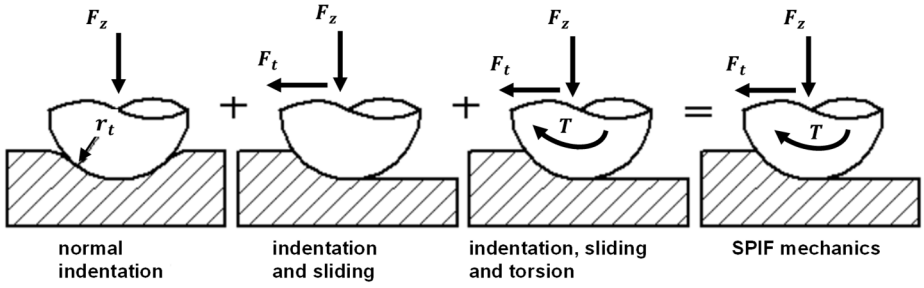

Figure 3-12: Forming mechanisms and friction conditions in SPIF (Samuel, 2010)

The size of the tool step depth determines the amount of material that needs to be worked and the amount of shear force required to plough or push the material along the forming trajectory, and the step therefore effects the rate of temperature rise and extent of plasticity. Heat is generated principally by viscous dissipation in the sheet material adjacent to the tool-tip, driven by high shear stresses at the tool-tip/sheet interface. The produced temperature and normal contact stresses differ widely over the tool, thus it is improbable that a single contact

state will be valid. Material at the contact zone may stick or it may slip, or there may be a combination of the stick and slip conditions (Threadgill *et al.*, 2009; Khaja *et al.*, 2013).

Non-rotation tool movement is a stick-slip motion, while tool rotation greatly reduces the stick time to almost zero. A tool moves only with a slip-mode; stick time is further reduced to a smooth motion by using lubricants. Given that sheet workpiece is firmly clamped along its periphery, and that the vertical step of the tool (Δz) is dictated by machine spindle head, the interaction between tool-tip and sheet will be accommodated by displacement of workpiece material, affected by indention, bending and stretching around the tool-tip.

Indentation is a function in sheet thickness— as thicker sheets are stiffer, they will bend less and indentation will increase; the reverse is true with thinner sheets. For the same sheet thickness, a larger tool-tip distributes the pressure better, and creates more bending and less indentation; the opposite is true with smaller tool-tip, which creates a bigger indentation effect.

The shape and size of indentation will depend on the hardness of blank material, and geometry of the component being fabricated as well as rigidity and shape of tool-tip.

3.3.1.2 Modelling the contact area in SPIF

In SPIF with a rotating tool, the area of the tool-tip/sheet interface is very complicated and difficult to measure accurately. The engaged rotating tool generates a set of interconnected mechanisms that alter both the friction conditions and the contact area. Nonetheless, simplified models of the contact zone are accessible in the ISF literature. Typically, in such approaches, the contact area is simplified by assuming it to be fixed when the feed and step depth are held constant, while the tool movement (see Figure 3-12) is considered to be stable and equivalent to indentation followed by sliding.

As discussed in Section 3.1, an approximation of the contact area in incremental sheet forming was introduced by Aerens et al. (2009); this work has been cited in several references. It takes account of the tool radius and the wall angle, based on half the area of indentation of a sphere-shaped ball into a flat surface, with an inclined wall adjacent to the ball. The predicted area is assumed as rectangular strip of constant width (w) and length (l_c), as observed in finite element modelling of the process.

An enhanced contact model was presented in the reference by Adams & Jeswiet (2014b); this model comprises more geometry parameters (depicted in Figure 3-13) and allows in-process approximation of the contact zone. The authors developed the model supposing perfect adherence of sheet to the tool and path shape, and there is no contact between tool and previously formed sheet from a preceding tool pass.

Given the initial blank thickness t_0 component wall angle θ then the height of indentation h_1 is:

$$h_1 = t_0 \cdot (1 - \cos\theta) \tag{3-16}$$

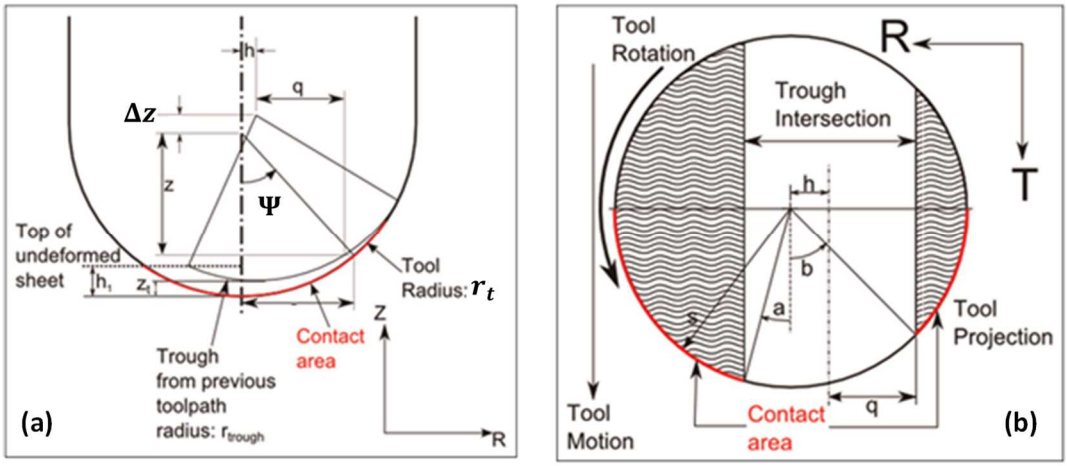

Figure 3-13: Modelling of contact area in SPIF (a); intersection of the tool-tip and the trough from the preceding pass; (b) plan view of the angle of the forming tool shows the intersection from preceding pass (Adams, 2014b).

For a given angle of the forming tool axis (Ψ) , the tool-tip projects a circle of radius, S. The preceding tool path assumed to project a rectangular width $(2q)$, with horizontal step-over of h; the two angles of contact $(a$ and $b)$ shown in Figure 3-13 is given by:

$$a = \sin^{-1}\frac{q-h}{s}, \text{ and } b = \sin^{-1}\frac{q+h}{s} \tag{3-17}$$

where q is half-width of the intersection between the tool and the previous tool path which can be found from:

$$q = \sqrt{{r_t}^2 - (r_t \cdot \cos\theta + \Delta z)} \tag{3-18}$$

The tool/sheet contact area is then determined as follows:

$$A = \int_0^{\cos^{-1}(\frac{r_t-\Delta z}{r_t})} \pi s r d\theta + \int_{\cos^{-1}(\frac{r_t-\Delta z}{r_t})}^{\cos^{-1}(\frac{r_t-h_1}{r_t})} (\pi - (a+b)) s r_t d\theta + \int_{\cos^{-1}(\frac{r_t-h_1}{r_t})}^{\pi/2} \left(\frac{\pi}{2} - b\right) s r_t d\theta \tag{3-19}$$

Equation 3-19 and the supporting formulae were developed by Adams (2014b), and compromises three discrete terms according assumptions illustrated in Figure 3-13. In order from left to right, these terms are area of full half circle swept below the bottom of the trough; area where contact on both sides of the tool-tip above the trough and below the bottom of the blank; area of one side contact above the bottom of the blank.

3.3.1.3 Relative velocity at tool/sheet interference

Increasing in relative velocity at too/sheet interface has been suggested to ease forming and improve maximum formability achieved in SPIF operations (Xu *et al.*, 2013; Otsu, Yasunaga, *et al.*, 2014). However, contact temperatures can extent sufficiently high to melt the sliding surfaces within the interface if the sliding speeds are high enough. The heat input in SPIF is a complex function of contact area along with process variables (feed rate and rotational speeds, and forming force), surface integrity of the material being formed, and the tool design. Contours of forming tool path correspond to spindle speed (rpm) and feed rate (mm/min), both effect sliding friction and frictional heating at the tool/sheet interface. For a given CP Grade 2 component and

blank thickness, with a particular tool-tip, the remaining SPIF factors are the step size, rotation and the feed rate.

At the interface, the forming tool is moving with relative velocity V_1 to the contact area and sheet is moving with velocity V_2 relative the same interface area. The rate of energy dissipated in the contact zone (q_{total}) is identified by the relative sliding velocity and friction force and the rate of frictional heating per unit area of contact (Bhushan and Kennedy, 2001) is given by:

$$q_{total} = \mu * P * V \tag{3-20}$$

where μ is the coefficient of friction, P is the contact pressure and V is the relative velocity = $|V_1 - V_2|$. More details on estimating the relative velocity factor during SPIF operations are set in section 4.3 and

3.3.2 Heat generation from plastic deformation

In addition to the frictional heat discussed in the preceding section, the localised plastic deformation induced in the bulk of the workpiece contributes to the total heat throughout forming. During plastic deformation, a significant amount (can be 90% to 95%) of the mechanical energy involved in the process is transformed into heat. In deformation processes such as deep drawing, extrusion, and similar continuous high-speed operations, a temperature rise of several hundred degrees Celsius is usually involved.

The large fraction of dissipated energy (generally noted β factor) also called Inelastic Heat Fraction (IHF) or Taylor–Quinney coefficient. The small portion of energy remaining after loading, usually called the stored or latent energy, is stored in the material as internal defects, phase changes and microstructure permeant changes (Pottier *et al.*, 2013; Knysh and Korkolis, 2015). The stored energy is a critical feature of the cold-worked state, and signifies the change in internal energy of the workpiece material.

In view of plastic deformation of a homogeneous solid body and the resulting, deformation-induced heating, two definitions of the instantaneous inelastic heat fraction usually specified:

IHF β is defined as the ratio of infinitesimal change in heat due to infinitesimal change in plastic work done. The integral IHF β_{int} is the ratio of finite change in heat generated during given finite change in plastic work denoted as Q and W^p. The both definition of the IHF (Knysh and Korkolis, 2015) can be written as:

$$\beta = \frac{\dot{Q}}{\dot{W}^p}, \text{and } \beta = \frac{Q}{W^p}$$

where upper dots means (rate) time derivative

General relations between the two quantities can be used to calculate β *or* β_{int} based on the known quantity (Knysh and Korkolis, 2015) as follows:

$$\beta_{int} = \frac{1}{W^p}\int_0^t \beta \dot{W} d\tau \text{ and } \beta = \beta_{int} + \frac{W^p}{\dot{W}^p}\dot{\beta}_{int}$$

Considering SPIF operations, mechanical energy input form a CNC machine is separated in two fractions. A part is stored in the material microstructure as shape forming energy, while the rest of the energy is dissipated in form of heat, which facilitated the forming process.

When incremental forming of a titanium sheet, a significant rise in workpiece temperature usually occurs due to both friction and plastic deformation. Although there are benefits associated with a raised forming temperature by increasing the forming speed, there is a limitation imposed by the strain rate that titanium can endure. Knysh and Korkolis (2015) investigated the IHF as a function of plastic strain for four materials: 303 and 316 stainless steels, commercially pure titanium and the alloy Ti-6Al-4V at a set of strain rates. In their experimental study, they indicated that the IHF is not constant with the plastic strain and is also sensitive to the strain rate. They also concluded that depending on the material, the IHF was generally ranged between 0.55 and 0.8, and could be as low as 0.3.

In the work by Ravichandran (2002), as shown in Figure 3-14(a), the plastic strain of titanium substantially reduces with an increase in strain rate. A material that is sensitive to the applied strain rate is α titanium; when deformation occurs at low strain-rate levels (Figure 3-14(b)), the relative ability of α titanium to store cold-work-energy in its microstructure is high (up to 65%). However, at high strain rates (3000 s^{-1}) this storage ability drops down to 80%, and it approaches to zero when forming at higher strain rate condition (Ravichandran et al., 2002 ; Mishra et al., 2014).

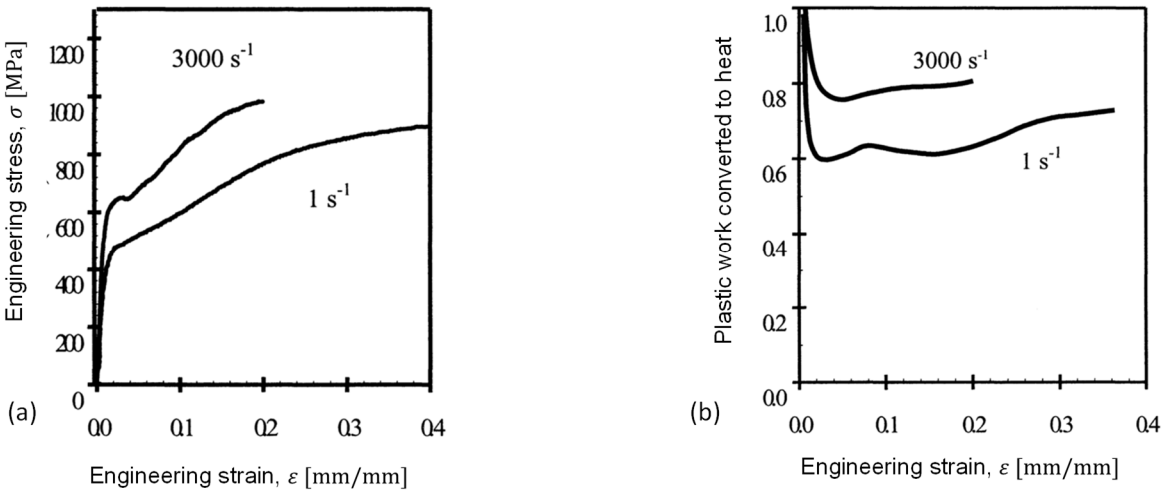

Figure 3-14: Strain rate sensitivity and dissipation of plastic-work of α-titanium in a compressive stress test: (a) strain versus stress at a high and a low strain rate, (b) portion of plastic work transformed to heat (Ravichandran, 2002).

3.3.3 Contact conditions

In SPIF operations, the choice of lubricant and lubrication strategy remains significant areas, particularly when forming titanium sheets. Severe contact conditions that could affect the quality of produced surface occur between tool-tip and sheet surface.

Titanium has high adhesion properties, which tend to cause galling upon contact with a tool-tip (similar to that of a built-up edge in machining). This results in material being picked up from the surface of the sheet by the tool-tip. These hardened material particles that were transferred to the tool-tip further scrape out the component surface and manifest damage along the forming path. That will detract from the aesthetic appearance of the produced component. If severe galling of material occurs, then besides having an extremely poor surface finish, a component may prematurely fail, or damage the forming tool (Jeswiet *et al.*, 2015).

Throughout the SPIF operation, the main factors affecting the efficiency of lubrication are the presence of a lubricant and its ability to stay in the path of the forming tool. Organic water-based and oil-based lubricants have been identified as unsuitable when applying SPIF to titanium, as these lubricants are squeezed out of tool/sheet interface under high deformation pressure, or they may decompose under elevated temperatures at high forming speeds. Solid lubricants are usually used for working conditions where lubricants are exposed to very high or very low temperatures, or very high pressure or very low pressures. The four basic types lubrication affecting the friction in metal forming are listed in Table 3-4 (Altan et al., 2005).

Table 3-4: Lubrication strategies in metal forming. Adapted from Altan (2005)

Strategy	Description	Friction coefficient
Dry/self-lubrication	Only oxide film on tool and workpiece act as separating layer; high friction (desirable in hot rolling and extrusion)	$\mu > 0.3$
Boundary lubrication	Typically, thin organic film physically adsorbed or chemically adhered to metal surface; used for high friction applications	$0.1 < \mu < 0.3$
Hydrodynamic lubricant	Thick layer of liquid lubricant exists between the surfaces; lubricant viscosity reduces with increased relative velocity	$\mu < 0.03$
Mixed-layer lubricant	Peaks of metal surface get boundary lubrication and valleys filled with liquid lubrication	$0.03 < \mu < 0.1$

The Stribeck curve shown in Figure 3-15(a) is typically used to categorize the friction properties between surfaces. It illustrates lubrication onset as function of the lubricant viscosity η sliding velocity v and normal pressure p (Altan, Ngaile and Shen, 2005). Figure 3-15(b), shows a comparison from experimental work, on the effect of the lubricating condition on the maximum forming angle achieved in SPIF of CP Grade 2 sheets (Hussain et al., 2007b). In addition to reducing the rate of tool wear, and protecting the sheet surface from getting scratched, proper lubrication will enhance the deformation and minimise the forming forces.

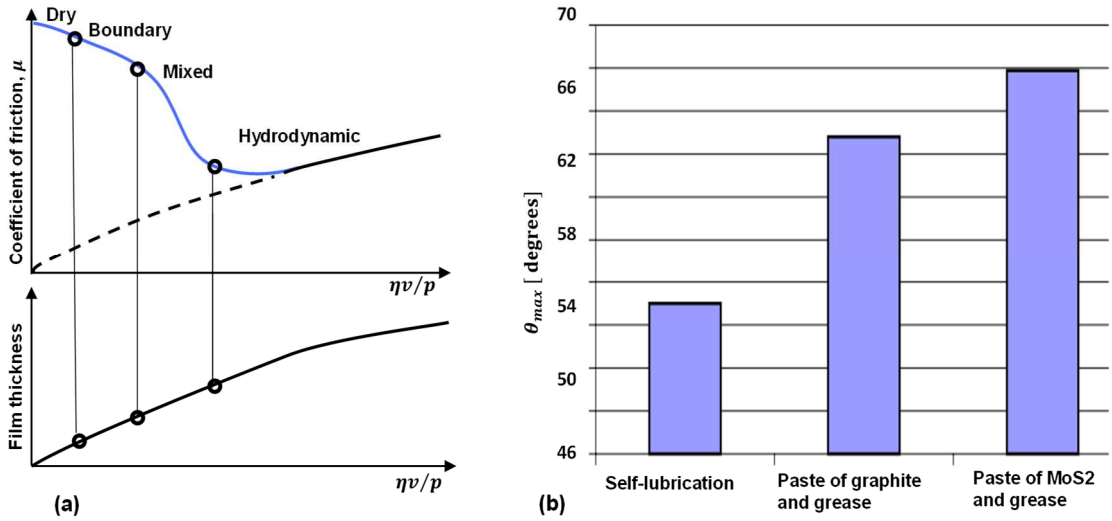

Figure 3-15: Effect of lubrication on the contact conditions (a) Stribeck curve showing the onset of various lubrication mechanisms (Altan, 2005); (b) Effect of friction condition on the formability of CP Grade 2 (Hussain, 2007b).

Azevedo et al. (2015) evaluated the influence of a range of specific lubricants on surface roughness of 1050 aluminium and DP780 steel sheets. They observed that opposing trends exist between workpiece hardness, the viscosity of the lubricant, and the obtained roughness. In another work by Gulati et al. (2015), the authors concluded that lubricant has the most influence on both the maximizing formability and surface quality in the SPIF of aluminium. Per their findings, the major effects on surface quality (in descending order) are attributed to lubrication, the feed rate, step size, tool-tip radius, sheet thickness and the spindle speed.

Solid lubrication in the form of molybdenum disulphide (98.5% pure MoS_2), graphite, boron nitride or a similar powder lubricant has been found to be more functional and is commonly used for titanium Grade 2 forming applications. The adhesive tendency of MoS_2 lubricant is slightly better than that of graphite or boron nitride, and gives a lower friction coefficient which is about 0.1 (Nolo *et al.*, 1996). To ensure the presence of MoS_2 lubricant at the interface, it should be mixed with white petroleum jelly in the ratio 4:1 (Hussain *et al.*, 2008); with an suitable pore size and thickness of coating to contain the lubricant mix, they successfully formed CP Grade 2 with good surface finish.

Contrary to this preceding outcome, another reference (Fan *et al.*, 2009; Fan and Gao, 2014) reported that a self-made oxide film failed when electrically assisted SPIF of Ti-6Al-4V was attempted. Instead, they established self-lubricating by depositing a nickel disulphide metal matrix composite (Ni-MoS_2) lubricant and produced better results when forming at high temperature.

Notwithstanding the results published by Hussain et al., (2008a), the author of this dissertation has observed the failure of their suggested lubrication strategy when he applied it. Throughout the SPIF of CP Grade 2 at a moderate rotational tool speed, the petroleum jelly in the mix melted and burned-out due a rise in temperature. Friction was greatly increased and the surface of titanium sheet was destroyed. It is noted that the method was originally developed for non-rotating tools. More details on the temperatures generated during the experiments are given in the chapter on data analysis.

3.3.4 Surface integrity of formed components

As significant product quality constraint, surface roughness in SPIF is still one of the major concerns. The relatively high surface roughness as compared to the mean values (4 – 12 μm) for sheet metal forming processes is considered a significant drawback in SPIF.

For the SPIF process to be more industrially relevant, components produced by the process need to have a satisfactory surface finish at the microscopic level, from both a functionality and an appearance point of view (Durante, Formisano and Langella, 2010; Liu *et al.*, 2014).

The topic of roughness topography in SPIF has been widely investigated in the literature, an indication of the drive to improve forming accuracy at a micro-scale and to understand the consequences of different forming conditions on surface quality. Experimental and analytical work done by Bhattacharya et al. (2011), Echrif and Hrairi (2014), and Liu et al. (2014), explored the dependency of roughness on process design and controlled variables. The common problems of rough surface quality in SPIF entail two criteria:

Internal surface roughness (Figure 3-16(a)) due to direct tool-tip/sheet contact, and external non-contact surface defects (Figure 3-16(b)) due to a familiar texture known as the orange peel effect (the OP effect is a surface defect occurs when the forming tool is in intimate contact only with one side of the sheet). In both magnitude and spacing, typical internal roughness exhibits large-scale waviness shaped by the tool path and small-scale roughness caused by large forming strains on surface. The external roughness (orange peel) is mainly caused be large surface strains.

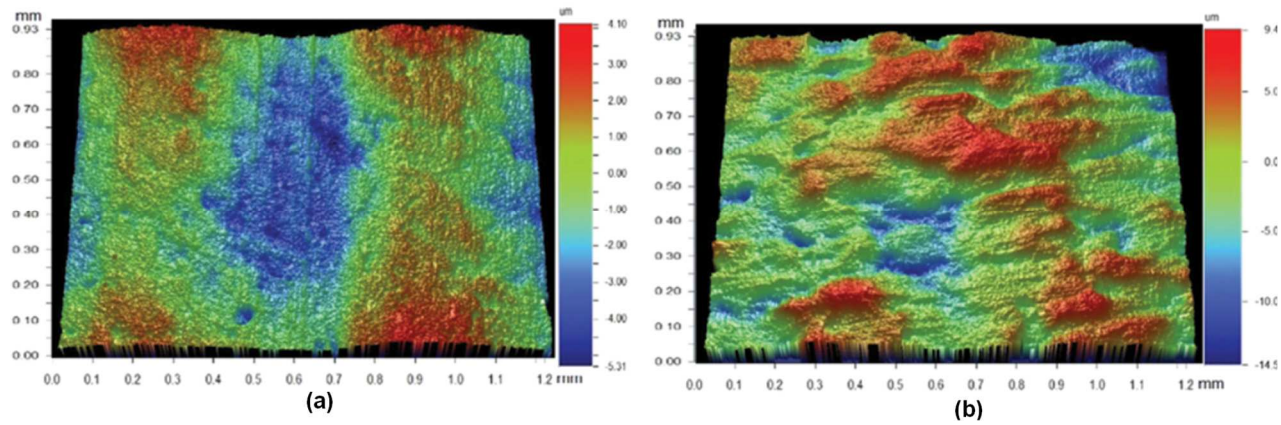

Figure 3-16: Surface topography produced by SPIF of AA7075-O (a) Internal too-tip/sheet interface; (b) outer non-contact surface (Liu *et al.*, 2014).

The applied tool-tip diameter, size of the step depth, as well as the wall angle to be formed have all been found to significantly influence on the surface quality of a component. Tool speeds in both the rotational and the feed rate direction, have an important role too. An improved surface finish can be achieved by selecting an appropriate tool-tip diameter and adjusting the other variables to suitable settings. Typical surface parameters that often used to evaluate surface finish (see Figure 3-17) are the mean roughness depth (R_z), the arithmetical mean roughness (R_a) the total height of the roughness profile (R_t).

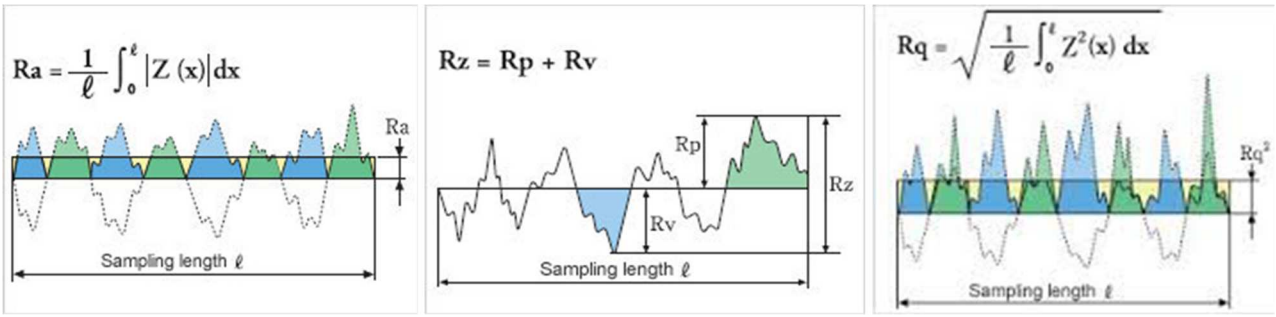

Figure 3-17: Typical 2D parameters of surface roughness (Anonym, 2016).

Few studies provide information on either measurement resolution, or the sampling interval implemented in characterisation of surface finish. In their work on surface topography, Powers et al. (2010) reported on the effect of the rolling direction of the blank, on the surface finish obtained in SPIF. They used statistical approach in the design of their experiments and provided quantitative statistical testing to support their conclusions. The study revealed that surface roughness is higher with the rolling marks perpendicular to the forming orientation. Particularly the non-contact side of sheet develops a roughened look (like an orange peel) because of the different alignments of neighbouring grains at the sheet surface. These grains tend to expand or shrink randomly and this results in a rough surface.

In SPIF, some forming parameters are more closely associated with alterations to the exterior surface. Step size Δz is a key factor affecting the surface finish obtained; roughness tends to be coupled to the step depth size and the immediate forming angle. In the literature (Hamilton & Jeswiet, 2010; Samuel, 2010), studies have been made of the orange peel phenomena and quality of the outer surface of the SPIF components. The amount of orange peel formation was concluded to be a function of the shape factor, $\sin\theta/\Delta z$ which is a ratio between the wall angle and step depth (Jeswiet *et al.*, 2015).

In Hamilton and Jeswiet (2010) it was reported that the equivalent outer roughness, R_{eqv}, is an empirical combination of the arithmetic average of the roughness, R_a , and the ten-point average roughness, R_z. The equivalent outer roughness is strongly dependent on a shape factor, $(r_t \cdot sin\,\theta/\Delta z)$, which is mainly affected by the step size embedded within it . A small wall inclination angle θ increases the absolute distance between two subsequent loops for a given tool pitch. Hamilton and Jeswiet (2010) developed an expression that describes the exterior roughness as:

$$R_{eqv} = \frac{K}{r_t}\left(\frac{AR_a - BR_z}{\sin\theta/\Delta z}\right) \tag{3-20}$$

where: for a tool radius of 6, 35 mm, A = 0.4 and B = 0.6 are respectively the corresponding weighting constants for Ra and Rz, and K= 25.4 is a constant for unit conversion when using metric units.

Exterior roughness is directly proportional to the size of tool step depth (see Figure 3-18). Large Δz increases the stair effect on the surface and results in high roughness, and reverse is true with small Δz.

In view of internal surface roughness, there is a strong relationship between the size of Δz and the value of two roughness parameters, the maximum profile height, R_t and the mean profile height / the ten-point average

roughness, R_z (Durante, Formisano and Langella, 2010). With a large step size, a higher material volume has to be processed at a single pass, which increases the forming force generated, and more area that is involved at the tool-tip/sheet interface, resulting in the lining pattern on the sheet. On the internal sheet surface (Figure 3-18), with a large step size, a wavy profile (sinusoidal type) surface is produced, perpendicular to the tool path direction. It transforms from wavy to strictly roughness without waviness as the increment decreases (Hagan and Jeswiet, 2004).

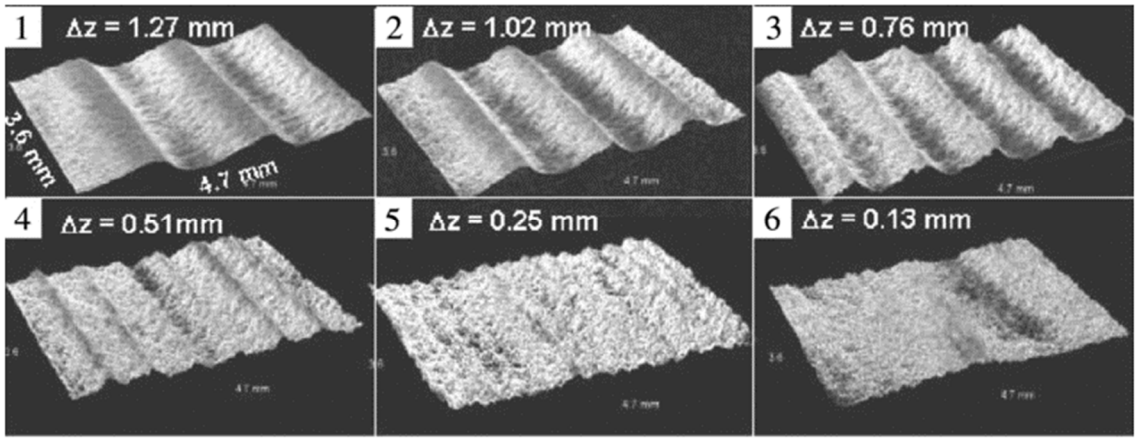

Figure 3-18: Effect of step depth on surface roughness. (Hagan and Jeswiet, 2004).

In assessing the roughness of a wavy profile shaped by SPIF, the average peak-to-valley height, R_z, is a more useful parameter than R_t, as it avoids surface irregularities from influencing the evaluation. Because formability in SPIF is very comparable to a shear forming operation, a similar equation to determine the theoretical peak-to-valley height, R_t has found to be useful. This can be seen from Equations 3-21 and 3-22, substituting tool radius (r_t) for the roller radius (r), and Δz for feed per revolution, V, in the formula of shear forming. In Equation 3-22, R_{tool} is an additional offset factor = 0.5 μm, developed empirically to compensate for the difference between the theoretical and the measured roughness for very small values of Δz (Hagan & Jeswiet, 2004).

In the shear operation:
$$R_{t\_shear} = r - \sqrt{r^2 - \frac{V^2}{4}} \tag{3-21}$$

In the SPIF:
$$R_{t\_SPIF} = r_t - \sqrt{{r_t}^2 - \frac{\Delta z^2}{4}} + R_{tool} \tag{3-22}$$

If a very small ratio of tool-tip size to sheet thickness is used ($\frac{r_t}{t_0} < 2$), it creates excessive contact pressure at the interface. The material is squeezed out from tool/sheet interface and piles up, forming a thin wall that grows in height with successive passes of the tool (Hussain *et al.*, 2013). Even with a tool radius to sheet thickness ratio bigger than two, there is still a distinctive ridge along the edge of the tool path when the tool diameter is small. As the tool size is increased, the contact area increases and expands to overlap the edge of the preceding tool path, and in the process flattening the upwelled material of that preceding tool run. Tool-tips with a diameter bigger than 9 mm have a tendency to reduce formation of the orange peel effect; This tendency is

attributed to the lower stress at the interface because the tool-tip better supports the sheet when the contact zone is increased (Hamilton & Jeswiet, 2010).

The tool-tip overlap has a negligible influence on the distribution of the formed thickness. However, when the tool-tip moves according to its helical tool path and depending upon the selected step depth and tool-tip diameter, certain parts of the material will be formed repeatedly due to the overlap. This will lead to an inhomogeneous reduction in thickness and strain hardening across the component, which in turn speeds up material failure because of thinning and low ductility. More important is the opposing relationship between tool-tip size and maximum formability, which limits the use of a larger tool size as a means of achieving a better surface quality.

The surface finish is related to the tool and sheet contact conditions. The tip of forming tool is neither a perfect cylinder in shape, nor straight. These factors can also affect the actual step height Δz of the tool path. In practice, this effect could be reduced or become negligible if the tool-tip is made with grounded surface, suitably hardened and polished before use. An extremely beneficial option to reduce friction and improve surface finish is a forming tool with a rigid rolling-ball attached. Such a solid hemispherical tool rolls over the surface without sliding over the workpiece surface and because there is very little friction, most of the applied force is transmitted to the workpiece.

SPIF deformation trajectory is a continuous path created for the tool to follow when producing the component and tool path strategy implemented has a core influence on surface quality. Forming using contour tool path in which the tool moves with a constant increment in the z-direction, particularly with large Δz, leaves marks (scars) at every transition between two successive layers of formed surface. For better results, step depth and scallop height need to be correctly set.

3.4 Characterisation of forming tool

The ISF process does not imply shape dependent tools of matched punches and dies; instead, it relies on the movement of a generic stylus in combination with proper tool trajectories, to shape the workpiece. These generic tool styli are usually designed and made by the users, as they are not yet commercially available. The characteristics of the tool stylus are a vital factor affecting both performance during forming and the product. The importance of the forming tool is enhanced when one considers that this tool provides the only path through which forces can be applied to the workpiece. It is assumed that most of this energy is converted into plastic deformation, and contributes to the deformation of the component shape. Inevitably, however, some of this energy is lost when it converted into less desirable forms of energy such as vibration, heat, and tool deflection.

The material of which tool is made, is of crucial importance due to the severe tribological interaction during the ISF process, where tool-tip is in continuous sliding contact with the sheet. High mechanical and thermal loads at the tool/sheet interface cause tool deterioration and premature wear. Thus far carbides, and cold-workable tool steel hardened and tempered to 60 HRC, have been found to exhibit sustained high mechanical and thermal stability, making them suitable materials for tool-tips; their strength and wear resistance allow

them to maintain their forming surface for a longer time (Meier *et al.*, 2013). However, for biomedical use, like body parts, contamination of the surface of the component by chemical elements harmful to health (such as Mn, Si, Ni, and Cr) may occur (Castelan *et al.*, 2014). Thus, a new tool-tip material, which is compatible with health requirements, needs to be identified; titanium might be a suitable material.

Tool design and stiffness:

Due to the main force F_z tool, stiffness in the axial direction is an important factor; though the other two in-plane forces can become influential with increasing the draft angle and/or step depth. Typically, increased force in the radial direction can result in tool-tip deviation from the target tool path, forming of shorter contours than intended (Asghar *et al.*, 2013). Owing to the incremental nature of the SPIF process, there can be a significant drop in the accuracy of the final product because of the cumulative effect of a small error in the contour cycle (Lingam *et al.*, 2015).

While there are no commercially available forming tools, it is the responsibility of the user to design and make suitable forming tools, taking cognizance of material properties and limiting deflections so that an acceptable product is produced. The designer needs to be concerned with tool deflection when selecting the dimensions and stiffness of the tool, especially when forming high strength alloys, or when working at higher speeds and/or increased step depths to increase productivity.

Designs incorporating different tool-tip geometries have been explored, in the literature, forming tools with spherical or hemispherical tips are most frequently cited, as depicted in Figure 3-19(a), the hemispherical tip shape is integrally tooled with the shank.

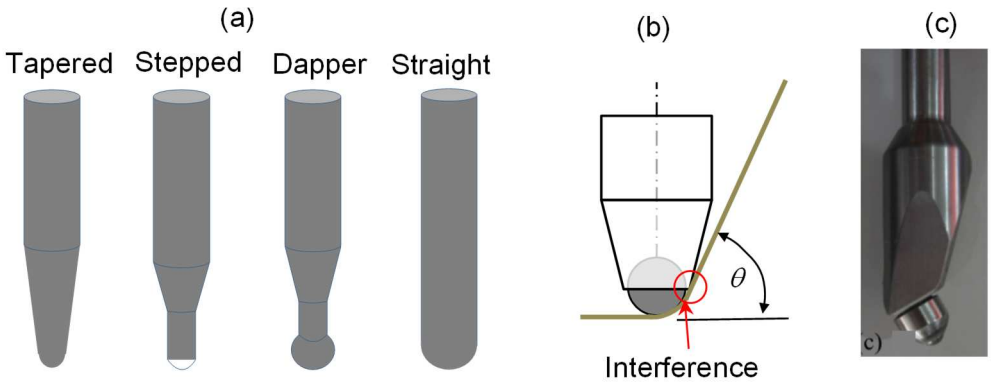

Figure 3-19: Common designs of SPIF tool-tip (a) different profiles of solid tool; (b), interference of ball-ended tool with sheet at large forming angles (c) oblique roller-ball tool (ORB) to avoid interference (Lu, Fang, *et al.*, 2014).

The hemispherical tool-tip is made in various forms. Tapered and stepped forming tools can have a small tip with a shaft thick enough to prevent tool bending; these forming tools are ideal for small areas. The one-based, over-hemispherical segment forming the tool-tip provides clearance to the tool-shank and reduces shank/sheet interference, allowing the forming of steep wall angles. However, due to sudden change of profile where the ball connects to the shank, it has low stiffness and can easily fail under lateral forming loads. The straight type has a simple and strong geometry.

A spherical tool-tip, or a straight ball-ended variation, shown in Figure 3-19(b), has a free, rotating ball made of hardened metal, which is attached to the tool head. Because of smooth, rolling action, this later design reduces friction forces, as well as surface roughness, and improves the forming process as compared to the solid hemispherical tool-tip. The disadvantage of the innovative spherical forming tool with its freely rotating, spherical tip, with pressurised fluid operation, increases the cost of production (Marabuto *et al.*, 2011; Li, Liu, Daniel, *et al.*, 2014).

In addition, the so-called vertical ball-type faces a restriction on maximum forming angle that can be accomplished. Due to possible interference between the tool-shank and the inclined wall of the component, this limitation on spindle alignment becomes obvious when using three axes machines. To overcome this problem, an oblique roller-ball (ORB) configuration as shown on Figure 3-19(c), was suggested by Lu et al. (2014a). Using this tool design, forming angles as large as 80 degrees have been achieved, it has the advantage of rolling action with no tool/sheet interference at steep wall angles. However, the ORB tool cannot be used directly with standard CAM tool paths; it necessities developing a dedicated NC code to pair the rotation of the forming tool with its feed rate.

Despite the advantages of spherical tool-tips, variations of the solid hemispherical forming tools are simpler and less expensive to make and operate. That is why they are most frequently used and cited in the literature. The main drawback of the solid or fixed head tool-tip is that, regardless of the solid lubricant conditions created, it leaves scratches on the component surface, especially when forming soft materials.

A forming tool's resistance to deflection is function of its shape, length diameter and material composition. As shown Figure 3-20 the free length that the tool extends from the collet, also known as overhang (L_{oh}), is the distance from tool-tip up to the point where the forming tool emerges from the collet.

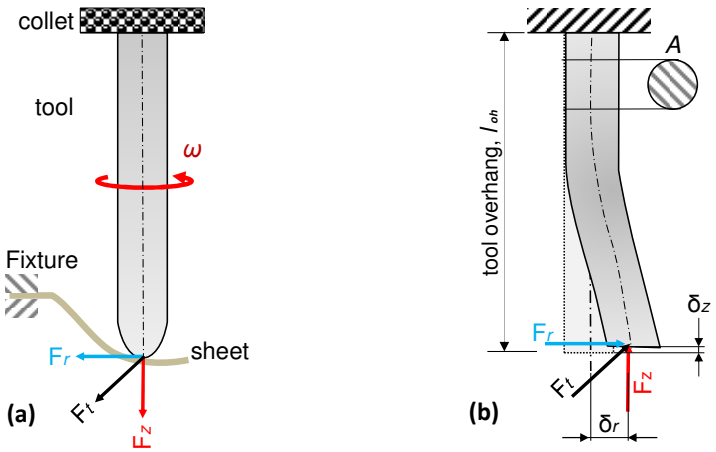

Figure 3-20: Force diagram for tool deflection in the SPIF: (a) Force imposed by tool on the sheet, and (b) deflection on the forming tool

Tool rigidity can only be increased by using material with high modulus of elasticity or reducing its length/diameter ratio. In this section, the focus will be on tool length and diameter; for simplicity, tool shape and material will be ignored.

The tool can be considered as a cantilever beam with single fixed support with end loads acting on its tip (Asghar *et al.*, 2013). For homogenous, linearly elastic materials and ignoring effect of beam rotations, deflection in tool (δ) can be calculated as:

$$\delta = \frac{F_r L_{oh}^3}{3EI} \tag{3-23}$$

Whereas: F_r is the radial force in newton N, E is modulus of tool material GPa, and I is moment of inertia in mm^4 (for a regular cylinder, $I = \pi d_s^4/64$). The ratio of L_{oh} to the tool shaft diameter is an important factor that affects the tool stiffness and resistance to deformation from the reaction forces. From the above equation, the rigidity is inversely proportional to cube power of its overhanging length. More simply stated a small increase in the length can result in a significant reduction in the rigidity. Guidance from theoretical and practical approaches advise that to reduce deflection and improve quality, tool overhang needs to be minimised, leaving sufficient clearance for the job requirements, the applied fixture and other obstacles.

The cross-sectional area of the tool-shank has even stronger effect than its length on the tool stiffness or rigidity. From the same equation, rigidity is directly proportional to the forth power of the shaft diameter, so that a small change in diameter can result in a change by four-fold in the rigidity (Jones and Town, 2013; Smith, 2013). Therefore, whenever possible it is preferable to select larger diameters; it must however be born in mind that an increased diameter will noticeably raise the forming forces required, as will be discussed later. The diameter of the forming tool will of course be limited by the scale of the smallest features of the component to be formed (Kiyak *et al.*, 2010; Bhattacharya, Bera and Thakur, 2015).

Besides ensuring maximum tool rigidity, it is also important to be aware on implications of tool rigidity on the forming forces. Also, how these forces can be used to gain as much productivity as possible. Forming tool deflection and forming tool forces are intimately related. Bigger forming forces not only mean larger deflections, but it also equate to a more plastic deformation in sheet material. In order to determine the error caused by the deflection, it is necessary to predict the forming forces at reasonable accuracy acting on the tool at stable equilibrium, along with current thickness prediction, and use their threshold to compensate for the tool and sheet deflections (Lingam *et al.*, 2015).

An example of failure because of an excessive tool deflection is shown in Figure 3-21. This was the 6 mm tool-tip initially used in the experiment for this reearch.

Figure 3-21: Image of tool failed by fracture during the SPIF test

CHAPTER 4 INTEGRATION OF CURRENT SPIF KNOWLEDGE

4.1 Overview

As a starting point, a benchmark process should be set up, governed by a set of standard input parameters. The properties of the process can then be gauged by systematically varying the input parameters, keeping the process within the characterization region. Although the extreme values of the range of the input parameters will most probably give a result within the safe limits of the process, such outlying values are likely to cause aberrations of the process, yielding outlying responses.

It is understood that the boundary of the non-operable regions is often not known prior to implementation of the DoE. For this reason, experimentation often requires replication, and it may be best to simply plan for two experimental stages. To begin, a minimal screening experiment can be used to verify the feasibility of the characterization region, and identification of the most significant processing factors. In some applications, it may be necessary to move the standard process away from the non-operable region (such as down and towards the right in Figure 4:1) or otherwise reduce the characterisation range. After verifying the feasibility of the characterization range with a screening experiment, the run conditions can be augmented with additional runs for higher model fidelity and an optimised process(Kazmer, 2009).

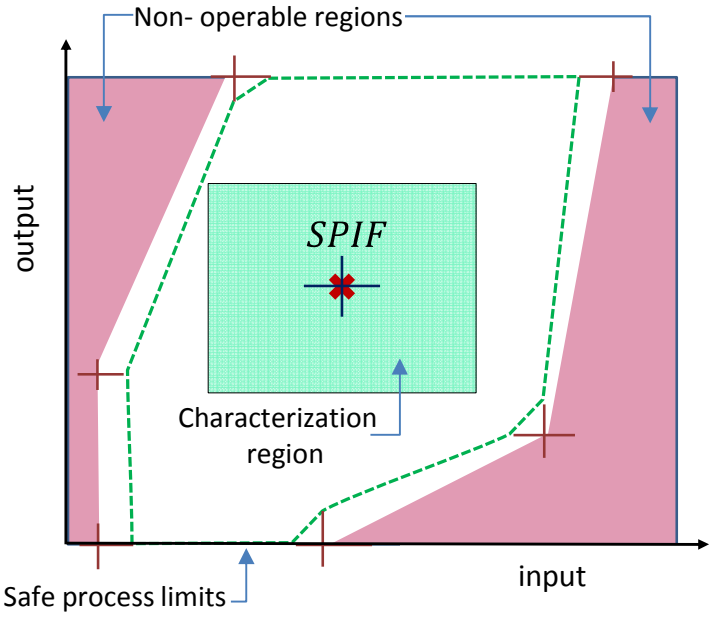

Figure 4-1: Identification of SPIF characterisation range in terms of two process factors Adapted from (Kazmer, 2009).

In this chapter, a systematic quantitative literature review as identified by Pickering and Byrne (2014), was applied. Information and statistical data extracted from other experimental work, found in the literature, were drawn on as references when the crucial design factors and their variable extremities were characterised (Uheida, Oosthuizen and Dimitrov, 2016).

Significant data on each operating parameter and forming condition, from more than 100 relevant research articles and studies, were analysed and documented. In selecting these values and their limits for the various parameters, the following conditions had to satisfy the maximum wall angle θ_{max}, the minimum load, and the surface quality requirements. Considering conclusions drawn by several authors, the suggested optimum values, together with their applicable upper and lower limits, were used to minimise the number of experiments required. Using this information narrowed down the scope of the experimental work. A separate list of the publications used to compile the raw data has been included as an Addendum A.

Furthermore, to explicate relationships between the applied forming conditions and the axial forces during steady-state deformation, a virtual study by means of approximate formulas and the reference data were employed throughout the sections that follow. A conceptual framework (processing window) of the SPIF process was developed based on this critical and evaluative review. This conceptual framework meets the requirements of Phase I.

4.2 SPIF mechanical demands

Using the key theoretical parameters, the effect of the generated force on the process output, could be analysed. This information provided a foundation for the development of a first layer of the process map, based on a safe process loading. In deciding on the forming conditions, the reference values assigned to each variable, as well as their applicable ranges were set in accordance with the knowledge gained from the above-mentioned evaluative review study. To evaluate the influence of a certain parameter, its value was varied within the applicable limits of its reference value; while the other variables were kept fixed at their respective reference values — see Table 4-1. The outcome of these trials was plotted to provide a set of graphs to assist with visualizing the relationships between the parameters and the resulting output; these graphs provided insight into the process mechanical demands.

4.2.1 Relevance of the SPIF reference data

The process factors listed in Table 4-1 are understood to be the most influential parameters in SPI; there accepted range and reference value were established from the literature and are given. The values given in Table 4-1 apply to the CP Grade 2, which was used as the reference material in this study. For calculations, the accepted reference values of the variables shown in the table are considered optimum (theoretical) values and this will be reasoned accordingly during this study.

Table 4-1: Accepted range and reference values of ISF variables used in the scheming of $\boldsymbol{F_Z}$ for CP Grade 2

Parameter expanse	*Material strength*	*sheet thickness*	*Tool diameter*	*Depth step,*	*wall angle,*
Unit	σ_u [MPa]	t_0 [mm]	d_t [mm]	Δz [mm]	θ [deg]
Range	110 - 1000	0.5 - 1.2	6 - 12	0.25 - 0.8	10 -75
Reference value	*350*	*0.8*	*10*	*0.35*	*45*

4.2.2 Relevance of the force formula used

The empirical formula used in computing the forming load is the generalised Equation 4-1 developed by Aerens et al. (2009). This formula has been derived from experimental studies, and analytical relationships obtained from finite element analyses. It states the relationship between the steady-state axial force, F_z as the largest and most important force, and the process key factors. The correlation between the force predicted by the formula and the force reported from experiments is high.

$$F_z = 0.0716 \cdot \sigma_u \cdot t^{1.5} \cdot {d_t}^{0.41} \cdot \Delta h^{0.09} \cdot \theta \cdot \cos\theta \tag{4-1}$$

where: F_z in N; σ_u in MPa; t_0 in mm; d_t in mm; Δh is the scallop height in mm; and θ in degrees.

As to the definition of scallop height as used in the Equation 4-1, Figure 4-2 depicts the distinction between scallop height and step depth in the SPIF process.

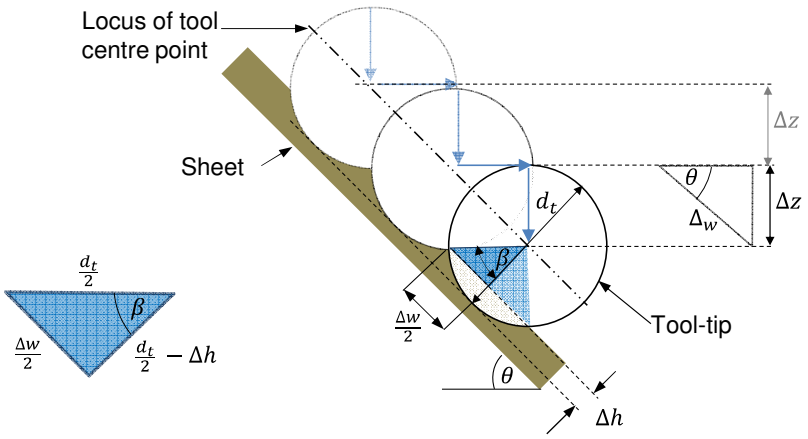

Figure 4-2: A SPIF component radial cross-section with the tool out shows the definition of the scallop height, $\Delta \boldsymbol{h}$, and scallop width, $\Delta \boldsymbol{w}$

The scallop angle (β) comprises half-wave interaction between two successive contours at the surface of the formed component and can be estimated using Equation 4-2.

$$\beta = \arccos\left(1 - \frac{2\Delta h}{\mathrm{d}_t}\right)$$

therefore:

$$\beta = \arcsin\left(\frac{\Delta z}{d_t \sin\theta}\right) \tag{4-2}$$

The motivation for using the scallop height instead of the step depth Δz as is a common practice in state-of-the-art SPIF is twofold. Firstly, the scallop height Δh is related to the roughness of inner surface of the sheet, thus the parameter affecting the surface quality of a component produced by SPIF. Secondly, when forming a wall with a varied angle, maintaining a fixed value for Δh fixes the number of tool passes per unit width perpendicular to the travel direction of the tool; this results in creating a uniform surface finish.

As shown on Figure 4-2, the scallop width Δw represents the theoretical distance between two scallop lines on the inner surface, and is a function only of Δh and d_t, as shown in Equation 4-3. The number of passes per unit width is the inverse of the scallop width Δw, where:

$$\Delta w = 2\sqrt{d_t \cdot \Delta h - (\Delta h)^2} \approx 2\sqrt{d_t \cdot \Delta h} \tag{4-3}$$

The first step in the design of the increment depth for a given tool-tip diameter is to specify Δh, while keeping the surface requirements in mind; the vertical step down Δz is then found by:

$$\Delta z = \sin\theta \cdot \Delta w \tag{4-4}$$

To rationalise using Δh instead of Δz in the prediction of F_z , the approximation Equation 4-5 relates Δh to the depth increment Δz; Aerens et al (2009) studied this effect and concluded that the impact of Δz on the predicted force remains valid using Δh.

$$\Delta z = 2\sin\theta \,.\sqrt{\Delta h(d_t - \Delta h)} \approx 2\sin\theta.\sqrt{\Delta h\, d_t}$$

$$\Delta h = \frac{(\Delta z)^2}{(2\sin\theta)^2 \cdot d_t} \tag{4-5}$$

As justification for using Equation 4-1 in this study, Table 4-2 provides a comparison between forces measured in experimental work cited in literature, and forces calculated by Equation 4-1, while using same forming conditions as reported in the corresponding reference. Good correlation is shown between the results as listed at the bottom of the table.

Table 4-2: Effect of material type on ISF forces ; comparison of the computed values of force $\boldsymbol{F_z}$ with experimental results from literature

Material type	Aluminium	Aluminium	Aluminium	Steel
Alloy	AA7075-O	AA3103-O	AA3003-O	DC05
UTS, σ_u [MPa]	198	135	120	290
Thickness, t_0 [mm]	1.6	2.0	1.2	1.0
Tool-tip $\emptyset_t$ [mm]	30	10	10	10
Step depth, Δz [mm]	0.5	0.5	0.5	0.5
Wall angle, θ [deg]	60	50	50	65
Scallop height, Δh [mm]	0.003	0.011	0.011	0.008
The predicted force, F_z [N]	**2044**	**1500**	**620**	**945**
The measured force, F_z [N]	**2000**	**1460**	**600**	**950**
Reference work	Li, Liu, Lu et al.(2014)	Duflou et al. (2007)	Bouffioux et al. (2008)	Petek et al. (2009)

4.2.3 Effect of material type and thickness

The type and thickness of a material have a direct bearing on its mechanical properties and deformation behaviour during forming. Selecting range of working parameters, loads generated, and thickness of final

product all are subjected to the initial thickness and strength of the material. Figure 4-3 highlights the common range of sheet thickness and types of materials as sourced from the literature. Most these materials are soft and ductile metals, like deep drawing steel, and aluminium, particularly the 3xxx series.

Some studies included the forming of hard-to-form alloys, for example titanium and titanium alloys, stainless steel, magnesium and high-strength aluminium. A few studies also uncovered the possibility of expanding the material capability window of SPIF beyond metals to include polymer plates (Martins *et al.*, 2009; Silva, Alves and Martins, 2010; Bagudanch *et al.*, 2015; Davarpanah *et al.*, 2015).

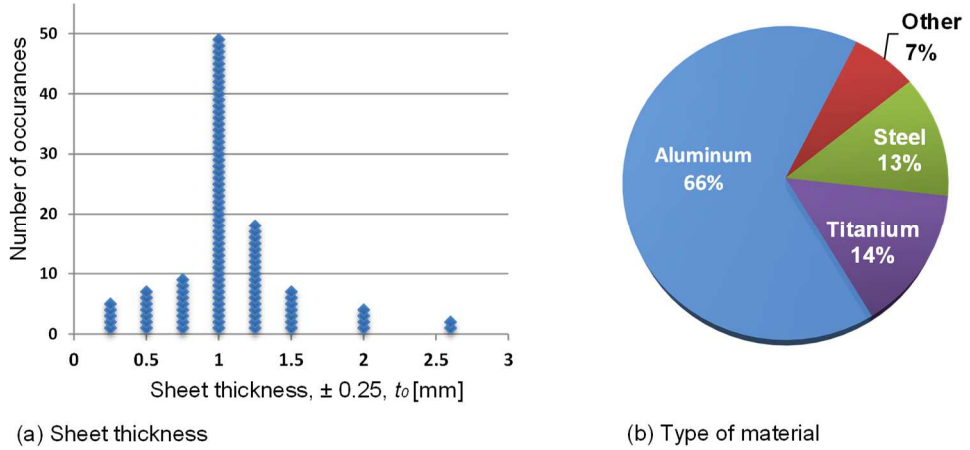

Figure 4-3: The prevalence of sheet thicknesses and material types encountered in the literature

The ISF process incurs high formability; it should be noted that the suitability of this process to effect deformation is clearly associated with material type used. Forming loads are strongly dependent on the material strength and thickness of the material formed. Also, the maximum forming angle θ_{max} that can be obtained in a single pass forming of high-strength metals such as alloyed Ti - 6Al - 4V titanium alloy, is low (~ 45 degrees). For aluminium and mild steel on the other hand θ_{max} is more than 75 degrees.

The mechanical properties of a material considered for forming, especially its tensile stress, provide the first clue of the forces that will be needed during deformation. Notwithstanding the requirement of relatively small forming forces because of the localised incremental deformations, the magnitude of these forces increases in proportion to increasing material strength; this is reflected in Equation 4-1. Higher F_z values are therefore anticipated when forming high strength titanium or stainless steel alloys in contrast to soft aluminium or other mild alloys.

To visualise the influence of material type and blank thickness on forming loads, the UTS values (σ_u) are given for a selection of engineering alloys typically utilised in sheet forming industries (see Table 4-3). For each material type the value of F_z was calculated for each of three sheet thicknesses, while the other process variables were kept at their reference values as given in the table— see Table 4-3. The most commonly occurring sheet thicknesses, namely 0.8, 1.0 and 1.2 mm, were chosen, as they were most often specified in the literature consulted.

Table 4-3: UTS data for common engineering alloys

Metal / Alloy	σ_u [MPa]	Typical applications
aluminium AA2024 – T3	490	aerospace industry
aluminium AA3003	114	building industry
aluminium-magnesium AA5754 – O	220	automotive industry
deep drawing steel DC05	280	automotive, body panels
magnesium AZ31	260	aerospace, aircraft fuselages
commercial pure titanium CP Grade 2**	350	medical applications
stainless steel SS304	505	industrial application
titanium alloy Ti - 6Al - 4V	1000	aerospace industry

For the material chosen in this study, namely commercially pure titanium Grade 2, axial force levels of 500–1500 N are predicted depending on the thickness of the sheet material — this material is indicated with a double asterisk in Table 4-3 and on the x-axis of Figure 4-4.

Magnesium AZ31 and titanium Ti-6Al-4V are difficult to form by cold-working due to their low ductility. With magnesium AZ31, the problem is brittleness, and large forming forces as well as high elastic recovery create problems when forming titanium Ti-6Al-4V. From Figure 4-4 compared to the other materials, a relatively higher level of force will be required when forming Ti-6Al-4V at the same forming conditions and sheet thickness. Although both the alloys AZ31 and Ti-6Al-4V are not on the green list of so-called cold-worked ISF-friendly materials, they are included here for comparison only; in the literature both these alloys appear in hyper versions of the ISF process, referred to as heat-assisted incremental forming.

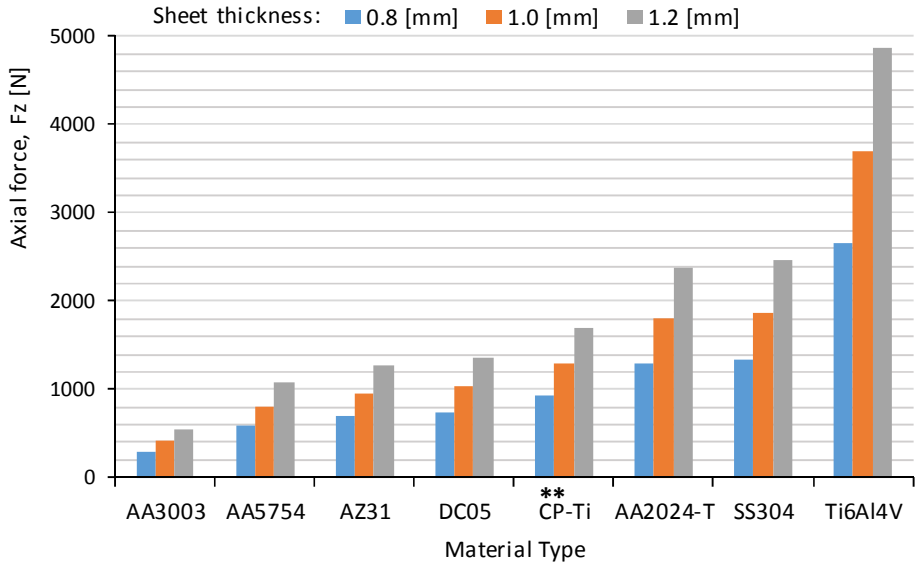

Figure 4-4: Influence of material type and blank thickness on force F_z as estimated from computed data (** indicates the material used in this study)

As can be seen from the graphs in Figure 4-4, the magnitude of the axial force typically required for SPIF, depends not only on the properties of the type of material used, but also on the initial blank thickness.

The axial force required is directly proportional to the blank thickness. This is to be expected because a thicker sheet is more rigid, which results in less bending and more shear. This in turn increases the volume of material subject to deformation, leading additional forming forces being required. The requirement for an increased force is intensified for material with a higher ultimate tensile stress. It is noted that both the material properties and the sheet thickness affect the required axial force, but the shape and trend of the graph linking these parameters does not materially change.

And finally, in the standard SPIF processes, a simple proportionality exists between the axial force, F_z and the UTS of the material; a scalar ratio can be applied to the UTS of the material to yield an approximate value for the axial force required to create plastic deformation in the workpiece — $F_z = 3.8 \cdot \sigma_u$ (Aerens *et al.*, 2009). This relationship between F_z and σ_u can be useful for the initial engineering of the punch and the fixture, as well as for the selection of suitable machine.

4.2.4 Effect of the component wall angle

Figure 4-5, presents graphs of both sheet thickness (on the left vertical axis) and the axial force (on right vertical axis), against the forming angle. The axial force and sheet thinning were determined using Equations 4.1 and 3.5 respectively. The initial sheet thickness set as 0.8 mm as well as keeping all other process variables at their reference values.

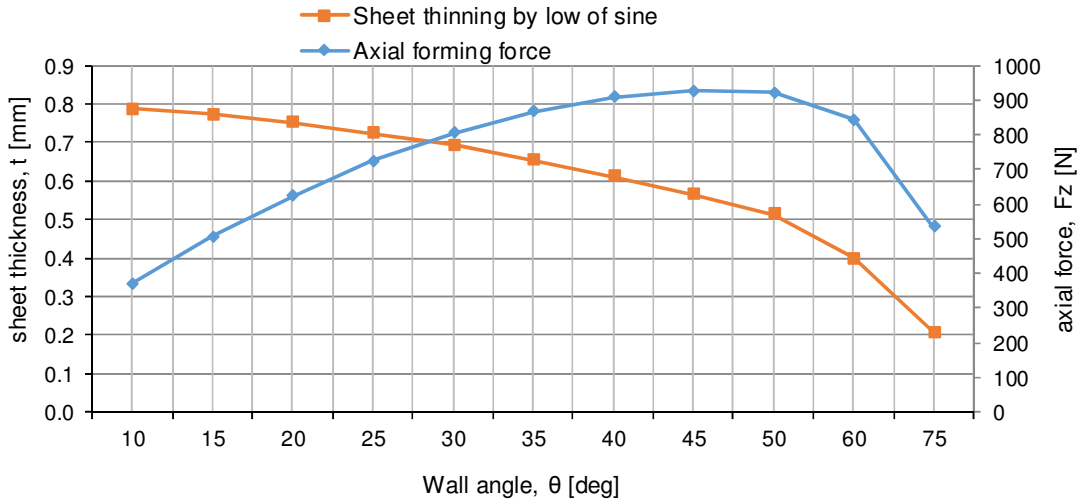

Figure 4-5: Variation of sheet thickness and force versus the wall angles for a sheet with initial thickness (computed data)

There is a strong correlation between thickness and the wall angle, and there is a strong correlation between the axial force and the forming angle. The rise of the force with growth of the wall angle is attributed to material strain hardening and the increase in the tool/sheet contact area. As per Equation 4-1, a larger wall angle equates to an increased tool/sheet contact area, requiring more force. The increasing trend of the axial force reaches its maximum, when the applied inclination angle reaches 50 degrees, after which the force declines. This drop of force can be reasoned by taking account of increased sheet thinning.

4.2.5 Effect of the tool-tip diameter

The tool-tip is taken to be only the part that is in a direct and continuous contact with sheet surface, inducing deformation. In addition to the importance of the material and profile used in the design of a forming tool, as discussed in Section 3.6, the diameter of the tool-tip (d_t) is also a critical design factor in SPIF which affects almost every aspect of the process including formability, loads, surface quality and processing time.

The relationship between the tool-tip diameter and the sheet thickness determines whether a tool-tip will be considered as being small or not small. Small diameter tool-tips impose a more localized deformation effect; they generate minimum loads, while increasing forming time. They also produce rough surfaces and exhibit reduced stability under severe forming conditions (Ambrogio, Filice and Micari, 2006; Silva *et al.*, 2011).

Forming with small diameter tool-tips creates scratches or cracks on the surface typically leads to premature fracture of the sheet (Carrino, Giuliano and Strano, 2006). Experimental studies of the forming of pyramidal profiles have shown that forming tools with $r_t < 2t_0$ significantly raise forming defects because of backward material folds. Such small tool-tip diameters can also cause galling of the sheet material and/or result in material squeezing out from under the tool/sheet contact zone. In addition, it was reported that penetration of forming tool into the sheet, and removal of material from workpiece surface, can also occur (Hussain, 2013).

As per the collected data from the literature, and depicted in Figure 4-6 the range of tool-tip diameters predominantly applied is between 8 and 12mm. In this range, it was found that the preferred diameter to thickness ratio d_t/t_0 was about 10.

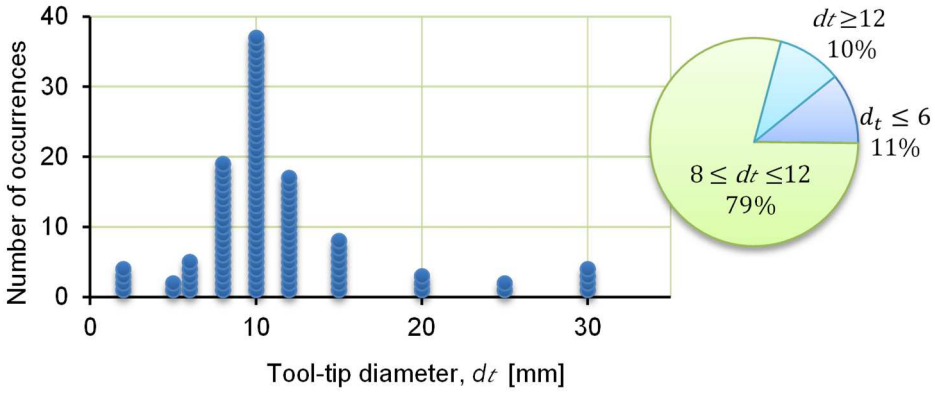

Figure 4-6: The occurrence of tool-tip diameter cited in the literature

By contrast, a large diameter tool-tip can distribute stresses better over the contact area, and has better sheet support due to a more suitable contact zone. Typically, large tool-tip diameters improve processing time and produce a more desirable surface quality, but they significantly increase forming loads due to an increased contact area. The raise in the contact zone drives/shifts the forming mechanism towards more global rather than a localized mode. The formability achievable reduces and the SPIF starts lessening advantages of incremental mechanisms, stretches near to conventional forming technologies. In addition, in many cases the diameter of the tool-tip is constrained because of possible interference with small features in shapes to be formed. In the production of satisfactory work, there is a strong relationship between tool-tip radius, r_t used, and the initial sheet thickness, t_0 (Silva *et al.*, 2011).

To maximise formability and avoid the development of forming defects, the appropriate r_t can be selected so that it complies with the threshold ratio, $\frac{r_t}{t_0} > 2.35$ (Hussain, 2013). In addition to its relationship to the sheet thickness, tool-tip diameter has also strong bearing on the selection of the step depth that can be applied.

4.2.6 Effect of the vertical step depth

Step depth is the vertical distance Δz between successive contours or is the amount of material deformed for each single pass of the forming tool. The step depth is comparable to the depth of cut in machining. It is selected mainly regarding d_t of the applied tool-tip, the target shape and the demands of surface quality.

The tool vertical step used impacts both on the surface finish of formed components and on the forces generated at the tool-tip. Figure 4-7 displays experimental values of Δz, as found in the literature consulted. The figure highlights the range of Δz most frequently used is form 0.25 – 0.5 mm.

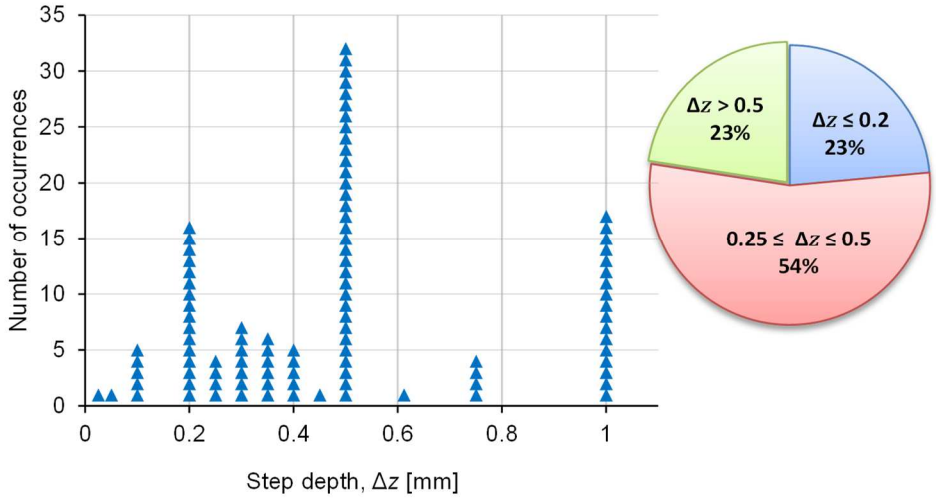

Figure 4-7: The occurrence of step depth cited in the literature

Typically, the component formed using a reduced step depth has a smooth and glossy surface. Conversely, components formed using a larger step depth, have reduced surface qualities with visible tool scars left on their surfaces. A balance should be found because if the tool step is too small, production time is dramatically increased and if the tool step is too big, surface quality suffers.

Data series of axial force shown on Figure 4-8 have been computed for the CP Grade 2 at three vertical increments Δz , using the same generalised formula given by Equation 4-1 and the reference data as per Table 4-1, varying only tool-tip diameter d_t. As indicated by the force trends shown in Figure 4-8, the axial force F_z is directly proportional to the vertical step, and is attributed to the increased tool/sheet interface.

More contact area implies a larger deformation of the material in each pass, and consequently bigger forming loads are generated. Considering the effect on formability of interaction between d_t and Δz , it is widely debated that the formable angle decreases with large incremental depths and small tool-tip (Bhattacharya *et al.*, 2011).

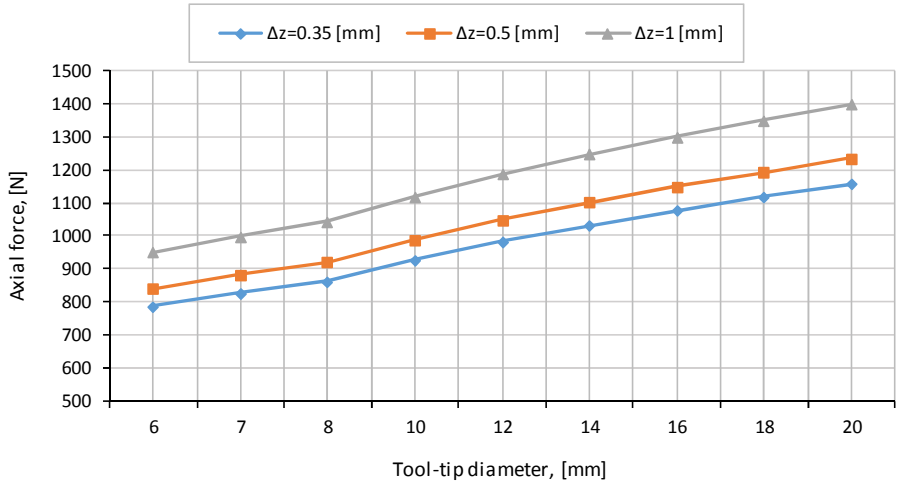

Figure 4-8: Force as function of tool-tip to step depth ratio (computed data)

By increasing the forming tool-tip diameter while the vertical step is kept constant, the deformation zone becomes larger and results in higher forming forces. Conversely, when the tool-tip diameter to step depth ratio ($d_t/\Delta z$) is small, the tool/sheet contact area becomes larger and results in higher forces leading to severe shear strains. Knowing the threshold value of the ratio $d_t/\Delta z$, the step size can be modified if needed, to reduce this ratio. Finally, the selected vertical step must be suited to the size of component to be formed; also, the maximum step size of the machine places a limitation on the precision.

4.3 SPIF thermal demands

In the context of the forming process, the thermal and mechanical loads are characteristics, which together establish the boundaries of the process. With the current dearth of information in the literature on the topic of thermal demands in the SPIF of titanium, a decision was made to focus on mapping of the thermal effect.

As discussed in Section 3.3, forming heat is generated mostly by two factors, namely the plastic deformation and the sliding friction. The first factor is material and thickness-dependent, while the second is based on material flow boundary condition at the tool/sheet interface, which is more related to the contact area and relative motion between the two sliding bodies. Consequently, the second factor is the more controllable heat source for designing the forming temperature throughout the SPIF operations.

The desired temperature can be managed by carefully tuning the operative parameters that create the material-flow boundary condition at the interface. These variables have been compiled in a single representative term named the relative forming velocity as given by Equation 4-6. The forming velocity or simply velocity (V) is the rate at which the outer edge of tool-tip moves along the tool-tip/sheet interface.

$$V = (2\pi \cdot r_t \cdot \omega_t \cdot \sin\theta \pm f_t\ )/1000 \text{ m/min} \tag{4-6}$$

4.3.1 Limits of tool rotational speed

Equation 4-6 designates that V is directly proportional to tool-tip diameter and its rotation speed. By adjusting ω_t controls the heating of contact zone.

The mechanism of interaction between tool-tip and sheet is of the utmost importance. Based on the assigned ω_t the following four varieties of tip/sheet interactions can be created:

Fixed (non-rotating) tool

Indenting the sheet without rotation increases the heat generated at sheet surface due to sliding friction, and contributes to better formability. However, extreme sliding friction creates high bending loads on the tool-shank, and the applied equipment; raises the generated heat, which increases the wear and surface degrading at the tool-tip; and lowers surface quality.

Considering forming the CP Grade 2, the sliding friction will be severe, leading to a build-up effect on the sheet surface, manifested by titanium material flacks and oxides. In addition, a non-rotating tool creates a very small indentation of about 10% of the requisite step size. With a rotating spindle, the tool indents the sheet closer to the required step size.

Rolling tool

In another way of interaction, forming tool rolls over the sheet surface with almost no sliding, and deformation occurs by the imposed forces and the rolling friction. This reduces both the relative motion between tool-tip and workpiece, as well as the heat generated at the tip/sheet interface. However, it employs the using of inventive tool with freely rotating hardened sphere as a tool-tip and pressurised fluid to operate, thus, increases tooling cost.

For typical tools with solid hemispherical head, rolling interaction requires the feed rate to be equal to approx. of tool-tip in contact with sheet multiplied by the spindle speed. The rolling ω_t can be set up as described by (Jeswiet *et al.*, 2005) Equation 4-7:

$$\omega_t = \frac{f_t}{\pi \cdot r_t \cdot \sqrt{\frac{1}{2}(1 - \cos(2\theta))}} \tag{4-7}$$

Another widely used interaction employs free (un-driven) tool movement, which leads to a reduction of slide friction (heat), bending and horizontal loads. When generated friction at tool-tip escalates, tool responds and upholds the load by passive rolling over the sheet.

Rotating tool

In contrast, while tool-tip moves onto the sheet, the high ω_t reduces friction forces. Also, attainable formability increases due to both a reduced friction and a local heating of the formed material. At very high ω_t, however, the tool slides more often on the same point. The occurring hot forming phenomena can result in chemical attrition at the tool/sheet contact zone. Chemical wear at the interface escalates at elevated speeds and temperatures. Consequently, the removal of titanium material at a micro level from contact area adds to the wear of the tool-tip which rapidly leads to a damaged tool-tip (Palumbo and Brandizzi, 2012). On the non-contact, exterior sheet side defects such as orange-peel effect and oxidation occur.

4.3.2 Limits of the feed rate

In the consulted literature, it is presumed that the upper limit of the practical forming rate is governed by the CNC machine traverse. Obviously, the rigidity of the applied machine and its tooling setup are critical variables and could be regarded as constraints. It is hypothesised that, the further the tool moves over the surface in a given time (faster feed rate), the lesser the opportunity for heat dissipation other than at the tool-workpiece interface. The interaction between the tool feed rate and the other contact factors maybe significant on the thermal and mechanical demands.

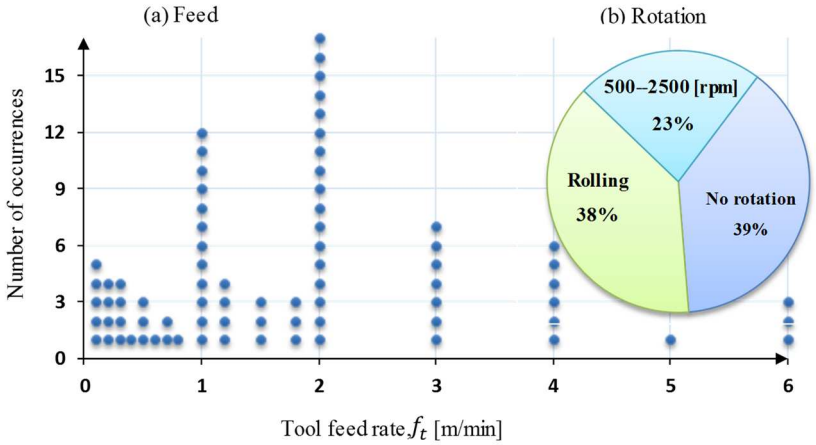

Figure 4-9: The occurrence of tool feed rate and rotation (a) feed rate and (b) tool rotational speed cited in the literature.

Finally, at any fixed combination of the tool-tip radius, spindle rotation and feed rate, the geometry of the part still has a significant impact on relative velocity at the contact interface. The relative velocity varies in relation to the wall angle of the component being formed. The SPIF key design variables and their predominantly used ranges were identified as summarised in Figure 4-10.

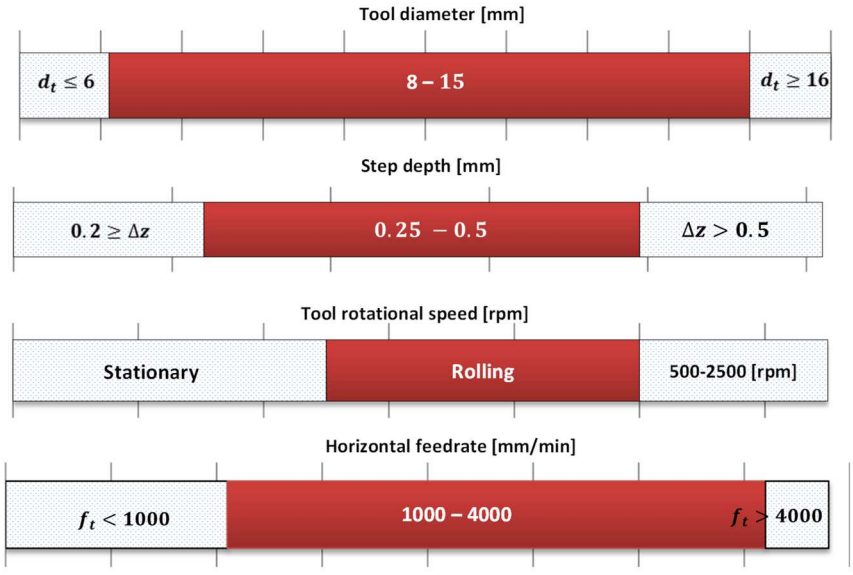

Figure 4-10: Predominant ranges of SPIF key variables (Uheida et al., 2016).

4.4 Assembling the SPIF conceptual framework

Analysis of the data, obtained from the systematic quantitative review of ISF literature, facilitated assembling of the important input and output of the SPIF process into a conceptual (map) framework. The following sections highlight steps involved in developing of the process conceptual map.

4.4.1 Thermal boundaries

4.4.1.1 Limitations on low relative velocity

Form Equation 4-6 the lower values of the material flow boundary (relative velocity) will result when ω_t and r_t are at the lower values of the respective ranges, and f_t is at the upper end of its range. However, physical constraints will limit the lower values of V because:

- Very low tool rotation results in higher forming forces, causing adhesive wear at the interface
- Very small r_t results in high surface roughness, as well as reducing tool rigidity
- Very high f_t increases in-plane forces, causing a bending moment on tool shank. The practical feed is also determined by the machine ability to traverse in short contours of the tool path

4.4.1.2 Limitation on high relative velocity

Maximum relative velocity is determined by increased ω_t , d_t or reduced f_t. However, physical constraints will limit the upper values of V because:

- At high speeds, coarse surface roughness and defects such as sheet waviness become more profound, result in reduced formability due to the increased roughness and wear of tool/specimen
- Tool wobble frequencies will increase with high speeds subject to tool overhang length, affecting the produced surface finish.
- Tool chatter will develop, leaving tool path marks on the titanium surface which will escalate the tool wear rate considerably
- High tool speeds reduce the efficiency of a lubricant. Under excessive heating, a lubricant reaches its melting temperature, breaks down, and loses its effectiveness.

4.4.2 Mechanical boundaries

- The applied force should be above the yield strength of the material to create plastic deformation of the workpiece
- High forces can lead to a global effect on the unsupported sheet, rather than constraining the deformation to a local zone

- Excessive forces can have a detrimental effect on the performance of the tool, fixtures and machine
- The axial force has a higher order of magnitude than either of the in-plane components and thus requires more attention during monitoring of forces
- Increased force in the radial direction generates a large moment on the tool shank. This can result in tool-tip deviation from the target tool path, causing tool failure by deflection or fracture

At this stage, based on the developed understanding of process demands, a hypothetical framework (process map) for the SPIF processing space can be established. Figure 4-11 highlights the boundaries of the anticipated operational framework SPIF as applied to the titanium Grade 2.

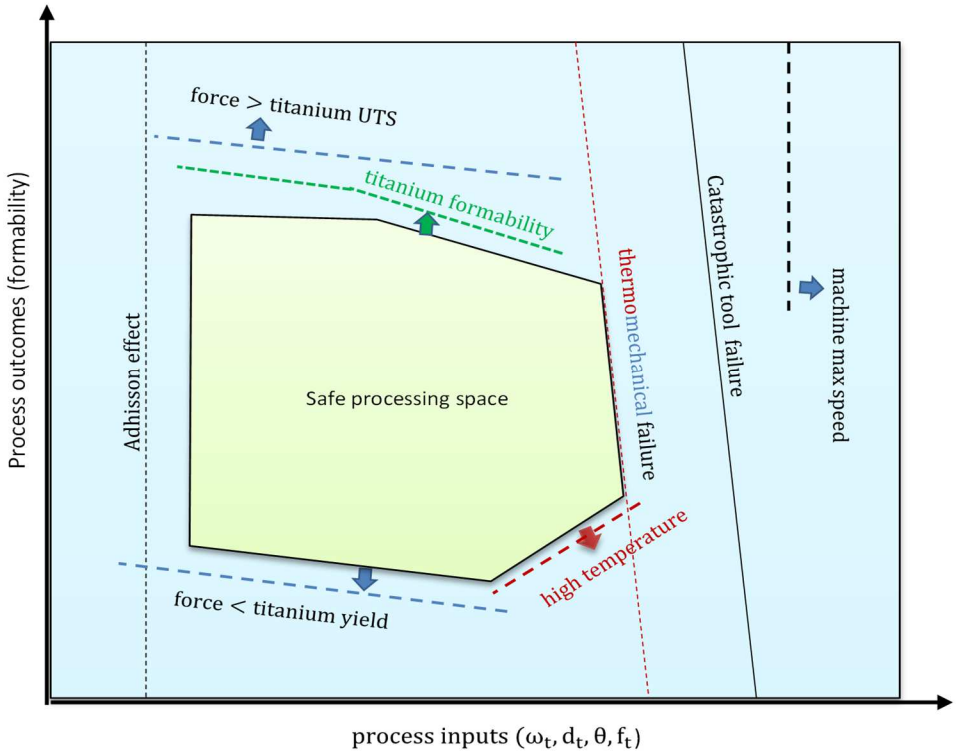

Figure 4-11: The established SPIF conceptual process map

The horizontal axis of the conceptual process framework (Figure 4-11) is identified by the SPIF measure inputs. These key parameters are the effective radius of the tool-tip ($r_t * \sin\theta$), the tool rotational speed and the tool feed rate.

The vertical axis of the process space is regarded as the SPIF formability outcomes. It is categorised by the maximum achievable forming angle, the axial forming forces and the forming temperatures at the interface.

In the two forthcoming sections, the interrelationships between these variables (process inputs and outcomes) are experimentally evaluated and reported. A statistical design of experiments and one-factor-at- a-time have been implemented for the validation of the conceptualised process map. A process window suitable for incremental forming of CP grade 2 sheets in terms of the five key process variables are presented.

CHAPTER 5 EXPERIMENTAL SETUP AND DESIGN

In this chapter, an overview of the equipment used for experimenting is set out, and the procedures and methodology followed are given. Details of the test platform used, the benchmark, the data acquisition apparatus, and the design of the experiments are demonstrated in this chapter. Steps implemented to enhance the quality, objectivity, and integrity of the investigation data are presented. Although the focus of this chapter is on the experimental work, necessary background information in the form of theory and explanations, have been slotted in at relevant places. This additional information has been obtained from other sources, as well as reproduced from the preceding parts of this dissertation. Broad classification of the experimental test procedures performed for this study includes:

- Split-plot DoE involves 16 runs with single replicate, on five key process variables, namely: sheet thickness, tool-tip size, step depth, tool feed and rotational speed, all ranged around their anticipated optimal settings
- One-factor-at-a-time (OFAT) experimental tests of the tool kinematics over an expanded range (outside the anticipated optimal range), for the purpose of verifications and assessing the potential of process enhancing window. The tests are structured as follows:

Table 5-1: Structure of the OFAT experimental tests

Type	Runs	Range
Rotational speed test	8	450 – 15000 rpm
Feed rate test	4	625 – 10000 mm/min
Step depth when retreating	4	(0.35 – 0.8 mm)
Step depth when advancing	4	

5.1 Components and setup of test platform

The key strategy is to create a functional SPIF test platform. This facilitates accurate process performance and precise control of the variables, and it provides reliable information. The main components and arrangements discussed in subsequent sections include: the design of and making of a functional blank-holding (fixture); forming styles; selecting a CNC machine; specifying geometrical and technological parameters; the design of a benchmark profile, and lastly, ensure that proper equipment for data collection and documenting responses has been acquired and correctly calibrated.

5.1.1 Forming fixture

Fixture designs typically reported in SPIF literature allow only a single sheet size and a single component to be formed at a time, which implies that a new platform has to be built if larger sheets are to be formed. Samuel (2010) developed an adjustable and more flexible blank holder that accommodates forming sheets of different sizes. Figure 5-1depicts the clamping fixture developed in the current study attached to a force dynamometer, and mounted on a CNC table.

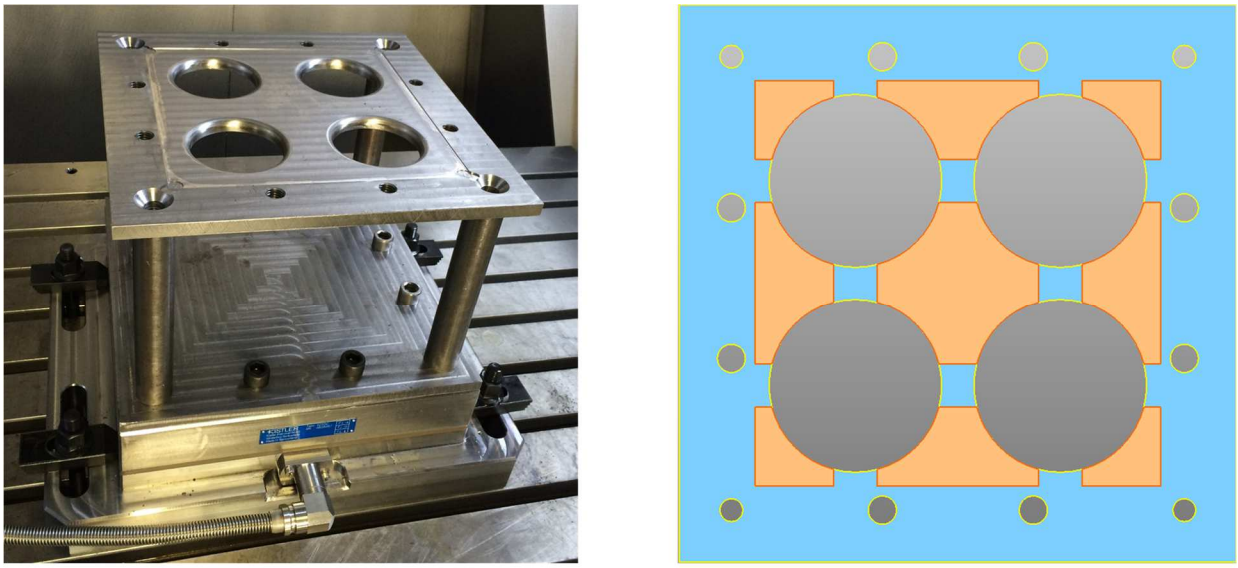

(a) (b)

Figure 5-1: Design of the SPIF forming fixture: (a) depiction of the fixture without top-plate; (b) schematic of the fixture top-plate (bottom side), shows the clamping planes (in orange) surround the four working spaces

The forming fixture consists of two main units, a clamping top-plate, and blank-holding (backing-plate) assembled on four pillars to a base; besides the backing plate being held down by the four pillars, there are also 8XM10 hexagon socket screws to mount the top-plate. As shown in the Figure 5-1(a), the fixture allows the execution of four consecutive test runs for a single test setup, thus lessening both the setting-up time and the need to clamp extra workpiece material. In addition, the chance of errors is limited.

The arras formed on the upper face of the top plate, where the 60 mm diameter working spaces have been cut out, is rounded by a radius (fillet) at least five times bigger than the workpiece thickness; this is to aid the drawing operation (Kalpakjian & Schmid, 2008). A recess created on the upper-face of the blank-holding plate to accommodate specimens, cut in line with acceptable tolerance, assists in the accurate positioning of the titanium specimens.

Equally spaced slots were made on the bottom side of the top-plate, (Figure 5-1(b)) to allow an even distribution of the clamping forces over the four working spaces. Finally, the dimensions of the fixture are well-matched to the Kistler type 9255C force dynamometer used. This backed equally distribution of forming forces over the four sensors of the dynamometer, and keeping the force application point of the vector of resulting forming forces within an optimal measuring range of the sensor. Detailed drawings of the fixture upper-plate and top-plate are enclosed as Addendum B.

5.1.2 Forming tools

Two ball-nosed forming tools, with tip diameters of 6 mm and 12 mm, and a hemispherical tool-tip with a 10-mm diameter stem made of tool steel 2312 and heat-treated using the TUFFRIDE[4] process, were used. Depiction of the three forming tools mounted in the CNC tool holders is shown in Figure 5-2.

[4] TUFFTRIDE® is a salt bath surface treatment to improve steel component quality by retarding wear, increasing fatigue strength and hardness, and enhancing appearance.

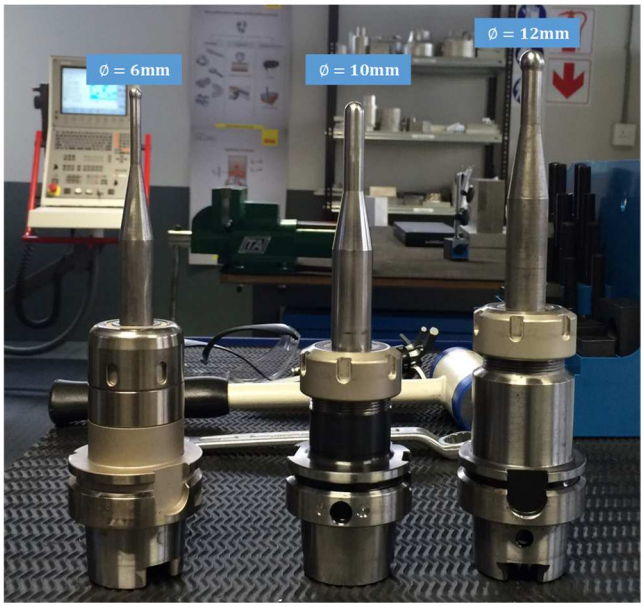

Figure 5-2: The SPIF tool-tips used

The tool-tips were ground and polished to minimise the friction and gouging action between tool-tip and blank, thereby extending the tool life.

5.1.3 Forming machine

The experimental work was performed at the facilities of the Stellenbosch Technology Centre - Laboratory for Advanced Manufacturing (STC-LAM), on a vertical CNC machining centre. The DMU 65 FD monoBlock from DMG MORI (see Figure 5:2) is a gantry type, 3-axis CNC machine, equipped with a stationary table and a milling head that moves across the x-, y- and z-axes. The advantage of a gantry-milling machine is that it is suitable for large axial loads, but this is at the cost of a reduction in rapid traverse.

Model
DMU 65 FD
mono-Block

Table
Stationary

Working Space XYZ
735/ 650/ 560 mm

Spindle power
35 KW

Max spindle speed
18 000 rpm

Max feed rate
40 000 mm/min

Figure 5-3: Technical data of the CNC machine used

5.1.4 Test benchmark

As discussed in Section 3.1, strain-based forming limit diagrams (FLDs) and forming limit curves (FLCs), that usually applied to evaluate the formability of materials under conventional processes are not applicable considering the ISF processes. These curves are developed assuming the materials are deformed mainly under plane-strain conditions. However in SPIF like process, combined effects of through-the-thickness shear, bending and cyclic loading are detected, and the FLCs prove inadequate to examine material formability. As an alternative, the maximum forming depth and maximum wall angle, obtained in a single processing pass, before sheet fracture are commonly taken as an artificial index for signifying material formability in SPIF (Xu *et al.*, 2013).

Hence, the manufacture of components with truncated, conical or pyramidal profiles is state-of-the-art in ISF and is regarded as the process benchmark. These profiles are constantly the subject of experimental work and analysis in research of late, and they are considered during this dissertation. Depending on the features to be evaluated: a varying wall angle conical frustum (VWACF), represents a homogeneous geometry with a symmetric section, and is eminently suitable for the evaluation of sheet formability. The maximum wall angle can be determined directly by forming cone-hyperboloid profile as detailed by Hossain and Gao (2007). The wall angle of the hyperbolic cone increases in relation to its depth, and is potentially suitable for predicting the maximum formability or θ_{max} with a minimum number of experiments. In the upcoming design of experiments, tool-tip depth recorded at sheet fracture (h_{max}) is converted into maximum formable angle (θ_{max}) using the model design equation 5-1, and will be regarded as criteria for characterizing titanium sheet formability.

Same steps as reported by Khalatbari *et al.*, (2015) were followed in the design of the test benchmark profile. The profile was designed to ensure evolution of its wall-angle θ along the component axis of symmetry ($Z-axis$) at a constant rate $d\theta \,/\, dz = a$; whereas a is a constant; consequently:

$$\theta = az + b \tag{5-1}$$

Considering $\tan(\theta) = \frac{dz}{dx}$, thus $\tan(az+b) = \frac{dz}{dx}$, the other horizontal coordinate (x) of the benchmark profile is found as follows:

$$\int dx = \int \cot(az+b)dz \tag{5-2}$$

From Eq. (5-2), the general equation of the benchmark profile with its wall angle increases at constant rate along its depth (Z) is:

$$x = \left(\frac{1}{a}\right)\ln[\sin(az+b)] + c \tag{5-3}$$

where $a, b,$ and c in Eq. (5-3) are constants, that can be found by implementing the boundary conditions of the profile, namely the radius of the component opening (28.5 mm), the initial wall angle ($b = 30°$ at $z = 0$), and

the maximum depth of the component is 25 mm. This depth corresponds to the maximum wall angle of the test model $\theta = 75°$, which presumed to be higher than formability limits of the CP grade 2 sheets.

From the above system of equations and using the boundary conditions, the generatrix of the contour (see Figure 5-4) for the condition of this experimental work, is given as:

At the cone opening Z=0

$$\theta = a(0) + b;\ b = \theta = 30° \text{ or } b = 0.523598776\ rad$$

At the cone bottom, Z =25mm

$$\theta = 75°\ and\ a = \frac{\theta - b}{z} = \frac{1.309 - 0.523598776}{-25} = a = -0.031415927$$

Solving for C from Eq. 5-3, at z = 0

$$c = x - \frac{1}{a} \cdot \ln[\sin(az + b)] = 25 + 31.831 \ln[(\sin 30°)] = 6.436$$

$$x = -31.831 \ln[\sin(-0.0314z + 0.5236)] + 6.436$$

Substituting the values of a and b from boundary conditions, in Eq. (1):

$$\theta = 1.8 * Z + 30°\ ;\ Z \in [0\text{–}25\ \text{mm}] \tag{5-4}$$

5.1.5 Forming strategy

A commercial CAD/CAM Package from Delcam, PowerSHAPE and PowerMill were respectively used to generate the benchmark geometry and the tool path. A varying wall angle conical frustum (VWACF) shown in Figure 5-4 was identified as the test benchmark. The CAD model of the VWACF has maximum inner diameter of 56 mm and a height of 25 mm. The profile (Figure 5-4) was designed with its angle increasing at a constant ratio (1.8) along its axis of symmetry (z-axis); this was done to minimise the effect due to the rate by which wall angle changes as the forming depth increases on the formability (Khalatbari *et al.*, 2015).

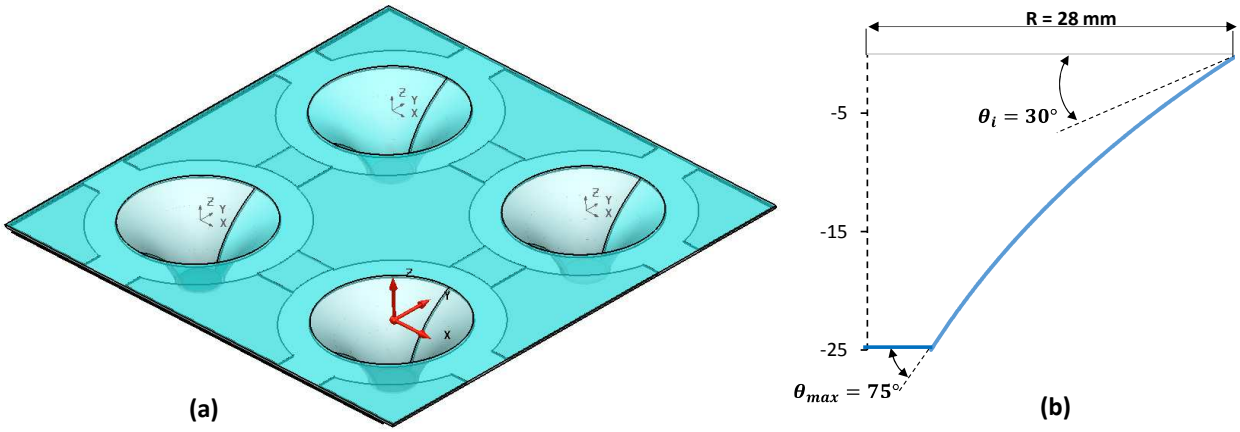

Figure 5-4: Design of the SPIF test benchmark; (a) the CAD model, (b) the geometrical details

In SPIF operations, the tool path has significant influence on almost every aspect of the process performance. It affects material formability, the distribution of sheet thinning, surface quality, and the geometrical accuracy of the formed component. Likewise, productivity, mechanical and thermal loads throughout the operation are strongly dependent on the applied forming strategy and the settings. Figure 5-5 is a screenshot of setting the forming tool path parameters using the PowerMill CAM-package

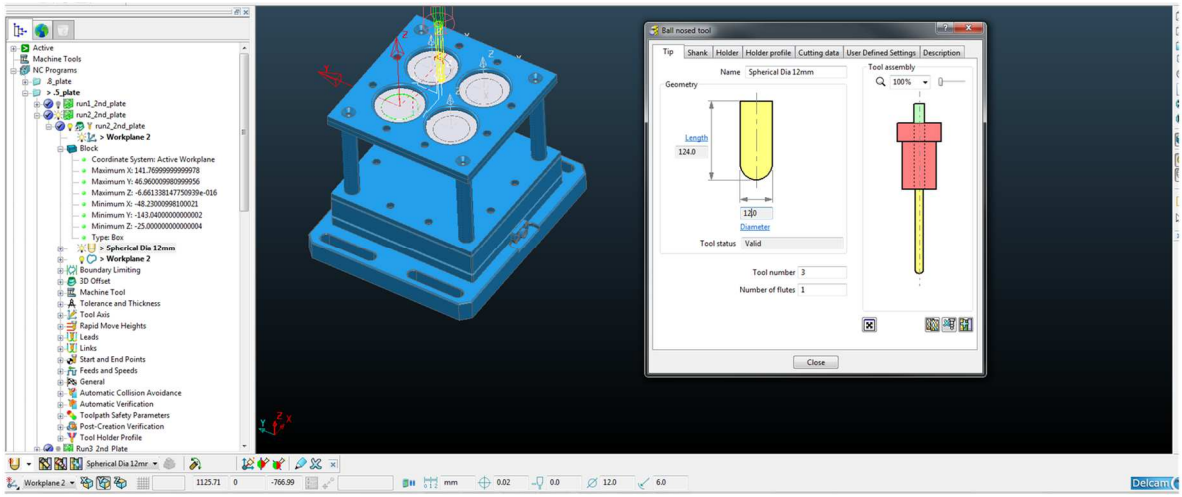

Figure 5-5: Setting the forming tool path parameters using PowerMill CAM

In the SPIF of CP Grade 2, conventional z-level tool path form grooves in the workpiece material, and trigger sticking of titanium sheet material to the tool-tip; this adversely affects forming (Hussain, Gao and Hayat, 2009). Three-dimensional tool paths create a nearly pure stretch forming mechanism to act on the specimen material and facilitate a uniform distribution of the component thickness (Buffa, Campanella and Fratini, 2013). The spiral tool path also eliminates the occurrence of force peaks and does not leave scars (step-down lines) on the sheet surface. Therefore, all the experimental components were produced using a 3D spiral, out-to-in tool path, with a constant step-down value.

In the experiments, tool rotation direction was fixed clockwise. Therefore, changing tool path direction method similar the one reported by Otsu et al (2014) was applied in order to change rotation direction. When the tool path is clockwise as shown in Figure 5-6(a), the relative velocity at the interface is added and higher.

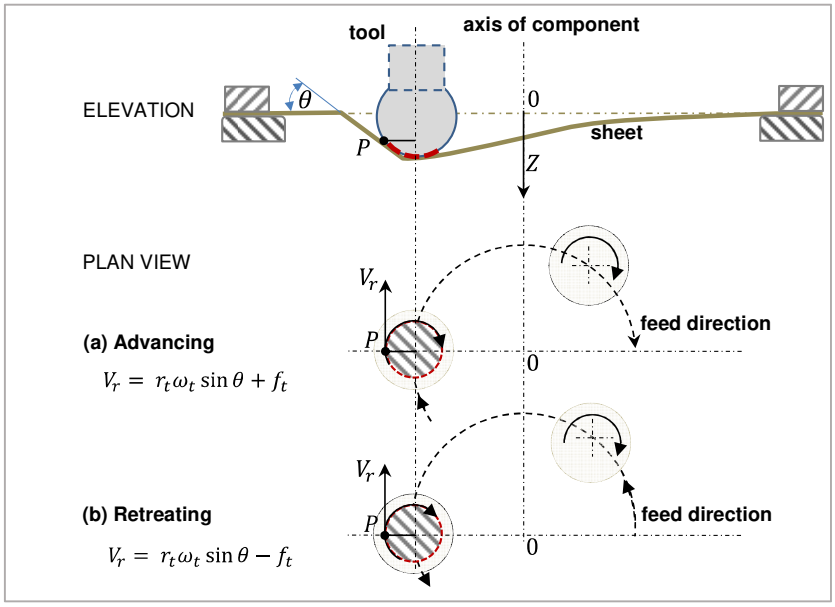

Figure 5-6: A typical material flow boundary condition at the interface (a) advancing motion, tool traverse along its rotation; (b) retreating motion, tool traverse against its rotation

When the tool path is anticlockwise as shown in Figure 5-6(b), the relative velocity is subtracted and minor. The earlier case is defined to "advancing direction" and the latter case is defined to "retreating" as typically used in friction stir-welding operations. The relative velocities at tool/workpiece surface (referred to in Section 4.3) in both the advancing and retreating (V_a , V_r) directions are determined by; the tool-tip radius r_t the spindle rotational speed ω_t, the present wall angle θ and tool feed speedf_t as it is described by Otsu et al (2014):

$$V = (2\pi * r_t * \omega_t * \sin\theta \pm f_t)/1000; \text{ (m/min)} \quad (4\text{-}6)$$

5.1.6 Test specimens

All test specimens were CP Grade 2, in the form of 0.5, 0.8 and 1.0 mm thick sheeting. An even-annealed condition of the specimens was obtained by agreement with the supplier who annealed all the specimens in a single batch. The specimen's sheets were 190 mm × 190 mm, and were fitted symmetrically over the four working spaces. To intensify pyrometer (IR camera) readings of the forming temperature, the underside of the specimens was spray-painted to enhance and unify the emissivity of the titanium specimens. SPRAYMATE heat-resistant (up to 110°C) black paint was used to paint the specimens. The upper sides of the specimens were then assigned their run codes in accordance with the experiment design. Molybdenum disulphide (98.5% pure MoS_2) powder was applied as a lubricant throughout the forming operations. The initialisation process and the applying of the MoS_2 powder are pictured in Figure 5-7.

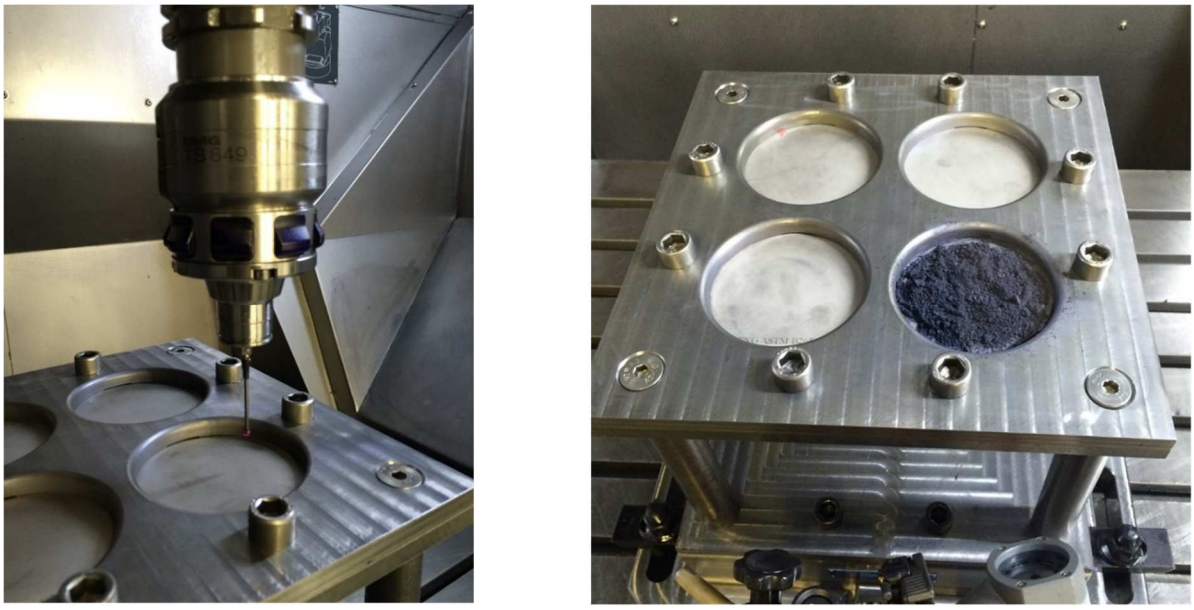

Figure 5-7: SPIF initialisation process: (a) using the CNC probe on top surface of the titanium workpiece (touch offs, and part zeroing), (b) applying the MoS2 lubricant

Guidelines for experimental design protocol and validation procedure for the measurement of the targeted response is enclosed as Addendum B. The protocol describes the procedures used in connecting and setting of the test platform. Information on the practical steps and instructions that have been followed in obtaining data from the experiments are also detailed in their subsequent orders.

5.2 Design of experiment framework

In the design of experiment (DoE), test runs need to be completely randomised to reduce the impact of any hidden factors that change over time could have on results obtained. To get the advantages of using the fixture with four working spaces, however, implies a restriction on full randomisation of the sheet thickness throughout the test runs. A split-plot DoE with one hard-to-change (HTC) factor was selected to accommodate this constraint. This design is a viable alternative to a fully randomized design when a factor such as the sheet thickness cannot be quickly changed. Hence, the HTC factor was grouped together with whole plots, within which the easy-to-change (ETC) factors were randomized in subplots.

The Split-plot design essentially combine two experiment designs into one design, therefore, produces both split-plot and whole-plot random errors. This consequences loss of power to pin down some effects on the factors, but this effect can be minimised by incorporating replicate testing in the design.

Nowadays, computer packages made exclusively for the DoE have created notable benefits in generating experimental design layouts, analysis, performing numeric optimization, and post- analysis (Myers, Montgomery and Anderson-Cook, 2016). In this work, the package DesignExpert[5] 10.01 has been used to build the design and for the post-processing of data. The selected DoE resolution version five (2_V^{5-1}) insures an acceptable power and freedom of aliases[6]. This design is widely recognised as being appropriate for estimating mean effects (MEs) and two-factor interactions (2FIs) (Myers, Montgomery and Anderson-Cook, 2016) . In this way, the generated DoE comprised 16 treatment combinations and a single replicate was needed for the whole design to reduce the noise added to the system from an extra source of variation. Therefore, a total layout of 32 treatments was carried out. Two central runs were also been added to improve the design. The selected range of each independent variable was anticipated to have a potential impact on the specified responses. Table 5-2 shows these design factors and their extremes.

Table 5-2: Summary of the factors in the DoE test

		Factor	Units	Change	Type	Subtype	Low (-1)	High (+1)
independent	a	Thickness	mm	Hard	Numeric	Discrete	0.5	1.0
	B	Rotation	rpm	Easy	Numeric	Continuous	750	3125
	C	Tool size	mm	Easy	Numeric	Discrete	6	12
	D	Feed rate	mm/min	Easy	Numeric	Continuous	500	750
	E	Step depth	mm	Easy	Numeric	Continuous	0.25	0.35
controlled		Wall angle	Cone-hyperploid profile with angle $\theta = 1.8 \cdot Z + 30°$					
		Tool path	3D out to in Spiral with a constant step					
		Lubricant	98.5% pure MoS_2					

[5] Design-Expert is a registered trademark of Stat-Ease, Inc.

[6] In resolution V, no main effect or two-factor interaction is confound with any other main effect or two-factor interaction (Rekab and Shaikh, 2005).

Other controlled process factors, such as the material type, profile, tool path type, and friction condition were held unchanged at their normal level. Note here that the hard-to-change factor is labelled lowercase ‘a ‘, while the easy-to-change factors are all uppercase; and the ‘+, - ‘represents the coded levels of the factors.

Due to time constraints, it was not possible to run all the experiments in a single day. A blocking technique was used to eliminate the variation for any non-homogeneous conditions during the experiments. Each test replicate of 16 runs was assigned to a single block, so it can be conducted during one working day. A run sheet of the randomised test treatments generated by the DesignExpert was then printed out, and the experiments were carried out accordingly.

5.3 Data acquisition procedures

In-process measurements of thermal and mechanical load were performed, and data acquisition was facilitated through an IR camera for measuring the forming temperature, and a Kistler dynamometer to pick up the forming forces; for both the thermal and the mechanical load the data was recorded concurrently (Figure 5-8) with run-time to additionally provide information on time-dependency.

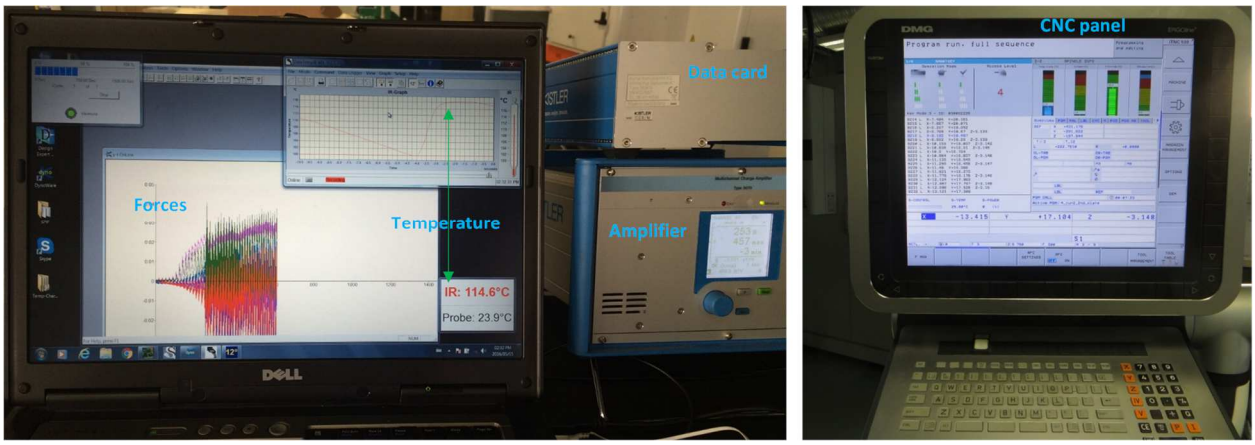

Figure 5-8: Online measuring systems of the process responses

5.3.1 Measuring the forming temperature

Online measurements of forming temperature for each test run allowed monitoring of the process and profiling of various trends in heat generation due to the different forming conditions. An infrared camera (pyrometer) was implemented to carry out the temperature measurements. Using an infrared camera avoids undesirable impacts on the process because the temperature is remotely recorded; there is no physical contact with the process. In addition, temperature distribution specifically in the proximity of the tool/sheet interface and the variation in heat resulting from the dynamically changing position of the deforming zone can easily be tracked.

The pyrometer was calibrated to match the emissivity of the titanium sheet specimens. The calibration was done using a thermocouple, which comes with the DataTemp MX software package. The software was also applied in temperature monitoring, recording and presenting of the temperature data.

In the calibration process, a titanium sheet specimen was exposed to a heat source and its surface temperature was measured using both the pyrometer and the thermocouple. The emissivity parameters of the pyrometer were then attuned until the reading matched that of the thermocouple reading. Figure 5-9 illustrates the positioning and most important specifications of the Ranger MX4 pyrometer from Raytek, used in obtaining the temperature measurements.

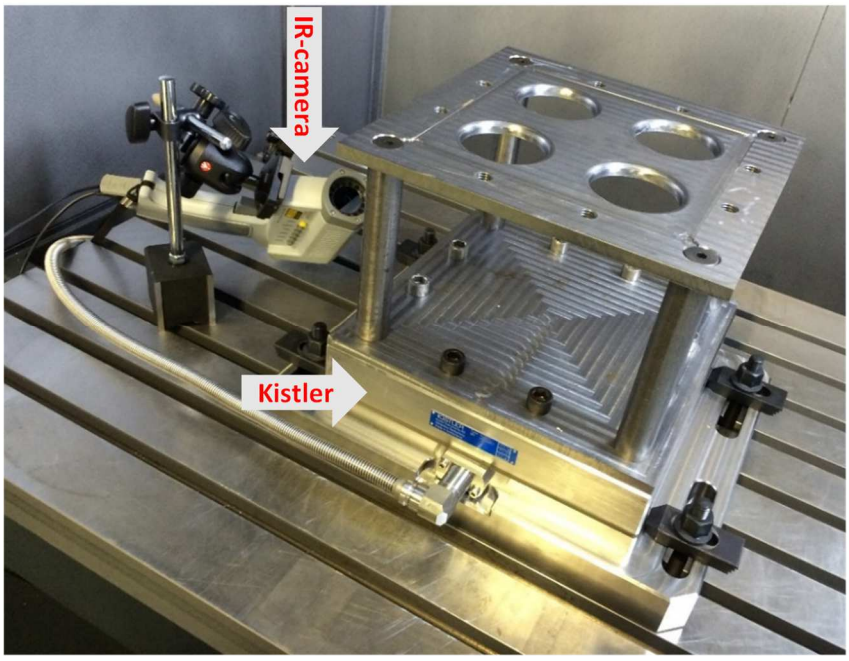

Pyrometer datal
Raytek MX4

Temperature range
$-30\ °C\ to\ 900\ °C$

Distance to spot
60:1

Adjustable emmisivity
from 0.1 to 1.0 by 0.1

Accuracy at ambint
$\pm\ 1\ °C$

Figure 5-9: Setup of the SPIF test platform mounting the force dynamometer and positioning the pyrometer

At the start of test run, the pyrometer was precisely aligned onto a target spot on the backside of the specimen, by using its laser focusing function. As shown in Figure 5-7, the pyrometer was mounted onto a movable tripod that has a magnetic base, so it could be easily moved to maintain its optimal measuring distance every time it was repositioned for a certain test run.

It should, however, be noted that throughout a test run the temperature was not recorded for the entire component geometry, but only on one side. Considering that test components formed are axisymmetric, and that the heat is generated only by friction and deformation, it is presumed that there was an equivalent temperature all along the contour path of each forming tool pass (Xu *et al.*, 2013). Presentation and analysis of the temperature data obtained from the tests are deliberated in Section 6.1.4.

5.3.2 Measuring the forming forces

As discussed in Chapter 3, the forming forces are of central importance, when planning the forming process. Achieved plastic deformation is solely dependent on magnitude of the force at tool/sheet contact area. Studying the mechanisms of forming, identifying excessive thinning and not the failure of sheet specimens are very cardinal when monitoring the magnitudes and trends of forming forces. In this study, in-plane and axial force components acting on the test specimen were measured using a six-component, table-type dynamometer.

The force measuring system included a dynamometer, a signal amplifier, and a data acquisition card plugged into a laptop computer. The stationary table-type Kistler 9255C dynamometer (see Figure 5-9) was mounted below the forming fixture throughout each test run. The dynamometer was paired to a Kistler 5070A 8-channel signal amplifier. The forces were recorded using a Type 5697 DAQ data card and DynoWare software.

5.3.3 Measuring the forming depth

To minimise the effect of material springback on obtained geometries, the dimensions of the completed workpiece prior to unclamping had to be taken. At the completion of each test run, direct measurements of achieved forming depth (see Figure 5-10) were taken using a depth Vernier. Also profiles of the obtained components were reproduced using a CMM.

Figure 5-10: Obtaining the formability response data , (a) measuring the forming depth and (b) the formed profile using the CMM

The process responses measured, and the equipment used are summarised in Table 5-3. The acquired response data from the 16 distinctive process settings (32 data points when considering the replicates) were processed by the DesignExpert software.

Table 5-3: Data acquired and measuring equipment

	Response	Variable	Units	Equipment
A	Thermal loads	Forming temperature	°C	Raytek Pyrometer
B	Mechanical loads	Forming forces	N	Kistler Dynamometer
D	Formability	Forming depth	mm	CMM + CNC-Panel
C	Productivity	Forming time	s	CNC-Panel + tool path
F	Accuracy	Deviation from CAD model	mm	CMM

CHAPTER 6 EXPERIMENTAL RESULTS AND DISCUSSION

As broadly specified in chapter 5, the empirical work conducted comprised two approaches, namely the DoE approach and a set of the OFAT campaigns. When during an experiment, a sheet fractured, or extreme heating occurred, the test run was immediately stopped; otherwise, the test continued until the design depth of 25 mm was reached.

In this chapter, the analysis of the obtained data will be done separately for the two design approaches. On completion of the two analyses, their output will be further processed to present a combined, comparative analysis of the whole process. To assist in navigating this chapter, a schematic roadmap of this chapter is provided in Figure 6:1.

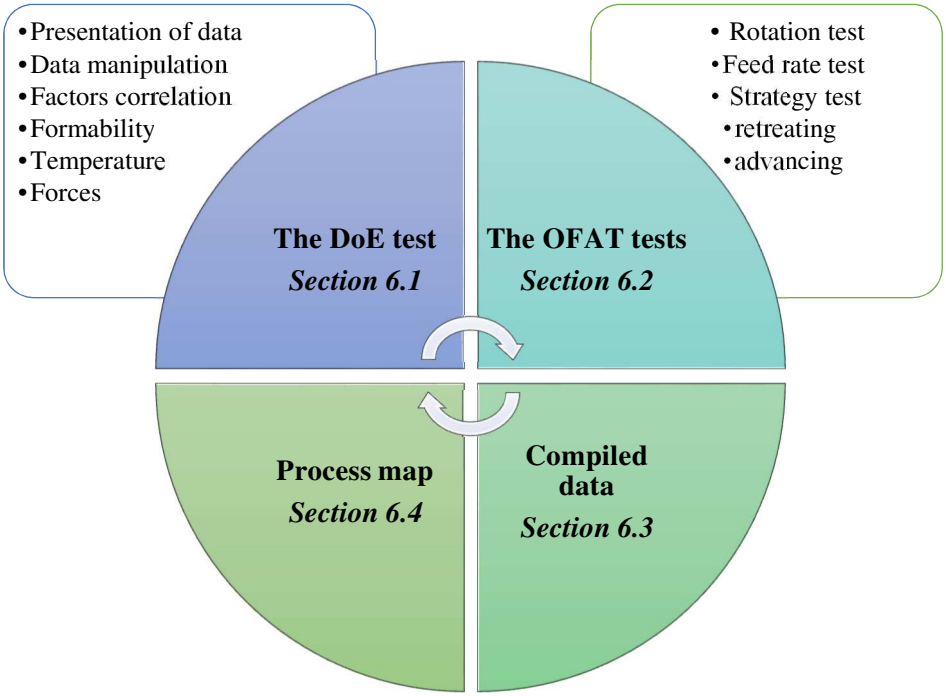

Figure 6-1: A schematic roadmap of the experimental results and discussion

6.1 The DoE test

In Table 6.1, a summary of the setting variables, as well as the response data obtained from the DoE approach is presented. In additional to the planned response data (temperature, forces, formability and cycle time) presented in Table 5-3, supplementary reference data are also reported.

T_{ref}, F_{ref} and V_{ref} shown in Table 6.1, they respectively are the reference values of forming temperature, axial force and relative velocity, computed at a specific point (9 mm) of forming depth. Whereas, T_{600} indicates test temperature obtained at 600 s from initiation of forming. Determination and reasoning of using these reference quantities when evaluating the process factors are correspondingly conveyed in section 6.1.1 and 6.2.1.

Table 6-1: The DoE layout and the responses data measured

	DoE			Design variables					Temperature			Forces				Formability		Cycle time			Relative
	ID	Block	Run	a:Thick	B:Speed	C:Tool	D:Feed	E:Step	T_max	T_600	T_ref	Fz-ref	Mean-Fz	Max-Fx	Fx-ref	Depth(h)	Angle[Θ]	t-ref	Estimated	Exper.	V-ref
	#		#	mm	rpm	mm	mm	mm/min	C	C	C	N	N	N	NA	mm	deg	s	s	s	m/min
1	6	B1	C3	0.5	3125	6	500	0.25	200	46	155	180	130	413.2	290	17.7	62	1426	1672	1500	49.6
2	4	B1	C4	0.5	750	12	500	0.35	122	42	115	436	384	1123	550	11	50	1013	1150	961	23.6
3	3	B1	C5	0.5	3125	12	750	0.35	214	186	167	368	369	831	600	7.7	44	678	766	550	99.5
4	5	B1	C6	0.5	750	6	750	0.25	84	34	75	313	280	805	550	17	61	953	1117	1000	11.3
5	12	B1	C7	1	750	12	500	0.35	187	60	163	1093	884	2664	1500	16	59	1013	1150	1074	23.6
6	13	B1	C8	1	3125	6	750	0.25	384	245	275	338	175	1130	600	18.4	63	951	1117	1060	49.4
7	11	B1	C9	1	3125	6	500	0.35	255	246	255	350	190	744	400	1	32	1025	1203	395	49.6
8	14	B1	C10	1	750	12	750	0.25	127	59	118	1105	876	2700	1500	16.8	60	940	1070	1000	23.3
9	2	B1	C11	0.5	750	12	500	0.25	115	30	100	549	446	620	350	11	50	1410	1601	1330	23.6
10	7	B1	C12	0.5	3125	6	750	0.35	220	173	194	235	160	211	190	20.6	67	685	800	763	49.4
11	1	B1	C13	0.5	3125	6	500	0.25	158	35	112	316	222	205	200	20.3	67	1427	1672	1650	49.6
12	8	B1	C14	0.5	750	12	750	0.35	110	84	86	613	497	737	400	11.4	51	675	766	655	23.3
13	9	B1	C15	1	750	6	500	0.25	169	38	131	792	624	460	310	24.8	75	1426	1672	1690	11.5
14	10	B1	C16	1	3125	12	500	0.25	408	116	290	283	184	558	300	5.5	40	1410	1601	1500	99.7
15	16	B1	C17	1	3125	12	750	0.35	378	325	269	369	273	290	320	11.4	51	675	766	600	99.5
16	15	B1	C18	1	750	6	750	0.35	158	116	134	716	629	626	300	24.5	74	683	800	780	11.3
17	2	B2	C23	0.5	750	12	500	0.25	121	27	102	389	340	453	300	10.1	48	1410	1601	1360	23.6
18	7	B2	C24	0.5	3125	6	750	0.35	206	144	185	253	190	182	175	21.5	69	685	800	780	49.4
19	3	B2	C25	0.5	3125	12	750	0.35	187	164	167	338	286	380	197	8.6	45	678	766	600	99.5
20	6	B2	C26	0.5	3125	6	500	0.25	174	36	145	234	205	210	165	15.6	58	1426	1672	1450	49.6
21	9	B2	C27	1	750	6	500	0.25	108	37	107	806	757	650	400	15.2	57	1426	1672	1390	11.5
22	13	B2	C28	1	3125	6	750	0.25	x	x		x	x	x	x	x	x	951	1117	x	
23	16	B2	C29	1	3125	12	750	0.35	402	318	251	410	322	466	320	11.5	51	675	766	595	99.5
24	12	B2	C30	1	750	12	500	0.35	126	52	122	948	798	1254	750	15.1	57	1013	1150	1100	23.6
25	11	B2	C31	1	3125	6	500	0.35	x	x		x	x	x	x	x	x	1025	1203	x	
26	15	B2	C32	1	750	6	750	0.35	x	x		x	x	x	x	x	x	683	800	x	
27	10	B2	C33	1	3125	12	500	0.25	209	119	290	320	258	400	500	4.9	39	1410	1601	777	99.7
28	14	B2	C34	1	750	12	750	0.25	139	59	128	1000	795	1223	740	16	59	940	1070	1000	23.3
29	5	B2	C35	0.5	750	6	750	0.25	x	x		x	x	x	x	x	x	953	1117	x	
30	8	B2	C36	0.5	750	12	750	0.35	89	80	89	450	376	563	300	9.2	47	675	766	625	23.3
31	1	B2	C37	0.5	3125	6	500	0.25	x	x		x	x	x	x	x	x	1427	1672	x	
32	4	B2	C38	0.5	750	12	500	0.35	116	45	115	437	361	507	250	10.1	48	1013	1150	920	23.6
33	0	B2	O19	0.8	1940	10	625	0.3	200		200	369.6	281	452	300	19.8	65.64	946		1070	51.23493
34	0	B2	O20	0.8	1940	10	625	0.3	210		210	398	330	564	374	18.78	63.804	946		1054	51.23493

Top-view photographs of the various test runs as produced in the DoE approach are shown in Figure 6-2; the tests are identified by their test run numbers. Of the total test runs that failed, three outliers failed (see Table 6-2) in a non-typical way and their data was omitted from the analysis to improve the fit of the developed models. In addition, five test replicates (see Table 6-2) were not accomplished due the non-availability of the required forming tool (the 6-mm tool broke during run number C27). Thus, the data obtained from the remaining 24 test runs, and two centre test runs (run numbers O19 and O20) were included in the analysis.

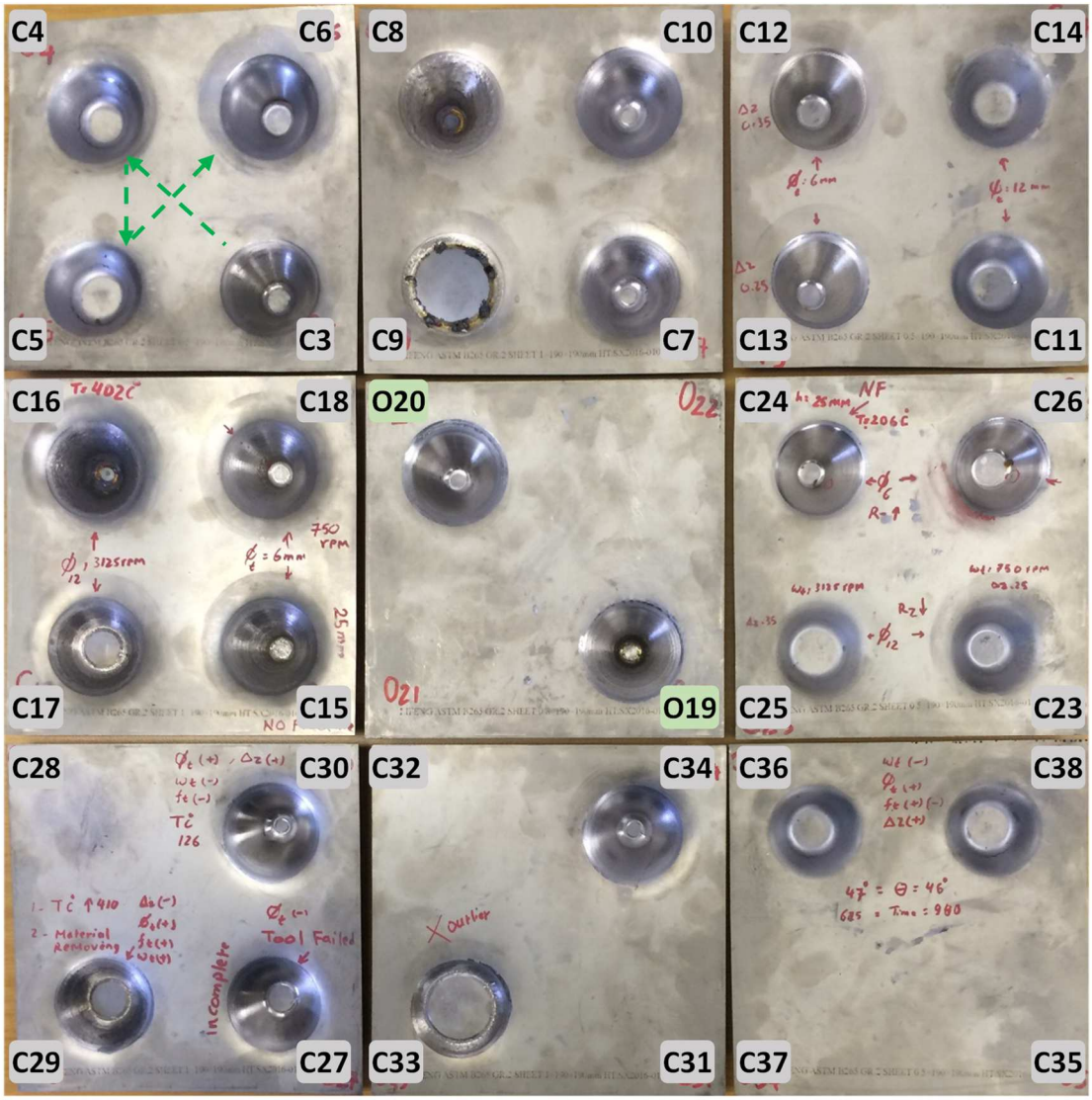

Figure 6-2: Depiction of the components obtained in the DoE : the dashed arrow indicates sequence of runs; centre runs are labelled as O19 and O20; non-conducted run replicates are labelled C28, C31, C32, C35, C37

Table 6-2: List of the test runs excluded from the analysis

Run	Outliers runs			Abandoned runs				
Sequence	7	21	27	22	25	26	29	31
Design ID	11	9	10	13	11	15	5	1
Run number	C9	C27	C33	C28	C31	C32	C35	C37

6.1.1 Data manipulation

Understanding the influence of SPIF factors on the produced thermal and mechanical demands is of crucial importance and represents a significant part of the work in this dissertation. Different settings of these factors were grouped as test treatments and allocated a test run number and an identity number (ID) in the DoE; each of these defined experiments were then run, subject to the assigned parameters, and monitored (except where a run had to be aborted or cancelled). This subsection sets out the rationale and underlines the importance of using a reference point from which the effect of the investigated SPIF factors can efficiently be assessed. It also shows the non-validity of using as-is or raw data for analysis and the assessments and conclusions derived from such an analysis.

During the experiments, in-process temperatures and forces data for each test run were recorded on their cycle time dependency, up until completion, or until mechanical or thermal failure of a test specimen occurred. Due to unique settings for each of the 16-designed test runs as well as their replicate test runs, in particular those tests involving difference in the feed rate, step depth and tool-tip, ended at different points in time. The settings also created variations between runs with differing parameters in terms of the forming speed and the interim position of the localised deformation along the forming path. This causes dissimilarities between the test runs, even at a same point along the processing time, in terms of forming depth, tool/sheet contact area, as well as the generated thermal and mechanical loads. An evaluating point to compare the ID therefore cannot be selected at specific point on the recorded cycle time.

To obtain a sensible assessment of the effect of the process settings on the outcomes of the different test runs, and to enable the generation of a representative model of the process, a reference point has to be taken at a stage where all the test runs were at a similar point of evolvement in the forming process. A reference point at a specific depth of forming was found to be an effective choice for the evaluation. To enable sensible comparison of the analysed results from the different test runs, a forming depth of 9 mm (see Figure 6:3) was selected as the common point.

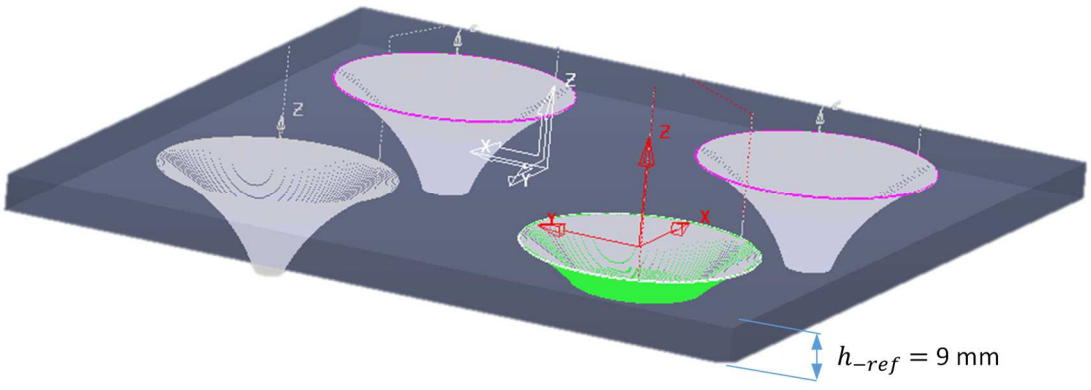

Figure 6-3: Graphic of the interim reference plane on forming tool path at the depth of 9 mm

At this depth of forming, material deformation is expected to be even out, meaning that forming conditions are such that tool/sheet contact area, temperature, and forces all anticipated to be sufficiently developed for all the test runs.

Hence, from the data recorded for each test run, data samples (excluding the formability) were extracted at a reference cycle time (t_{ref} : s) that coincided with a 9 mm depth of forming. This required simulating each of the test runs (the16 ID) using PowerMill, the same CAM software as was used for the initial data collection, to regenerate tool paths for the same test profiles, but with a shallower depth of 9 mm. The corresponding cycle time, t_{ref} of these shortened tool paths for each test run were then taken as the reference line when selecting the values of the responses.

The consistency of this simulating approach was verified beforehand for the full profiles depths (25 mm), by comparing the computed cycle times to the actual measured time, which indicated matched durations. A reference data point for each of the temperature (T_{ref}: °C) and the force (F_{ref}: N), corresponding to this reference cycle time were then determined by taking an average of an interval of 500 readings of the response data points around t_{ref} as given in Table 6-1. These reference measurements were then fed into the DesignExpert software for the subsequent analysis.

6.1.2 Correlation of the tested factors

Prior to analysing the data collected from the test runs, a preliminary exploratory analysis of cause and effect was established by compiling a correlation matrix of the applied parameters and the data output. The correlation matrix is a powerful tool to understanding the influences that the selected input parameters have on the recorded output. Table 6.3 illustrates a colour-coded correlation matrix of the SPIF input factors generated in the DesignExpert.

Table 6-3: Correlation matrix of the SPIF factors from the DoE test

	a: t_0	B: ω_t	C: r_t	D: f_t	E: Δ_z	T_{ref}	F_z	F_x	θ_{max}	t_{ref}
a: thickness										
B: rotation										
C: tool-tip size										
D: feed rate										
E: step depth										
temp @ 9mm	0.481	0.700	-0.012	0.156	0.051					
max F_z	0.604	-0.678	0.367	-0.025	0.023					
max F_x	0.467	-0.466	0.360	0.008	-0.032					
max angle θ_{max}	0.332	0.040	-0.774	-0.013	-0.281					
time, t @ 9mm	-0.073	-0.044	-0.245	-0.828	-0.780					

The correlation direction and magnitude are scaled by colour: red indicates a proportional effect of +1; blue is for an inverse relationship and represents -1, the darker colours indicate a higher correlation, while a correlation approaching zero is shown as white.

Considering the examined range of the input variables, a wide spread in the values of the responses can be seen; the main effect of the input variables on the responses can be read from the correlation matrix. With reference to Table 6-3 the following can be concluded:

- The larger blank thickness t_0 the larger the temperatures and the forces will be.
- With higher tool rotation, ω_t the most significant factors are an elevated temperature and reduced forming forces.
- A bigger tool-tip diameter moderately raises the forces, but considerably reduces the formability, and slightly reduces the cycle time.
- A higher feed rate has no influence on the forming forces or the formability, but there is considerable reduction in the cycle time.
- A large step depth significantly reduces the cycle time and slightly reduces[7] formability.

This coarse picture on the cause and effect will be now refined by post processing the resulted data with the help of DesignExpert program.

6.1.3 Analysis of the formability

This section presents an analysis of formability of CP Grade 2 as a function of the investigated range of the SPIF operative parameters. The maximum material formability θ_{max}, was obtained by measuring the maximum forming depth, h_{max}, at specimen fracture point; this depth is then converted into a forming angle using the equation of the CAD profile ($\theta_{max} = h_{max} * 1.8 + 30°$) as discussed in the previous chapter.

Figure 6-4 shows a plot of the computed values of the θ_{max} obtained from the 26 test runs performed, verses their run ID number on the horizontal axis. As highlighted by the horizontal lines in the figure, the data points are spread vertically over a wide span, from a lower level of $\theta_{max} = 43°$, to a remarkably high value of $\theta_{max} = 75°$; the latter being associated with two non-fractured test samples.

Good process repeatability can also be noticed, illustrated by plots of the forming angles for the runs with the same ID number, representing a test run and its replicate. It should be noticed that the vertical spread of the formability data on the Figure 6:4 highlights the strong relationship between achievable formability and process design, as well as justifying the ability of the implemented DoE in characterising the input/output relationships between the factors.

[7] The results from the DoE do not reflected the actual effect of the step depth on formability, this can be attributed to the small and narrow range of the tool step investigated

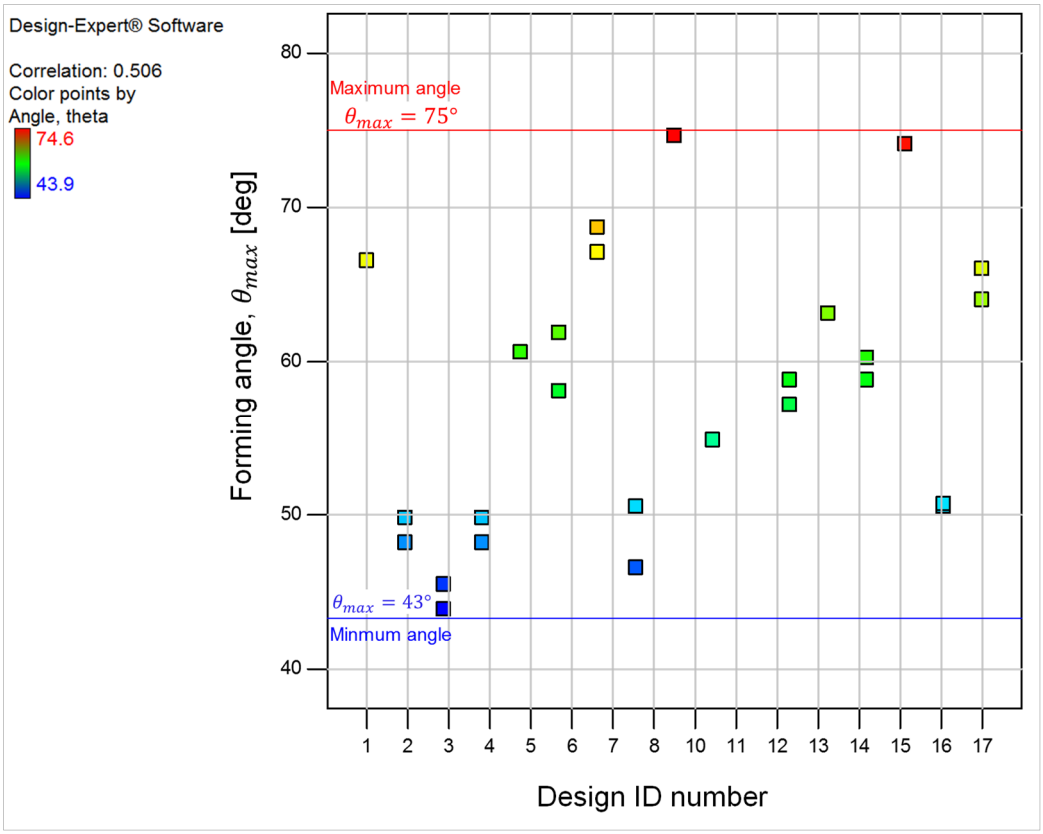

Figure 6-4: Scatter plot of measured wall angles vs run ID numbers

6.1.3.1 Modelling the formability response

"*All models are wrong; some are useful*", George Box (1976)

The aim of a modelling process is always to simplify it as much as possible, while obtaining a sufficiently accurate approximation of the specific output region of interest. To identify the significant process parameters and their effects, the above-mentioned formability data was fed into the DesignExpert program to create a regression analysis. When there are hard-to-change factors creating a split-plot design, statistical analysis of variance (ANOVA) is done using the restricted maximum likelihood (REML[8]) approach. This is applied similarly to a standard AVOVA, but in multiple parts (Stat-Ease, 2016). The whole-plot effect of the HTC factor (which in this study was the sheet thickness) is tested separately from the subplot effects of the easy-to-change factors.

Fitting of the empirical model is done with multiple regression, and testing is done with F-tests (Vinet and Zhedanov, 2011). From the analysis, terms with a probability, P-value is < 0.05 are significant and were included in the model; those with a P-value > 0.10 are not significant terms. After several iterations, and using the automatic model selection function offered in DesignExpert, the selected 2FI design model (main effect and two-factor interaction) was therefore reduced to the significant terms based on the analysis. Table 6-4, shows the terms of the reduced mathematical model, which gives the best fit to describe the formability response.

[8] REML— with P-values are fine-tuned via the Kenward-Roger method.

Table 6-4: The REML results of the formability model

Fixed Effects [Type III]

Source	Term df	Error df	F-value	P-value prob. > F	
whole-plot	1	18.62	28.00	< 0.0001	significant
a - thickness	1	18.62	28.00	< 0.0001	
subplot	5	18.28	23.54	< 0.0001	significant
B - rotation	1	18.03	4.47	0.0488	
C - tool size	1	18.81	105.06	< 0.0001	
D - feed rate	1	18.00	2.29	0.1472	
E - step depth	1	18.24	3.16	0.0921	
C∗E - interaction	1	18.02	10.19	0.0050	

The hierarchy of the factors with respect to their importance is indicated by their F-values; the larger the F-value, the higher the significance is. The model equations in terms of coded and actual factors are presented in Table 6-5. They include the five investigated factors and the interaction ($C * \mathrm{E}$) of tool-tip and step depth.

Table 6-5: Equations of the empirical model for formability

Equation in terms of coded factors	Equation in terms of actual factors
$\theta_{max} =$	$\theta_{max} =$
$+60.9$	$+31.7$
$+3.9 \times a$	$+15.7 \times t_0$
$-1.55 \times B$	$-1.3\ E\text{-}3 \times \omega_t$
$-8.7 \times C$	$+1.9 \times d_t$
$-1.2 \times D$	$-9.2\ E\text{-}3 \times f_t$
$+1.5 \times E$	$+173.5 \times \Delta z$
$-2.4 \times CE$	$-16.1 \times d_t \times \Delta z$

The coded equation can be used for identifying the relative influence of the factors by comparing the factor coefficient. The equation in terms of actual factors is used to make predictions about the response inside given levels of each factor.

Statistical diagnosis of the theoretical model revealed that the model (whole-plot) is significant. Restricted analysis was then performed to verify that the assumptions for the REML approach are met. Box-Cox plot is used to determine the most appropriate power transformation to apply to response data. The Box-Cox plot (Figure 6-5(a)) confirms that the model has the correct power of (λ) lambda and no transformation of response data was required.

Considering only the significant terms, the above statistical analysis led to the six–dimensional response surface summarised in Table 6-5. In the normal probability plot shown in Figure 6-5(b), there are no obvious irregularities in this model—the points fall in line as expected from normally distributed data. A detailed report of the statistical test is provided in Addendum C1.

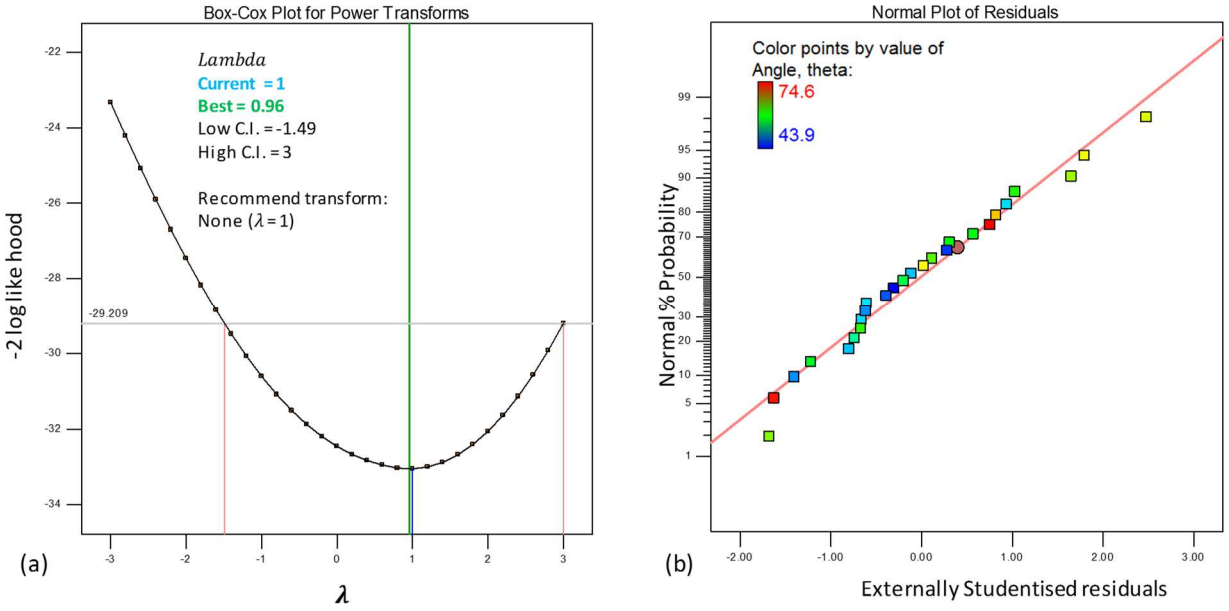

Figure 6-5: Diagnostic plots to confirm the assumption of the ANOVA are met (a) Box-Cox plot for a low power transformation shows no transformation of data was required, (b) diagnosing the normal probability plot of the residuals

As far as formability is concerned, the results from the analysis revealed that the empirical model shown in Table 6-5 meets the assumption. The reduced model still providing useful information and can effectively be applied to navigate the design space. It predicts the formability of CP Grade 2 for the proposed SPIF settings within the investigated range.

6.1.3.2 Influence for process factors on the formability

The relationship between the achievable θ_{max} and the operative parameters (Figure: 6-6) will now be individually discussed based on the developed model. Graphical representations of the relationships were generated using model graphs function in the DesignExpert and were used for illustrating the effects.

For factorial designs, primary graphs of interest are the one factor to look at main effect for the factors not part of interaction; interaction graphs are used to display two-factor interactions; and the cube is useful to viewing the relationship mong three factors.

An interaction represents a non-linear response of second order. It may be helpful to look at contour and 3D views of the interaction to get a feel for the non-linearity. A contour plot provides a 2D view of the surface where points that have the same response are connected to produce contour lines of constant response. The 3D plot displays a 3D view of the surface and can provide a clear concept of the response surface than contour plots. In the following discussion, graphs that best help describe the behaviour of the process are used.

The I-bar symbols (vertical bars) around the predicted means as shown on the effect graphs (see Figure 6-6), are result of a 95% least significant difference (LSD). The height of the bars is determined by the design, the model, the confidence level and unexplained variation. When the REML reveals a significant result of the overall model test (F-Test), these I-bars can be used to gauge the significance of the difference in the predictions.

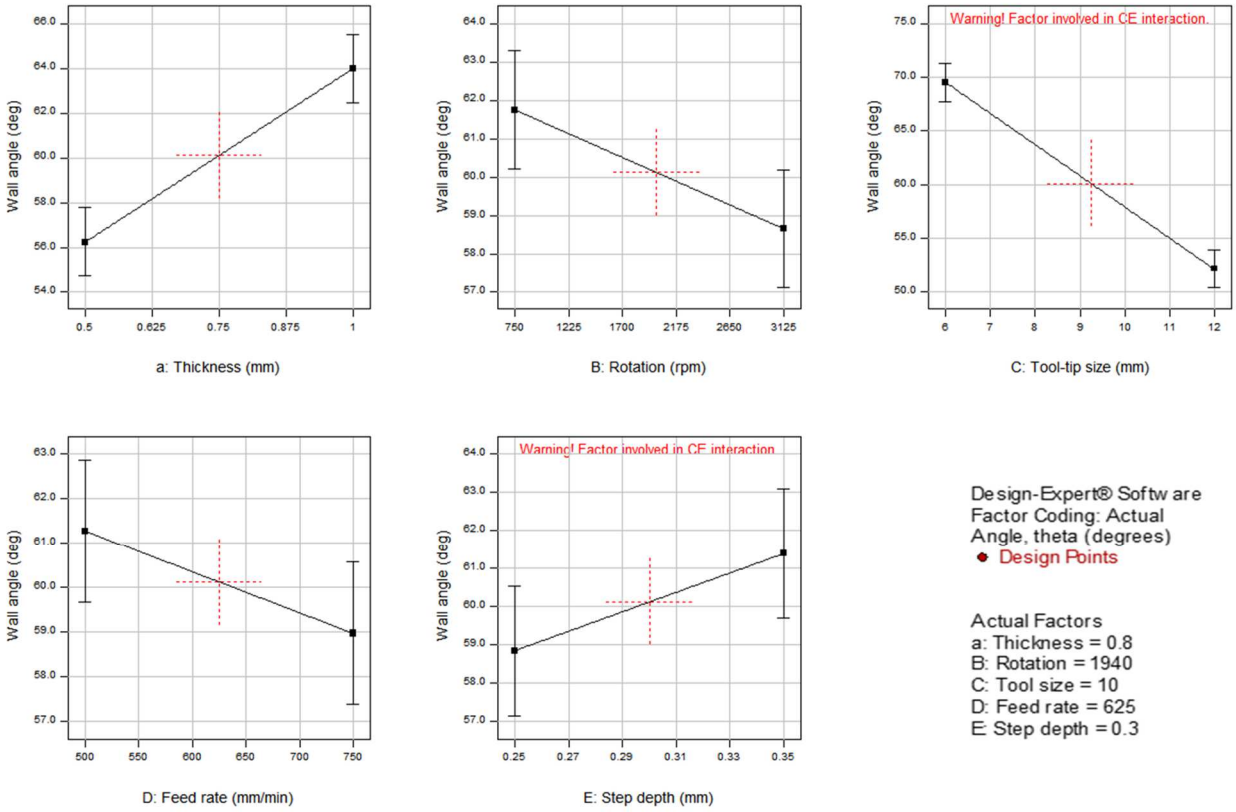

Figure 6-6: Graphics of the all factors main effect on the formability; Legend on the bottom right views the reference settings the factor (note the warning of interaction on the tool-tip and step depth plots).

Note that the step depth and tool-tip factors have not been separately plotted; they are involved in the interaction and only their interactive plot is provided, because plots of their main effect would provide misleading information.

i The effect of sheet thickness

As it shown in the REML table (Table 6.4), the main influence of the blank thickness t_0 , on the achieved θ_{max} was significant. From the pairwise comparison viewed in Figure 6-7, for the 0.5 mm sheet, $\theta_{max} = 57°$, and it is predicted to increase up to 65˚ under the same process settings, using a 1 mm thick plate. This increase in formability (~ 16%) can to a some extent be related to the deformation of material by stretching mechanism in SPIF.

The well-known formula (the low of sine), which describes strong relationship between the initial sheet thickness, the final sheet thickness, and the maximum obtainable drawing angle has broadly been discussed in Section 3 and Section 5.1.4. This relationship is useful for selecting the starting blank, in particular when forming components with large depths or steep walls.

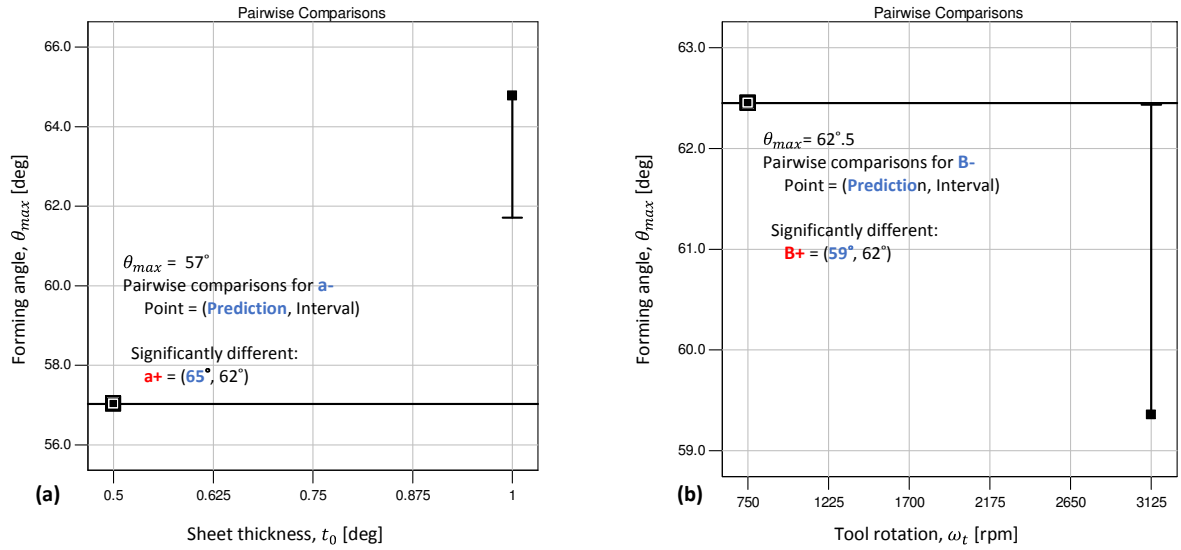

Figure 6-7: Thickness and rotation effect on the formability: (a) thickness main effect views the result of the pairwise comparison performed for lower thickness (a-:0.5 mm); (b) pairwise comparison for the rotation effect performed for the low rotation (B-:750 rpm)

ii The effect of tool rotational speed

Noteworthy is the minor and even inverse impact observed of the tool rotational speed ω_t on the formability of CP Grade 2. As shown in the pairwise comparison (Figure 6-7(b)), stepping up the spindle speed ω_t from 750 rpm to 3125 rpm, the angle θ_{max} decreased slightly from 62˚ to 59˚. This opposing effect was not anticipated, since during the experiments higher forming temperatures were measured corresponding to the higher ω_t, (the higher speeds were expected to increase the formability).

The decreased values of θ_{max} at higher ω_t reflect that several runs were curtailed because failure conditions occurred. Failures were not always associated to the titanium specimens, but they reach the forming tool too. More details are provided in Section 6.2.2. These failures were mainly due to extreme heating, which required termination of the tests concerned. These outcomes were contrary to the initial hypothesis that based on activating the thermal effect via an increased rotational speed would enhance the formability window of titanium sheets. A further work to investigate this phenomenon was put forward as is discussed in subsequent sections.

iii The feed rate effect

Amongst the all design factors, the feed rate f_t as indicated by the default REML approach and plotted in Figure 6-8 (a), has the least significant effect on θ_{max}. Stepping up the feed rate from 500 to 750 mm/min reduces θ_{max} from 61˚ to 59˚. This minor impact could be related to the narrow range of the feed rate used.

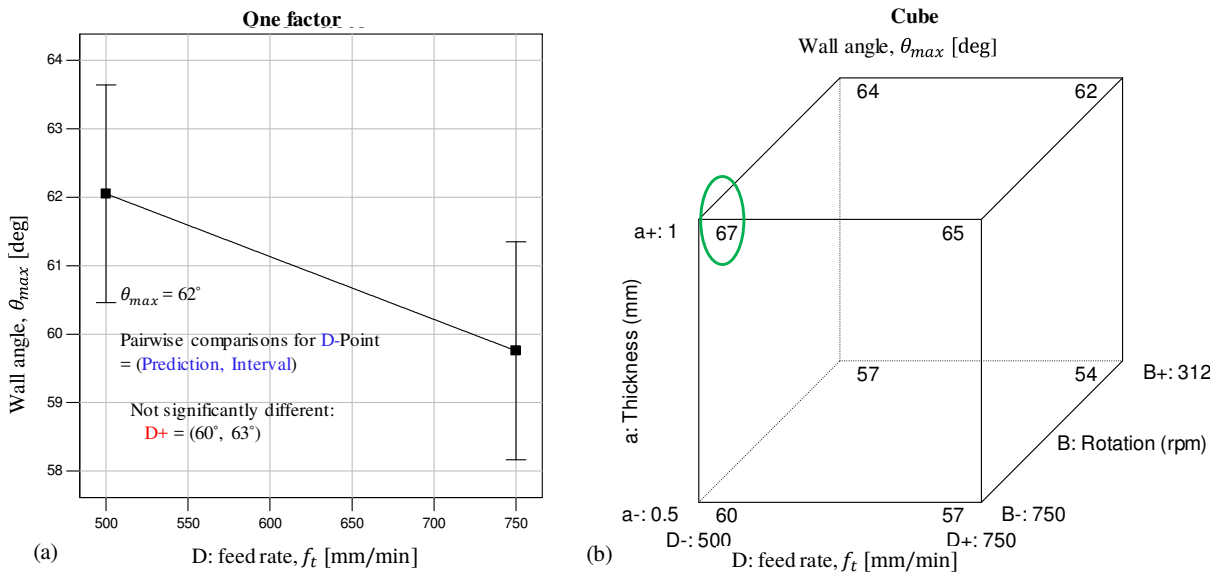

Figure 6-8: Influence of the tested factors on formability of the CP Grade 2 : (a) the main effect of the feed rate, (b) cube plot shows the predicted values of θ_{max} from the combinations of t_0, ω_t and f_t.

The marginal influence of the feed speed on formability is well-established knowledge in the state-of-the-art SPIF of materials other than titanium. Even so, Hussain et al. (2009) claimed a significant reduction in the formability of titanium sheets at higher feed rates. In this DoE, the low and narrow range of f_t were deliberately chosen in attempt to magnify the heating potential of tool rotation on the workpiece material. The intention was to thermally activate titanium formability by raising the tool rotation and slowing down tool plunging. Lastly, the non-significant impact of the feed rate in SPIF is crucial when process productivity is considered; the cycle time can be considerably reduced without affecting θ_{max} achievable. The cube plot in Figure 6-8(b) shows the predicted values of θ_{max} from the coded values of the -1 and +1 of the three factors discussed above. As shown on the cube plot, the best θ_{max} (67°) was achieved by the combination of higher sheet thickness, lower tool rotation and minimum feed rate.

iv The interactive effect of the tool-tip diameter and step depth

Consistent with related literature, the tool-tip diameter d_t is the most significant factor affecting the formability obtainable in the SPIF process; this can also be seen in Table 6-4. In the same reference mentioned, the impact of the step depth on θ_{max}, has however, been a debatable topic. Some publications state that smaller step sizes reduce the formability and this is attributed hardening of the material due to an increased percentage of tool-tip overlapping between successive forming contours. Other publications revealed that forming with large depth steps and smaller tool-tips leads to stress concentration at the small tool/sheet interface, which prompts material fracture, and suggested that tool diameter should be as large as possible to delay the fracture (Li, Liu, Daniel, *et al.*, 2014).

As seen from the REML approach presented in Table 6-4, there is agreement with previous findings by Hussain et al. (2009). The main effect of step depth factor is insignificant (P-value is large and the F-value is low). However, the interaction of the step depth and tool-tip diameter (CE) shows a more significant (P-value =

0.005) term for the formability response. Hence, the interactive term is included in the model, and the step depth term has to be combined to maintain model hierarchy.

Figure 6-9(a) shows the interaction plot of tool-tip diameter and step depth (CE); the points on the left side that have non-overlapping intervals (LSD bars do not intersect or overlap from left to right through an imaginary horizontal line), and are significantly different.

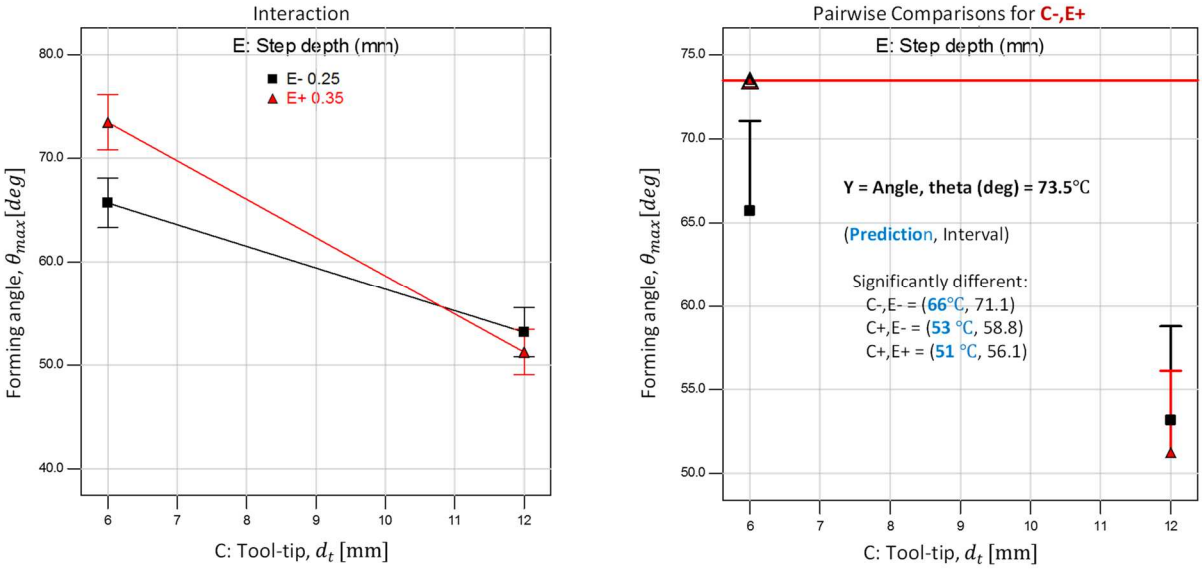

Figure 6-9: Effect of tool-tip and step depth on formability: (a) interaction effect of the step depth and tool-tip size; (b) a pairwise comparison of LSDs between at (C-, E+), and the rest of predictions displays with factor combinations that are significantly different

As can be seen from the interaction plot, the corresponding magnitude of θ_{max} is higher at a small tool-tip diameter ($d_t = 6$ mm) for both the lower and higher step depths (0.25 and 0.35 mm), and the angle value drops significantly as d_t increases. Note that the spread of the points on the right side (larger d_t) of the graph Figure 6-9(a) is smaller than that on the left side (lower d_t).

On the left side of the plot θ_{max} corresponds to larger step depth size Δz, whereas on the right end of the plot comparable results for the two process settings are apparent. In another word, the impact of Δz is less significant when forming with large tool-tips (the I-bars are overlapping).

A pairwise comparison was done at the point (C-, E+), with highest reading of θ_{max} and is illustrated in Figure 6-9(b). The legend of the figure tabulates the factors combinations, which are significantly different. The response varies as a function of interaction between the two factors; contours and a 3D response surface of the relationship between $d_t, \Delta z$ and θ_{max} are presented in Figure 6:10. The contour plot in Figure 6-10(a) reflects the contours of the response surface as shown in Figure 6-10(b); these contours are curves of tool-tip diameter and the step depth pairs that have the same response value

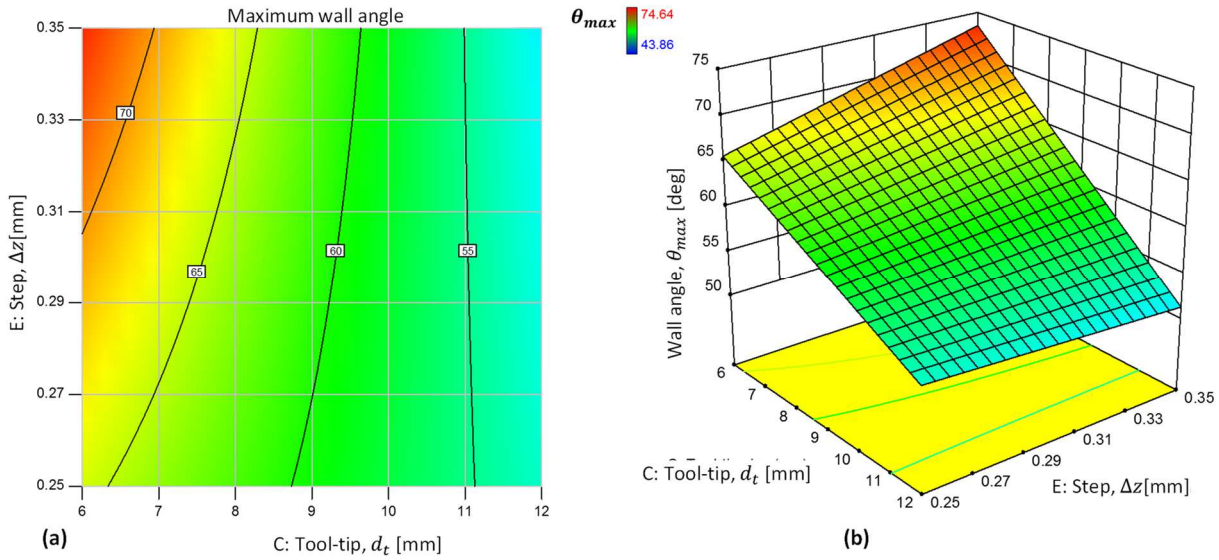

Figure 6-10: Interactive effect of step depth and tool-tip on the formability; (a) colour-scaled contour graph and (b) 3D response surface plot.

As it can be seen at the top left corner of the contour plot, θ_{max} is realised at highest Δz and lowest tool-tip diameter shown on the graphs, and θ_{max} falls-off as one move from left side to right in the direction of a larger tool-tip diameter.

Looking at the 3D plot of the response surface Figure 6-10(b) in direction parallel to the axis of the tool-tip size, there is a notable 28% decline in the magnitude of θ_{max} (from 74˚ to 53˚) as tool-tip diameter is doubled. The relationship between θ_{max} and Δz is more obvious; on the far-left side of the surface, where d_t is small the angle increased from 65˚ to 74˚ (14%). This effect diminishes for the same step values on the parallel right side, where d_t is large. This emphasizes the dominant impact of tool-tip diameter on the formability achievable.

The 3D plot can be a useful tool for designing the SPIF settings; for instance, to reduce the cycle time a bigger step size can be used without affecting formability. The trend of using a larger step depth while maintaining formability, was also observed in the work by Hussain et al. (2009).

This assumed trend in formability is further investigated (section 6.2.3), showing that with all other process settings kept constant at their reference levels, and altering only the step depth over wider range alike, the results of increased formability were confirmed.

6.1.4 Analysis of the thermal effect

During the SPIF operation, heat is generated mostly by sliding friction and the adiabatic plastic deformation of workpiece. The friction occurs at the tool/sheet interface due to the speed difference between the moving tool and the stationary workpiece. Significant portion of the mechanical energy is transformed into heat that raises the temperature, and mainly concentrates at the contact interface and is apportioned between the tool and the sheet.

Due to the small depth of incremental steps used in the SPIF, the forming tool can pass repeatedly over the same point on the sheet; this repetitive passing is mainly subject to the ratios between t_0, Δz, and d_t as selected for the process, and it will affect the real contact area. Interaction of these factors, together with the applied tool speed, defines the frequencies with which the heat source approaches the same point on the forming path. When the cycle of the tool sweeps is short, the tool returns to the same point before the heat from the preceding cycle had dissipated, so that heat accumulates and the temperature at that point builds up.

Of particular importance, are the consequences of this dynamic heating process; the resulting rise in thermomechanical stress around the contact interface can significantly influence the plastic behaviour of the material being formed and the applied lubricant, as well as escalate wear at tool/sheet interface. Figure 6-11 depicts an example of the CP Grade 2 samples produced in the current DoE. The dashed arrows on the figure show the sequence in which the test runs were conducted (refer to Table 6-1) for the treatment settings of the various test runs.

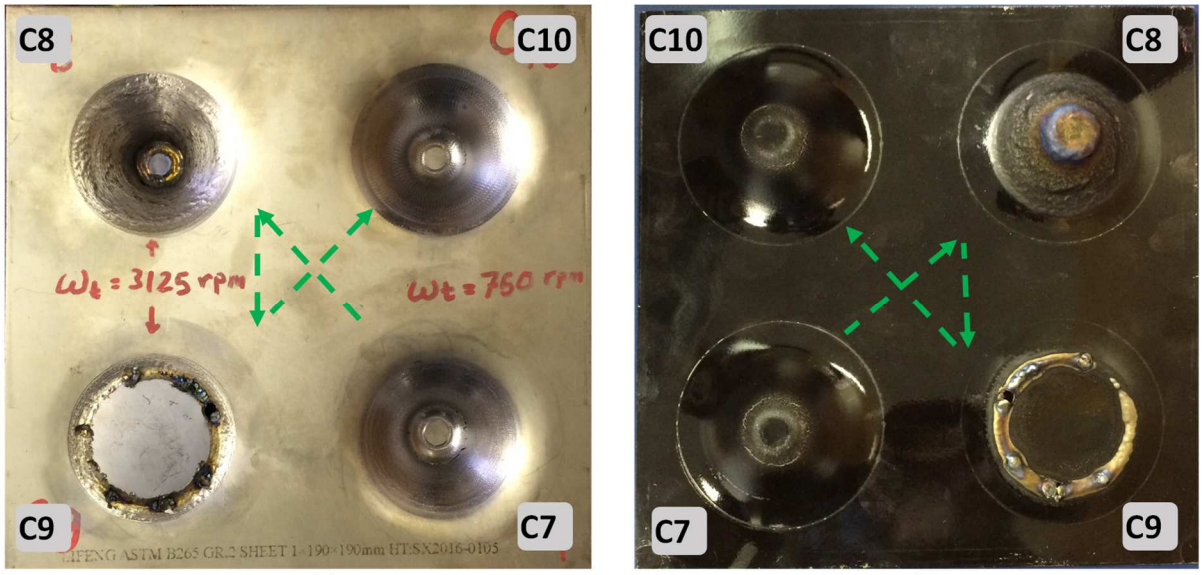

Figure 6-11: Image of heat-affected titanium samples , showing the effect of thermal defects. Note: inside and outside views are mirror images; the dashed arrow shows the sequence; C8 and C9 were conducted at high (3125 rpm) rotation speeds

A close look at the inner side of sample C8 reveals a surface worn by the removal of material, while on the outer side it shows signs of material burnt by extreme temperatures, producing a very rough surface. In test sample C9, catastrophic (adhesive and abrasive) wear of the tool and gouging of the sample sheet occurred at the start of forming. Unlike the preceding two examples discussed, samples C7 and C10 were shaped at a lower speed; after undergoing a typical deformation process, material failure occurred in these two samples when ductile fracture was observed. These observations clearly indicate that the design of SPIF operating settings and the control of thermal effects are the key to successful manufacturing of components exposed to frictional heating.

Although there are well-established and widely used analytical and numerical methods of analysing forming temperature, reliability of these methods necessitate accurate predictions of the real contact area along the sliding path, within which the frictional heat is being generated; "*Seldom is that real area of contact known with any certainty a priori*" (Bhushan & Kennedy, 2001). To understand the thermal requirements in SPIF and acquire information about the thermal effects that both the tool and sheet will accommodate due to the sliding friction, it is often essential to quantify the contact temperature experimentally.

In this study, a field radiation-based temperature measurement was performed on the radiation emitted by the outside surface of the titanium samples, using an infrared sensor. The Excel diagram in Figure 6-12 presents an example of four data series of instantaneous temperature collected during the forming of two different test samples and their replicates plot versus their time dependency.

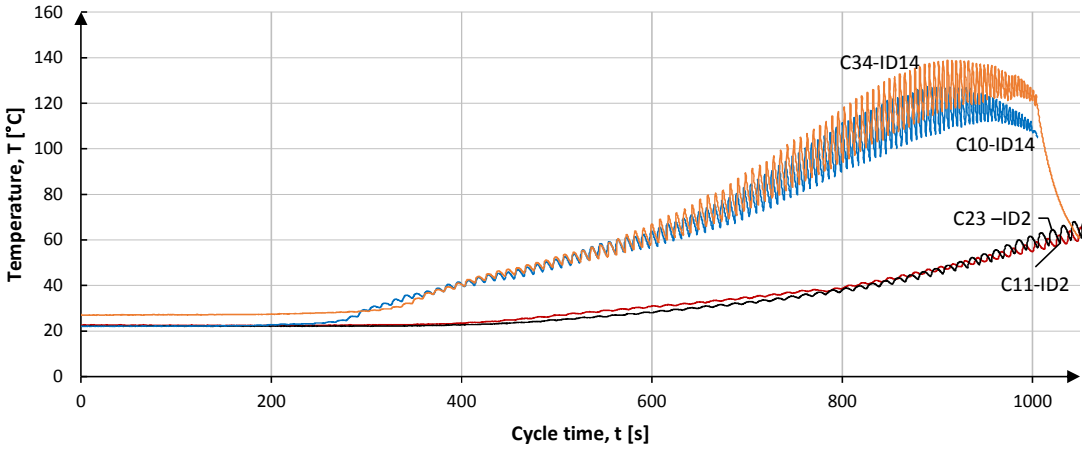

Figure 6-12: Measured temperature gradients versus the cycle time, showing good process repeatability for each two runs with the same design ID

It is apparent from the plot that the temperature profiles for the runs with the same ID (replicates) reveal good repeatability, which signifies the reliability of the subsequent analyses of the SPIF thermal demand. The plots of thermal profiles for all the conducted test runs are provided as an Addendum D.

6.1.4.1 Forward remarks

Before the analysis of the thermal loads, a summary of basic concepts illustrated on the temperature diagrams is presented here, as a background to the subsequent discussion:

- The fluctuations (spikes) seen on the temperature curves are due to the heat source (forming tool) changing its relative position to the measuring spot of the IR camera. the instant temperature readings were maximums (peaks), when the tool was processing the material directly above the measuring spot, and these readings were minimums when the tool-tip was forming the far side of the components, diametrically opposite the measuring point.

- Also, the frequencies at which these spikes occurred increased with growing component depth due to the reduction in the component diameter. As the diameter became smaller, the heat source approached to the measuring point faster.

- Temperature gradients start from room temperature and rise as the forming proceeds; this is the result of frictional heat and plastic deformation, as well as the increased percentage of heat accumulated in the workpiece material over the processing time.

- The continuous rise in the measured temperature during the run of the test is attributed to the growth in the tool/sheet contact area, which is a function of the component wall angle and the depth. Upon completion of forming, there was a steep decline in temperature.

- The temperature profile with its specific maximum level is dictated by the applied process settings. At maximum temperature, the material reaches its heat saturation capacity, and sub-equilibrium occurs between the generated heat and the heat dissipated to adjacent tool, fixture and the environment.

As previously mentioned in Section 6.1.1, data points were taken at the cycle time corresponding to the reference depth of forming ($h_{ref} = 9$ mm). Figure 6-13 is a scatter plot graph of reference temperatures T_{ref} in degree Celsius, versus the run ID; colours scale the cycle time (see legend).

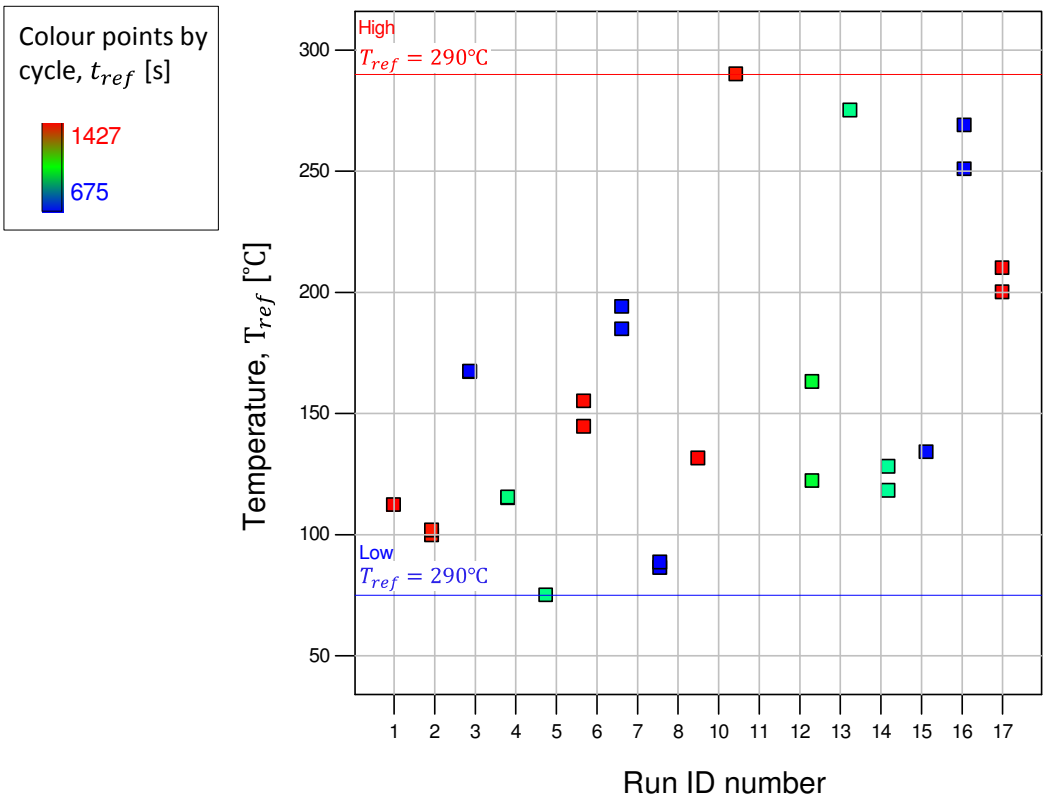

Figure 6-13: References temperatures versus the run orders, the scatter plot is scale coloured by runs reference cycle time

As shown on Figure 6-13, the readings of T_{ref} vary along the test ID. The horizontal blue line on the graph highlights the minimum T_{ref} level (75℃), which was recorded in test run number C6 with run ID 5. The highest temperature in this run was 84℃; the maximum T_{ref} (290℃) for test run number C16 with run ID 10, where the actual maximum during the run increased to 408℃ .

The vertical spread of the data points highlights two issues: the significant impact of the process settings on the generated thermal effects in the SPIF process, and the ability of the planned DoE to create the change in the thermal response targeted for studying the cause and effect.

It is apparent (Figure 6-13) from the random vertical spread of the colours over the range blue to red, that the T_{ref} readings are independent of the cycle time. Some of higher T_{ref} values are blue and correspond to short cycle times (625 s), while the opposite is true for some of lower T_{ref} readings, which are red and have long cycle times (1425 s). The forming temperature is therefore more dependent on the chosen forming conditions than the cycle time.

6.1.4.2 Modelling the thermal response

Similar to the manner in which formability was analysed, a regression analysis of variance of REML was performed for the temperature data collected. For this analysis, however, more interaction terms were suggested to be significant for the 2FI empirical model, which gave the best fit to the temperature responses as listed in Table 6-6.

Table 6-6: The REML results of the selected temperature model

Fixed Effects [Type III]

Source	Term	Error	F-value	P-value	
	df	df		prob. > F	
whole-plot	1	15	126.87	< 0.0001	significant
a-Thickness	1	15	126.87	< 0.0001	
subplot	9	15	34.79	< 0.0001	significant
B-Rotation	1	15	213.76	< 0.0001	
C-Tool size	1	15	0.32	0.5800	
D-Feed rate	1	15	6.87	0.0193	
E-Step depth	1	15	7.72	0.0141	
aB	1	15	36.23	< 0.0001	
aC	1	15	5.13	0.0388	
aD	1	15	4.83	0.0441	
CE	1	15	17.71	0.0008	
DE	1	15	7.86	0.0134	

Given the dearth of such information on the SPIF thermal demands in the literature consulted, more attention was paid to this analysis by attempting to incorporate any surmised effects into the model. This will be further clarified when analysing the effect of these interactions and presenting the 3D response surface within the

investigated region of process variables. With respect to their importance, the hierarchy of the factors listed in Table 6-6 are indicated by their F-values; the larger the F-value, the higher the significance.

Statistical analysis of the 2FI theoretical model for the response surface showed that the model (whole-plot) is significant. Testing of the model fitness showed its reliability to representing the response, and will not be presented in this section, instead, a detailed report of the statistical analysis of this model is shown in Addendum C2.

In the subsequent sections the main influence of the factors listed in Table 6-6 on temperature variation during SPIF, will be discussed. The model equation (see Table 6-7) in terms of coded factors (the high levels of the factors are coded as +1 and low levels as -1 is useful for identifying the relative impact of the factors by comparing the factor coefficients.

Table 6-7: Equations of the empirical model for temperature

Equation in terms of coded factors	Equation in terms of coded factors
$T_{ref} =$	$T_{ref} =$
+179.4	-761.4
+38.5 × a	+265.0 × t_0
+62.0 × B	-1.9E-3 × ω_t
-2.2 × C	+38.8 × d_t
-9.1 × D	+0.7 × f_t
+10.7 × E	+2310.5 × Δz
+21.4 × aB	+0.072 × $t_0 \times \omega_t$
-8.6 × aC	-11.5 × $t_0 \times r_t$
-7.4 × aD	-0.236 × $t_0 \times f_t$
-15.5 × CE	-103.2 × $d_t \times \Delta z$
-11.7 × DE	-1.9 × $f_t \times \Delta z$

6.1.4.3 The impact of the applied SPIF factors on the forming temperature

Considering the terms of derived empirical model viewed in Table 6-6 and Table 6-7, each of these terms was involved in one or more significant interactions. Therefore, plots of main effects would not have been useful for the analysis. Instead, the plots of each significant pair factor interactions will be used in the subsequent discussion.

i Sheet thickness and tool rotation

This significant interaction aB (Figure 6-14) involves a pair of the critical factors that potentially drive the thermal outcomes in the SPIF. Heat generated at the interface due to both sliding friction and plastic deformation, are strongly associated to the workpiece thickness and the imposed tool rotation.

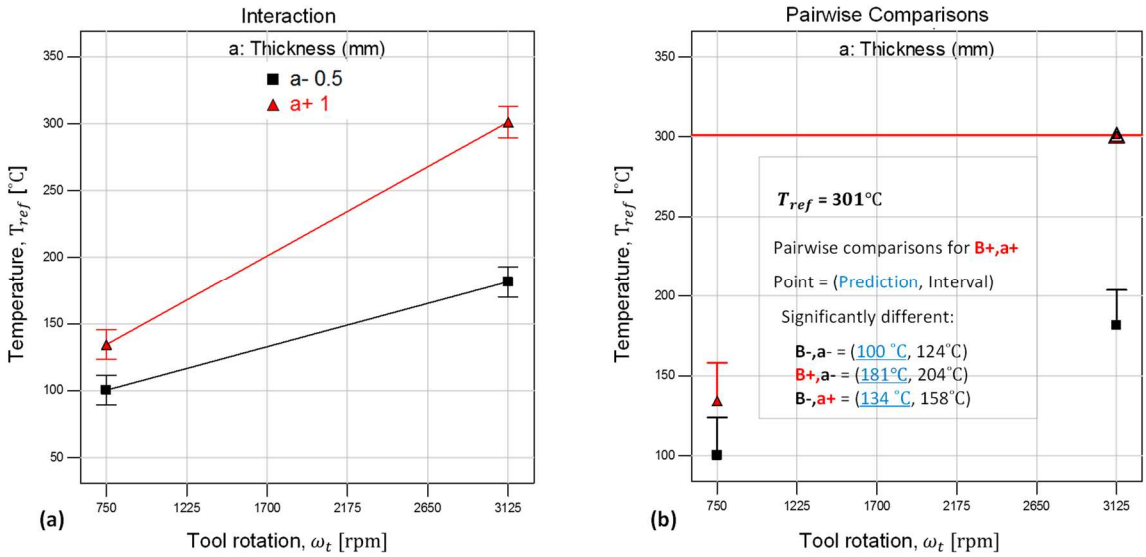

Figure 6-14: The effect of the thickness and rotation on the temperature: (a) the combined effect of the two-factor interaction; (b) the pairwise comparison between the maximum point at (B+, a+) and the rest of the predictions, displaying the significant changes due to the setting combination

As shown on the interaction graph Figure 6-14(a), the measured temperature T_{ref} is related to the rotation ω_t and the thickness. The two non-parallel lines on the interaction plot indicate that the forming temperature is different depending on the settings of two the factors and signifying that the effect of one factor depends on the magnitude of the other.

The spread of the points at the left side of the graph (lower ω_t value) is smaller than that on the right side of the graph where ω_t is maximum. Put differently, the generated heat is not only dependent on ω_t, which is presumed as the heating source, but also on the workpiece thickness. The significant rise in T_{ref} with increased thickness at same ω_t, can be attributed to the heat generated due adiabatic plastic deformation and the higher strain resistance of a thicker titanium specimen. This can also be noticed from large forming forces typically associated with the forming of thicker plates.

The interactive effect on T_{ref} can further be interpreted with the help of a pairwise comparison graph offered by the DesignExpert program and shown in Figure 6-15(b). Referring to Figure 6-14(a) the I-bars do not overlaps with the horizontal line drawn through the predicted mean of the highlighted red tringle at the maximum thickness and speed (a+, B+). As illustrated in Figure 6-14(b) they are significantly different from the selected point.

Note that even though the displayed pairwise tests are two-sided, only half of the interval is displayed for easier interpretation. The legend on the diagram of Figure 6-14(b), displays the significantly different means of the predicted temperatures, and the interval when comparing the different pairs of the settings with the selected point (a+, B+) at which $T_{ref} = 301$°C occurred. The second data row in the legend (B+, a-) views the effect of reducing thickness in relating to the (B+, a+), the temperature decreased from 301°C to 181°C at the same high rotation. Further insight is provided by Figure 6-15, which presents a visual illustration in 3D and 2D of how the thermal effect varies as a function of these settings; the graphs are scale coloured.

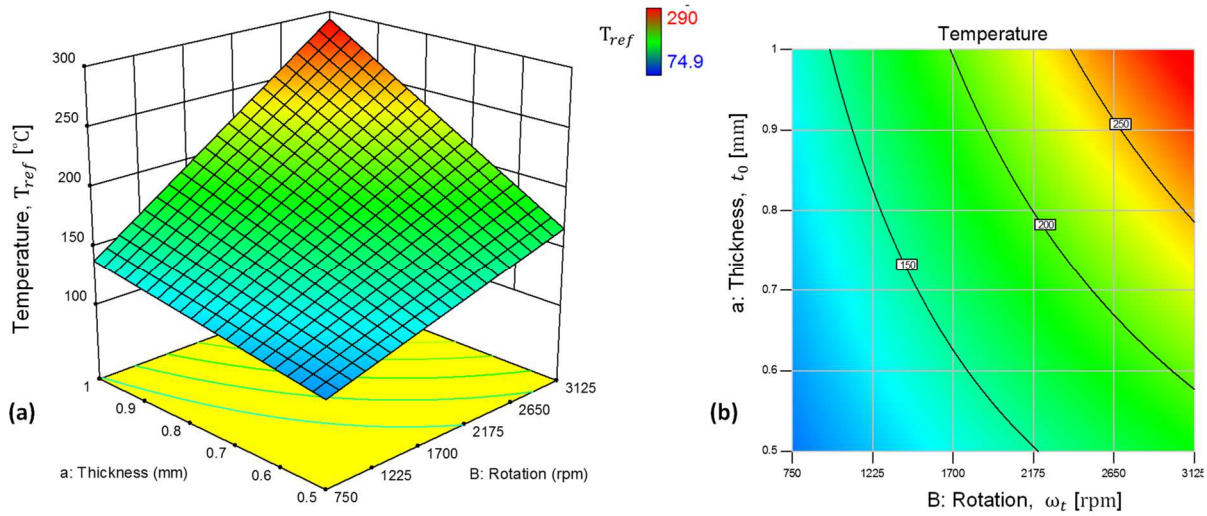

Figure 6-15: Effect of rotation and thickness on temperature, shows the non-linear thermal response due the interaction of tool rotation and the blank thickness: (a) the 3D view of aB interaction, (b) contour plot of the aB

A summary for navigating the boundaries of the non-linear response in Figure 6-15(a), starting from the cool blue zone (low T_{ref}) at front centre of the plot, is given below:

- The temperature is a minimum (~100˚C) when ω_t and t_0 at their lowest settings
- At thinner blank (0.5 mm), maximising the rotation T_{ref} raises by about 56%
- For the thicker blank (1.0 mm), maximising the rotation T_{ref} raises by about 160%
- At a low rotation (750 rpm), doubling the blank thickness T_{ref} raises by about 28%
- At a high rotation (3125 rpm), doubling the blank thickness T_{ref} raises by about 68%

The contours of the surface shown in Figure 6-15(b) graph the curves of the t_0 and ω_t pairs that have the same response value on the 3D surface. The labels on contours and the colour code clearly indicate that temperature raises parallel to the diagonal line from lower left to upper right of the graph, corresponding to a higher setting of the two factors.

ii The interactive impact of the thickness and tool-tip

Figure 6-16 illustrates the interactive effect of tool-tip diameter and thickness (aC) on the obtained T_{ref}. Results from the pairwise analysis as shown in Figure 6:16(a) indicated that at a sheet thickness of 1.0 mm there is a significant decrease in T_{ref} as tool-tip diameter increases. While for the thinner sheet of 0.5 mm, the effect of tool-tip size on T_{ref} was insignificant; this is clearer from the 3D plot of the response as shown in Figure 6-16(b). From the colour scaled response surface it can be seen that the maximum temperature was 225℃ when using the 6-mm diameter tool-tip and the 1.0 mm sheet (far right corner), and the temperature decreased to 205℃ for a 12 mm diameter tool-tip with the sheet thickness unchanged at 1.0 mm. The T_{ref} surface on the near side (thinner sheet) runs almost parallel to the axis of tool size and a small variation of the temperature (from 137℃ to148℃) could be predicted.

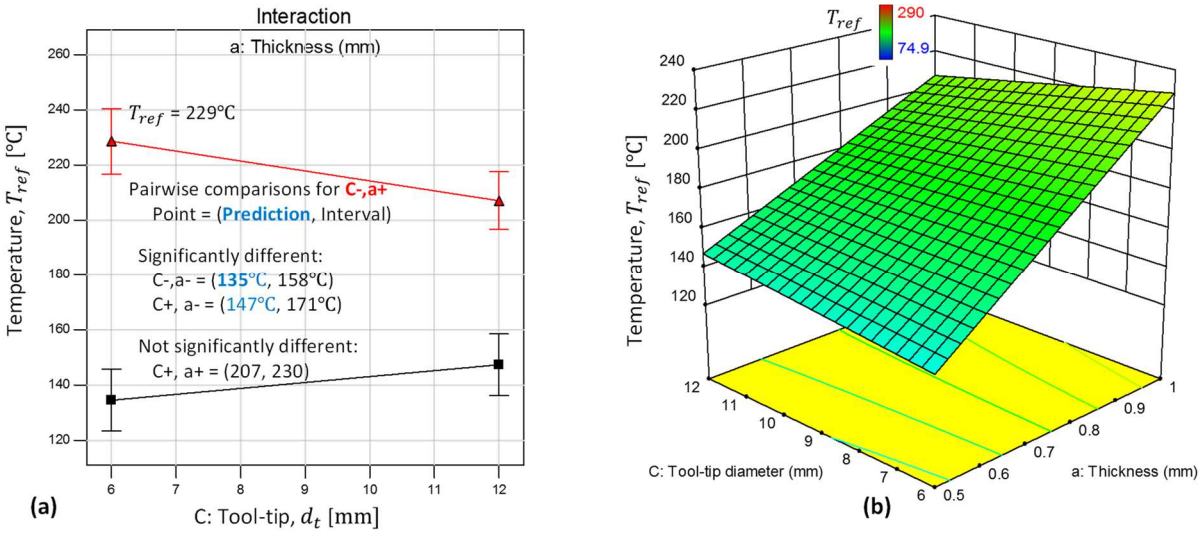

Figure 6-16: Tool and thickness interactive impact on the temperature ; (a) interaction plot, (b) the colour coded 3D response surface

The decrease in forming temperature when using a large tool diameter can be attributed to partitioning of the frictional heat at the interface between the tool and sheet. At high sliding velocities most of the heat enters the moving body which presents a larger area of new material per unit of time to the heat source (Bhushan & Kennedy, 2001).

In SPIF, the workpiece surface is the moving body in respect to the heat source (interface) and forming tool is the stationary body. Also, the heat portion that goes into the forming tool per unit time per unit area will rise when applying a larger tool-tip diameter. This is also true when considering the lower thermal conductivity of the samples made of titanium material as compared to the forming styli made of tool steel. Developing knowledge from concurrent measurements of temperature on the both sliding bodies is a worthwhile research point.

iii The interactive effect of the feed rate and thickness

From Table 6-6, the interactive effect of the blank thickness and the feed rate (aD) on temperature showed a P-value of 0.0441. The vertical distance between the two curves in Figure 6-17(a) shows a significant change in T_{ref} due to an increase in t_0 at all feed rates, but not in a comparable way. In other words, there is slight decrease in T_{ref} with increasing f_t at both sheet thicknesses, but this decrease of T_{ref} is more rapid for the larger thicknesses.

An easy way to verify this separation is to do a pairwise comparison based on the model predictions as shown in the legend of Figure 6-17(a). Outcomes of the pairwise comparison to the selected point (D+, a+), or $T_{ref} = 201$°C and the rest of predictions are shown as a legend on Figure 6-17(a). The inverse and non-linear influence of the f_t on the temperature can better be navigated on the 3D view in Figure 6-17(b). As the cool blue colour on the plot labels the lowermost temperatures (far right corner), it corresponds to the lower thickness and higher feed rate.

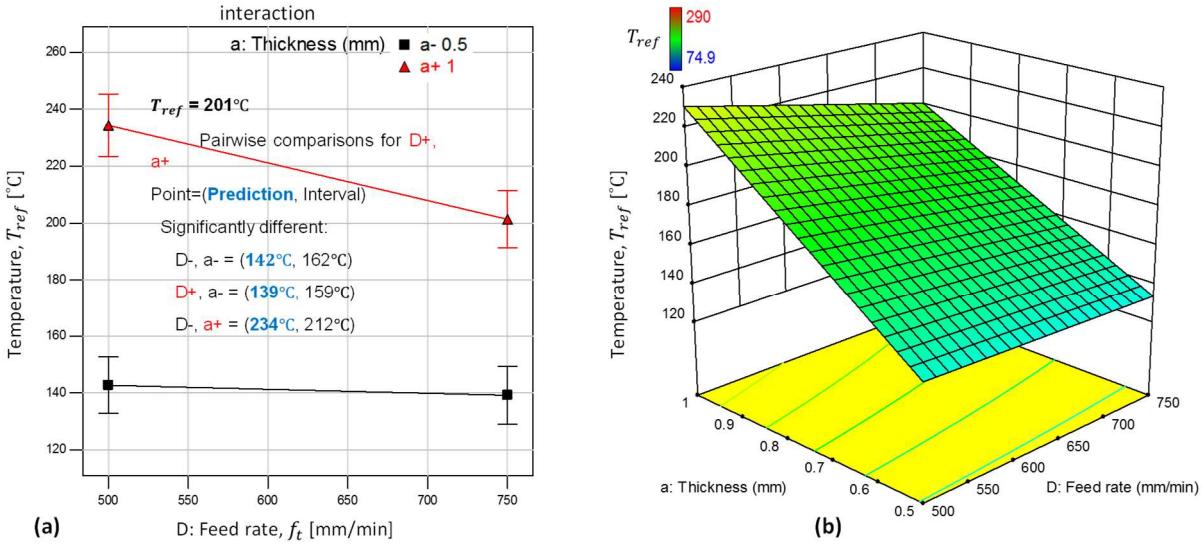

Figure 6-17: The effect of thickness and feed on the temperature: (a) interaction plot pairwise comparison done at (a+, D+), legend displays the factor combinations significantly different; (b) the 3D view

Moving from this lowest T_{ref} point in the direction of increased thickness towards the far corner, there is a substantial rise of T_{ref} by about 47%. However, doing a similar evaluation-path considering the two corners at near side of the surface (low feed rate), increasing the thickness will cause T_{ref} to rise by 62%. Finally, the drop in T_{ref} due to an increased feed rate at the larger thickness is around 14%, while the drop in T_{ref} due same increase in feed rate at smaller thickness is less than 4%.

Even at the lower and narrow range of the feed rate applied, it was possible to notice its reverse impact on the temperatures with the thicker plates. This reverse impact is controversial, and could be attributed to the reduced time for the frictional heat at the interface to develop when a large feed rate is applied; because the tool leaves the interface more quickly. However, at high feed the tool may also sweep the same interface point more frequently. Therefore, there will be specific process settings where the effect of the feed could have a point of switching impact on the temperature (see Section 6.2.3).

Regarding the smaller variation in the low temperature observed when forming the thin 0.5 mm sheet, which is subject to further thinning due the stretch forming, it is doubted whether the pyrometer was picking up the temperature of the forming tool instead of the blank (due to the mentioned thinning effect). Because the temperature at tool-tip is always saturated and is the maximum of the two sliding bodies. This was not the case for thicker plates of titanium with its property of low thermal conductivity. Concurrent measuring of temperature on both the tool and the workpiece could provide an accurate answer to this demand, but that was not feasible in this study due the lack of an extra measuring device.

iv Effect of the step depth — tool-tip diameter interaction

The significant impact of this interaction (EC) was reported when analysing formability in the previous section; also, the EC was shown to be the second-most significant interactive term (F-value: 17.7 and P-value: 0.0008), after the rotation and thickness term (aB), when considering the model of temperature response.

Firstly, looking at the interaction plot shown in Figure 6-18(a), this relationship is represented by the intersection of the graphs for the two depths of the step and can be seen at the intersecting plot lines. At the small tool-tip diameter ($d_t = 6$ mm) the temperature T_{ref} increased considerably from 155℃ to 208℃ when the step depth has increased from 0.25 to 0.35 mm. At the large $d_t = 12$ mm, the two response lines changed over with the 0.25 mms plot now above the 0.35 mm plot, with the I-bars overlapping, predicting a lower static value of the T_{ref}.

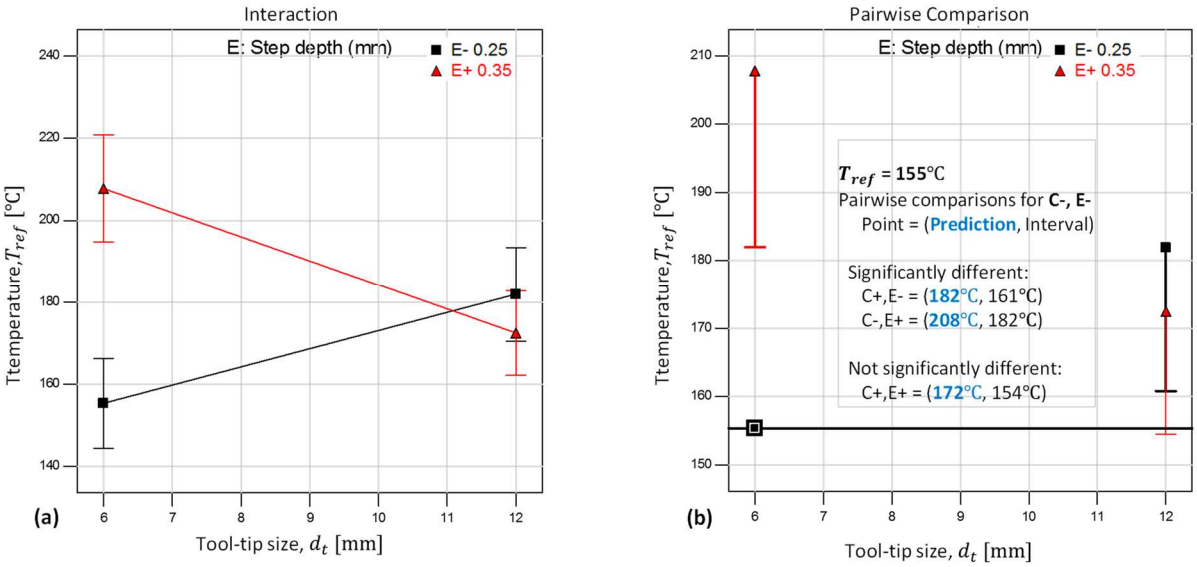

Figure 6-18: Effect of tool and step interaction on temperature (a) view of the interaction, and (b) pairwise comparison done for the reference point at (C-, E-) of the prediction; legend shows which pair setting is significantly different from the reference point

Trailing the descending red line of the plot, the higher T_{ref} at larger step depth and small tool-tip diameter can be explained by the relatively higher contact angle at the interface compared to the flat angle with larger tool-tip; also, a consideration is the concentration of the heat generated at the smaller contact zone. This effect diminishes as tool-tip diameter increases. For the lower starting black line (small step), the T_{ref} ascending trend is due to increased percentage of tool cyclically overlapping the same point of surface with increased tool-tip diameter.

The two opposing (ascending and descending) trends intersect inside the investigated range, which are shown in Figure 6-19 as the saddle-shaped contour and tilted 3D graphs of the response.

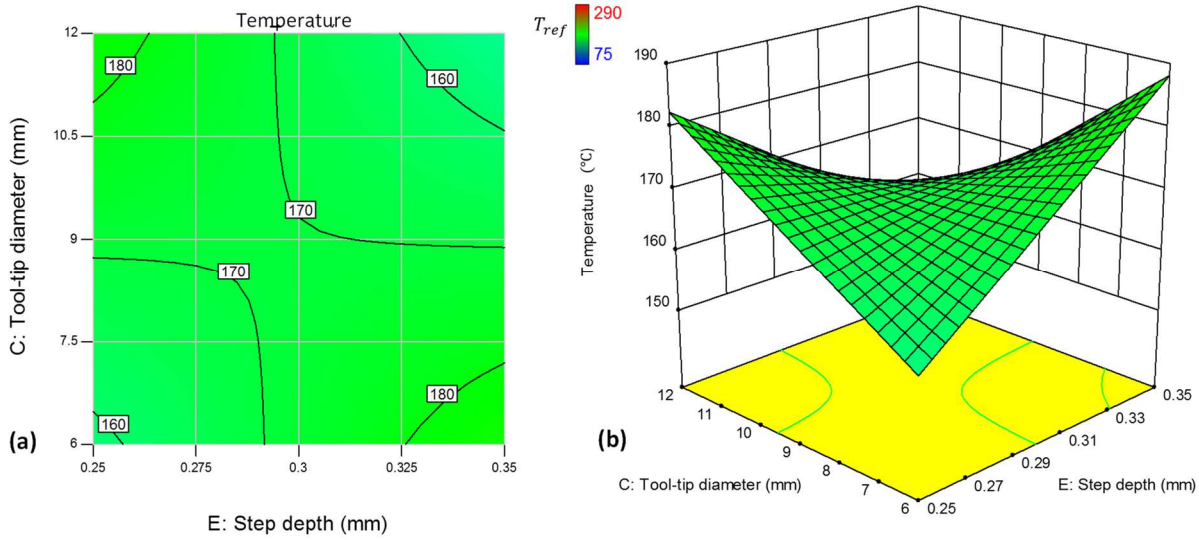

Figure 6-19: The interactive effect of tool and step on temperature (a) contour plot of the non-linear thermal response due the interaction (CE)of tool-tip and step depth, (b) the 3D view of the CE interaction

As clearly shown in the 3D plot in Figure 6-19(b), the T_{ref} reading is a maximum at the two nodes with the contrasting combinations (C-, E+) and (C+, E-); T_{ref} is however a minimum, when the two items that make up a pair, have matched settings (C-, E-), and (C+, E+). The interactive effect of both the matched pairs and the contrasting pairs yields an extremum within the given range of the response, so the deformation they presented was considered not appropriately stabilised and therefore not in line with the aims set for this study. Step depth and tip diameter need to be selected in proper ratio to avoid the extreme heating.

The predicted response surface showed a saddle point between these peaks, near the crossing point of its diagonals and at a step depth of about 0.3 mm and a tool-tip diameter of 10 mm. This saddle is located around the midpoint of the DoE and yields a moderately desirable and stable heating effect. It is anticipated that this heating effect will back the deformation of the titanium samples by softening the material, and reducing the forces, while creating minimum side effects on the outcomes.

Two verification test runs (numbers O19 and O20) were successfully performed with these values. They gave acceptable results, keeping temperature around 200℃. In this work, these settings of step and tool were referenced as a benchmark when developing the conceptual map. They also used for designing of the OFAT experiments in the subsequent studies (Section 6.2).

v Effect of the feed rate — step depth interaction

The last significant term in the derived model pairs is the step and feed interactive impact (DE) on the generated heat. As shown in Figure 6-20(a), the trend of T_{ref} looks similar to that of the CE interactive, but at a smaller scale. This can be seen from the pairwise comparison of (D-, E-); the only significant effect was at (D-, E+) where the temperature rises from 166℃ to 211℃ or by 27%. Differently to the CE effect in the discussion above, here T_{ref} rose by 34% for the same increase in step depth.

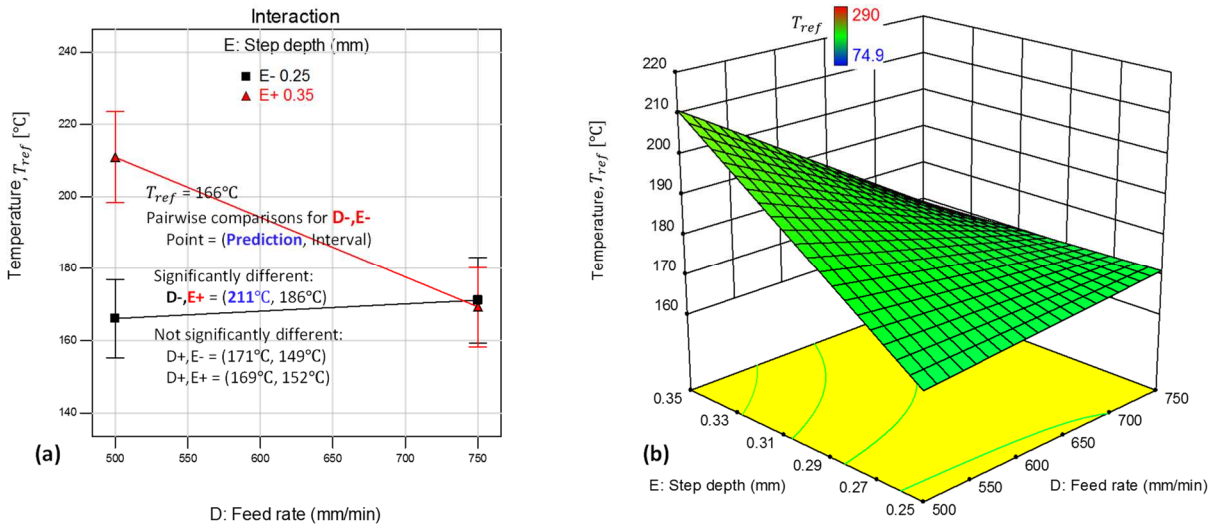

Figure 6-20: The interactive effect of feed and step on the temperature: (a) interaction plot pairwise comparison done at (D-, E-); the legend displays the factor combinations significantly different; (b) the colour-scaled 3D view

The similarity between the trends of T_{ref} in CE and DE terms can also be related to weighting of the step depth effect and boost from the habitually ignored impact of the minor duo on the feed rate.

6.1.5 Analysis of the axial forces

6.1.5.1 Forward remarks

Unlike the thermal effect on SPIF characteristics, the effect of the force factor is inevitable, and sufficient forces are essential to create the plastic change in the material being produced. The ability to predict the forming forces is very necessary for the design of the forming process if dimensional control is to be increased and failure is to be averted. Excessive wear at tool/sheet interface, system vibrations, and deflection of tooling system during forming, could all be avoided if the forming force is clearly understood and determined prior to the design process. Therefore, a force analysis was carried out to monitor the process and study the interactive effects of forming conditions on the response like that compiled for the thermal effects.

Given that forming forces were extensively studied in the relevant literature, a fair amount of knowledge on the association between the SPIF key variables and the forces is accessible, only a brief reference to forces is presented in this section. Furthermore, the relationship between the thermal and mechanical effects will also be summarised in subsequent sections dealing with the OFAT speed tests. In the literature consulted, there were few references, which investigated the forming forces in the SPIF of titanium, and most of these reported using the OFAT approaches.

Because of the centrosymmetric profile of the samples being formed, the in-plane force F_X and, F_Y was analogous to sine profiles and should be similar in (magnitude and trend), but at a phase difference of $\frac{\pi}{2}$, dependent on the position of the forming tool within the contour (Xu *et al.*, 2013). An example of instantaneous axial and in-plane forces collected using the six-component dynamometer for the test run number C27 is plotted versus their time dependency, and is graphically presented in Figure 6-21.

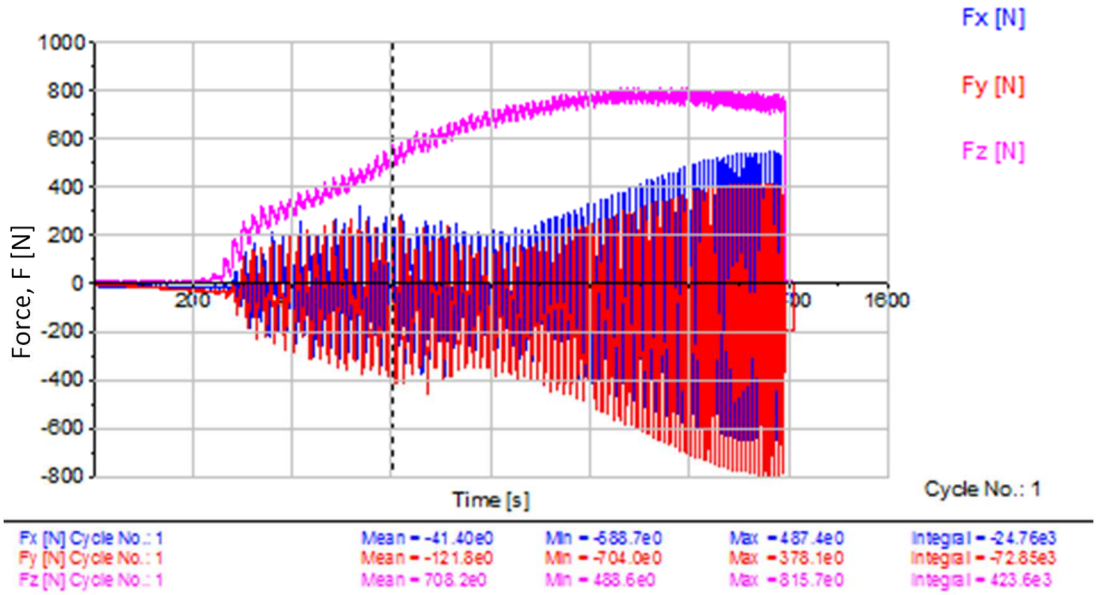

Figure 6-21: The profiles of measured force components F_X, F_Y and F_Z , showing their mean values. The test run number C27, settings: $t_0 = 1.0$ mm; $d_t = 6$mm, $f_t = 500\,mm/min$; Δz: 0.25mm ; $\omega_t = 750$rpm

It can be seen that F_Z has the larger value and is therefore more significant. To study the impact of different process settings on the mechanial loads in SPIF of CP Grade 2, the force data obtained for the conducted runs were taken (average of 500 readings) around the cycle time corresponding to $h_{ref} = 9$ mm. The data then were fed into the DesignExpert program for the subsequent analysis. Figure 6-22 views the scatter plot of the measured forces.

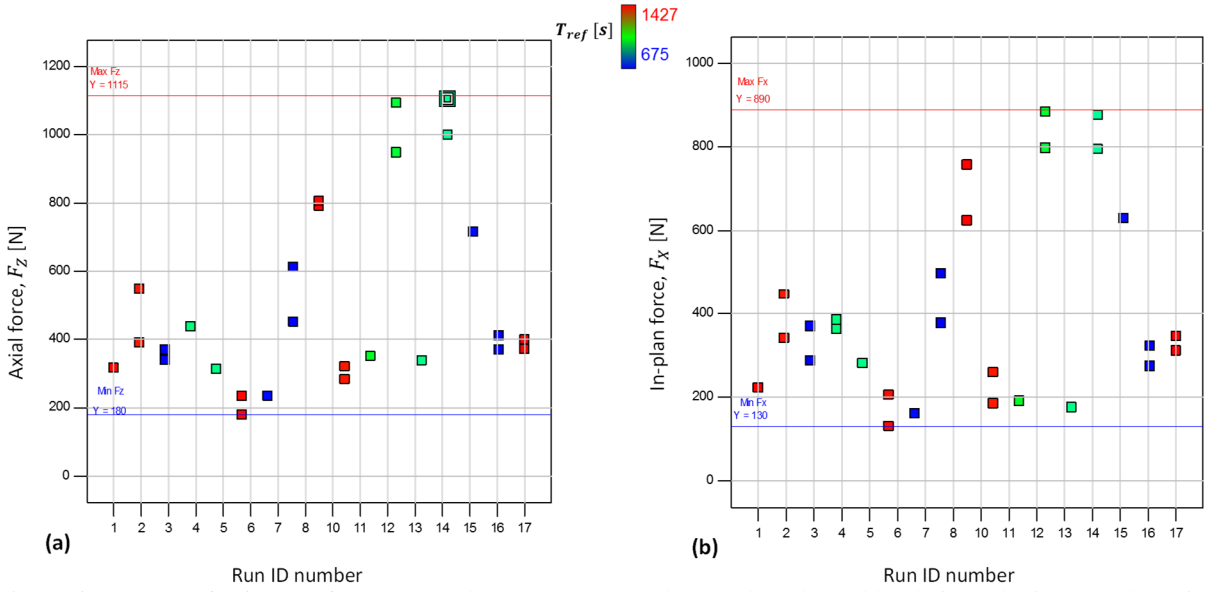

Figure 6-22: Data of reference force versus the test run ID number, scale-coloured by their cycle time: (a) the axial force, (b) the in-plane force

As shown in the scatter plots in Figure 6-22, both the F_Z and F_X readings show diverse values along the run ID on the horizontal axis, from a level of less than 200 N to a maximum force of about 1000 N. The vertical spread of the data between the runs with different ID numbers shows that the force is dependent on the chosen forming

conditions. In addition, the selected DoE can create changes in the response being studied. From the random vertical spread of the colours, over the range from blue to red, it can be seen that force rdata are independent of the cycle time. Some of higher forces are blue and correspond to short cycle times (675 s), while the opposite is true for some of lower force data which are red and have long cycle times (1427 s).

6.1.5.2 Modelling the force response

In the same manner followed in the preceding analyses of the formability and tempertures, multiple model selection methods and criterion were used to algorithmically select the 2FI mathematical model terms (shown in Table 6-8), which gave the best fit to the axial force response.

Table 6-8: The REML results of the axial force model

Fixed Effects [Type III]

Source	Term df	Error df	F	P-value prob. > F	
Whole-plot	1	7.81	19.92	0.0022	significant
a-Thickness	1	7.81	19.92	0.0022	
Subplot	6	11.17	321.99	< 0.0001	significant
B-Rotation	1	11.18	1131.48	< 0.0001	
C-Tool size	1	11.22	170.49	< 0.0001	
D-Feed rate	1	11.07	10.62	0.0076	
E-Step depth	1	11.31	8.96	0.0119	
aB	1	11.17	489.20	< 0.0001	
CE	1	11.33	29.36	0.0002	

Statistical analysis of the 2FI theoretical model for the response surface indicated that the model (whole-plot) is significant. The testing of the model fitness also revealed its reliability to represent the response. For the continuity of reading, the statistical diagnosing report of the model has been enclosed as Addendum C3. Table 6-9 shows the model equation in terms of coded and actual factors.

Table 6-9: Equations of the empirical model for axial force

Equation in terms of coded factors	Equation in terms of actual factors
$F_Z =$	$F_Z =$
+431.15	+41.96
+129.5 × a	+1385.86 × t_0
-180.3 × B	+0.19 × ω_t
+96.9 × C	-31.46 × d_t
+18.4 × D	+0.23 × f_t
-22.7 × E	-2548.74 × Δz
-130.7 × aB	-0.46 × $t_0 \times \omega_t$
+38.6 × CE	+212.87 × $d_t \times \Delta z$

6.1.5.3 Effect of the process factors on the forming force

As stated in 6.1.5, here a shortened form of the analysis of the force will be presented. The focus of this brief discussion is twofold:

Firstly, to present the data of the forming forces as recorded during the SPIF of CP Grade 2 as a function of the different settings of the five key process factors; secondly, to highlight the two significant interactive terms of the factors, namely thickness – rotation and step – tool-tip diameter on the reactional force generated. Recorded force data of all test runs conducted is outlined in Addendum E. The impact of the thermal loads on the forming forces response is however not studied in this section and will be discussed in Section 6.2.2.

i Thickness and tool rotation interactive effect

The significance of the interactive term (aB) originates from the fully opposing action of the two factors. Increased sheet thickness is strongly linked to higher forces to overcome increasing material strength, while rotation reduces sliding friction and heat softening of the workpiece material. This relationship is graphically presented in Figure 6-23 as a contour plot, and a 3D response surface.

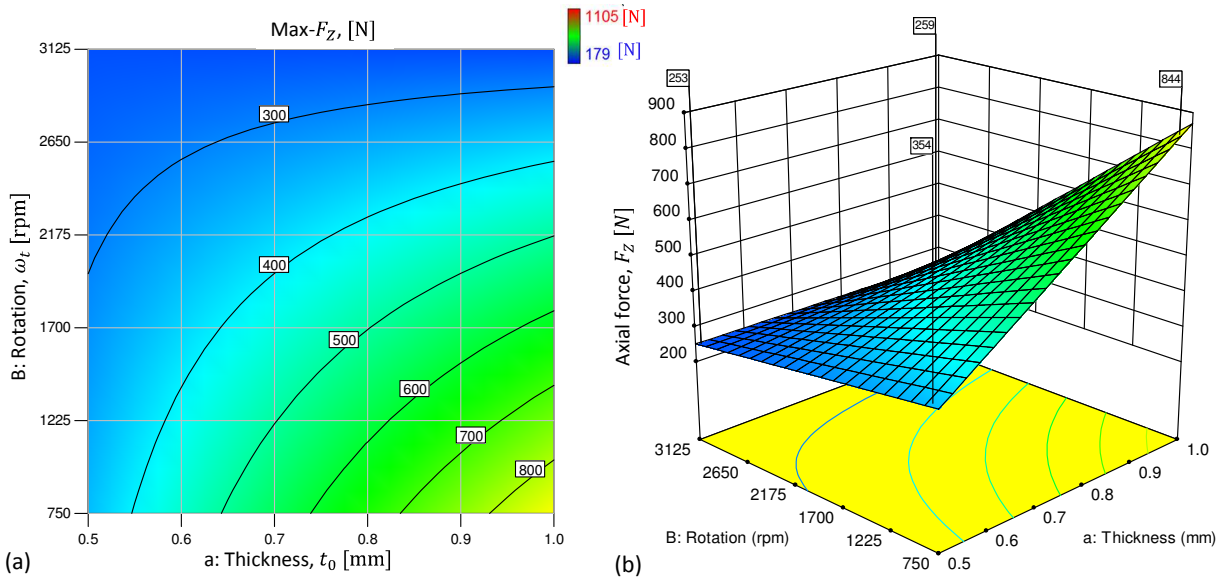

Figure 6-23: The interactive effect of the thickness and rotation on the axial force. (a) the contour plot; (b) the 3D response surface

As shown in the contour plot, starting at the lower left corner (a-, B-) Figure 6-23(a) and moving right, parallel to the thickness axis, F_Z constantly increases up to its maximum, which occurs at t_0 = 1 mm. The opposite is true when moving up from (a-, B-), parallel to the rotation axis; F_Z quickly approaches its minimum when ω_t surpasses 2000 rpm.

The four-flagged corners of the 3D surfaces (Figure 6-23(b)) highlight the surface peak values at every pair of the settings as predicted by the response model. At low rotation, enlarging the thickness escalates the axial force by about 140%.

At high rotation, the speed factor is dominant, and doubling the thickness has almost no effect on the force (0.4%), which diminishes slightly. The drop in the axial force due to high rotation is more obvious when forming the thicker plates than that expected when forming thinner plates, where the already low F_Z values decreases only by about 30%.

Finally, forming thicker sheets can bring serious load challenges to the applied tool and to the CNC machine. Higher tool rotation, more than any other SPIF factors can effectively bring down the level of these forces; this is further reasoned in Section 6.2.2.

ii Effect of the tool-tip and step depth interaction

As shown in Figure 6-24(a), the factors (CE) again plot as crossing lines over the investigated span. This is always important in the DoE for predicting the response change. At both step depths, the axial force significantly increases with increasng the tool-tip diameter.

Changes in F_Z can be ntoticed on either side of the interaction point. The 3D surface in Figure 6-24(b) highlights this non-linear relationship, particulrlly for the smaller d_t, while no signifcant differences predicted when using a larger tool-tip.

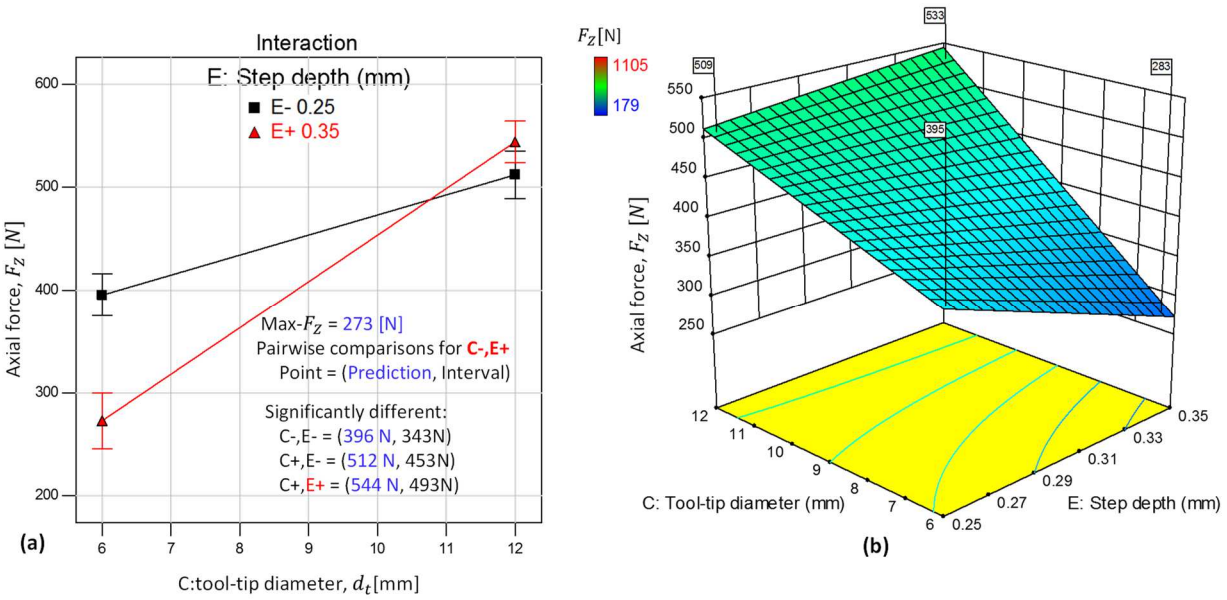

Figure 6-24: The interactive effect of tool and step on the axial force: (a) a pairwise comparison for the (C-, E+) point; (b) a scale coloured 3D plot of the interaction

The impact of d_t is secondary to the effect of t_0 in increasing the axial force. F_Z varies as follows:

at: $\Delta z = 0.35$ mm, changing d_t (from 6 to 12 mm), the F_z increases by about 90%

at: $\Delta z = 0.25$ mm, changing d_t (from 6 to 12 mm) the F_z rises by less than 30%

The impact of the large Δz and a small tool-tip on reducing F_Z is, however, difficult to determine, and can not be sperated from the maximum thermal influance found for the CE interaction as shown in Section 6.1.4.2.

iii Effect of the feed rate

It is well established in state-of-the-art SPIF that tool feed rate has a less important influence on the process mechanism. This was also confirmed in the preceding sections on formability and temperture analyses. The same lower effect of f_t on F_Z can be seen in Figure 6-25, wherein stepping the feed rate from 500 to 750 mm/min raises the F_Z by less than 9%.

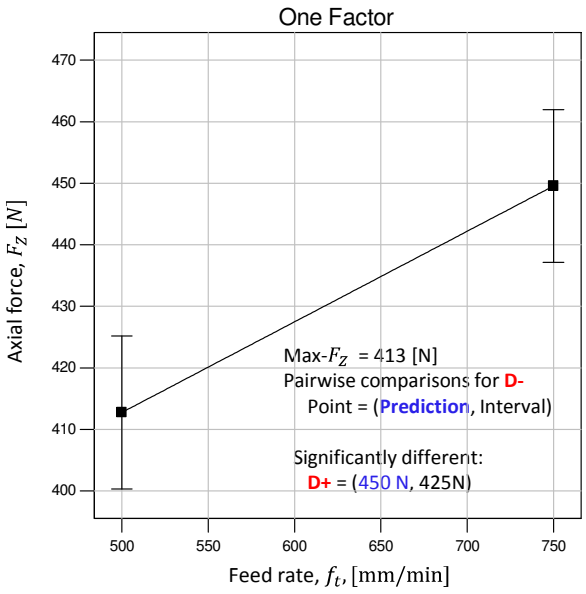

Figure 6-25: Minor impact of the feed rate on the axial force

The minor influence of tool feed rate on the outputs is aknowledged as a means of increasing SPIF productivity by reducing the cycle time (Section 6.1.7).

6.1.6 Analysis of the in-plane forces

The response of the in-plane forces (F_x *and* F_y) showed typical behaviour in line with the previously discussed axial force response, but at a slightly smaller magnitude. In order to save more space for other more pertinent analyses in this work, the in-plane analysis will not be presented.

6.1.7 Analysis of the cycle time

For the same design produced, it is obvious that there are only three of the tested factors that can influence the production cycle time. They are the feed rate, step depth and tool-tip diameter. The reference cycle time (t_{ref}) as the response data was interred into the DesignExpert program, from which a reduced mathematical model has derived. The statistical diagnosing report of the model has been enclosed as Addendum C4.

The scatter of the plot of t_{ref} shown in Figure 6-26, compares the importance of the process setting on the cycle time. The data of the cycle time on the figure is coloured-scaled by the corresponding maximum angle obtained to each run ID. At some settings, such as ID15 has a short t_{ref} (683 s) combined with a very high θ_{max} (74˚). Concerning process productivity, such combination will always be preferred in manufacturing.

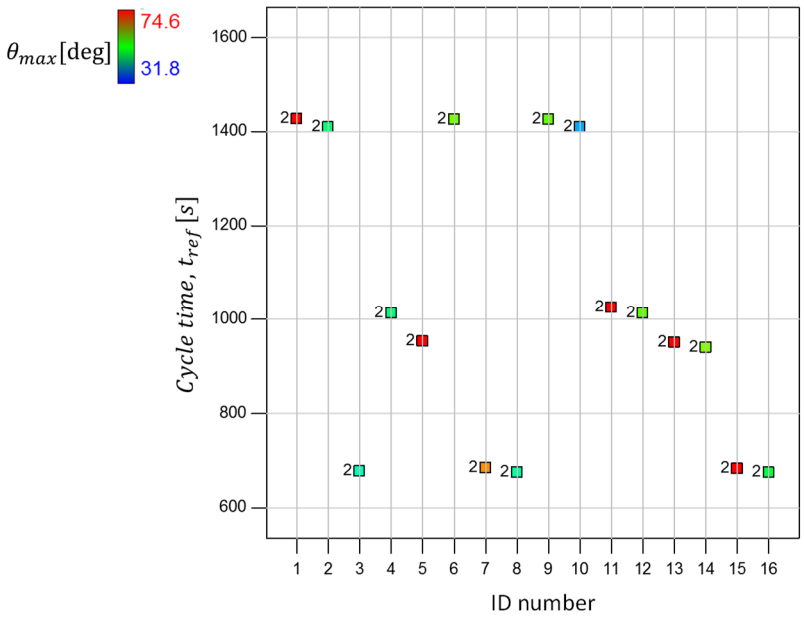

Figure 6-26: Test reference time verses run ID numbers, colour-scaled with the forming angle obtained. The digits (2) showing the replicates

As can be noticed from the F-value in Table 6-10, the feed rate has the most significant effect, followed by the step depth term, with the effect of the tool-tip diameter on the t_{ref} being far less pronounced.

Table 6-10: The REML results of the selected model of the cycle time

Fixed Effects [Type III]

Source	Term df	Error df	F	P-value prob. > F	
subplot	5	26.00	2.838E+005	< 0.0001	significant
C-Tool size	1	26.00	556.41	< 0.0001	
D-Feed rate	1	26.00	6.245E+005	< 0.0001	
E-Step depth	1	26.00	3.936E+005	< 0.0001	
CE	1	26.00	27.23	< 0.0001	
DE	1	26.00	17130.76	< 0.0001	

The rounded equation of this model in terms of coded and actual factors is listed in Table 6-11.

Table 6-11: Equations of the empirical model for cycle time

Equation in terms of coded factors		Equation in terms of actual factors	
t_{ref} =		t_{ref} =	
+1015.64		+4077.32	
-6.05	× C	-4.70	× d_t
-202.80	× D	-3.23	× f_t
-166.29	× E	-6765.00	× Δz
+1.34	× CE	+8.93	× d_t × Δz
+33.59	× DE	+5.37	× f_t × Δz

The 3D plots of the two pairs of the interctive terms (CE, DE) are shown side-by-side in Figure 6-27. In the Figure 6-27(a) it is the step depth factor in CE that creates the significant impact on t_{ref}, as can easily be read from the flagged points on both sides of the E-axis. Increasing the step depth by 40% (from 0.25 mm to 0.35 mm), reduces t_{ref} by 27%.

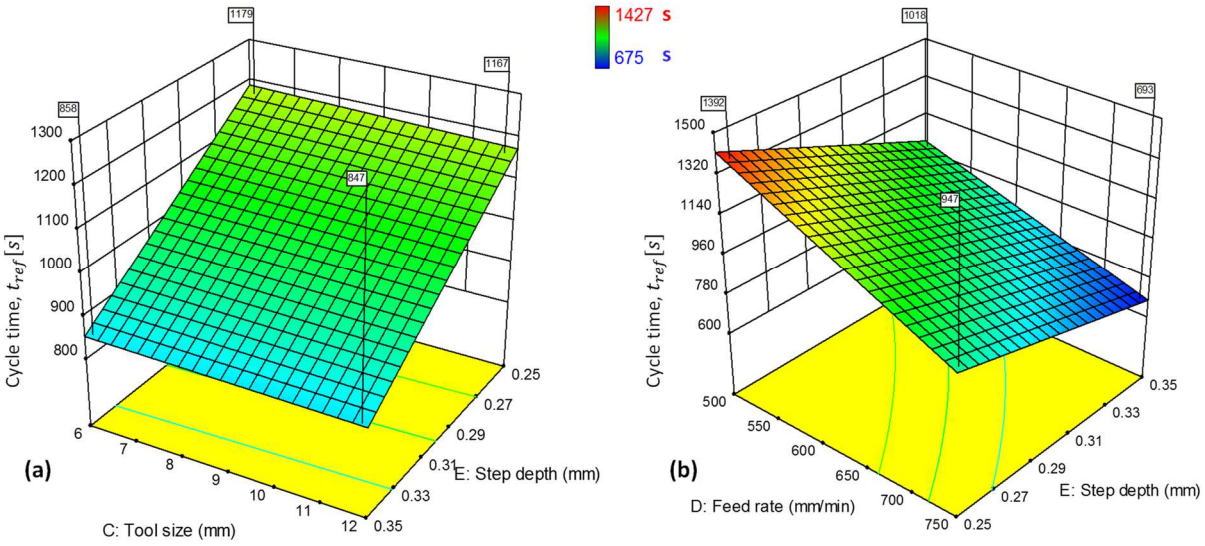

Figure 6-27: Interactive effect of the SPIF factors on the cycle time: (a) the effect of the step depth – tool-tip; (b) the effect feed rate—step depth

When increasing the tool-tip diameter by 100%, a non-significant 1% drop in t_{ref} is obtained. It should also be noted that the minimal features of the components to be made arise from the geometrical constriants imposed by the selection the tool-tip diameter. Thus variations of the tool-tip size is not an option for improving SPIF productivity.

Finally, the feed rate and step depth are the significant terms in the cycle time model, as highlighted in the colour-scaled plot in Figure 6-27(b). there is a significant time variation on the four sides of the response surface as indicated by the flags. Even between the chosen low settings in the DoE, swiching the feed from D- to D+ reduces t_{ref} by 33%, and changing the step depth from E- to E+ reduces t_{ref} by 26%.

6.1.8 Summary of the DoE analysis

At this point, the core discussion of the DoE on the SPIF key factors has been accomplished, including planning the experiment, analysing the response data with main effect and interaction plots. Following conclusions can be drawn:

- Designing experiments statistically is a more efficient approach when studying several factors simultaneously, and additionally useful information on each factor and its interaction is obtained. The approach also requires fewer time and material resources, when considering the amount of information gathered.

- Results from the formability analysis showed that tool-tip diameter is the most influential process variable that inversely affects the forming angle obtained, while the angle will increase with increasing blank thickness and an increase in the size of the step depth. Tool feed showed minor effects.

- Regarding the thermal effect, tool rotation speed is the dominant variable for increasing the forming temperature, followed by blank thickness, while tool-tip and feed rate both revealed a minor impact. However, the impact of the interactive effect of the step and tool-tip diameter on temperature is more complex and depends on the ratio between the two factors.

- Forming temperature is directly proportional to the relative forming speed calculated at the references time as shown Figure 6-28.

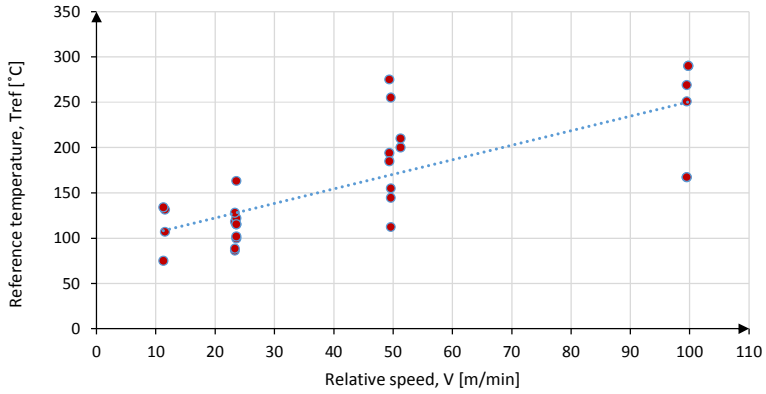

Figure 6-28: Relationship between relative velocity and forming temperature obtained at the reference (9 mm) depth of forming

- The axial forming force is more related to the blank thickness and tool-tip diameter. It significantly reduces with increased tool rotation and it is not affected by the feed rate. The large step depth increases the axial force.

- Regarding the productivity, it is the feed rate followed by the step depth factors, which play the major role on reducing the cycle time. A minor gain in productivity is obtained by increasing the tool-tip diameter.

6.2 The OFAT test

As referred to at several places in the preceding discussion of the DoE, there were quite a few points where the relationship between the tested variables and response was not clearly understood. Examples of such uncertain relationships are the non-significant or even a negative correlation between material formability and the tool rotational speed, the increased formability at larger step depth, as well as the doubtful thermal effect at larger step depths.

These uncertainties could not be fully answered through the analyses of the response models produced in the DoE. Significant interactive effects of factor pairs give a better understanding of the whole process, but due to the leaner character of the factorial designs (only the upper and lower level), they could not efficiently predict the curvature along the response space. Although the DoE can be used to check for curvature in the response, one advantage of the OFAT experiment over the DoE is, that it can be used to estimate curvature of the factors, namely curvature in the response along the factor space (Czitrom, 1999).

In this section, an overview of the OFAT experimental tests of the tool-kinematics over an expanded range (outside the anticipated optimal range) is presented, with the purpose of verifying the conclusions drawn and assessing the potential of process enhancing window. The presentation of the analysis and discussion of the results in the subsequent sections, are structured as illustated in Figure 6-29.

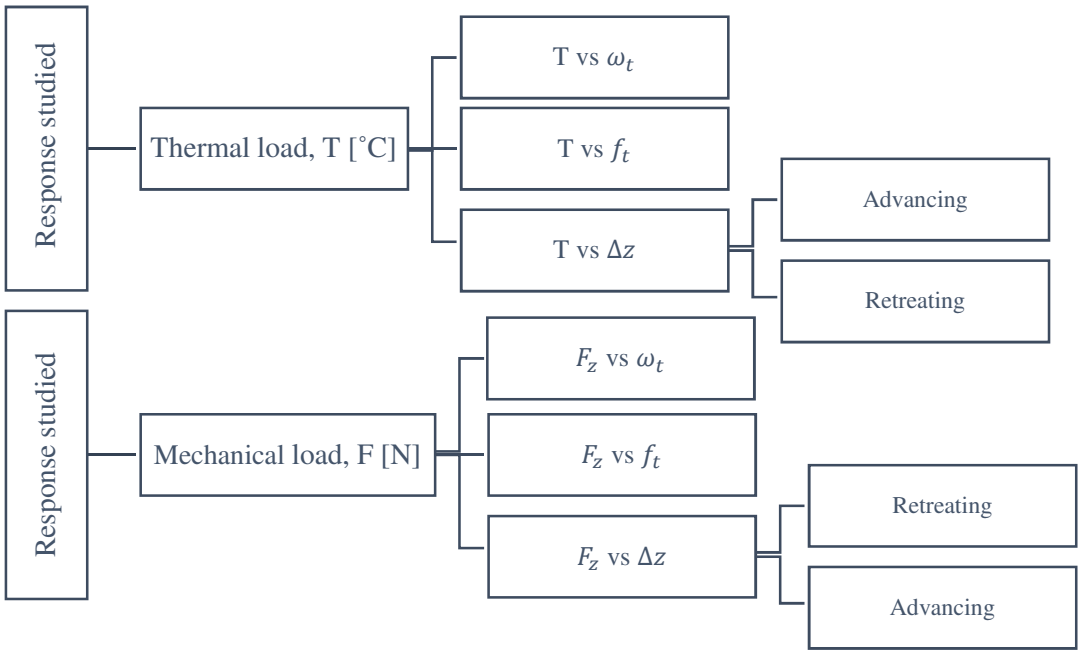

Figure 6-29: A schematic roadmap of the OFAT discussion section

6.2.1 Test layout and results

As illustrated in Figure 6-29, an OFAT experimental study was performed to establish more sophisticated data on the influences of the tool relative velocity on the thermo-mechanical demands in the SPIF of CP Grade 2 sheets (Uheida, Oosthuizen and Dimitrov, 2017). The effect of forming in advancing and retreating directions has also been investigated over different sizes of step depth. The knowledge from this extended-range test is an essential in constructing the horizontal axis and highlighting the boundaries of the processing window. In Table 6-12, a summary of the setting of the variables, as well as the obtained response data from the three types of experiment, is presented.

References point at 600 s of test cycling time was chosen to compare the results of measured temperatures (T_{600}) between the runs in the OFAT test. But measurements of the forming forces at the reference (600 s) time both in axial and in plane directions were found comparable to the maximum forming forces during the test, and therefore only the maximum values of the forces were studied and reported.

Table 6-12: Layout of the OFAT experiments and obtained responses

		Process variables					Response measured					
	Run	Sheet	Feed	Tool	Step	Speed	Temperature		Force		Formability	
	No	t_0	f_t	d_t	Δz	ω_t	T_{max}	T_{600s}	F_z	F_x	Depth	Angle
		mm	mm/min	mm	mm	rpm	℃	℃	N	N	mm	deg
Rotation	C39	0.8	625	10	0.30	**450**	90	42	603	600	18.5	63
	C40	0.8	625	10	0.30	**900**	116	49	560	500	17.8	62
	C41	0.8	625	10	0.30	**1500**	151	67	508	420	16.2	59
	C42	0.8	625	10	0.30	**2500**	177	84	483	380	14.9	57
	C43	0.8	625	10	0.30	**4000**	372	183	226	250	16.4	59
	C44	0.8	625	10	0.30	**5500**	334	245	124	170	7.9	44
	C45	0.8	625	10	0.30	**7500**	342	342	94	94	6.8	42
	C46	0.8	625	10	0.30	**15000**	----	296	53	63	1.7	33
Retreating	C47	0.8	625	10	**0.35**	1940	188		444	400	19.0	64.
	C48	0.8	625	10	**0.50**	1940	225		475	500	20.5	67
	C49	0.8	625	10	**0.65**	1940	230		589	600	19.1	64
	C50	0.8	625	10	**0.80**	1940	240		601	605	20.3	66
Feed rate	C51	0.8	**1200**	10	0.30	1940	195		544	410	14.9	56
	C52	0.8	**2000**	10	0.30	1940	242		526	400	14.7	56
	C53	0.8	**4000**	10	0.30	1940	181		546	500	15.1	57
	C54	0.8	**10000**	10	0.30	1940	186		594	550	15.7	58
Advancing	C55	0.8	625	10	**0.35**	1940	235		414	300	25	75
	C56	0.8	625	10	**0.50**	1940	263		388	250	25	75
	C57	0.8	625	10	**0.65**	1940	342		328	270	24	75
	C58	0.8	625	10	**0.80**	1940	355		286	300	25	75

6.2.2 The spindle rotation test

The tool rotational rate ranged from 450 rpm to 15 000 rpm, while all the other process settings were kept at their reference values, as shown in Table 6-12. The profiles of the measured temperatures versus forming time are illustrated in Figure 6-30.

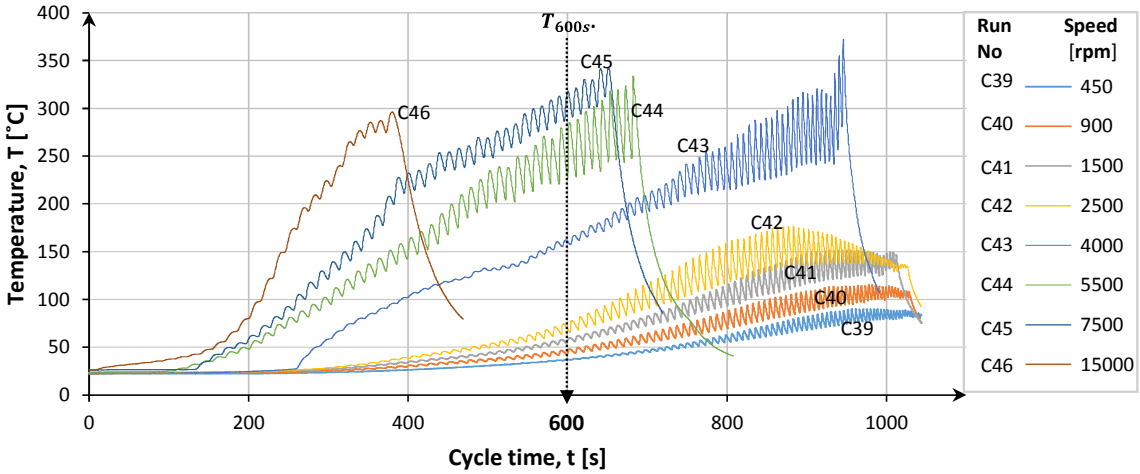

Figure 6-30: Temperature gradients at different rotational speeds

To obtain a sensible comparison between the eight runs, a reference temperature reading was taken for each run at the same cycle time of 600 s, being a common point (except for C46) for the temperature profiles. As can be seen in Figure 6-30 at the reference point (vertical dotted line in Figure 6-30), the temperature profiles are directly related to the spindle speeds. Following the order of run numbers, higher temperatures correspond to higher speeds.

It should be noted that the applied settings of the test variables have no effect on the processing time. The differences in the cycle times of the tests as seen in Figure 6-30 indicate that runs were curtailed at differing times because failure conditions occurred. These failures were mainly due to extreme heating, which required termination of the tests concerned.

The runs with relatively low speeds (C39 – C42) continued to a cycle time of about 1000 seconds before termination due to the occurrence of sheet fracture. By contrast, the second group, which was formed at higher tool rotations (C43 – C46), had noticeably shorter cycle times. With all the other process settings kept constant, the shorter the cycle time, the less the forming angle (dependent on the depth) will be. Therefore, the ability to shape a CP Grade 2 sheet is decreased at very high tool rotations (above 2500 rpm).

Note that this finding related to rotation speed is only applicable to the range of parameters used and subject to the selected process settings. The finding is in contrast to that of some references (Buffa, Campanella and Fratini, 2013; Xu *et al.*, 2013; Khalatbari *et al.*, 2015), which reported that the formability of aluminum sheets was improved with higher tool rotation.

Figure 6-31 depicts the eight formed components. The dashed arrows show the sequence of the runs, so that they can easily be matched with their settings in Table 6-12 and their temperature profiles in Figure 6-30. On the inside of the components (Figure 6-31(a)), an improvement of surface quality in terms of a reduced waviness effect in direction of tool feed was observed at increased speeds.

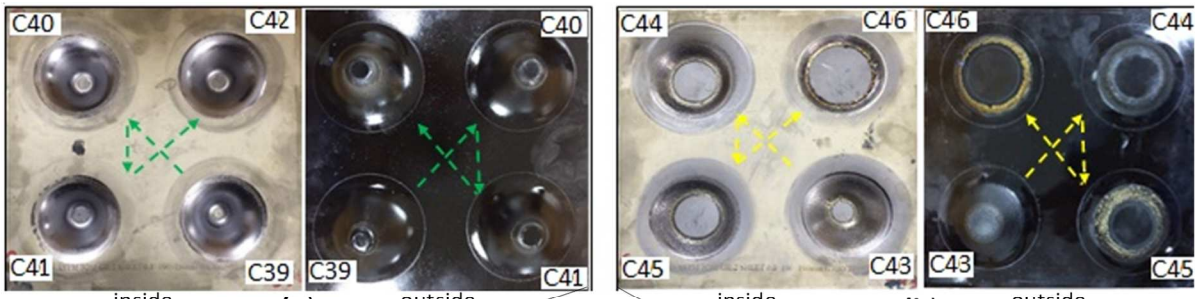

C39	C40	C41	C42	Run number	C43	C44	C45	C46
450	*900*	*1500*	2500	Tool rotation, ω_t [rpm]	4000	5500	7500	15 000
42	49	67	84	Temperature, T_{600s} [°C]	183	245	342	296
63	*62*	*59*	57	Forming angle, θ_{max} [deg]	59	44	42	33

Figure 6-31: Depiction of titanium samples formed in the rpm test (note that inside and outside views are mirror images): (a) large formed depth at relatively low rpm; (b) rise of thermal defects and failure with increased rpm

On the external surface, though, following the direction of the arrow, there is slight decrease in quality manifested by a defect known in sheet forming as the orange peel (OP) phenomena. This is mainly apparent on the last two runs (C41 and C42).Regarding the second test run depicted in Figure 6-31(b), it is evident that there are speed effects on both surfaces of the produced components. In this test, even at 4000 rpm, a rough surface occurred on the inner side due to the removal of titanium material, while on the outer surface a coarse OP effect developed. Also, following the same order as indicated by the arrows in the second test, there is obvious deterioration of the inner surfaces, together with evidence of material removal which increased at higher tool rotations. Of more concern was the reduction of the forming depth obtained at higher speeds; these test runs were stopped early because of the manifestation of overheating conditions. The increased temperature caused glowing of the forming tool, and sparking of titanium particles at the tool-tip/sheet interface. Figure 6:32 highlights the relationship between the forming forces and the forming temperature.

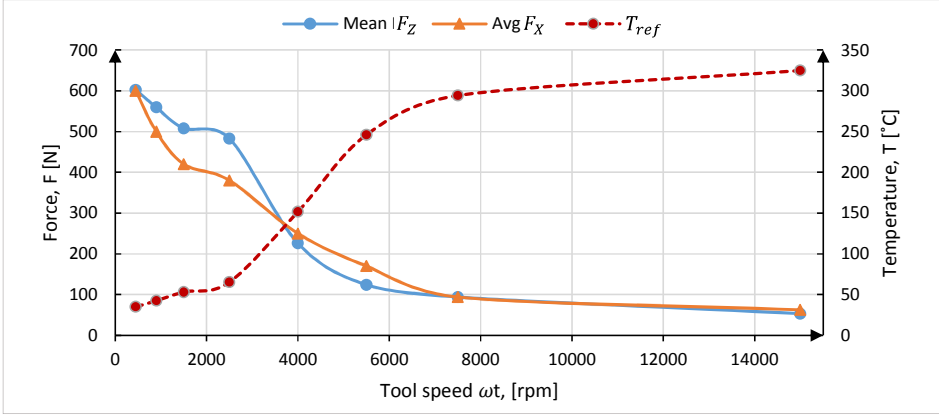

Figure 6-32: The relationships between tool rotation and thermomechanical loads in SPIF. Note that temperature data obtained at 360 s from the initiation of forming.

As shown in Figure 6-32, inverse relationship between components of forming force (F_z and F_X) and the forming temperature (T_{360}) obtained at different tool rotational speeds. Both the axial force, F_Z and the in-plane force, F_X decreased with an increase in tool rotation.

In the first two runs with lower tool rotations, the drop in the forces is attributed to the decreased sliding friction, and not to softening of the titanium material, because the actual temperature (not the shown T_{ref}) during the test did not exceed 120℃.

As the rotational speed of tool was stepped up, forces were determined by the combined effect of the reduced friction and the evolving heat. The heat effect was dominant for the last four runs with higher rotation, contributing to the softening of the titanium workpiece and the substantially reduced force. In the last four treatments, measured temperatures surpassed 330℃. This is in agreement with the previous finding earlier, shown in Figure 6-14 and obtained from the DoE, namely the strong effect of high tool rotation (3125 rpm) on reducing the forming force.

6.2.3 The feed rate test

In this test, the tool feed speed was experimentally examined over a wide range, starting at a low speed of 1200 mm/min, which was increased up to 10000 mm/min, while keeping the other process variables at their reference values as listed in Table 6-12. The lower limit was chosen, based on the experience accumulated from previously designed experiments (see Section 6.1) using relatively low feed rates (500, 625 and 750 mm/min), whereby no significant effects of the feed rate were observed. The upper limit, however, was selected on the premise of the maximum feasible traverse speed that the machine can develop. Figure 6-33 is a graphical representation of the measured temperature during the feed speed test.

From the temperature profiles in Figure 6-33, and considering the investigated range of SPIF variables, it can be stated that variation in the tool feed rate has a marginal impact on heat generated at the forming zone.

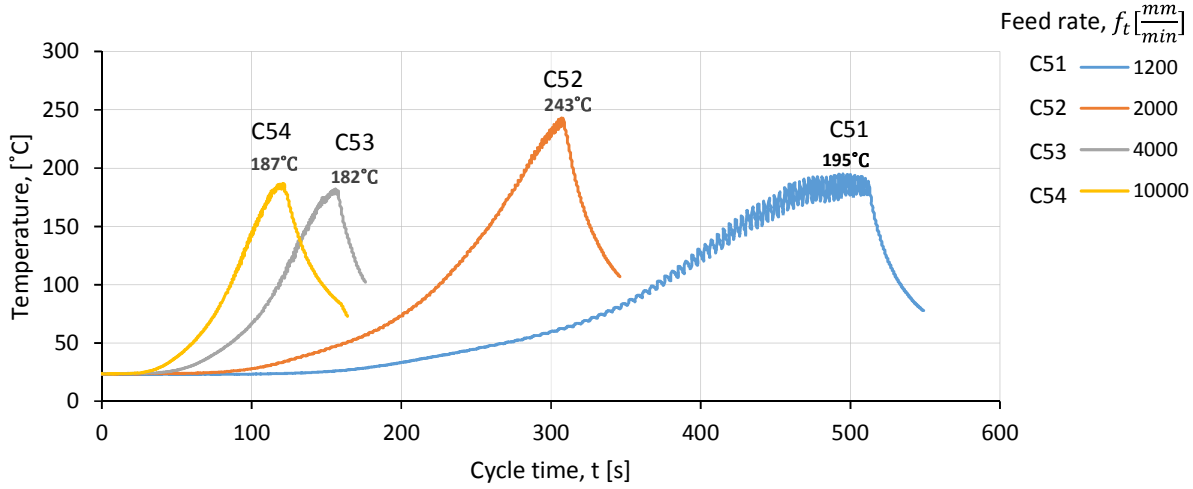

Figure 6-33: The thermal load profiles at different feed rate versus cycle time

The important role of the feed speed on SPIF productivity can be observed from the x-axis of the graph in Figure 6-33. As the feed rate was stepped up from 1200 to 4000 mm/min, the cycle time was reduced from 530 to 140 seconds, where the processing time of the same profiles in the rotation test (feed rate is 625 mm/min) was about 1000 seconds.

It should be noted in Figure 6-33 that for the last two runs (4000, 10000 mm/min) the resulting profiles are similar. In fact, for the 10000 mm/min feed rate, the gantry type CNC machine used could not accelerate over the short contours of the small component used as a test model. As indicated by the graph of feed rate versus cycle time (Figure 6-34), the slope of cycle time become flatter after a certain feed rate. During the test, the actual feed rate fluctuated and was about 5500 mm/min. This implies a serious constraint on the idea of increasing the productivity of the SPIF based on high feed rates, as reported in various publications (Hamilton and Jeswiet, 2010; Ambrogio *et al.*, 2013; Khalatbari *et al.*, 2015). This applies particularly to CNC milling machines, especially when geometries with complex tool paths are to be produced.

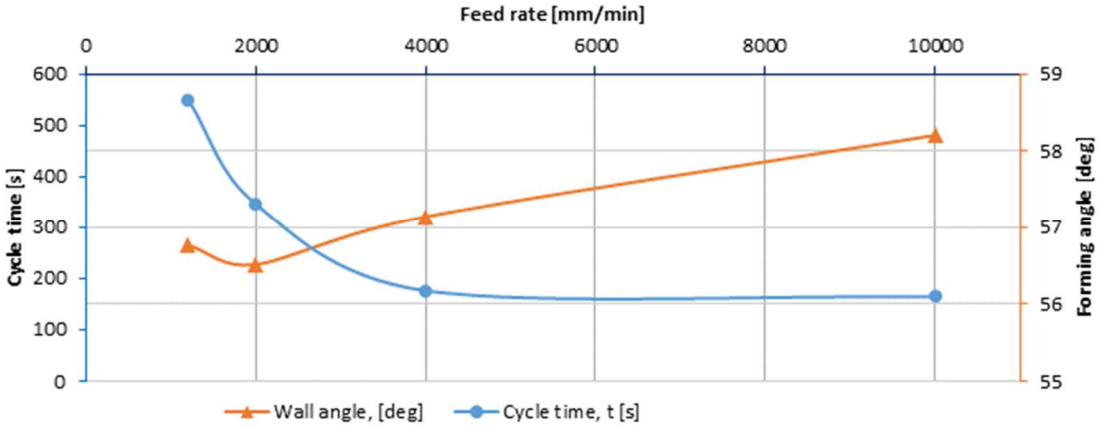

Figure 6-34: The effect of the feed rate on the forming angle and cycle time

Consistent with cited references (Otsu, Katayama, *et al.*, 2014; Khalatbari *et al.*, 2015), the test results shown in Figure 6:34 revealed no significant change due to the feed rate in the formability of the CP Grade 2 between the four formed components (maximum wall angle was 57˚ ± 1˚). However, this angle remains far below the formability angle (65˚) that was obtained in another experiment at the same settings, but with a reduced feed rate of 625 mm/min.

Large feed rates slightly increase the forces, in particular the in-plane component, as shown in Figure 6-35. There is a minor reduction in the temperature at large feed rates. This can be linked to a diminished opportunity for the localised heat build-up in the material at high feed speeds, as the heat source (tool) rolls faster over the workspace surface and more heat is dissipated than accumulated in a specific zone. The exception was found in the run with a feed of 2000 mm/min, in which a temperature of 243℃ occurred; interaction between this feed level and the applied tool rotation is suspected for the increase in temperature. In line with data obtained from a relative speed test in Section 6.2.4, further study of this phenomenon is envisaged.

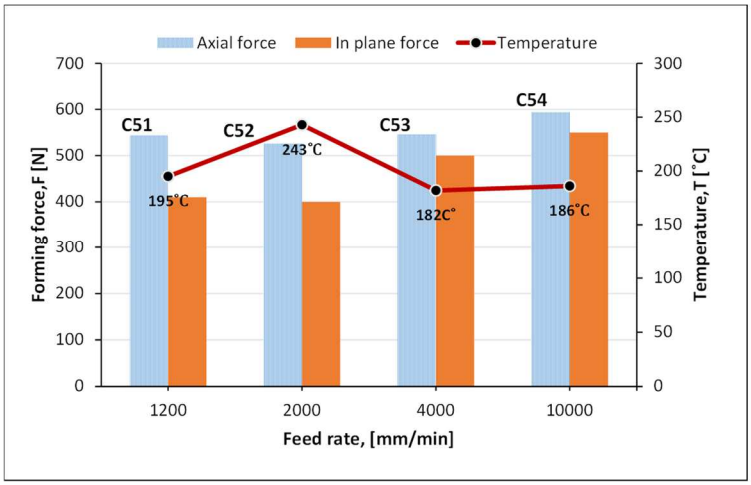

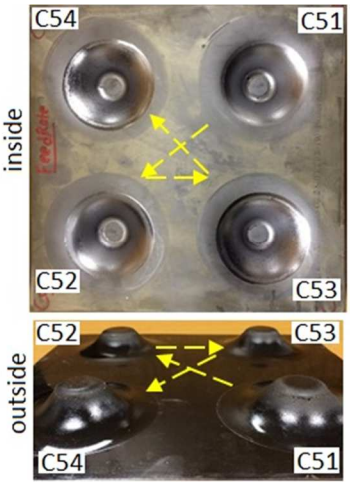

Figure 6-35: The influences of the feed speed in SPIF: (left) on the process demands; (right) on the obtained titanium components

6.2.4 The strategy test

The experimental work previously discussed was performed using a 'conventional' milling method, that is, the tool was rotating clockwise, while the feed rotation was anticlockwise. In this test, the focus was on the relative speed (V, m/min). To understand the effect of changing the relative speed at sheet/tool interface on the formability and thermomechanical demands. The relative speed at the interface, both in advancing and retreating (V_a , V_r) directions are given by Eq. 4-6. In the retreating (conventional) direction, the feed is subtracted; reducing the relative speed, while in the advancing direction (climb) f_t is added, making the relative velocity larger.

$$V = 2\pi \cdot \omega_t \cdot r_t \cdot \sin\theta \pm f_t \tag{4-6}$$

where $(r_t \cdot \sin\theta)$ is the effective tool-tip radius.

In this study, the tool rotation direction used was fixed in the clockwise direction and the switching of the rotation direction during forming was made by changing the tool path direction in a similar way as described by Otsu et al. (2014). Different load conditions were tested by altering the tool step depth on each test run from 0.35–0.8 mm at a constant ratio of 0.15 mm, along with the increase in the wall angle of the VWACF being formed. The settings of eight test treatments (four in each strategy) and the data resulted are listed in Table 6-12, with the pictures of the produces samples shown in Figure 6-36.

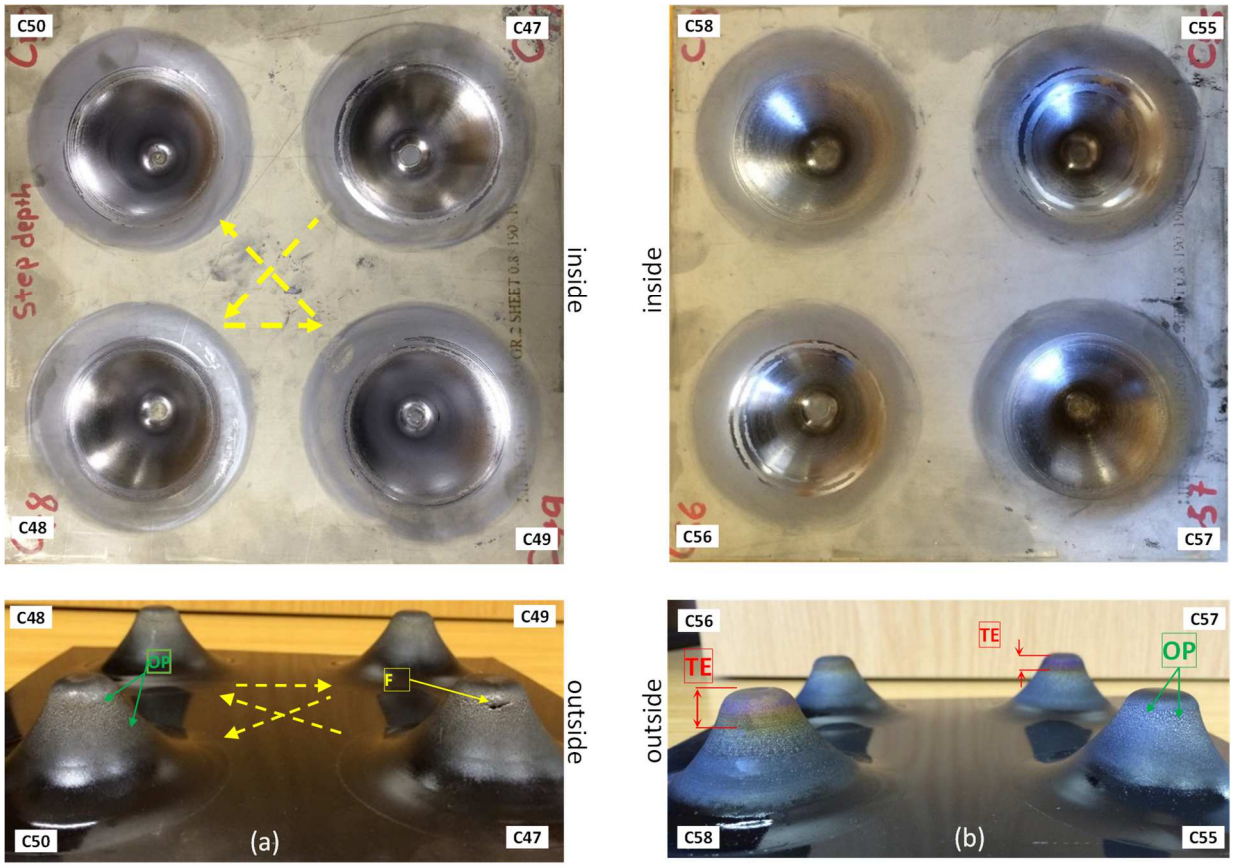

Figure 6-36: Depictions of the samples formed in the strategy test :(a) in the retreating direction; (b) in the advancing direction

As far as the quality of produced surface is concerned, in the first test group (Figure 6-36(a)) formed by retreating direction, the inside of the samples displayed a good surface quality with low roughness; the roughness did increase slightly between these samples as the applied Δz was increased in accordance with the ascending sequence of test run numbers. On the outside of these samples an OP surface defect appeared, showing the same increasing trend relative to the increasing size of the step depth.

The samples formed by the advancing method (Figure 6-36(b)) however, showed a higher roughness even at the lower $\Delta z = 0.35$ mm. On the outside of these samples, thermal effects (TE) appeared in form of burn marks and a change in the colour of the titanium sheet. This TE is more obvious close to the bottom of the sample, and not apparent at the opening; this is because the diameter of the model sample decreases with the depth, and therefore the heat source sweeps the surface more often because of shorter cycles. The height of TE differs between the samples and rises in relation to step depth. This can be further clarified looking at the profiles of the temperature data shown in Figure 6-37.

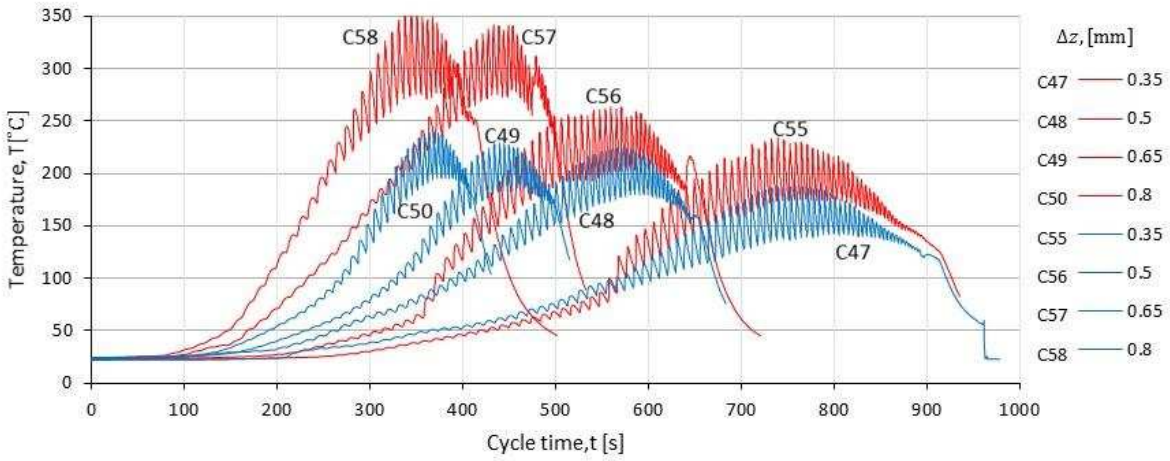

Figure 6-37: Temperature gradient at different step depth. Note the colour code: the blue is in the retreating, the red is in advancing direction.

It should be noticed that for each test, all the setting affecting the relative speed were held constant, except the direction and the step size, which was increased. As shown in the above diagram, the temperatures develop in a direct proportion to the step size and in an analogous way in the both methods.

Comparing any pair of runs with the same Δz form the two strategies (blue for retreating and red for advancing), there is always a considerable rise in the temperature (ΔT) in the samples formed by the advancing method, particularly at large Δz. This rise is shown as a percentage between each pair of the runs from both methods in Table 6-13.

Table 6-13: Effect of forming strategy on temperature rise in the advancing comparing to the retreating

Run	C47–C55	C48–C56	C49–C57	C50–C58
Δz [mm]	0.35	0.5	0.65	0.8
ΔT [%]	25%	17%	49%	48%

More notable result is the variation of the forming angle of CP Grade 2 between the two methods. Figure 6-38 illustrates the maximum forming depth obtained in each strategy, before fracture of the sample material occurred. As shown in the figure, in the retreating test the values of θ_{max} are above 64° and have a maximum of 67° at $\Delta z = 0.5$ mm.

On the other hand, in the advacncing test, none of the spacemns was fractured and the forming contiued to the maximum design depth of 25 mm, corrosponding to $\theta_{max} = 75°$. To the best of the knowledge, this high wall angle signifies a considerable enhancement in the formability of the 0.8 mm titanium sheets, which has not been reported in the SPIF literature consulted, not even for higher thicknesses.

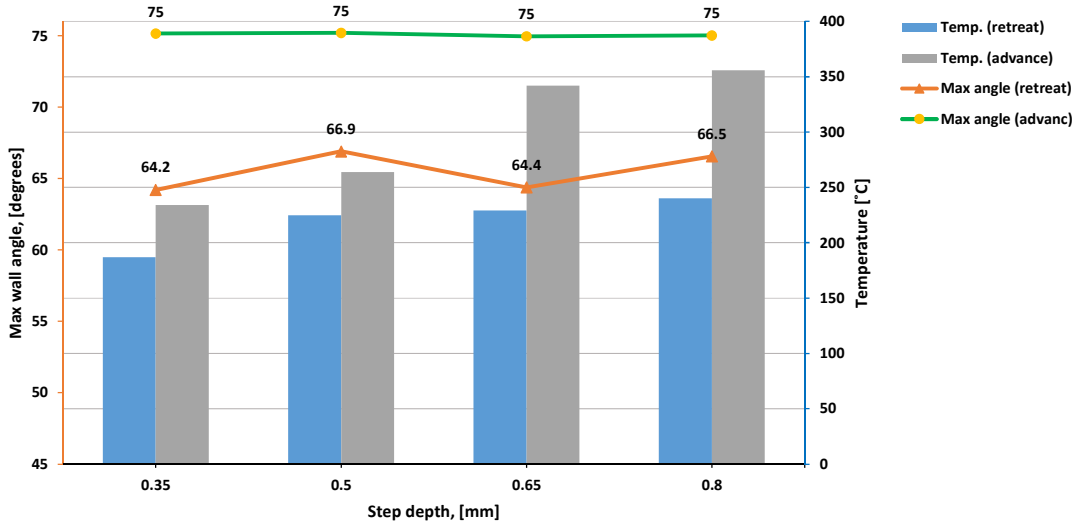

Figure 6-38: The effect of tool rotation direction; on the forming forces and temperatures

The variation in the relative speed between the two tests was firstly suspected to be a reason for the temperature variation and the enhanced formability of titanium. Using Equation 6-1 for the both methods, the retreating and advancing speeds were calculated. For both advancing and retreating, the relative speeds calculated were plotted against the corresponding forming angle (Figure 6-39).

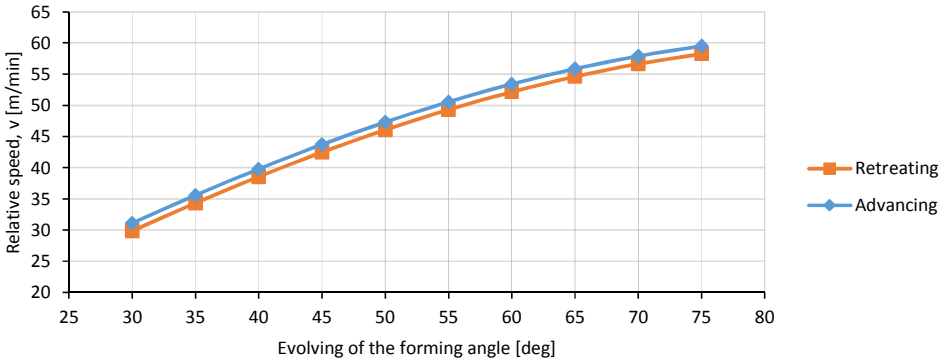

Figure 6-39: Relative velocity calculated as function of the forming angle in both the advancing and retreating direction

As can be seen from the plot Figure 6-39, for the two curves, the calculted relative velocity V is in direct proportion to the forming angle, and it is higher in the case of the advancing direction. The two relative speeds plot a comparable curves, and the difference in magnitude of the speed is always constant and equals twice the feed rate (1.25 m/min) used. This narrow gap between retreating and advancing resulted from the large effect of the tool rotation ($\omega_t = 1940$ rpm) on the positive term of Equation 6-1, in comparison to the effect tcaused by he small feed of 625 mm/min. The significant increase in the temperature and titanium formability could not only be explained by the effect of the minor increase in V. Thus it represents a worthwhile topic for future studies.

6.3 Correlation of the compiled data

The variation of some process factors (f_t and Δz) about their set point were intentionally tightly controlled during the DoE test. Therefore, conclusions drawn from their correlation to the response, needed to be established over their widely applicable ranges. DesignExpert software offers an historical design interface that allows for the evaluation of any historical data gathered without a designed experiment. Hence, the data compiled from both the DoE and OFAT campaigns were imported into this software to build an augmented design that holds the entire data set obtained from 54 runs. The intention was to gain a broader insight into the spectrum of the cause and effects of the SPIF factors over the wider space tested, and verify the trends of the responses previously attained. In a similar way to the step presented in Section 6.1.2, a preliminary analysis of cause and effect was established by constructing a correlation matrix of the applied parameters and the outcomes. Table 6-14 illustrates the colour-coded correlation matrix of the SPIF factors, generated in DesignExpert.

Table 6-14: General correlation matrix of the SPIF key factors

	a:	B:	C:	D:	E:	F:	T:	F_z:	F_x:	θ_{max}:	Ref. t:	Est-t:
	mm	rpm	mm	$\frac{mm}{min}$	mm	$\frac{m}{min}$	°C	N	N	deg	s	s
a:sheet	1.000											
B:rotation		1.000										
C:tool-tip			1.000									
D:feed rate				1.000								
E:Step depth					1.000							
F:Relative velocity						1.000						
Temperature	0.332	0.691	0.052	0.040	0.457	0.687	1.000					
Axial force	0.475	-0.677	0.254	0.140	0.037	-0.596		1.000				
In-plane force	0.376	-0.520	0.293	0.158	0.042	-0.417			1.000			
Wall angle	0.069	-0.305	-0.399	0.003	0.381	-0.464				1.000		
Ref. time	0.051	-0.051	-0.203	-0.842	-0.776	-0.160					1.000	
Est. time	-0.038	-0.001	-0.222	-0.519	-0.623	-0.037					0.999	1.000

The constructed correlation grid of the compiled data revealed more comprehensive statistics on the effect of the step depth and feed rate in comparison to the data from only the DoE test shown in Table 6-3; this can be shortened as follows:

- The step depth in the augmented design is more closely related (0.457) to the forming temperature; in comparison to the correlation of the step depth (0.051) resulted from the DoE. This was due to the tight range (0.25–0.35 mm) of the step used in the DoE, whereas in the collective design the step varied from 0.25–0.8 mm.
- The proportional relationship (0.381) between the forming angle and the step size, which has also been observed in the experiments, was not clearly correlated proportional relationship established in DoE.
- While the feed rate at its extended range (500 –10 000 mm/min) is related to the axial force, it bears a stronger relationship with the in-plane force.
- The falsified minor effect of the sheet thickness to the formability (maximum angle) which is apparent in the compiled correlation is due to an inhomogeneous value of sheet thickness factor considering the total input data. As in the compiled correlation, plates of 0.8 mm thickness have appeared throughout the 22 runs of the OFAT experiments, comparing to lower data included the 0.5, 1.0 mm sheets.

6.3.1 Relative velocity factor

In order to set out a working window for the SPIF process, a more representative term for the process input needed to be determined. For this purpose, the relative velocity (V) at the interface was calculated using the Equation 6-1 for each test setting, and V term was added to the total design as a new process factor. As can be seen in Table 6-14, the analysis revealed that V has relationships like that of rotation speed factor; except for the slightly increased relationship to the forming time. This increase can directly be linked to the effect of the tool-tip radius term in the relative velocity factor. For justifying the use of relative velocity, Figure 6-40 illustrates scatter plots of rotation versus axial force, and relative velocity V versus axial force axial force.

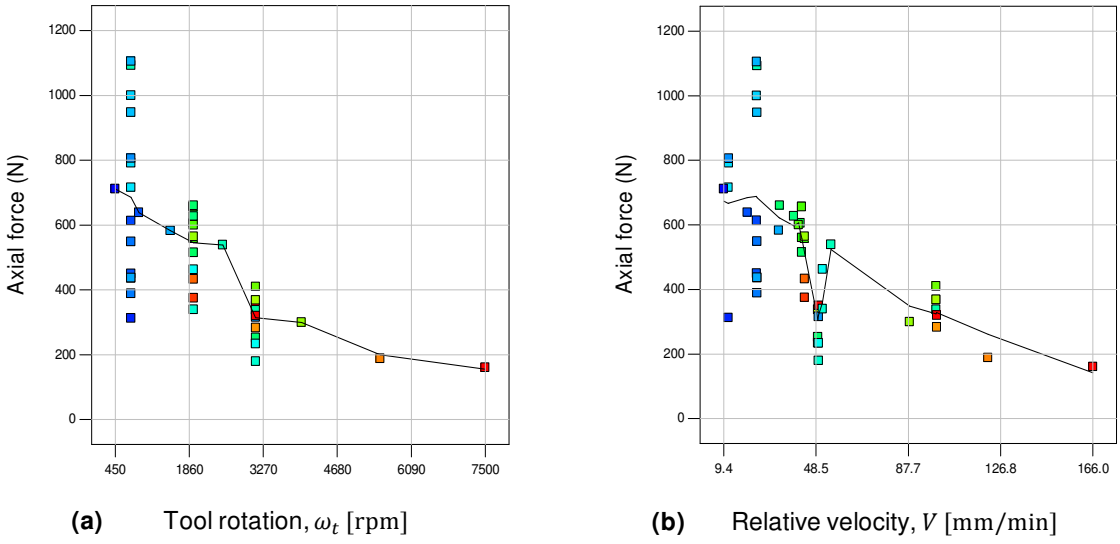

Figure 6-40: Comparison between two speed terms on forming force (a) axial force vs the tool rotation speed , (b) axial force vs the relative velocity

As can be noticed from the horizontal spread of the data points on the both graphs (Figure 6-40) the V term represents the relationships between the SPIF variables and the outputs better than using the tool rotation term. Similar correlations between V and the other SPIF outputs were confirmed.

6.3.2 The assembled relationship correlation

The relationships between the process key variables and the process outcomes can be presented in visual format such as the bar diagram presented in Figure 6-41.

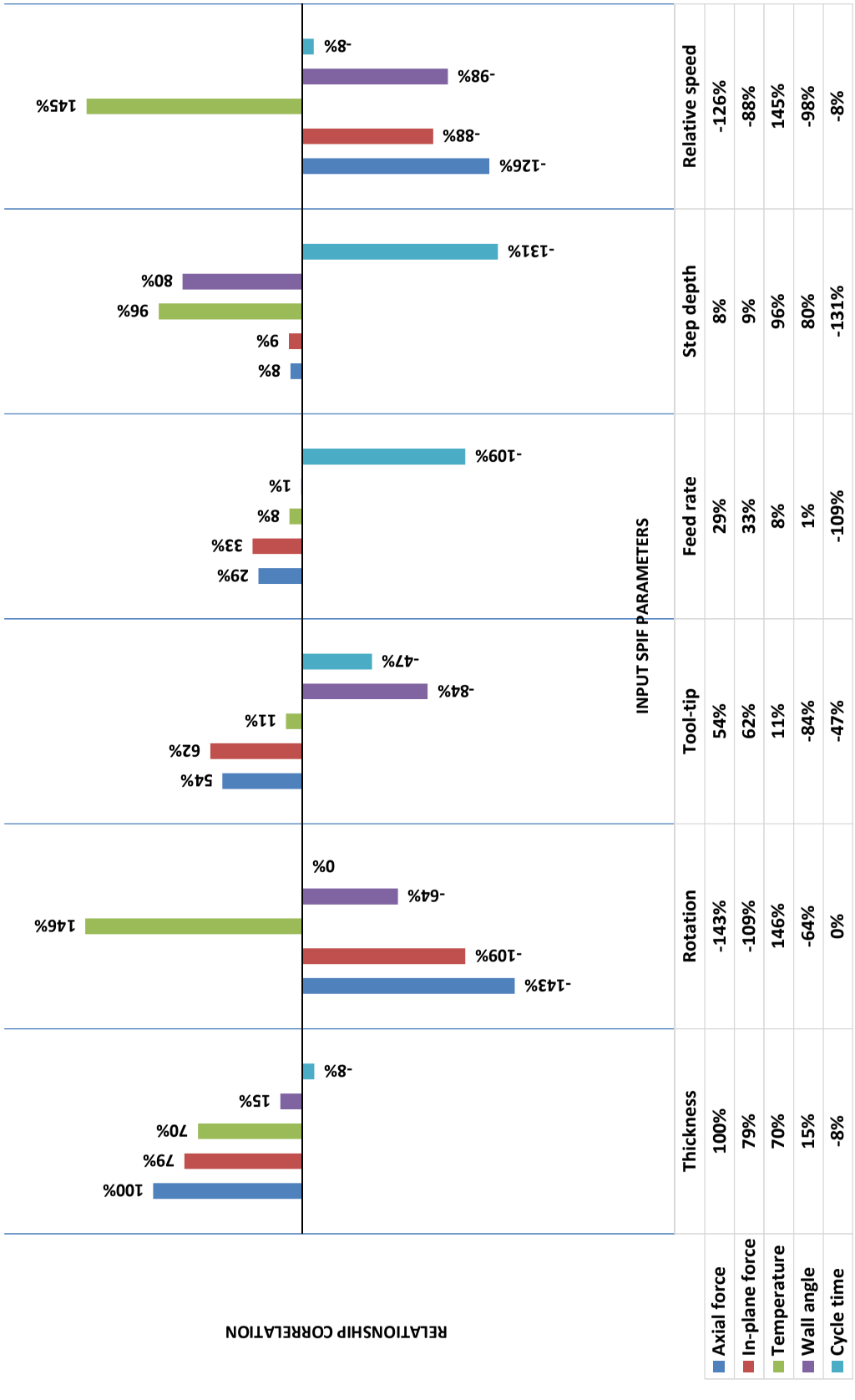

Figure 6-41: The SPIF cause and effect (C&E) diagram showing the main effect of the SPIF input variables on the response

In constructing of this diagram, the strong regression of the blank thickness to the axial force (0.475) is highlighted by thick-box-border in the correlation matrix (Table 6-14) was set at unity. The relationships of the blank thickness to the other SPIF responses were computed as a percentage of this unity value. In addition, the relations of the other process variables to the process outcomes were determined by dividing their regressions by (0.475) this unity.

The usefulness of this diagram becomes apparent when designing, optimising and characterising the SPIF process performance. It gives accelerated insight into the cause and effect (C&E) in the process performance and highlights the main factors affecting each response. The validity of the digits identifying the correlations is applicable to the material type and test settings used in the investigation. Further, significant outputs such as forming accuracy and surface quality can easily be integrated into the diagram for more comprehension process map.

6.3.3 The developed process map

The developed knowledge assisted in revealing the relationships of the SPIF variables to the resulting outcomes, and provided the justification for drawing the feasible SPIF framework of the parameters and incoming product quality attributes. A unifying framework of the process has been developed by imposing the data obtained in the form of the experimentally derived relationships (curves) into the conceptual processing framework conferred in 4.4. This enabled construction of the diagram shown in Figure 6-42, which can be considered as a working window for SPIF of the CP Grade 2.

The horizontal axis of this diagram is identified by the process main inputs, signified by the relative forming velocity, which is composed of the tool-tip radius, the rotational speed, the tool feed rate and the forming angle.

The vertical axis of the diagram is shared between the process outcomes of interest, namely the formability, the force and the temperature. The overlapping of the superimposed curves (as illustrated in Figure 6-42) outlines the boundaries between the regions of failure and regions of safety in the processing space. The region outside the intersection is the region of failure, while the intersection describes the expansion of the safe workable window (W-W) for the SPIF process.

Table 6-15: Empirical models used for constructing the process map

Model	Mathematical representation	
Formability	$\theta_{max} = 31.7 + 15.7 * t_0 - 1.3 * 10^{-3} * \omega_t + 1.9 * d_t - 9.2 * 10^{-3} * f_t$ $+173.5 * \Delta z - 16.1 * d_t * \Delta z$	(6- 1)
Temperature	$T = -761.4 + 265 * t_0 - 1.9 * 10^{-3} * \omega_t + 38.8 * d_t$ $+0.7 * f_t + 2310.5 * \Delta z + 0.072 * t_0 * \omega_t - 11.5 * t_0 * r_t$ $-0.236 * t_0 * f_t - 103.2 * d_t * \Delta z - 1.9 * f_t * \Delta z$	(6- 2)
Axial force	$F_z = 41.96 + 1385.868 * t_0 + 0.19 * \omega_t - 31.46 * d_t$ $+0.23 * f_t - 2548.74 * \Delta z - 0.46 * t_0 * \omega_t + 212.87 * d_t * \Delta z$	(6- 3)

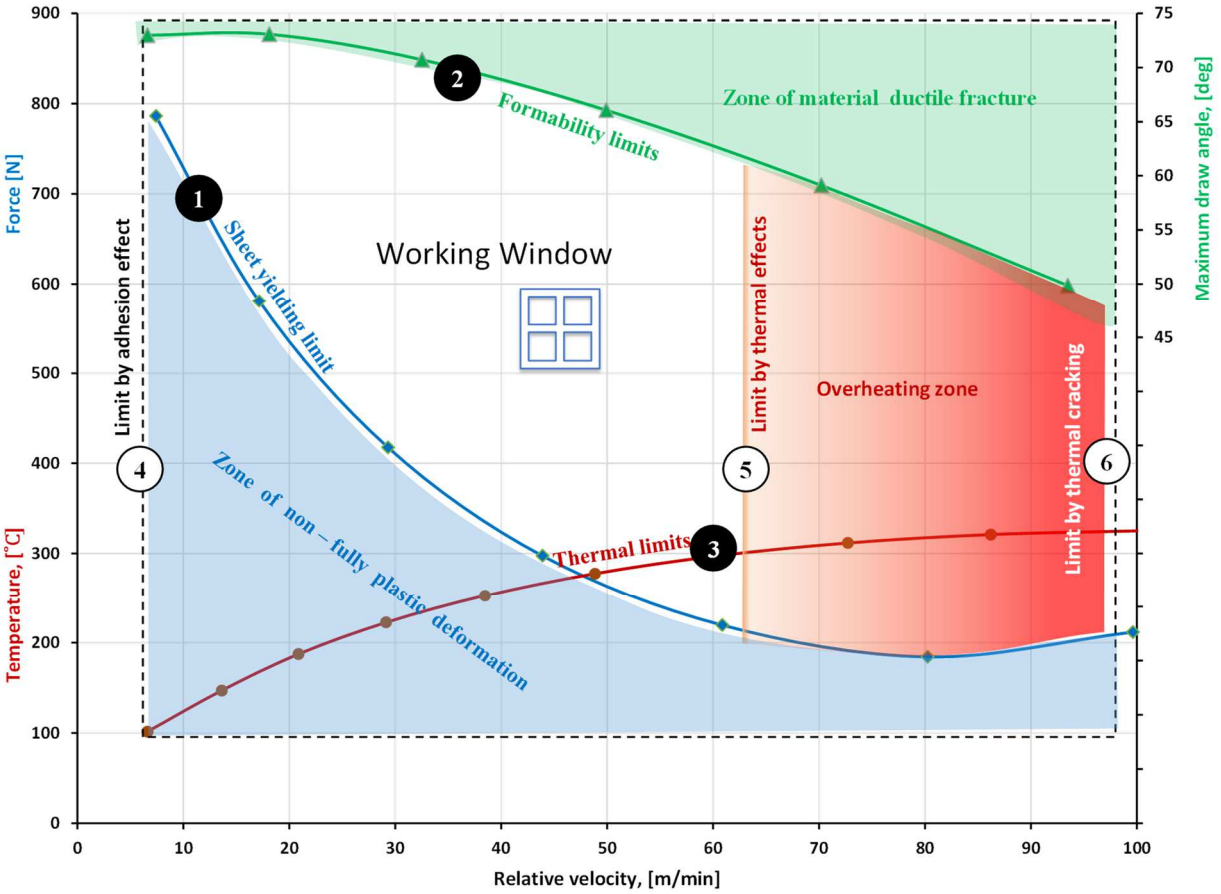

Figure 6-42: Schematic plot of the SPIF process map for the CP Grade 2

The three numbered curves of the outcomes (the formability, the force and the temperature, numbered 1, 2, and 3 respectively) are constructed using the mathematical models (Table 6-15) developed from the DoE as presented in Section 6.1. The data used in the construction of these three frontiers are only applicable for the material and operating range of tests used in this research.

The other three numbered boundaries were however, constructed based on general process knowledge from obtained from the literature, as well as supporting confirmations from the experiments run as part of this study.

A brief interpretation of the relationships of these labelled boundaries can accordingly be summarised as follows:

❶ The area beneath the curve of the forming force constructed using Equation 6-4 is the area that characterises the yielding behaviour the titanium sheets being formed. This curve defines the lower periphery below which a non-complete plastic or even a pure elastic deformation is predicted. As shown by the blue-coloured region in the figure, as the rotational speed increases, the rate of change in the titanium yielding plots similarly TO an exponential decay curve. As far as the W-W space is concerned, graph 1 expands the processing space by pulling down the lower boundary of the W-W.

❷ The upper boundary of the W-W is defined by the curve drawn using Equation 6-2 representing the maximum forming angle predicted. This curve plots the change in maximum angle of the titanium as a function of the velocity at different process settings. As shown in the figure, increasing the tool

velocity, causes this graph drop, bringing down the upper boundary of the W-W. Therefore, in selecting the forming speed there is a trade-off to be considered between good process quality aspects at a slow forming speed and the increasing negative thermal effects at higher forming speeds.

❸ Uniquely, by superimposing the graph derived using equation 6-4 and representing the forming temperature, the framework determines that the W-W for the titanium will be more effective. This thermal trend is the main reason behind the opening-out of the working space (the lower yield of workpiece and the enhanced formability) as stated earlier in the preceding two bullet points. Gains in terms of the reduced force and increased ductility can be achieved as long as this graph is still below a certain level, after which opposing thermal effects start to emerge. As shown in the illustration, with increasing relative velocity this graph cuts in the W-W above the force graph, lifting the lower boundary of the W-W. At higher relative speed values, there is a reduction in lubricant effectiveness and worsening of the produced surface qualities.

④ The vertical dashed line in the left side of processing space (numbered 4), extends to the horizontal axis and is associated with the lowest useful speed for forming. To the left of this line a higher force is predicted. The higher force increases the possibility of material adhesion to tool-tip, and intensifies wear on the both sliding surfaces.

⑤ Moving towards the right side of the W-W, the dash-dot line numbered 5, identifies the zone, where to the right of this line, the thermal defects are predicted. Due to several factors affecting the sliding friction behaviour, it is difficult to quantify this effect. In the region beyond this boundary to the right, these thermal effects become progressively worse — this is indicated by a colour-scaled red shading of this zone. In the tests, galling and seizing were observed on samples that were formed in this zone, because of a combination of the high contact pressure and high temperature. Surface defects described in Section 6.2.2 as thermal effects (TE), were observed on the produced samples.

⑥ Finally, owing to the on-going impact of the sliding friction effects throughout operation in the red zone, as the operating point moves to the right, the outside limit of the virtual thermal wall (coloured dark red) is reached. Here, at very high velocities, elevated temperatures significantly weakening the ability of the lubricant to support the load, promoting drastic changes in the behaviour of friction and wear. These changes can be responsible for large thermal and mechanical stresses, which cause thermo-cracking of the titanium sheets. As well as an escalation of the wear mechanisms, form mild to severe oxidational wear, or maybe even to melt wear.

CHAPTER 7 CONCLUSIONS AND FUTURE RESEARCH

In In this dissertation, an effectual two-stage process mapping approach is implemented. Firstly, to characterise the SPIF conceptual processing space and identify the key design factors, a systematic quantitative literature review has been undertaken, analysing results from a hundred SPIF relevant publications. Secondly, the DoE and OFAT have been systematically implemented to verify the developed conceptual framework.

The goal is to design a process suitable for incremental forming of CP Grade 2 sheets that can consistently deliver a product that meets its quality attributes. While it is recognised that other variables (such as the material properties, the tool path type and the friction conditions) may affect the outcomes depending on the SPIF process, the established approach involves mapping the SPIF of the CP Grade 2 in terms of the five key process variables. Once the behaviour of the SPIF process has been mapped, a thorough study of the role of a secondary process variable can be accomplished to evaluate its effect on the process across the full five-key-variables working window.

In this study, the process characteristics of interest were the maximum material formability and the control of the thermomechanical effects. The original contribution can be summarised in two main points as follows:

Firstly, deepen the understanding of SPIF process limits

In this study the influence of SPIF parameters on the formability of CP Grade 2 was investigated based on the forming temperature, the forming forces and the process productivity. Albeit the parameters are interdependent and the interaction between them was evident, the results delivered insight into physics of the SPIF process, which deepens the understanding of the dependence of the process outcomes on different variables:

- The maximum forming angle of the CP Grade 2 attainable is inversely related to increased tool-tip diameter. It is particularly applicable for small tips. If a large step is used, surface quality is reduced.
- Forming forces are inversely related to the spindle rotation. Forces approach a minimum when the rotation speed exceeds 2000 rpm.
- Relative (linear) velocity **V** is a significant and more relevant term to characterise the forming speed than the commonly used rotation or feed rate terms. In addition to the feed rate and rotation, the **V** term accounts for the tool-tip radius. Additionally, and more importantly, the **V** term also takes account of the dynamically developed wall angle throughout the forming, which can substantially alter the actual material flow conditions at the interface. Therefore, **V** is suggested to be included as characterising aspect when designing the SPIF.

- The relative directions of tool rotation (advancing/retreating) to the tool path direction evidently affect the relative velocity at the interface, which is higher in the advancing mode, and consequently affects the overall process outcomes.

- Heat is generated mainly due to two factors: plastic deformation work, determined by the volume of material being deformed, and affected by thickness and angle. The heat generated by sliding frictional work, determined by the relative speed at the interface ($\boldsymbol{\omega_t, r_t, \theta, f_t}$) and the tool force, whereby the sheet thickness and the step depth play a significant role.

- The heat factor is explicitly studied and integrated into the developed processing framework. Reasonable results in titanium formability can be achieved with reduced forces, less tool wear and free of thermal defects, if forming conditions are optimised by maintaining a forming temperature of about $220 \pm 25℃$.

- The high forming temperature caused by high tool rotation results not only in work hardening of the titanium samples, but also in decreasing hardness of the tool-tip material, which in turn leads to high tool wear. Tool rotation must be neither too low nor too high; neither must the tool be stationary.

- The failure mechanisms at differing tool rotations are not the same. Extreme tool rotational speeds have been tested, it appears that above the upper bound of high rotation (such as 15 000 rpm) it is not possible to deform the titanium. Excessive friction damage in the material occurs as the forming starts.

- Cyclic time can be minimised by stepping up the feed rate and the step depth factors. There are trade-offs to be considered, when changing these parameters, particularly in the case of the step depth:

    - If the step depth is too small ($\Delta z \leq 0.3$ mm) the resulting frictional stresses tend to be recurrently applied to the same zone of the titanium, with the consequence that escalated surface wear, and material hardening occur. This in turn exacerbates thermal effects and can trigger workpiece failure.

    - Larger step depth sizes ($\Delta z > 0.35$ mm) enabled extended formability obtained, though the surface quality will be lower when using small tool tips.

- The feed rate has the lowest impact on the produced titanium formability, forces and temperatures. Therefore, high feeds are a handy tool to enhance SPIF productivity. Feed rates up to 10 000 mm/min have been tested. However, for the 10 000 mm/min, the gantry type CNC machine (maximum 40 000 mm/min) used could not accelerate over the short contours of the small component used as a test model. The ability of the CNC machine to accelerate when forming with complex tool path or components with small features has therefore to be considered; these machines often have limitations.

Secondly, the developed process-map:

The region of the SPIF process variable space, where successful forming of the CP Grade 2 can be anticipated is identified throughout the process mapping approach. The processed data have been presented in practical formats of a two-dimensional input-output plot, accessible through a synchronism of the C-E and W-W diagrams:

- The C-E diagram is a collective 2D plot that can be used to prioritise causes and importance, based on an identified overall score calculated for the process input variables. The central impact of the relative velocity factor is also integrated in the C-E.

- The process map (W-W) included the thermal effect factor, which has not been previously explicitly considered. The developed W-W can be a handy design tool for reducing process qualification times, improve quality and reducing the dependency on skilled operators, thus contributing to a lowering of the overall manufacturing costs.

- Inside the suggested W-W for the CP Grade2, components of 0.5, 0.8 and 1 mm thicknesses have successfully been produced with unreported levels of strain, which surpassed the designed benchmark ($\mathbf{75}°$) angle.

Scope for future research:

The produced samples and data resulted from the different thermal and mechanical conditions; suggest that the following research points are viable avenues for further study:

- Microstructure analysis and material transformation of the deformed titanium; evaluation of subsurface microstructure and surface integrity, micro-hardening tests are essential to clarify the effects of thermal and mechanical stress on the components produced.

- A finite element approach can be deployed to provide consistent conclusions on the developed C-E. More process parameters can be integrated in the analysis for refining the process boundaries and enabling confident choices of process variables.

- It was possible to elevate forming temperature (~ 400℃) at the interface by altering the forming conditions. Applying the same method to enhance the formability of advanced Ti 6Al 4V is a research worthy topic and it is the intention to investigate this topic. The same mapping approach can be applied to extend the SPIF processing window for further quality attributes, and different types of sheet metal.

REFERENCE LIST

Adams, D. and Jeswiet, J. (2014) 'Single-point incremental forming of 6061-T6 using electrically assisted forming methods', *Proceedings of the Institution of Mechanical Engineers, Part B: Journal of Engineering Manufacture*, 228(7), pp. 757–764. doi: 10.1177/0954405413501670.

Adams, D. and Jeswiet, J. (2015) 'Design rules and applications of single-point incremental forming', *Proceedings of the Institution of Mechanical Engineers, Part B: Journal of Engineering Manufacture*, 229(5), pp. 754–760. doi: 10.1177/0954405414531426.

Adamus, J. (2007) 'Forming of the titanium implants and medical tools by metal working', *Archives of Materials Science and Engineering*, 28(5), pp. 313–316.

Aerens, R., Eyckens, P., Bael, A. and Duflou, J. R. (2009) 'Force prediction for single point incremental forming deduced from experimental and FEM observations', *The International Journal of Advanced Manufacturing Technology*, 46(9–12), pp. 969–982. doi: 10.1007/s00170-009-2160-2.

Akinlabi, E. T., Shukla, M. and Akinlabi, S. A. (2012) 'Laser forming of titanium and its alloys – An Overview', *World Academy of Science, Engineering and Technology 71 2012*, pp. 1522–1525.

Allwood, J. M., Duncan, S. R., Cao, J., Groche, P., Hirt, G., Kinsey, B., Kuboki, T., Liewald, M., Sterzing, A. and Tekkaya, A. E. (2016) 'Closed-loop control of product properties in metal forming', *CIRP Annals - Manufacturing Technology*. The Author(s), 65(2), pp. 573–596. doi: 10.1016/j.cirp.2016.06.002.

Allwood, J. M. and Utsunomiya, H. (2006) 'A survey of flexible forming processes in Japan', *International Journal of Machine Tools and Manufacture*, 46(15), pp. 1939–1960. doi: 10.1016/j.ijmachtools.2006.01.034.

Altan, T., Ngaile, G. and Shen, G. (2005) *Cold and Hot Forging: Fundamentals and Applications*. A S M International (Cold and Hot Forging: Fundamentals and Applications).

Altan, T. and Tekkaya, A. E. (2012) *Sheet Metal Forming: Processes and Applications*. ASM International.

Ambrogio, G., Filice, L., Fratini, L., Ingarao, G. and Manco, G. L. (2007) 'Measuring of Geometrical Precision of Some parts Obtained by Asymmetric Incremental Forming Process After Trimming', *Proceedings of the 9th International Conference on Numerical Methods in Industrial Forming Processes*, 908, pp. 431–436. doi: 10.1063/1.2740849.

Ambrogio, G., Filice, L. and Gagliardi, F. (2012) 'Formability of lightweight alloys by hot incremental sheet forming', *Materials & Design*. Elsevier Ltd, 34, pp. 501–508. doi: 10.1016/j.matdes.2011.08.024.

Ambrogio, G., Filice, L. and Micari, F. (2006) 'A force measuring based strategy for failure prevention in incremental forming', *Journal of Materials Processing Technology*, 177(1–3), pp. 413–416. doi: 10.1016/j.jmatprotec.2006.04.076.

Ambrogio, G., Gagliardi, F., Bruschi, S. and Filice, L. (2013) 'On the high-speed Single Point Incremental Forming of titanium alloys', *CIRP Annals - Manufacturing Technology*. CIRP, 62(1), pp. 243–246. doi: 10.1016/j.cirp.2013.03.053.

Anonym (2016) *Roughness (2D) parameter | Olympus IMS*. Available at: http://www.olympus-ims.com/en/knowledge/metrology/roughness/2d_parameter/.

Asghar, J., Lingam, R., Shibin, E. and Reddy, N. (2013) 'Tool path design for enhancement of accuracy in single-point incremental forming', *Proceedings of the Institution of Mechanical Engineers, Part B: Journal of Engineering Manufacture*, 228(9), pp. 1027–1035. doi: 10.1177/0954405413512812.

Azevedo, N. G., Farias, J. S., Bastos, R. P., Teixeira, P., Davim, J. P. and Alves de Sousa, R. J. (2015) 'Lubrication aspects during Single Point Incremental Forming for steel and aluminum materials', *International Journal of Precision Engineering and Manufacturing*, 16(3), pp. 589–595. doi: 10.1007/s12541-015-0079-0.

Bagudanch, I., Garcia-Romeu, M. L. L., Centeno, G., Elías-Zúñiga, A. and Ciurana, J. (2015) 'Forming force and temperature effects on single point incremental forming of polyvinylchloride', *Journal of Materials Processing Technology*, 219, pp. 221–229. doi: 10.1016/j.jmatprotec.2014.12.004.

Bauer, S., Schmuki, P., von der Mark, K. and Park, J. (2013) 'Engineering biocompatible implant surfaces', *Progress in Materials Science*, 58(3), pp. 261–326. doi: 10.1016/j.pmatsci.2012.09.001.

Belforte, D. (2012) *2012 Annual Economic Review and Forecast*. Available at: http://www.industrial-lasers.com/articles/print/volume-28/issue-1/features/2012-annual-economic-review-and-forecast._saveArticle.html (Accessed: 9 July 2013).

Bhattacharya, A., Bera, T. K. and Thakur, A. (2015) 'On Cutter Deflection Profile Errors in End Milling: Modeling and Experimental Validation', *Materials and Manufacturing Processes*, 30(8), pp. 1042–1059. doi: 10.1080/10426914.2014.973598.

Bhattacharya, a., Maneesh, K., Venkata Reddy, N. and Cao, J. (2011) 'Formability and Surface Finish Studies in Single Point Incremental Forming', *Journal of Manufacturing Science and Engineering*, 133(6), p. 61020. doi: 10.1115/1.4005458.

Bhushan, B. and Kennedy, F. E. (2001) 'Frictional Heating and Contact Temperatures', in *Methods*. illustrate. CRC Press (Mechanics & Materials Science), p. 1760.

Box, G. E. P. (1976) 'Science and Statistics', *Journal of the American Statistical Association*, 71(356), pp. 791–799. doi: 10.1641/B570910.

Boyer, R. (2010) 'Attributes, characteristics, and applications of titanium and its alloys', *JOM Journal of the Minerals, Metals and Materials ….*

Brecher, C. and Özdemir, D. (2015) 'Introduction', in *Lecture Notes in Production Engineering*, pp. 1–8. doi: 10.1007/978-3-319-12304-2_1.

Buffa, G., Campanella, D. and Fratini, L. (2013) 'On the improvement of material formability in SPIF operation through tool stirring action', *International Journal of Advanced Manufacturing Technology*, 66(9–12), pp. 1343–1351. doi: 10.1007/s00170-012-4412-9.

Campbell, F. C. (2011) *Manufacturing Technology for Aerospace Structural Materials*. Elsevier Science

(Aerospace engineering materials science).

Cao, Z. Cedric Xia, Timothy G. Gutowski and John Roth (2012) *A Hybrid Forming System: Electrical-Assisted Double Side Incremental Forming (EADSIF) Process for Enhanced Formability and Geometrical Flexibility*. Golden, CO (United States). doi: 10.2172/1039329.

Carrino, L., Giuliano, G. and Strano, M. (2006) 'The effect of the punch radius in dieless incremental forming', in *in Intelligent Production Machines and Systems--2nd IPROMS*, pp. 204–209.

Carson, B., Daehn, G., Psyk, V. and Tekkaya, A. (2010) 'Agile Production of Sheet Metal Aviation Components Using Disposable Electromagnetic Actuators', in *4th International Conference on High Speed Forming*, pp. 35–46.

Castelan, J., Schaeffer, L., Daleffe, A., Fritzen, D., Salvaro, V. and Silva, F. P. da (2014) 'Manufacture of custom-made cranial implants from DICOM® images using 3D printing, CAD/CAM technology and incremental sheet forming', *Revista Brasileira de Engenharia Biomédica*. SBEB - Sociedade Brasileira de Engenharia Biomédica, 30(3), pp. 265–273. doi: 10.1590/rbeb.2014.024.

Chen, J.-J., Liu, W., Li, M.-Z. and Wang, C.-T. (2005) 'Digital manufacture of titanium prosthesis for cranioplasty', *The International Journal of Advanced Manufacturing Technology*, 27(11–12), pp. 1148–1152. doi: 10.1007/s00170-004-2309-y.

Czitrom, V. (1999) 'One-Factor-at-a-Time Versus Designed Experiments', *American Statistical Association*, 53(2), p. 6. doi: 10.2307/2685731.

Daehn, G. S. (2007) 'Agile sheet metal forming: Basic concepts and the role of electromagnetic metal forming', in *IDDRG*. Győr, Hungary, pp. 1–10.

Date, P. P. (2013) 'Sheet Metal Forming: Issues and Recent Developments', in Uday S. Dixit, R. G. N. (ed.) *Metal Forming: Technology and Process Modelling*. Bombay: McGraw Hill Education.

Davarpanah, M. A., Mirkouei, A., Yu, X., Malhotra, R. and Pilla, S. (2015) 'Effects of incremental depth and tool rotation on failure modes and microstructural properties in Single Point Incremental Forming of polymers', *Journal of Materials Processing Technology*. Elsevier B.V., 222, pp. 287–300. doi: 10.1016/j.jmatprotec.2015.03.014.

Davis, B. and Hryn, J. (2008) *Innovative forming and fabrication technologies: new opportunities*. Argonne National Laboratory (ANL).

Dixit, U. S. (2013) 'Epilogue', in *Metal forming: technology and process modeling*. McGraw Hill Educatio.

Dubey, A. K. and Yadava, V. (2008) 'Experimental study of Nd:YAG laser beam machining—An overview', *Journal of Materials Processing Technology*, 195(1–3), pp. 15–26. doi: 10.1016/j.jmatprotec.2007.05.041.

Duflou, J., Tunçkol, Y., Szekeres, A., Vanherck, P. and Tunckol, Y. (2007) 'Experimental study on force measurements for single point incremental forming', *Journal of Materials Processing Technology*, 189(1–3), pp. 65–72. doi: 10.1016/j.jmatprotec.2007.01.005.

Durante, M., Formisano, A. and Langella, A. (2010) 'Comparison between analytical and experimental roughness values of components created by incremental forming', *Journal of Materials Processing Technology*. Elsevier B.V., 210(14), pp. 1934–1941. doi: 10.1016/j.jmatprotec.2010.07.006.

Durante, M., Formisano, A., Langella, A. and Capece Minutolo, F. M. (2009) 'The influence of tool rotation on an incremental forming process', *Journal of Materials Processing Technology*, 209(9), pp. 4621–4626. doi: 10.1016/j.jmatprotec.2008.11.028.

Echrif, S. B. M. and Hrairi, M. (2011) 'Research and Progress in Incremental Sheet Forming Processes', *Materials and Manufacturing Processes*, 26(11,211), pp. 1404–1414. doi: 10.1080/10426914.2010.544817.

Echrif, S. B. M. and Hrairi, M. (2014) 'Significant Parameters for the Surface Roughness in Incremental Forming Process', *Materials and Manufacturing Processes*. Taylor & Francis, 29(6), pp. 697–703. doi: 10.1080/10426914.2014.901519.

Emmens, W. C. and van den Boogaard, A. H. (2009) 'An overview of stabilizing deformation mechanisms in incremental sheet forming', *Journal of Materials Processing Technology*, 209(8), pp. 3688–3695. doi: 10.1016/j.jmatprotec.2008.10.003.

Emmens, W. C., van der Weijde, D. H. and van den Boogaard, A. H. (2009) 'The FLC, Enhanced Formability, and Incremental Sheet Forming', in *IDDRG 09 Conference Proceedings*, pp. 773–784.

Eyckens, P., Bael, A. Van and Aerens, R. (2008) 'Small-scale finite element modelling of the plastic deformation zone in the incremental forming process', ... *of Material Forming*, pp. 1159–1162. doi: 10.1007/s12289-008-0.

Faller, K. and Froes, F. H. (2001) 'The use of titanium in family automobiles: Current trends', *Jom-Journal of the Minerals Metals & Materials Society*, 53(4), pp. 27–28. doi: 10.1007/s11837-001-0143-3.

Fan, G. and Gao, L. (2014) 'Mechanical property of Ti-6Al-4V sheet in one-sided electric hot incremental forming', *International Journal of Advanced Manufacturing Technology*, 72(5–8), pp. 989–994. doi: 10.1007/s00170-014-5733-7.

Fan, G., Sun, F., Meng, X., Gao, L. and Tong, G. (2009) 'Electric hot incremental forming of Ti-6Al-4V titanium sheet', *The International Journal of Advanced Manufacturing Technology*, 49(9–12), pp. 941–947. doi: 10.1007/s00170-009-2472-2.

Fang, Y., Lu, B., Chen, J., Xu, D. K. and Ou, H. (2014) 'Analytical and experimental investigations on deformation mechanism and fracture behavior in single point incremental forming', *Journal of Materials Processing Technology*, 214(8), pp. 1503–1515. doi: 10.1016/j.jmatprotec.2014.02.019.

Fei, Y. (1995) 'Thermal expansion', in *Rock Physics and Phase Relations*, pp. 29–44. doi: 10.1029/RF002p0029.

Filice, L., Ambrogio, G. and Micari, F. (2006) 'On-Line Control of Single Point Incremental Forming Operations through Punch Force Monitoring', *CIRP Annals - Manufacturing Technology*, 55(1), pp. 245–248. doi: 10.1016/S0007-8506(07)60408-9.

Filice, L., Fratini, L. and Micari, F. (2002) 'Analysis of Material Formability in Incremental Forming', *CIRP Annals - Manufacturing Technology*, 51(1), pp. 199–202. doi: 10.1016/S0007-8506(07)61499-1.

Gulati, V., Aryal, A., Katyal, P. and Goswami, A. (2015) 'Process Parameters Optimization in Single Point Incremental Forming', *Journal of The Institution of Engineers (India): Series C*. Springer India, 97(2), pp. 221–229. doi: 10.1007/s40032-015-0203-z.

Hagan, E. and Jeswiet, J. (2002) 'A review of conventional and modern single point sheet metal forming methods', *J. Engineering Manufacture*, 217(Part B), pp. 1–14.

Hagan, E. and Jeswiet, J. (2004) 'Analysis of surface roughness for parts formed by computer numerical controlled incremental forming', *Proceedings of the Institution of Mechanical Engineers, Part B: Journal of Engineering Manufacture*, 218(10), pp. 1307–1312. doi: 10.1243/0954405042323559.

Hamilton, K. and Jeswiet, J. (2010) 'Single point incremental forming at high feed rates and rotational speeds: Surface and structural consequences', *CIRP Annals - Manufacturing Technology*. CIRP, 59(1), pp. 311–314. doi: 10.1016/j.cirp.2010.03.016.

Hasan, R. Z., Kinsey, B. L. and Tsukrov, I. (2011) 'Effect of Element Types on Failure Prediction Using a Stress-Based Forming Limit Curve', *Journal of Manufacturing Science and Engineering*, 133(6), p. 61002. doi: 10.1115/1.4005044.

Hölscher, H., Schirmeisen, A. and Schwarz, U. D. (2008) 'Principles of atomic friction: from sticking atoms to superlubric sliding.', *Philosophical transactions. Series A, Mathematical, physical, and engineering sciences*. The Royal Society, 366(1869), pp. 1383–404. doi: 10.1098/rsta.2007.2164.

Hussain, G. (2013) 'Experimental investigations on the role of tool size in causing and controlling defects in single point incremental forming process', *Journal of Engineering Manufacture*. doi: 10.1177/0954405413498864.

Hussain, G. Ã., Gao, L., Hayat, N. and Qijian, L. (2007) 'The effect of variation in the curvature of part on the formability in incremental forming : An experimental investigation', *International Journal of Machine Tools & Manufacture*, 47, pp. 2177–2181. doi: 10.1016/j.ijmachtools.2007.05.001.

Hussain, G., Gao, L. and Hayat, N. (2009) 'Empirical modelling of the influence of operating parameters on the spifability of a titanium sheet using response surface methodology', *Proceedings of the Institution of Mechanical Engineers, Part B: Journal of Engineering Manufacture*, 223(1), pp. 073–081. doi: 10.1243/09544054JEM1259.

Hussain, G., Gao, L., Hayat, N., Cui, Z., Pang, Y. C. and Dar, N. U. (2008) 'Tool and lubrication for negative incremental forming of a commercially pure titanium sheet', *Journal of Materials Processing Technology*, 203(1–3), pp. 193–201. doi: 10.1016/j.jmatprotec.2007.10.043.

Hussain, G., Hayat, N. and Gao, L. (2008) 'An experimental study on the effect of thinning band on the sheet formability in negative incremental forming', *International Journal of Machine Tools and Manufacture*, 48(10), pp. 1170–1178. doi: 10.1016/j.ijmachtools.2008.02.003.

Hussain, G., Hayat, N. and Lin, G. (2012) 'Pyramid as test geometry to evaluate formability in incremental forming: Recent results', *Journal of Mechanical Science and Technology*, 26(8), pp. 2337–2345. doi: 10.1007/s12206-012-0617-y.

Hussain, G., Khan, H. R., Gao, L. and Hayat, N. (2013) 'Guidelines for Tool-Size Selection for Single-Point Incremental Forming of an Aerospace Alloy', *Materials and Manufacturing Processes*, 28(3), pp. 324–329. doi: 10.1080/10426914.2012.700151.

Inagaki, I. (2014) *Application and Features of Titanium for the Aerospace Industry*.

Isik, K., Silva, M. B., Tekkaya, A. E. and Martins, P. A. F. (2014) 'Formability limits by fracture in sheet metal forming', *Journal of Materials Processing Technology*. Elsevier B.V., 214(8), pp. 1557–1565. doi: 10.1016/j.jmatprotec.2014.02.026.

IWU (2016) 'Electromagnetic forming (EMF)'. Chemnitz, Germany: Fraunhofer Institute for Machine Tools and Forming Technology, Chemnitz, Germany, pp. 1–2.

Jeswiet, J., Adams, D., Doolan, M., McAnulty, T. and Gupta, P. (2015) 'Single point and asymmetric incremental forming', *Advances in Manufacturing*, 3(4), pp. 253–262. doi: 10.1007/s40436-015-0126-1.

Jeswiet, J., Geiger, M., Engel, U., Kleiner, M., Schikorra, M., Duflou, J., Neugebauer, R., Bariani, P. and Bruschi, S. (2008) 'Metal forming progress since 2000', *CIRP Journal of Manufacturing Science and Technology*, 1(1), pp. 2–17. doi: 10.1016/j.cirpj.2008.06.005.

Jeswiet, J., Micari, F., Hirt, G., Bramley, A., Duflou, J. and Allwood, J. (2005) 'Asymmetric single point incremental forming of sheet metal', *CIRP Annals - Manufacturing Technology*, 54(2), pp. 88–114. doi: 10.1016/S0007-8506(07)60021-3.

Ji, Y. H. and Park, J. J. (2008) 'Formability of magnesium AZ31 sheet in the incremental forming at warm temperature', *Journal of Materials Processing Technology*, 201(1–3), pp. 354–358. doi: 10.1016/j.jmatprotec.2007.11.206.

Jones, E. J. H. and Town, H. C. (2013) *Production Engineering: Jig and Tool Design*. Elsevier Science.

Jurisevic, B., Sajn, V., Kosel, F. and Junkar, M. (2007) 'Introduction of laminated supporting tools in water jet incremental sheet metal forming', *The International Journal of Advanced Manufacturing Technology*, 37(5–6), pp. 496–503. doi: 10.1007/s00170-007-0994-z.

Kai, H., Li, J. H., Luo, Q., Mao, H. and Du, R. X. (2011) 'A study on dieless incremental sheet metal forming using water jet technology', *Advanced Materials Research*, 189–193, pp. 795–800. doi: 10.4028/www.scientific.net/AMR.189-193.795.

Kalpakjian, S. and Schmid, S. (2008) 'Sheet-Metal Forming Processes', in *Manufacturing processes for engineering materials*. 5th edn. Upper Saddle River: Prentice Hall, pp. 374–403.

Kazmer, D. O. (2009) *Plastics Manufacturing Systems Engineering*. München: Carl Hanser Verlag GmbH & Co. KG. doi: 10.3139/9783446430143.

Kegg, R. L. (1961) 'A New Test Method for Determination of Spinnability of Metals', *Journal of Engineering for Industry*, 83(2), p. 119. doi: 10.1115/1.3664438.

Khaja, S., Technology, O., Prof, A. and Engg, M. (2013) 'Friction Stir Welding of Similar and Dissimilar Aluminum Alloys : A Review', *International Journal of Mechanical, Aerospace, Industrial and Mechatronics Engineering*, 7(12), pp. 72–82.

Khalatbari, H., Iqbal, A., Shi, X., Gao, L., Hussain, G. and Hashemipour, M. (2015) 'High-Speed Incremental Forming Process: A Trade-Off Between Formability and Time Efficiency', *Materials and Manufacturing Processes*, 30(11), pp. 1354–1363. doi: 10.1080/10426914.2015.1037892.

Kiyak, M., Kaner, B., Sahin, I., Aldemir, B. and Cakir, O. (2010) 'The dependence of tool overhang on surface quality and tool wear in the turning process', *International Journal of Advanced Manufacturing Technology*, 51(5–8), pp. 431–438. doi: 10.1007/s00170-010-2654-y.

Knysh, P. and Korkolis, Y. P. (2015) 'Determination of the fraction of plastic work converted into heat in metals', *Mechanics of Materials*. Elsevier Ltd, 86, pp. 71–80. doi: 10.1016/j.mechmat.2015.03.006.

Koc, B. and Thangaswamy, S. (2011) 'Design and analysis of a reconfigurable discrete pin tooling system for molding of three-dimensional free-form objects', *Robotics and Computer-Integrated Manufacturing*, 27(2), pp. 335–348. doi: 10.1016/j.rcim.2010.07.017.

Li, M.-Z., Cai, Z.-Y. and Liu, C.-G. (2007) 'Flexible manufacturing of sheet metal parts based on digitized-die', *Robotics and Computer-Integrated Manufacturing*, 23(1), pp. 107–115. doi: 10.1016/j.rcim.2005.09.005.

Li, P. J. J., Chen, Y. W. W., Male, a. T. A. a. T. A. and Zhang, Y. M. M. (2000) 'Flexible forming of sheet metal using a plasma arc', *Proceedings of the Institution of Mechanical Engineers, Part B: Journal of Engineering Manufacture*, 214(1), pp. 61–64. doi: 10.1243/0954405001517496.

Li, Y., Liu, Z., Daniel, W. J. T. (Bill. and Meehan, P. A. (2014) 'Simulation and Experimental Observations of Effect of Different Contact Interfaces on the Incremental Sheet Forming Process', *Materials and Manufacturing Processes*, 29(2), pp. 121–128. doi: 10.1080/10426914.2013.822977.

Li, Y., Liu, Z., Lu, H., Daniel, W. J. T., Liu, S. and Meehan, P. A. (2014) 'Efficient force prediction for incremental sheet forming and experimental validation', *The International Journal of Advanced Manufacturing Technology*, 73(1–4), pp. 571–587. doi: 10.1007/s00170-014-5665-2.

Lingam, R., Bhattacharya, A., Asghar, J. and Reddy, N. V. (2015) 'Deflection Compensations for Tool Path to Enhance Accuracy During Double-Sided Incremental Forming', 138(September), pp. 1–8. doi: 10.1115/MSEC20159404.

Liu, Z., Liu, S., Li, Y. and Meehan, P. A. (2014) 'Modeling and Optimization of Surface Roughness in Incremental Sheet Forming using a Multi-objective Function', *Materials and Manufacturing Processes*, 29(7), pp. 808–818. doi: 10.1080/10426914.2013.864405.

Lu, B., Fang, Y., Xu, D. K., Chen, J., Ou, H., Moser, N. H. and Cao, J. (2014) 'Mechanism investigation of friction-related effects in single point incremental forming using a developed oblique roller-ball tool',

International Journal of Machine Tools and Manufacture, 85, pp. 14–29. doi: 10.1016/j.ijmachtools.2014.04.007.

Lu, B., Ou, H., Shi, S. Q., Long, H. and Chen, J. (2014) 'Titanium based cranial reconstruction using incremental sheet forming', *International Journal of Material Forming*. doi: 10.1007/s12289-014-1205-8.

Madeira, T., Silva, C. M. a., Silva, M. B. and Martins, P. a. F. (2015) 'Failure in single point incremental forming', *The International Journal of Advanced Manufacturing Technology*, pp. 1471–1479. doi: 10.1007/s00170-014-6381-7.

Malhotra, R., Xue, L., Belytschko, T. and Cao, J. (2012) 'Mechanics of fracture in single point incremental forming', *Journal of Materials Processing Technology*. Elsevier B.V., 212(7), pp. 1573–1590. doi: 10.1016/j.jmatprotec.2012.02.021.

Marabuto, S. R., Afonso, D., Ferreira, J. a. F., Melo, F. Q., Martins, M. and De Sousa, R. J. A. (2011) 'Finding the Best Machine for SPIF Operations - a Brief Discussion', *Key Engineering Materials*, 473, pp. 861–868. doi: 10.4028/www.scientific.net/KEM.473.861.

Martins, P. A. F., Kwiatkowski, L., Franzen, V., Tekkaya, A. E. and Kleiner, M. (2009) 'Single point incremental forming of polymers', *CIRP Annals - Manufacturing Technology*, 58(1), pp. 229–232. doi: 10.1016/j.cirp.2009.03.095.

Meier, H., Magnus, C., Buff, B. and Zhu, J. H. (2013) 'Tool Concepts and Materials for Incremental Sheet Metal Forming with Direct Resistance Heating', in *Key Engineering Materials*, pp. 61–67.

Meier, H., Magnus, C. and Smukala, V. (2011) 'Impact of superimposed pressure on dieless incremental sheet metal forming with two moving tools', *CIRP Annals - Manufacturing Technology*, 60(1), pp. 327–330. doi: 10.1016/j.cirp.2011.03.134.

Mishra, R. S., De, P. S. and Kumar, N. (2014) *Friction Stir Welding and Processing*. Cham: Springer International Publishing. doi: 10.1007/978-3-319-07043-8.

Music, O. and Allwood, J. M. (2011) 'Flexible asymmetric spinning', *CIRP Annals - Manufacturing Technology*, 60(1), pp. 319–322. doi: 10.1016/j.cirp.2011.03.136.

Myers, R. H., Montgomery, D. C. and Anderson-Cook, C. M. (2016) *Response Surface Methodology: Process and Product Optimization Using Designed Experiments*. Wiley (Wiley Series in Probability and Statistics).

Narendra B. Dahotre, S. P. H. (2008) *Laser fabrication and machining of materials*. Boston, MA: Springer US. doi: 10.1007/978-0-387-72344-0.

Nolo, H., Seitzman, L. E., Bolster, R. N. and Singer, I. L. (1996) 'lubrication of titanium alloys', *Surface and Coatings Technology*, 78, pp. 10–13.

Oosthuizen. G. A. (2017) 'presentation:Investigating the Impact of Tool Velocity on the Process Conditions in Incremental Forming of Titanium Sheets', *[PowerPoint presentation]*. Skukuza,: International Conference on Sustainable Materials Processing and Manufacturing, SMPM 2017, 23-25 January 2017, Skukuza, Kruger

National Park.

Otsu, M., Katayama, Y., Muranaka, T. and M. Otsu, Y. Katayama, T. M. (2014) 'Effect of Difference of Tool Rotation Direction on Forming Limit in Friction Stir Incremental Forming', *Key Engineering Materials*. Edited by Intergovernmental Panel on Climate Change. Cambridge: Cambridge University Press, 622(623), pp. 390–397. doi: 10.4028/www.scientific.net/KEM.622-623.390.

Otsu, M., Yasunaga, M., Matsuda, M. and Takashima, K. (2014) 'Friction stir incremental forming of A2017 aluminum sheets', *Procedia Engineering*. Elsevier B.V., 81(October), pp. 2318–2323. doi: 10.1016/j.proeng.2014.10.327.

Overton, G., Belforte, D. A. and Nogee, A. (2015) 'Laser Marketplace 2015 : Lasers surround us in the Year of Light', *Laser Focus World*, 11(2), pp. 1–100.

Palumbo, G. and Brandizzi, M. (2012) 'Experimental investigations on the single point incremental forming of a titanium alloy component combining static heating with high tool rotation speed', *Materials & Design*. Elsevier Ltd, 40, pp. 43–51. doi: 10.1016/j.matdes.2012.03.031.

Paunoiu, V., Squeo, E. a., Quadrini, F., Gheorghies, C. and Nicoara, D. (2008) 'Laser Bending of Stainless Steel Sheet Metals', *International Journal of Material Forming*, 1(S1), pp. 1371–1374. doi: 10.1007/s12289-008-0119-8.

Petek, A., Jurisevic, B., Kuzman, K. and Junkar, M. (2009) 'Comparison of alternative approaches of single point incremental forming processes', *Journal of Materials Processing Technology*, 209(4), pp. 1810–1815. doi: 10.1016/j.jmatprotec.2008.04.033.

Pickering, C. and Byrne, J. (2014) 'The benefits of publishing systematic quantitative literature reviews for PhD candidates and other early-career researchers', *Higher Education Research & Development*, 33(3), pp. 534–548. doi: 10.1080/07294360.2013.841651.

Pottier, T., Toussaint, F., Louche, H. and Vacher, P. (2013) 'Inelastic heat fraction estimation from two successive mechanical and thermal analyses and full-field measurements', *European Journal of Mechanics - A/Solids*. Elsevier Masson SAS, 38, pp. 1–11. doi: 10.1016/j.euromechsol.2012.09.002.

Powers, B. M., Ham, M. and Wilkinson, M. G. (2010) 'Small data set analysis in surface metrology: An investigation using a single point incremental forming case study', *Scanning*, 32(4), pp. 199–211. doi: 10.1002/sca.20202.

Q. Nadeem, Q. N. and S. J. Na, S. J. N. (2013) 'An approach to form the dome shape by 3D laser forming', *Chinese Optics Letters*, 11(2), pp. 21402–21405. doi: 10.3788/COL201311.021402.

Rajput, R. K. (2007) *A Textbook of Manufacturing Technology: Manufacturing Processes*. Laxmi.

Rauch, M., Hascoet, J.-Y. Y., Hamann, J.-C. C. and Plenel, Y. (2009) 'Tool path programming optimization for incremental sheet forming applications', *Computer-Aided Design*. Elsevier Ltd, 41(12), pp. 877–885. doi: 10.1016/j.cad.2009.06.006.

Ravichandran, G., Rosakis, A. J., Hodowany, J. and Rosakis, P. (2002) 'On the Conversion of Plastic Work into Heat During High-Strain-Rate Deformation', *AIP Conference Proceedings*, 620(1), pp. 557–562. doi: doi:10.1063/1.1483600.

Rekab, K. and Shaikh, M. (2005) *Statistical Design of Experiments with Engineering Applications*. CRC Press (Statistics: A Series of Textbooks and Monographs).

Ren, H., Moser, N., Zhang, Z., Ndip-Agbor, E., Smith, J., Ehmann, K. F. and Cao, J. (2015) 'Effects of Tool Positions in Accumulated Double-Sided Incremental Forming on Part Geometry', *Journal of Manufacturing Science and Engineering*, 137(5), p. 51008. doi: 10.1115/1.4030528.

Rocha, A. B., Araújo, R., Teixeira, P., Silva, M. B., Reis, A., Lino, J. and Martins, P. (2013) 'Damage prediction in incremental forming of titanium alloy ticp', in *Analytical, Computational, and Experimental Inelasticity in Deformable Solids*, pp. 49–51.

Roohi, A. H., Gollo, M. H. and Naeini, H. M. (2012) 'External force-assisted laser forming process for gaining high bending angles', *Journal of Manufacturing Processes*. The Society of Manufacturing Engineers, 14(3), pp. 269–276. doi: 10.1016/j.jmapro.2012.07.004.

Saldarriaga, J. and Vélez, S. (2011) 'Design and manufacturing of a custom skull implant', *American Journal of …*, 4(1), pp. 169–174.

Samuel, K. A. H. (2010) *Friction and external surface roughness in single point incremental forming: a study of surface friction, contact area and the 'Orange Peel' effect*. Queen‟s University.

Sherif, E. M., Almajid, a a, Latif, F. H. and Junaedi, H. (2011) 'Effects of Graphite on the Corrosion Behavior of Aluminum- Graphite Composite in Sodium Chloride Solutions', *International Journal of Electrochemical Science*, 6, pp. 1085–1099.

Shidid, D. P., Gollo, M. H., Brandt, M. and Mahdavian, M. (2013) 'Study of effect of process parameters on titanium sheet metal bending using Nd: YAG laser', *Optics & Laser Technology*. Elsevier, 47, pp. 242–247. doi: 10.1016/j.optlastec.2012.07.033.

Silva, M. B., Alves, L. M. and Martins, P. a. F. (2010) 'Single point incremental forming of PVC: Experimental findings and theoretical interpretation', *European Journal of Mechanics - A/Solids*. Elsevier Masson SAS, 29(4), pp. 557–566. doi: 10.1016/j.euromechsol.2010.03.008.

Silva, M. B., Nielsen, P. S., Bay, N. and Martins, P. A. F. (2011) 'Failure mechanisms in single-point incremental forming of metals', *The International Journal of Advanced Manufacturing Technology*, 56(9–12), pp. 893–903. doi: 10.1007/s00170-011-3254-1.

Silva, M. B., Skjoedt, M., Bay, N. and Martins, P. A. F. (2009) 'Revisiting single-point incremental forming and formability/failure diagrams by means of finite elements and experimentation', *The Journal of Strain Analysis for Engineering Design*, 44(4), pp. 221–234. doi: 10.1243/03093247JSA522.

Smith, G. T. (2013) *CNC Machining Technology: Volume 3: Part Programming Techniques*. Springer London (CNC Machining Technology).

Sortais, H. C., S.Kobayashi and G, E. T. (1963) 'Mechanics of conventional spinning', *Journal of Engineering for Industry*, 85, pp. 346–350.

Stat-Ease (2016) *Handbook for Experimenters: A concise collection of handy tips to help you set up and analyze your designed experiments*. Minneapolis: Stat-Ease, Inc.

Strano, M. (2005) 'Technological representation of forming limits for negative incremental forming of thin aluminum sheets', *Journal of Manufacturing Processes*, 7(2), pp. 122–129. doi: 10.1016/S1526-6125(05)70089-X.

Threadgill, P. L., Leonard, A. J., Shercliff, H. R. and Withers, P. J. (2009) 'Friction Stir Welding of Aluminium Alloys', *International Materials Reviews*, 54(2), pp. 49–93. doi: 10.1179/174328009X411136.

Triform (2012) *Next Generation Sheet Hydroforming Presses*. Available at: www.triformpress.com.

Trotec (2016) *Comparison of different Laser Types - CO2, Fiber Laser, Vanadat, Yag*. Available at: http://www.troteclaser.com/en-US/Support/FAQs/Pages/Laser-Types.aspx (Accessed: 5 July 2013).

Uheida, E. H., Oosthuizen, G. A. and Dimitrov, D. (2016) 'Toward Understanding the Process Limits of Incremental Sheet Forming of Titanium Alloys', in *Proceedings, COMA16' Int. Conf. on Competitive Manufacturing, 27-29 January 2016 Stellenbosch, South Africa*. Faculty of Engineering, Department of Industrial Engineering, Stellenbosch University., pp. 161–172.

Uheida, E. H., Oosthuizen, G. A. and Dimitrov, D. (2017) 'Investigating the Impact of Tool Velocity on the Process Conditions in Incremental Forming of Titanium Sheets', *Procedia Manufacturing*. Elsevier, 7(2016), pp. 345–350. doi: 10.1016/j.promfg.2016.12.085.

Vieira, L. C., Almeida, R. H. Z. De and Martins, F. P. R. (2010) 'Application of computer vision methods to estimate the coverage of peen formed plates', *Journal of Achievements in Materials and Manfacturing Engineering*, 43(2), pp. 743–749.

Vinet, L. and Zhedanov, A. (2011) 'A "missing" family of classical orthogonal polynomials', *Journal of Physics A: Mathematical and Theoretical*. W. H. Freeman, 44(8), p. 85201. doi: 10.1088/1751-8113/44/8/085201.

Wagner, M. and Norris, G. (2009) *Boeing 787 Dreamliner*. MBI Publishing Company.

Xu, D., Wu, W., Malhotra, R., Chen, J., Lu, B. and Cao, J. (2013) 'Mechanism investigation for the influence of tool rotation and laser surface texturing (LST) on formability in single point incremental forming', *International Journal of Machine Tools and Manufacture*, 73, pp. 37–46. doi: 10.1016/j.ijmachtools.2013.06.007.

Yadav, A. D. (2008) *Process Analysis and Design in Stamping and Sheet*. Ohio State University.

Yang, H., Fan, X., Sun, Z., Guo, L. and Zhan, M. (2011) 'Recent developments in plastic forming technology of titanium alloys', *Science China Technological Sciences*, 54(2), pp. 490–501. doi: 10.1007/s11431-010-4206-y.

Zettler, J. and Papadopoulos, M. P. (2011) 'Innovative manufacturing of complex Ti sheet components (INMA)', *International Journal of Structural Integrity*. Emerald Group Publishing Limited, 2(4), p. null. doi: 10.1108/ijsi.2011.43602daa.002.

Zimm, P. (2015) *Aerospace Production & Supply Chain Outlook*. Orlando, FL: icfi.com/aviation|Passion. Experties.Results.

Addendum A List of publications used in the conceptualisation stage

Adams, D. and Jeswiet, J. (2014) 'Single-point incremental forming of 6061-T6 using electrically assisted forming methods', *Proceedings of the Institution of Mechanical Engineers, Part B: Journal of Engineering Manufacture*, 228(7), pp. 757–764. doi: 10.1177/0954405413501670.

Adams, D. and Jeswiet, J. (2015a) 'A new model for contact geometry in single-point incremental forming', *Proceedings of the Institution of Mechanical Engineers, Part B: Journal of Engineering Manufacture*, 229(6), pp. 982–989. doi: 10.1177/0954405414535580.

Adams, D. and Jeswiet, J. (2015b) 'Design rules and applications of single-point incremental forming', *Proceedings of the Institution of Mechanical Engineers, Part B: Journal of Engineering Manufacture*, 229(5), pp. 754–760. doi: 10.1177/0954405414531426.

Aerens, R., Eyckens, P., Bael, A. and Duflou, J. R. (2009) 'Force prediction for single point incremental forming deduced from experimental and FEM observations', *The International Journal of Advanced Manufacturing Technology*, 46(9–12), pp. 969– 982. doi: 10.1007/s00170-009-2160-2.

Al-Ghamdi, K. a., Hussain, G. and Butt, S. I. (2014) 'Force Variations with Defects and a Force-Based Strategy to Control Defects in SPIF', *Materials and Manufacturing Processes*, 29(July 2014), p. 140730120216008.doi:10.1080/10426914.2014.93091.

Al-Ghamdi, K. and Hussain, G. (2014) 'The Pillowing Tendency of materials in single-point incremental forming: Experimental and finite element analyses', *Proceedings of the Institution of Mechanical Engineers, Part B: Journal of Engineering Manufacture*. doi: 10.1177/0954405414530906.

Allwood, J. M., Braun, D. and Music, O. (2010) 'The effect of partially cut-out blanks on geometric accuracy in incremental sheet forming', *Journal of Materials Processing Technology*. Elsevier B.V., 210(11), pp. 1501– 1510. doi: 10.1016/j.jmatprotec.2010.04.008.

Ambrogio, G., L. Filice, F. G., Ambrogio, G., Filice, L. and Gagliardi, F. (2012) 'Formability of lightweight alloys by hot incremental sheet forming', *Materials & Design*. Elsevier Ltd, 34, pp. 501–508. doi: 10.1016/j.matdes.2011.08.024.

Ambrogio, G., Filice, L. and Gagliardi, F. (2012) 'Improving industrial suitability of incremental sheet forming process', *The International Journal of Advanced Manufacturing Technology*, 58(9–12), pp. 941– 947. doi: 10.1007/s00170-011-3448-6.

Ambrogio, G., Filice, L. and Manco, G. L. (2008) 'Considerations on the incremental forming of deep geometries', *International Journal of Material Forming*, pp. 1143–1146. doi: 10.1007/s12289-008-0.

Ambrogio, G., Filice, L. and Manco, G. L. (2008) 'Warm incremental forming of magnesium alloy AZ31', *CIRP Annals - Manufacturing Technology*, 57(1), pp. 257– 260. doi: 10.1016/j.cirp.2008.03.066.

Ambrogio, G., Filice, L. and Micari, F. (2006) 'A force measuring based strategy for failure prevention in incremental forming', *Journal of Materials Processing Technology*, 177(1–3), pp. 413–416. doi: 10.1016/j.jmatprotec.2006.04.076.

Ambrogio, G., Gagliardi, F., Bruschi, S. and Filice, L. (2013) 'On the high-speed Single Point Incremental Forming of titanium alloys', *CIRP Annals - Manufacturing Technology*. CIRP, 62(1), pp. 243–246. doi: 10.1016/j.cirp.2013.03.053.

Ambrogio, G., De Napoli, L., Filice, L., Gagliardi, F. and Muzzupappa, M. (2005) 'Application of Incremental Forming process for high customised medical product manufacturing', *Journal of Materials Processing Technology*, 162–163(SPEC. ISS.), pp. 156–162. doi: 10.1016/j.jmatprotec.2005.02.148.

Arfa, H., Bahloul, R. and BelHadjSalah, H. (2013) 'Finite element modelling and experimental investigation of single point incremental forming process of aluminum sheets: Influence of process parameters on punch force monitoring and on mechanical and geometrical quality of parts', *International Journal of Material Forming*, 6(4), pp. 483–510. doi: 10.1007/s12289-012-1101-z.

Asghar, J., Lingam, R., Shibin, E. and Reddy, N. (2013) 'Tool path design for enhancement of accuracy in single-point incremental forming', *Proceedings of the Institution of Mechanical Engineers, Part B: Journal of Engineering Manufacture*, 228(9), pp. 1027– 1035. doi: 10.1177/0954405413512812.

Asghar, J. and Reddy, N. (2013) 'Importance of Tool Configuration in Incremental Sheet Metal Forming of Difficult to Form Materials using Electro-Plasticity', in *Proceedings of the World Congress on Engineering*. London. Available at: http://www.iaeng.org/publication/WCE2013/W CE2013_pp1734-1738.pdf (Accessed: 22 May 2014).

Azaouzi, M. and Lebaal, N. (2012) 'Tool path optimization for single point incremental sheet forming using response surface method', *Simulation Modelling Practice and Theory*. Elsevier B.V., 24, pp. 49–58. doi: 10.1016/j.simpat.2012.01.008.

Bagudanch, I., Centeno, G. and Vallellano, C. (2013) 'Forming force in Single Point Incremental Forming under different bending conditions', in *5th Manufacturing Engineering Society International Conference*. Zaragoza, pp. 1–6.

Bambach, M. (2010) 'A geometrical model of the kinematics of incremental sheet forming for the prediction of membrane strains and sheet thickness', *Journal of Materials Processing Technology*, 210(12), pp. 1562–1573. doi: 10.1016/j.jmatprotec.2010.05.003.

Behera, A. K., Verbert, J., Lauwers, B. and Duflou, J. R. (2013) 'Tool path compensation strategies for single point incremental sheet forming using multivariate adaptive regression splines', *Computer-Aided Design*. Elsevier Ltd, 45(3), pp. 575–590. doi: 10.1016/j.cad.2012.10.045.

Belchior, J., Guines, D., Leotoing, L. and Ragneau, E. (2013) 'Force Prediction for Correction of Robot Tool Path in Single Point Incremental Forming', *Key Engineering Materials*, 554–557, pp. 1282–1289. doi: 10.4028/www.scientific.net/KEM.554-557.1282.

Bhattacharya, A., Maneesh, K., Venkata Reddy, N. and Cao, J. (2011) 'Formability and Surface Finish Studies in Single Point Incremental Forming', *Journal of Manufacturing Science and Engineering*, 133(6), p. 61020. doi: 10.1115/1.4005458.

Centeno, G., Silva, M. B., Cristino, V. A. M., Vallellano, C. and Martins, P. A. F. (2012) 'Hole-flanging by incremental sheet forming', *International Journal of Machine Tools and Manufacture*. Elsevier, 59, pp. 46–54. doi: 10.1016/j.ijmachtools.2012.03.007.

Chezhian Babu, S. and Senthil Kumar, V. S. (2012) 'Experimental studies on incremental forming of stainless steel AISI 304 sheets', *Proceedings of the Institution of Mechanical Engineers, Part B: Journal of Engineering Manufacture*, 226(7), pp. 1224–1229. doi: 10.1177/0954405412441286.

Crina, R. (2010) 'New Configurations of the SPIF Process - A Review', *Journal of Engineering Studies and Research*, 16(4), pp. 33–39.

Daleffe, A., Schaeffer, L., Fritzen, D. and Castelan, J. (2013) 'Analysis of the Incremental Forming of Titanium F67 Grade 2 Sheet', *Key Engineering Materials*, 554–557, pp. 195–203. doi: 10.4028/www.scientific.net/KEM.554-557.195.

Dejardin, S., Thibaud, S., Gelin, J. C. and Michel, G. (2010) 'Experimental investigations and numerical analysis for improving knowledge of incremental sheet forming process for sheet metal parts', *Journal of Materials*, 210, pp. 363–369. doi: 10.1016/j.jmatprotec.2009.09.025.

Dittrich, M. A., Gutowski, T. G., Cao, J., Roth, J. T., Xia, Z. C., Kiridena, V., Ren, F. and Henning, H. (2012) 'Exergy analysis of incremental sheet forming', *Production Engineering*, 6(2), pp. 169–177. doi: 10.1007/s11740-012-0375-9.

Duflou, J. R., Callebaut, B., Verbert, J. and De Baerdemaeker, H. (2007) 'Laser Assisted Incremental Forming: Formability and Accuracy Improvement', in *CIRP Annals - Manufacturing Technology*, pp. 273–276. doi: 10.1016/j.cirp.2007.05.063.

Duflou, J. R. and D'hondt, J. (2011) 'Applying TRIZ for systematic manufacturing process innovation: the single point incremental forming case', *Procedia Engineering*, 9, pp. 528–537. doi: 10.1016/j.proeng.2011.03.139.

Duflou, J. R., Vanhove, H., Verbert, J., Gu, J., Vasilakos, I. and Eyckens, P. (2010) 'Twist revisited: Twist phenomena in single point incremental forming', *CIRP Annals - Manufacturing Technology*, 59(1), pp. 307– 310. doi: 10.1016/j.cirp.2010.03.018.

Duflou, J. R., Verbert, J., Belkassem, B., Gu, J., Sol, H., Henrard, C. and Habraken, A. M. (2008) 'Process window enhancement for single point incremental forming through multi-step toolpaths', *CIRP Annals - Manufacturing Technology*, 57(1), pp. 253–256. doi: 10.1016/j.cirp.2008.03.030.

Duflou, J., Tunçkol, Y., Szekeres, A., Vanherck, P. and Tunckol, Y. (2007) 'Experimental study on force measurements for single point incremental forming', *Journal of Materials Processing Technology*, 189(1–3), pp. 65–72. doi: 10.1016/j.jmatprotec.2007.01.005.

Durante, M., Formisano, A. and Langella, A. (2011) 'Observations on the Influence of Tool-Sheet Contact Conditions on an Incremental Forming Process', *Journal of Materials Engineering and Performance*, 20(6), pp. 941– 946. doi: 10.1007/s11665-010-9742-x.

Durante, M., Formisano, A., Langella, A. and Capece Minutolo, F. M. (2009) 'The influence of tool rotation on an incremental forming process', *Journal of Materials Processing Technology*, 209(9), pp. 4621–4626. doi: 10.1016/j.jmatprotec.2008.11.028.

Echrif, S. B. M. and Hrairi, M. (2014) 'Significant Parameters for the Surface Roughness in Incremental Forming Process', *Materials and Manufacturing Processes*. Taylor & Francis, 29(6), pp. 697–703. doi: 10.1080/10426914.2014.901519.

Essa, K. and Hartley, P. (2010) 'An assessment of various process strategies for improving precision in single point incremental forming', *International Journal of Material Forming*, 4(4), pp. 401–412. doi: 10.1007/s12289-010-1004-9.

Fan, G. and Gao, L. (2014) 'Mechanical property of Ti-6Al-4V sheet in one-sided electric hot incremental forming', *International Journal of Advanced Manufacturing Technology*, 72(5–8), pp. 989–994. doi: 10.1007/s00170-014-5733-7.

Fan, G., Gao, L., Hussain, G. and Wu, Z. (2008) 'Electric hot incremental forming: A novel technique', *International Journal of Machine Tools and Manufacture*, 48(15), pp. 1688–1692. doi: 10.1016/j.ijmachtools.2008.07.010.

Fan, G., Sun, F., Meng, X., Gao, L. and Tong, G. (2009) 'Electric hot incremental forming of Ti-6Al-4V titanium sheet', *The International Journal of Advanced Manufacturing Technology*, 49(9–12), pp. 941–947. doi: 10.1007/s00170-009-2472-2.

Fang, Y., Lu, B., Chen, J., Xu, D. K. and Ou, H. (2014) 'Analytical and experimental investigations on deformation mechanism and fracture behavior in single point incremental forming', *Journal of Materials Processing Technology*, 214(8), pp. 1503–1515. doi: 10.1016/j.jmatprotec.2014.02.019.

Fiorentino, A., Marenda, G. P., Marzi, R., Ceretti, E., Kemmoku, D. T. and Silva, J. V. L. (2011) 'Rapid Prototyping techniques for individualized medical prosthesis manufacturing', in *Innovative Developments in Virtual and Physical Prototyping*. CRC Press, pp. 589–594. doi: 10.1201/b11341-94.

Fu, Z., Mo, J., Han, F. and Gong, P. (2012) 'Tool path correction algorithm for single-point incremental forming of sheet metal', *The International Journal of Advanced Manufacturing Technology*, 64(9–12), pp. 1239–1248. doi: 10.1007/s00170-012-4082-7.

Gulati, V., Kathuria, S. and Katyal, P. (2015) 'A Paradigm to Produce Customized Ankle Support Using Incremental Sheet Forming', *Journal of Engineering and Technology*, 5(1), p. 14. doi: 10.4103/0976-8580.149474.

Hamilton, K. and Jeswiet, J. (2010) 'Single point incremental forming at high feed rates and rotational speeds: Surface and structural consequences', *CIRP Annals - Manufacturing Technology*. CIRP, 59(1), pp. 311–314. doi: 10.1016/j.cirp.2010.03.016.

HAN, F., MO, J., QI, H., LONG, R., CUI, X. and LI, Z. (2013) 'Springback prediction for incremental sheet forming based on FEM-PSONN technology', *Transactions of Nonferrous Metals Society of China*, 23(4), pp. 1061–1071. doi: 10.1016/S1003-6326(13)62567-4.

Henrard, C., Bouffioux, C., Eyckens, P., Sol, H., Duflou, J. R., Van Houtte, P., Van Bael, A., Duchêne, L. and Habraken, a. M. (2011) 'Forming forces in single point incremental forming: prediction by finite element simulations, validation and sensitivity', *Computational Mechanics*, 47(5), pp. 573–590. doi: 10.1007/s00466-010-0563-4.

Hmida, R. Ben, Thibaud, S., Gilbin, A. and Richard, F. (2012) 'Influence of the initial grain size in single point incremental forming process for thin sheets metal and microparts: Experimental investigations', *Materials & Design*. Elsevier Ltd, 45, pp. 155–165. doi: 10.1016/j.matdes.2012.08.077.

Hussain, G. (2013) 'Experimental investigations on the role of tool size in causing and controlling defects in single point incremental forming process', *Journal of Engineering Manufacture*. doi: 10.1177/0954405413498864.

Hussain, G., Al-Ghamdi, K. A., Khalatbari, H., Iqbal, A. and Hashemipour, M. (2014) 'Forming Parameters and Forming Defects in Incremental Forming Process: Part B', *Materials and Manufacturing Processes*, 29(4), pp. 454–460. doi: 10.1080/10426914.2014.880457.

Hussain, G., Gao, L. and Hayat, N. (2009) 'Empirical modelling of the influence of operating parameters on the spifability of a titanium sheet using response surface methodology', *Proceedings of the Institution of Mechanical Engineers, Part B: Journal of Engineering Manufacture*, 223(1), pp. 073– 081. doi: 10.1243/09544054JEM1259.

Hussain, G., Gao, L., Hayat, N. and Dar, N. U. (2010) 'The formability of annealed and pre-aged AA-2024 sheets in single-point incremental forming', *International Journal of Advanced Manufacturing Technology*, 46(5–8), pp. 543–549. doi: 10.1007/s00170-009-2120-x.

Hussain, G., Gao, L. and Zhang, Z. Y. (2007) 'Formability evaluation of a pure titanium sheet in the cold incremental forming process', *The International Journal of Advanced Manufacturing Technology*, 37(9–10), pp. 920–926. doi: 10.1007/s00170-007-1043-7.

Hussain, G., Hayat, N. and Gao, L. (2008) 'An experimental study on the effect of thinning band on the sheet formability in negative incremental forming', *International Journal of Machine Tools and Manufacture*, 48(10), pp. 1170–1178. doi: 10.1016/j.ijmachtools.2008.02.003.

Hussain, G., Hayat, N. and Lin, G. (2012) 'Pyramid as test geometry to evaluate formability in incremental forming: Recent results', *Journal of Mechanical Science and Technology*, 26(8), pp. 2337–2345. doi: 10.1007/s12206-012-0617-y.

Hussain, G., Khan, H. R., Gao, L. and Hayat, N. (2013) 'Guidelines for Tool-Size Selection for Single-Point Incremental Forming of an Aerospace Alloy', *Materials and Manufacturing Processes*, 28(3), pp. 324–329. doi: 10.1080/10426914.2012.700151.

Hussain, G., Lin, G. and Hayat, N. (2010) 'A new parameter and its effect on the formability in single point incremental forming: A fundamental investigation', *Journal of Mechanical Science and Technology*, 24(8), pp. 1617–1621. doi: 10.1007/s12206-010-0514-1.

Ingarao, G., Ambrogio, G., Gagliardi, F. and Di Lorenzo, R. (2012) 'A sustainability point of view on sheet metal forming operations: material wasting and energy consumption in incremental forming and stamping processes', Journal of Cleaner Production, 29–30, pp. 255–268. doi: 10.1016/j.jclepro.2012.01.012..

Isik, K., Silva, M. B., Tekkaya, A. E. and Martins, P. A. F. (2014) 'Formability limits by fracture in sheet metal forming', *Journal of Materials Processing Technology*. Elsevier B.V., 214(8), pp. 1557–1565. doi: 10.1016/j.jmatprotec.2014.02.026.

Junchao, L., Junjian, S. and Bin, W. (2013) 'A multipass incremental sheet forming strategy of a car taillight bracket', *The International Journal of Advanced Manufacturing Technology*, 69(9–12), pp. 2229–2236. doi: 10.1007/s00170-013-5179-3.

Jurisevic, B., Kuzman, K. and Junkar, M. (2006) 'Water jetting technology: an alternative in incremental sheet metal forming', *The International Journal of Advanced Manufacturing Technology*, 31(1–2), pp. 18– 23. doi: 10.1007/s00170-005-0176-9.

Khalatbari, H., Iqbal, A., Shi, X., Gao, L., Hussain, G. and Hashemipour, M. (2015) 'High-Speed Incremental Forming Process: A Trade-Off Between Formability and Time Efficiency', *Materials and Manufacturing Processes*, 30(11), pp. 1354–1363. doi: 10.1080/10426914.2015.1037892.

Kurra, S., HR, N., Regalla, S. and Gupta, A. K. (2015) 'Parametric study and multi-objective optimization in single-point incremental forming of extra deep drawing steel sheets', *Proceedings of the Institution of Mechanical Engineers, Part B: Journal of Engineering Manufacture*. doi: 10.1177/0954405414564408.

León, J., Salcedo, D., Ciáurriz, C., Luis, C. J., Fuertes, J. P., Puertas, I. and Luri, R. (2013) 'Analysis of the Influence of Geometrical Parameters on the Mechanical Properties of Incremental Sheet Forming Parts', *Procedia Engineering*. Elsevier B.V., 63, pp. 445–453. doi: 10.1016/j.proeng.2013.08.206.

Li, Y., Liu, Z., Daniel, W. J. T. (Bill. and Meehan, P. A. (2014) 'Simulation and Experimental Observations of Effect of Different Contact Interfaces on the Incremental Sheet Forming Process', *Materials and Manufacturing Processes*, 29(2), pp. 121–128. doi: 10.1080/10426914.2013.822977.

Li, Y., Liu, Z., Lu, H., Daniel, W. J. T., Liu, S. and Meehan, P. A. (2014) 'Efficient force prediction for incremental sheet forming and experimental validation', *The International Journal of Advanced Manufacturing Technology*, 73(1–4), pp. 571–587. doi: 10.1007/s00170-014-5665-2.

Liu, Z., Daniel, W. J. T., Li, Y., Liu, S. and Meehan, P. A. (2014) 'Multi-pass deformation design for incremental sheet forming: Analytical modelling, finite element analysis and experimental validation', *Journal of Materials Processing Technology*. Elsevier B.V., 214(3), pp. 620–634. doi: 10.1016/j.jmatprotec.2013.11.010.

Liu, Z., Li, Y. and Meehan, P. A. (2013) 'Experimental investigation of mechanical properties, formability and force measurement for AA7075-O aluminum alloy sheets formed by incremental forming', *International Journal of Precision Engineering and Manufacturing*, 14(11), pp. 1891–1899. doi: 10.1007/s12541-013-0255-z.

Liu, Z., Liu, S., Li, Y. and Meehan, P. A. (2014) 'Modeling and Optimization of Surface Roughness in Incremental Sheet Forming using a Multi-objective Function', *Materials and Manufacturing Processes*, 29(7), pp. 808–818. doi: 10.1080/10426914.2013.864405.

Lora, F. A. and Schaeffer, L. (2014) 'Incremental forming process strategy variation analysis through applied strains', *Brazilian Journal of Science and Technology*, 1(2005), pp. 1–8. doi: 10.1186/2196-288X-1-5.

Lu, B., Chen, J., Ou, H. and Cao, J. (2013) 'Feature-based tool path generation approach for incremental sheet forming process', *Journal of Materials Processing Technology*, 213(7), pp. 1221–1233. doi: 10.1016/j.jmatprotec.2013.01.023.

Malhotra, R, Huang, Y, Xue, L, Cao, J & Belytschko, T 2010, An investigation on the accuracy of numerical simulations for single point incremental forming with continuum elements. in *AIP Conference Proceedings*. vol. 1252, pp. 221-227, 10th International Conference on Numerical Methods in Industrial Forming Processes Dedicated to Professor O. C. Zienkiewicz (1921-2009), NUMIFORM 2010, Pohang, Korea, Republic of, 13-17 June. DOI: 10.1063/1.3457555.

Malhotra, R., Reddy, N. V. and Cao, J. (2010) 'Automatic 3D Spiral Toolpath Generation for Single Point Incremental Forming', *Journal of Manufacturing Science and Engineering*, 132(6), p. 61003. doi: 10.1115/1.4002544.

Malhotra, R., Xue, L., Belytschko, T. and Cao, J. (2012) 'Mechanics of fracture in single point incremental forming', *Journal of Materials Processing Technology*. Elsevier B.V., 212(7), pp. 1573–1590. doi: 10.1016/j.jmatprotec.2012.02.021.

Manco, L., Filice, L. and Ambrogio, G. (2011) 'Analysis of the thickness distribution varying tool trajectory in single-point incremental forming', in *Proceedings of the Institution of Mechanical Engineers, Part B: Journal of Engineering Manufacture* …. SAGE, pp. 348– 356. doi: 10.1177/09544054JEM1958.

Martins, P. A. F., Kwiatkowski, L., Franzen, V., Tekkaya, A. E. and Kleiner, M. (2009) 'Single point incremental forming of polymers', *CIRP Annals - Manufacturing Technology*, 58(1), pp. 229–232. doi: 10.1016/j.cirp.2009.03.095.

Meier, H., Buff, B., Laurischkat, R. and Smukala, V. (2009) 'Increasing the part accuracy in dieless robot-based incremental sheet metal forming', *CIRP Annals - Manufacturing Technology*, 58(1), pp. 233– 238. doi: 10.1016/j.cirp.2009.03.056.

Mohammadi, A., Vanhove, H., Van Bael, A. and Duflou, J. R. (2013) 'Influence of laser assisted single point incremental forming on the accuracy of shallow sloped parts', in *NUMISHEET 2014*. Melbourne, pp. 864–867. doi: 10.1063/1.4850107.

Mosecker, L., Göttmann, A., Saeed-Akbari, A., Bleck, W., Bambach, M. and Hirt, G. (2013) 'Deformation Mechanisms of Ti6Al4V Sheet Material during the Incremental Sheet Forming with Laser Heating', *Key Engineering Materials*, 549, pp. 372–380. doi: 10.4028/www.scientific.net/KEM.549.372.

Nguyễn, T. and Phan, Đ. (2009) 'Research on the forming angle of A1050-h14 aluminum material processed by using single point incremental forming technology (SPIF), *Vnulib. Edu.Vn*, 12(16), pp. 72–79. Available at: http://www.vnulib.edu.vn:8000/dspace/ handle/ 123456789/3525.

Obikawa, T., Satou, S. and Hakutani, T. (2009) 'Dieless incremental micro-forming of miniature shell objects of aluminum foils', *International Journal of Machine Tools and Manufacture*. Elsevier, 49(12–13), pp. 906–915. doi: 10.1016/j.ijmachtools.2009.07.001.

Oleksik, V., Pascu, A., Deac, C., Fleacă, R., Bologa, O. and Racz, G. (2010) 'Experimental study on the surface quality of the medical implants obtained by single point incremental forming', *International Journal of Material Forming*, 3(S1), pp. 935–938. doi: 10.1007/s12289-010-0922-x.

Palumbo, G. and Brandizzi, M. (2012) 'Experimental investigations on the single point incremental forming of a titanium alloy component combining static heating with high tool rotation speed', *Materials & Design*. Elsevier Ltd, 40, pp. 43–51. doi: 10.1016/j.matdes.2012.03.031.

Petek, a., Jurisevic, B., Kuzman, K. and Junkar, M. (2009) 'Comparison of alternative approaches of single point incremental forming processes', *Journal of Materials Processing Technology*, 209(4), pp. 1810–1815. doi: 10.1016/j.jmatprotec.2008.04.033.

Petek, a. and Kuzman, K. (2009) 'Deformations and forces analysis of single point incremental sheet metal forming', *international scientific Journal*, 35(2), pp. 107–116. Available at: http://archivesmse.org/ vol35_2/3527.pdf (Accessed: 18 June 2012).

Rattanachan, K. (2009) 'Formability in Single Point Incremental Forming of Dome Geometry', *Aijstpme.Kmutnb.Ac.Th*, 2, pp. 57–63. Available at: http://www.aijstpme.kmutnb.ac.th/PDF/Vol.2 No.4/11.pdf (Accessed: 18 June 2012).

Robert, C., Ben Ayed, L., Delamézière, a., Dal Santo, P. and Batoz, J.-L. (2010) 'Development of a simplified approach of contact for incremental sheet forming', *International Journal of Material Forming*, 3(S1), pp. 987–990. doi: 10.1007/s12289-010-0935-5.

Sarraji, W. K. H., Hussain, J. and Ren, W.-X. (2012) 'Experimental Investigations on Forming Time in Negative Incremental Sheet Metal Forming Process', *Materials and Manufacturing Processes*, 27(5), pp. 499–506. doi: 10.1080/10426914.2011.585550.

Shi, X., Gao, L., Khalatbari, H., Xu, Y., Wang, H. and Jin, L. (2013) 'Electric hot incremental forming of low carbon steel sheet: accuracy improvement', *The International Journal of Advanced Manufacturing Technology*, 68(1–4), pp. 241–247. doi: 10.1007/s00170-013-4724-4.

Silva, M. B., Nielsen, P. S., Bay, N. and Martins, P. A. F. (2011) 'Failure mechanisms in single-point incremental forming of metals', *The International Journal of Advanced Manufacturing Technology*, 56(9–12), pp. 893– 903. doi: 10.1007/s00170-011-3254-1.

Silva, M. B., Skjoedt, M., Bay, N. and Martins, P. A. F. (2009) 'Revisiting single-point incremental forming and formability/failure diagrams by means of finite elements and experimentation', *The Journal of Strain Analysis for Engineering Design*, 44(4), pp. 221–234. doi: 10.1243/03093247JSA522.

Smith, J., Malhotra, R., Liu, W. K. and Cao, J. (2013) 'Deformation mechanics in single-point and accumulative double-sided incremental forming', *The International Journal of Advanced Manufacturing Technology*, 69(5–8), pp. 1185–1201. doi: 10.1007/s00170-013-5053-3.

Suresh, K., Bagade, S. D. and Regalla, S. P. (2015) 'Deformation Behavior of Extra Deep Drawing Steel in Single-Point Incremental Forming', *Materials and Manufacturing Processes*, 30(10), pp. 1202–1209. doi: 10.1080/10426914.2014.994755.

Van Sy, L. and Thanh Nam, N. (2013) 'Hot incremental forming of magnesium and aluminum alloy sheets by using direct heating system', in *Proceedings of the Institution of Mechanical Engineers, Part B: Journal of Engineering Manufacture*, pp. 1099–1110. doi: 10.1177/0954405413484014.

Takano, H., Kitazawa, K. and Goto, T. (2008) 'Incremental forming of nonuniform sheet metal: Possibility of cold recycling process of sheet metal waste', *International Journal of Machine Tools and Manufacture*, 48(3–4), pp. 477–482. doi: 10.1016/j.ijmachtools.2007.10.009.

Tanaka, S., Nakamura, T., Hayakawa, K., Nakamura, H. and Motomura, K. (2007) 'Residual Stress In Sheet Metal Parts Made By Incremental Forming Process', in *AIP Conference Proceedings*. AIP, pp. 775–780. doi: 10.1063/1.2740904.

Tisza, M. (2012) 'General overview of sheet incremental forming', *Manufacturing Engineering*, 55(1), pp. 113–120. Available at: http://www.journalamme.org/papers_vol55_1/5 5114.pdf (Accessed: 23 October 2012).

Tisza, M., Panity, I. and Kovács, P. Z. (2010) 'Experimental and numerical study of a milling machine-based dieless incremental sheet forming', *International Journal of Material Forming*, 3(S1), pp. 971–974. doi: 10.1007/s12289-010-0931-9.

Wei, H., Chen, W. and Gao, L. (2011) 'Springback Investigation on Sheet Metal Incremental Formed Parts', *waset.org*, 55(1), pp. 285–289. Available at: http://waset.org/journals/waset/v55/v55-57.pdf (Accessed: 29 May 2013).

Ziran, X., Gao, L., Hussain, G. and Cui, Z. (2010) 'The performance of flat end and hemispherical end tools in single-point incremental forming', *International Journal of Advanced Manufacturing Technology*, 46(9– 12), pp. 1113–1118. doi: 10.1007/s00170-009-2179-4.

Addendum B Protocol for design and implementation of experiments

B-1-1 Preparations, mounting and positioning the test platform

Test elements and terminology described in the protocol are:

No	Acronym	Description
1	CNC	DMU 65 triple-axis CNC machine
2	Kistler	Six-component dynamometer table-type 9255C
3	Fixture	Blank holding (clamping) fixture
4	Pyrometer	Infrared camera type Ranger MX4
5	PC	Laptop for measurement control and data storing unit
6	Cables	Signal connecting wires in test platform
7	W.P	Workpiece prepared of commercial pure titanium sheet
8	Tool	Round nose punch made for the forming operations
9	Lubricant	98.5% pure MoS_2 powder

Note

- *Adhere to general laboratory safety procedures and rules*
- *To improve the experimental reproductively all workflow steps must be performed in the prescribed instructions and order. Please confirm by ticking the accomplished plug as follows:*
- *Workflow steps marked with ❶ to be confirmed by experimenter,*
- *other with ❷ should be confirmed by both the experimenter and lap technician*

Mounting and positing the KISTLER dynamometer on the CNC table

❷ Ensure mounting surface on CNC table is thoroughly cleaned

❷ Align the Kistler to accessible position on CNC table, to align use side wall of Kistler flange

❷ Make sure the Kistler rests absolutely flat on the CNC table

❷ Mount the Kistler with M16 bolts/claws, tightening moment 4 X M16 bolts=280 N·m

Mounting the SPIF fixture on top of the Kistler

❷ Bottom surfaces for the Fixture must be face-ground and thoroughly cleaned

❷ Ensure the correct assembly of the Fixture, and mounting bolts are tighten firmly

❷ Mount the Fixture onto the Kistler with 8 M12X15 bolts, tighten moment = 60 N·m

Circuitry and Cabling the Kistler

Connecting cable from Dynamometer to Charge Amplifier

- ❷ Remove the protective caps from the connection only immediately before connecting
- ❷ Connect the Dynamometer to Charge Amplifier using cable 1687B5-type (see Figure B-1)
- ❷ Lay the connecting Cable so that it cannot get cut off or torn out when working
- ❷ Make sure all work with electrical connections is done carefully and cleanly

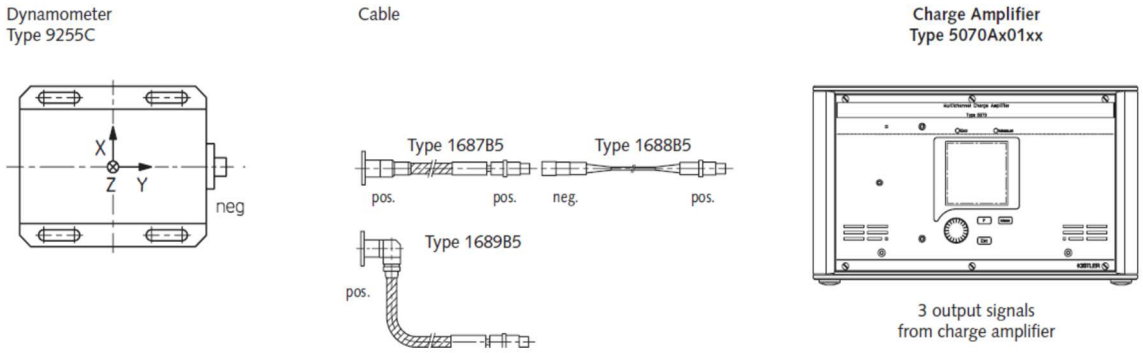

Figure B-1: Allocating and connecting Cable Type 1687B

Setting up the Type 5697 DAQ system software

- ❶ Ensure DynoWare software is completely installed on the PC
- ❶ Switch power switch of the DAQ to OFF position (refer to Figure B-2)
- ❶ Tightened the outer ring of the connector clockwise
- ❶ Connect the other end of the power adapter to the main power
- ❶ Connect the DAQ to the PC with the included USB cable
- ❶ Insert the USB runtime license dongle (HASP Key) into the matching slot in the DAQ
- ❶ Switch the DAQ system for DynoWare ON after starting the Windows operating system

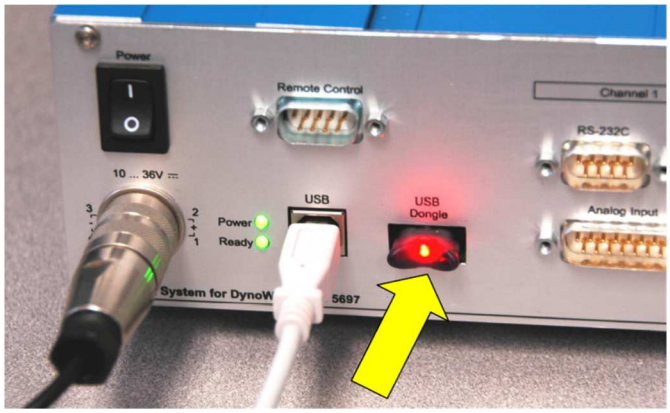

Figure B-2: Connecting 5697 DAQ system

Components configuring and putting in Operation

Configuring the DAQ using InstaCal

- USB-253 DAQ board must be configured using Measurement Computing – InstaCal
- Set up RS232 – C drivers to allow DAQ 5697 communication with Kistler amplifier
- Insert the USB Hasp stick (HASP License Key) into USB dongle port

Configuring the Kistler

- Confirm right connecting of all the components (sensor, amplifier, DAQ and PC)
- Switch ON the Amplifier 5070 and allow for worming 30 minutes
- Set measuring range (maximum force expected) as 4KN on channels 1,2&3
- Set sensor Sensitivity for Channel 1, 2& 3 according to the Calibration Sheet
- Select appropriate interval (expected time) for the Measuring Cycle
- When ready, press start measuring cycle (Green button) on screen
- When measure cycle ends, Save resulted data with File name = Run code
- Repeat the last underlined three steps for all upcoming test runs

Configuring the Pyrometer

- Attach the Pyrometer through onto stand with magnetic base, lock the quick-release clip
- Switch the DIP Switch Lock to ON position and connect the AC power adapter
- Keep optimal distance between Pyrometer sensor and object (from 10 cm up to 50 cm)
- Locate the stand on the CNC table and turn ON the Magnetic Base switch
- Connect the Pyrometer to PC via RS-232 and confirm the Online mode
- Align the Pyrometer precisely (use Laser Function) at target spot on backside of the W.P
- Start Measuring command and. Start Recording when test run is started
- When test ends, press Stop Recording. Save measured data, File Name = run code
- Repeat the underlined steps in every test run

Forming strategy

- All experimental runs must be performed using the same provided benchmark profile
- Original flat top surface of the mounted W.P is the reference surface i.e. x-y plane and z = 0
- During operation, Tool moves from outside edge, point, toward the W.P centre (Out – to – in)
- Select Finishing pass, Roll over all surfaces, and centre of the tool follows a Spiral tool path
- Tool feed anticlockwise, tool rotation clockwise (retreating) direction
- Test runs start at Fixture Ref Angle (as outlined in Figure B-3) and follow execution sequence
- Extremes (High, Low) levels of remaining necessary forming parameters, namely, sheet thickness, tool size, step down, tool rotation speed and feed rate, are provided in the test layout

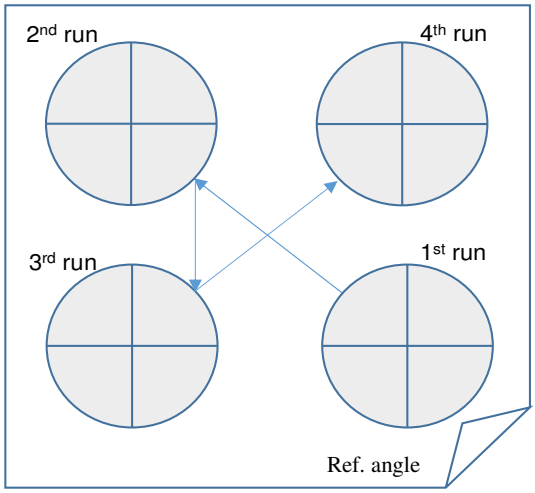

Figure B-3: Sequence of run execution

Perfuming experiments and data acquisition

01) Ensure forming tool is polished, cleaned and stably clamped onto CNC spindle

02) Unscrew the 8 bolts on top of the Fixture and remove the blank-holding plate

03) Pick a marked W.P according to the current run code

04) Position W.P (painted side downward) in Fixture recess and align it precisely to the Ref angle

05) Place the blank-holder back and tighten the 8 x M12 blots evenly (moment =130 N·m)

06) Apply one scale-unit of MoS2 powder, rub gently on the surface. Fill the working space with the powder spread uniformly to fully cover working surface.

07) Start forming operation following the strategy specified in Section 3

08) Keep close monitoring of both CNC and the produced force graph on the PC

09) Halt the CNC immediately when W.P breaks (produces sound/sharp drop of force graph)

10) Record final tool Z-level and forming duration as shown on the CNC panel

11) Measure and record maximum forming achieved height using depth Varner

12) Save resulted data from Kistler and Pyrometer to their corresponding files and directory

13) On Layout Table, corresponding accomplished run, mark as Done

14) Repeat steps (from 06 to 11) in the second, third and fourth run on the same W.P

15) After the 4 consecutive runs have been done, detach the blank-holder

16) Remove and clean the component and store it safe from any post-processing alterations

17) Pick the next marked W.P corresponding to upcoming run code

18) Go through steps from 01 to 15 up until the all runs on the layout have been concluded

Designed by	Approved by	Date
EH Uheida	Dr. Oosthuizen	25/04/016

B-2 Design drawing of the forming fixture main parts

The Top-plate of forming fixture

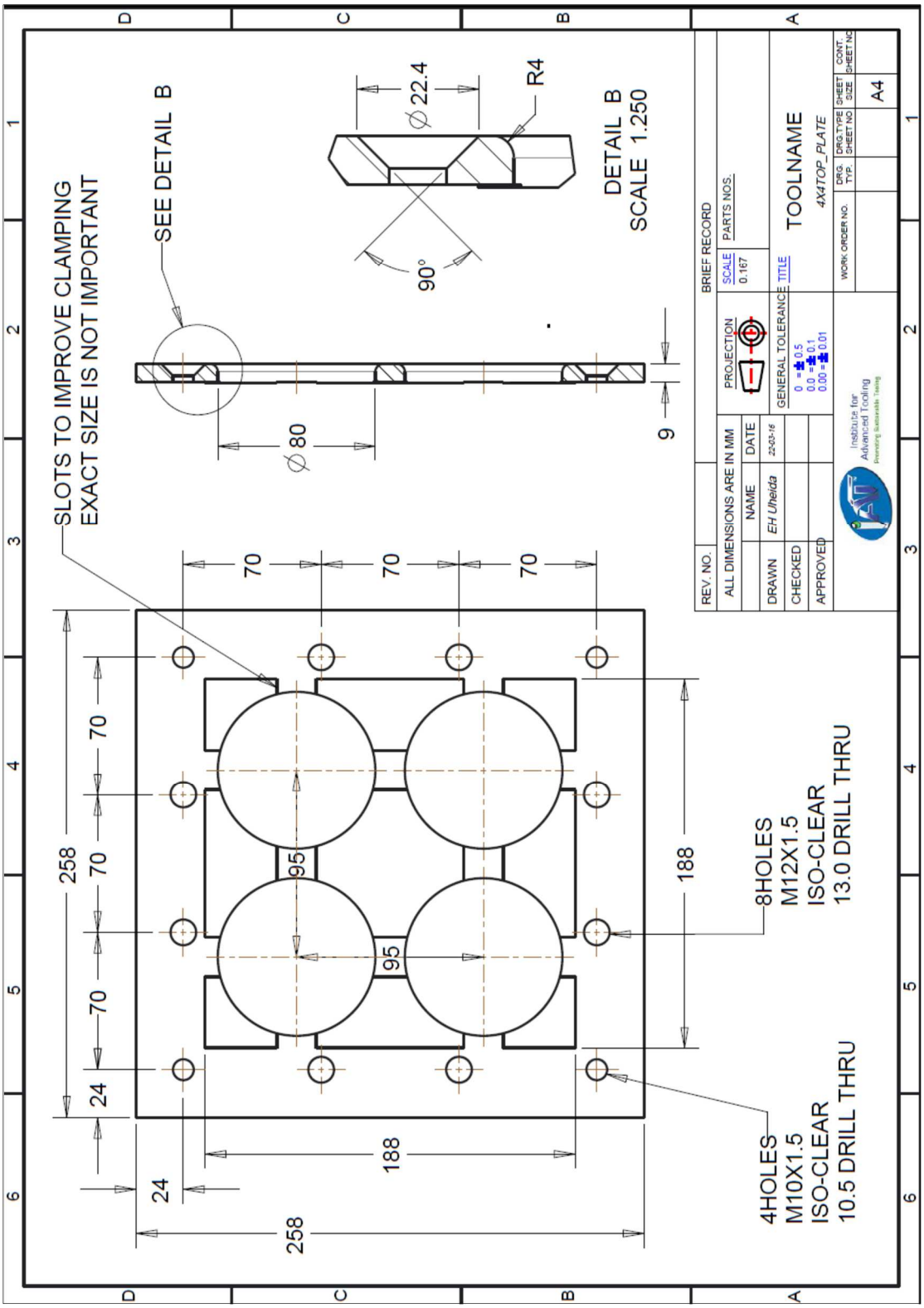

Upper-plate of forming fixture

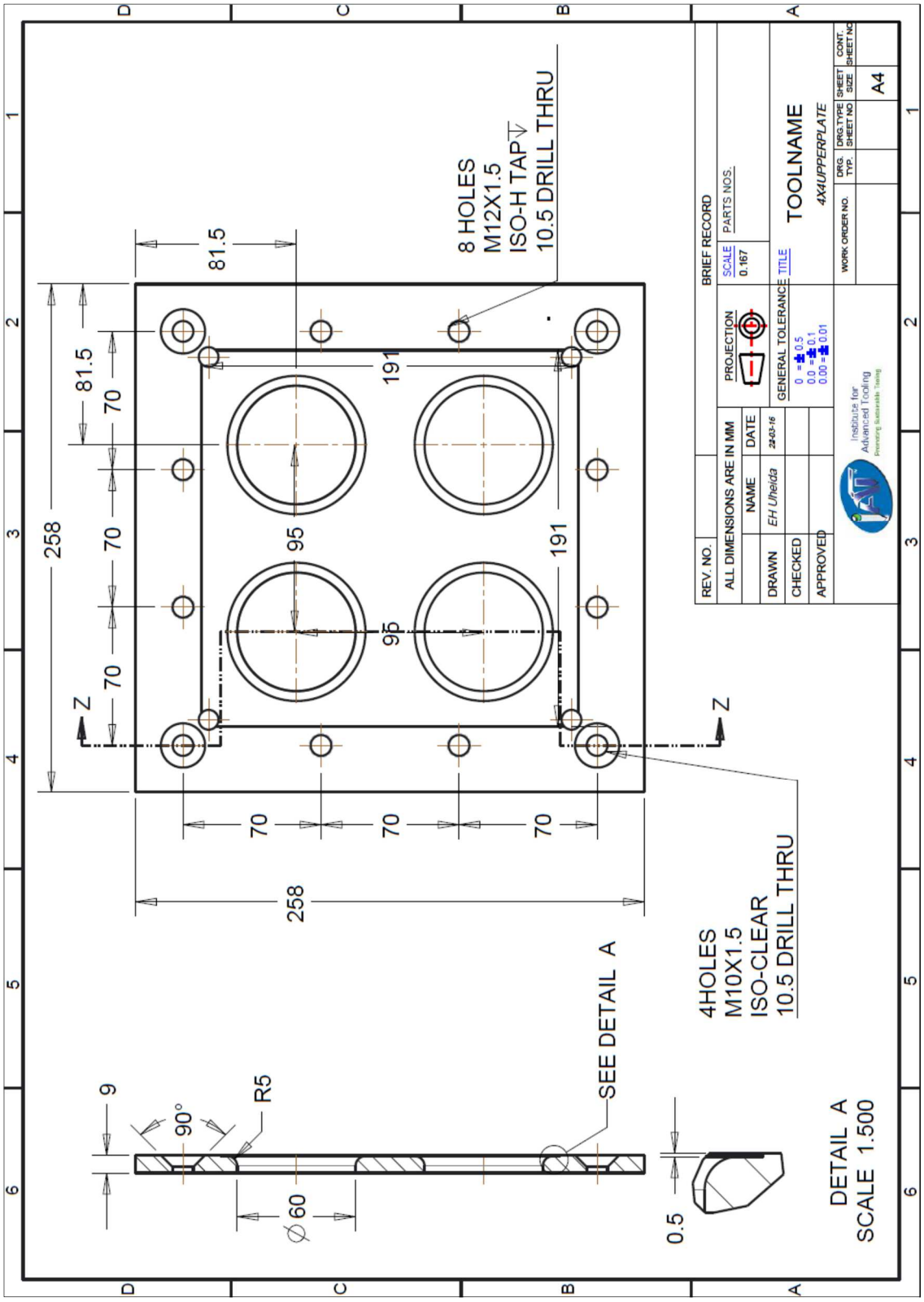

Addendum C Statistical reports for the DoE

C-1 the formability model

C-1-1 the REML ANOVA of formability model

Response ***1*** ***Maximum Forming angle*** θ_{max}

These rows were ignored for this analysis. 7, 21, 22, 31, 25, 26, 29, 27

REML (Restricted Maximum Likelihood) analysis for selected model

Kenward-Roger p-values

Fixed Effects [Type III]

Source	Term df	Error df	F	p-value Prob > F
Whole-plot	1	18.61949	27.99538	4.45E-05
a-Thickness	1	18.61949	27.99538	4.45E-05
Subplot	5	18.27764	23.54062	2.25E-07
B-Rotation	1	18.028	4.466287	0.048772
C-Tool size	1	18.80985	105.0582	3.91E-09
D-Feed rate	1	18	2.294404	0.147204
E-Step depth	1	18.23577	3.160323	0.092129
CE	1	18.02485	10.18747	0.005046

Variance Components

Source	Variance	Std. Err	95% CI Low	95% CI High
Block	0.479433	2.144504	-3.72372	4.682584
Group	0	0	0	0
Residual	10.77631	3.592103	6.152739	23.56695
Total	11.25574			

-2 Log Likelihood	120.9996	BIC	153.5806
R-Squared	0.893077	AIC	140.9996
Adj R-Squared	0.832932	AICc	155.6663

Source	Coefficient Estimate	Standard Error	VIF
Intercept	60.90481	1.004659	
Whole-plot Terms:			
a-Thickness	3.87289	0.731968	1.069938
Subplot Terms:			
B-Rotation	-1.5471	0.732059	1.18173
C-Tool size	-8.69097	0.847917	1.307175
D-Feed rate	-1.14698	0.75722	1.268503
E-Step depth	1.461455	0.822091	1.434102
CE	-2.42448	0.759601	1.149697

C-1-2 the diagnostics plots (formability)

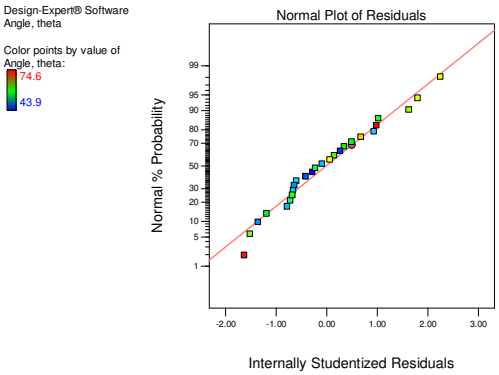

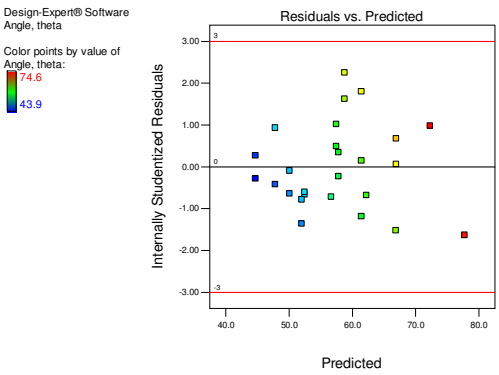

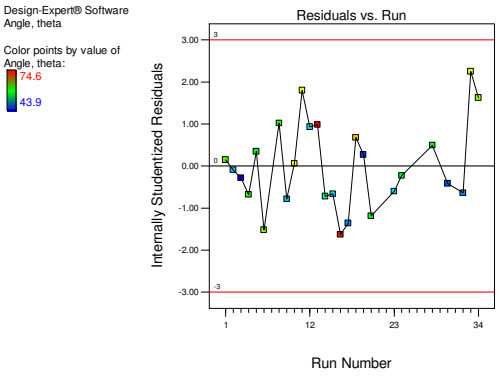

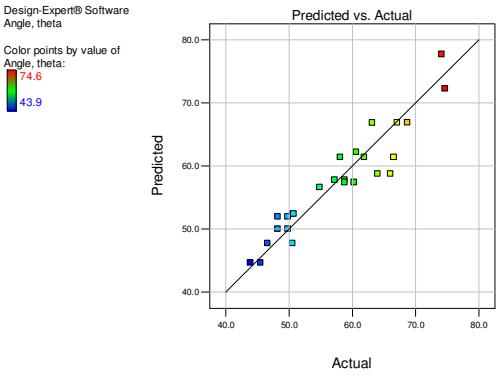

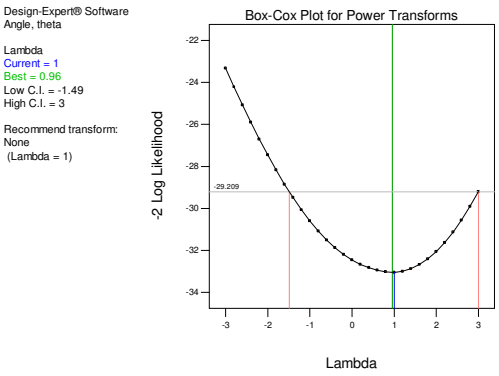

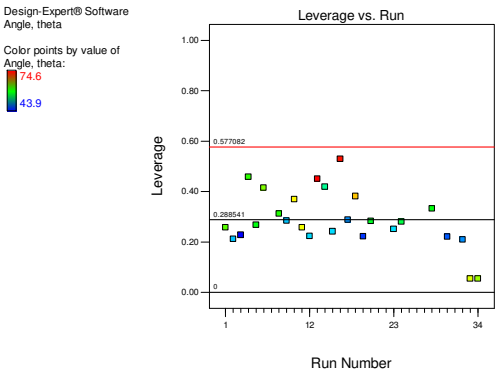

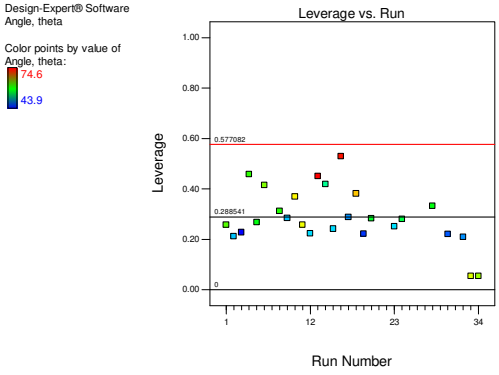

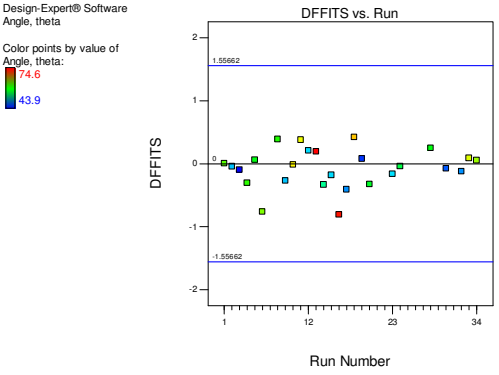

C-2 the forming temperature model

C-2-1 the REML ANOVA of the temperature model

Response	***2***	***Forming temperature***	***(T_{ref})***	(°C)
These rows were ignored for this analysis. 7, 21, 22, 31, 25, 26, 29, 27				
REML Kenward-Roger p-values *Fixed Effects [Type III]*				
	Term	**Error**	**F**	**p-value**
Source	df	df		Prob > F
Whole-plot	1	15	126.8712	1.02E-08
a-Thickness	1	15	126.8712	1.02E-08
Subplot	9	15	34.78748	1.89E-08
B-Rotation	1	15	213.7598	2.79E-10
C-Tool size	1	15	0.319949	0.580002
D-Feed rate	1	15	6.8694	0.019277
E-Step depth	1	15	7.720521	0.014054
aB	1	15	36.23138	2.35E-05
aC	1	15	5.127694	0.038796
aD	1	15	4.827258	0.044139
CE	1	15	17.71263	0.00076
DE	1	15	7.857517	0.013375
Variance Components				
Source	Variance	Std. Err	95% CI Low	95% CI High
Block	0	0	0	0
Group	0	0	0	0
Residual	216.1435	78.92443	117.9462	517.7388
Total	216.1435			
-2 Log Likelihood	155.9819		BIC	201.5953
R-Squared	0.965208		AIC	183.9819
Adj R-Squared	0.927516		AICc	222.1638
	Coefficient	Standard		
Source	**Estimate**	**Error**	**VIF**	
Intercept	179.3831	3.992952		
Whole-plot Terms:				
a-Thickness	38.44874	3.413505	1.27125	
Subplot Terms:				
B-Rotation	62.02258	4.242158	1.985463	
C-Tool size	-2.19433	3.879379	1.567517	
D-Feed rate	-9.13658	3.485975	1.340679	
E-Step depth	10.74495	3.867063	1.649828	
aB	21.42625	3.559622	1.397933	
aC	-8.60736	3.801099	1.5932	
aD	-7.38546	3.361456	1.246611	
CE	-15.4795	3.678029	1.34804	
DE	-11.6683	4.162609	1.726648	

C-2-2 the diagnostics plots of the temperature model

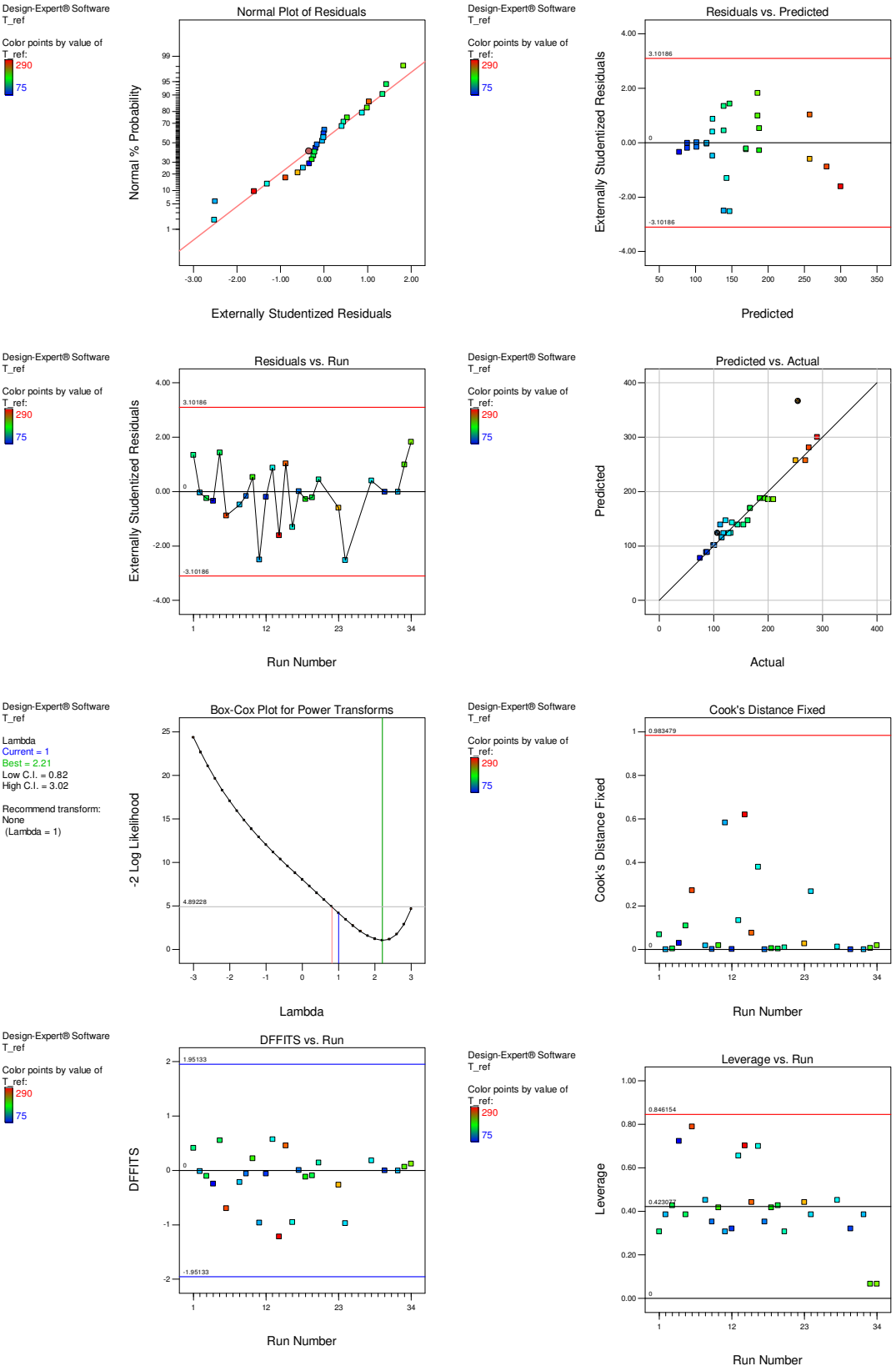

C-3 the axial force model

C-3-1 the REML ANOVA of the axial force model

Response	***3***	***Axial force***	***Max F_Z***	***(N)***
These rows were ignored for this analysis. 7, 18, 22, 31, 25, 26, 29				

REML Kenward-Roger p-values

Fixed Effects [Type III]

Source	Term df	Error df	F	p-value Prob > F
Whole-plot	1	7.807938	19.91768	0.002233
a-Thickness	1	7.807938	19.91768	0.002233
Subplot	6	11.16638	321.987	7.65E-12
B-Rotation	1	11.1756	1131.479	1.38E-12
C-Tool size	1	11.21883	170.4896	3.93E-08
D-Feed rate	1	11.06629	10.61822	0.007562
E-Step depth	1	11.31009	8.959897	0.011886
aB	1	11.17466	489.2002	1.4E-10
CE	1	11.33105	29.36094	0.00019

Variance Components

Source	Variance	Std. Err	95% CI Low	95% CI High
Block	0	0	0	0
Group	6534.875	3435.835	-199.238	13268.99
Residual	572.4881	244.3459	287.1302	1652.5
Total	7107.364			

-2 Log Likelihood	224.6244	BIC	260.8786
R-Squared	0.992158	AIC	246.6244
Adj R-Squared	0.987256	AICc	264.2244

Source	Coefficient Estimate	Standard Error	VIF
Intercept	431.1486	26.39701	
Whole-plot Terms:			
a-Thickness	129.4959	29.01593	1.007926
Subplot Terms:			
B-Rotation	-180.286	5.359677	1.100475
C-Tool size	96.90385	7.421508	1.916142
D-Feed rate	18.40951	5.649583	1.335002
E-Step depth	-22.6718	7.574148	1.998261
aB	-130.679	5.908318	1.338167
CE	38.62469	7.128202	1.193487

C-3-2 the diagnostics plots of the axial force model

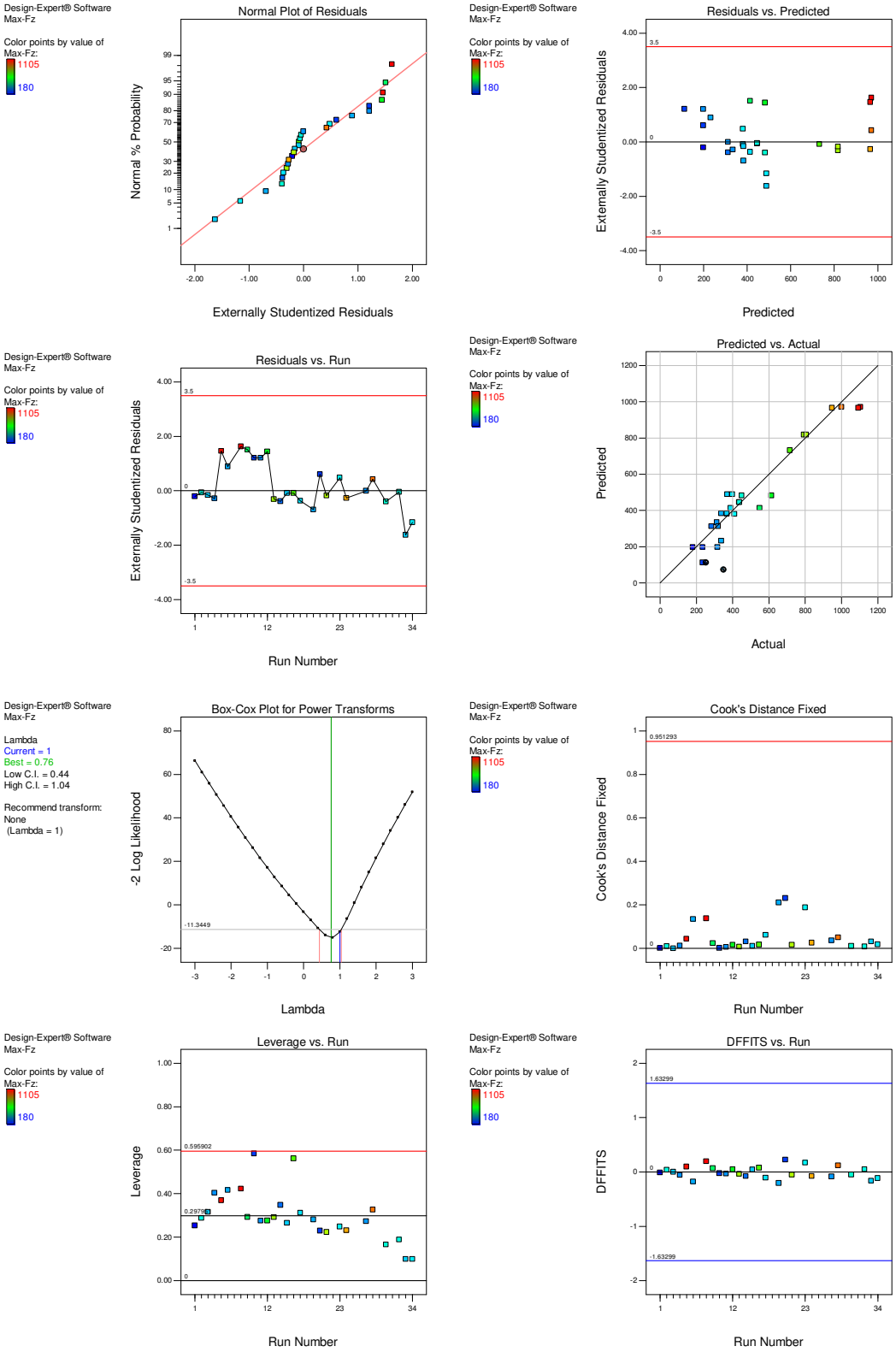

C-4 the cycle time model

C-4-1 the REML ANOVA

Response	***6***	***Cycle time (s)***	t_{ref}	
These rows were ignored for this analysis.				
34, 33				
***REML** (REstricted Maximum Likelihood) analysis for selected model*				
Kenward-Roger p-values				
Fixed Effects [Type III]				
	Term	Error	F	p-value
Source	df	df		Prob > F
Subplot	5	26	261940.6	3.01E-60
C-Tool size	1	26	498.3601	1.74E-18
D-Feed rate	1	26	577119.4	4.88E-58
E-Step depth	1	26	362544.3	2.06E-55
CE	1	26	21.89003	7.85E-05
DE	1	26	15957.84	8.66E-38
Variance Components				
Source	Variance	Std. Err	95% CI Low	95% CI High
Block	0	0	0	0
Group	0	0	0	0
Residual	2.131868	0.591274	1.322146	4.003825
Total	2.131868			
-2 Log Likelihood	113.9941		BIC	145.1857
R-Squared	0.99998		AIC	131.9941
Adj R-Squared	0.999973		AICc	140.1759
Source	Coefficient Estimate	Standard Error	VIF	
Intercept	1015.5	0.275931		
C-Tool size	-5.96429	0.267169	1.071429	
D-Feed rate	-202.964	0.267169	1.071429	
E-Step depth	-166.143	0.275931	1.142857	
CE	1.25	0.267169	1.004464	
DE	33.75	0.267169	1.004464	

C-4-2 the diagnostic plots of the cycle time model

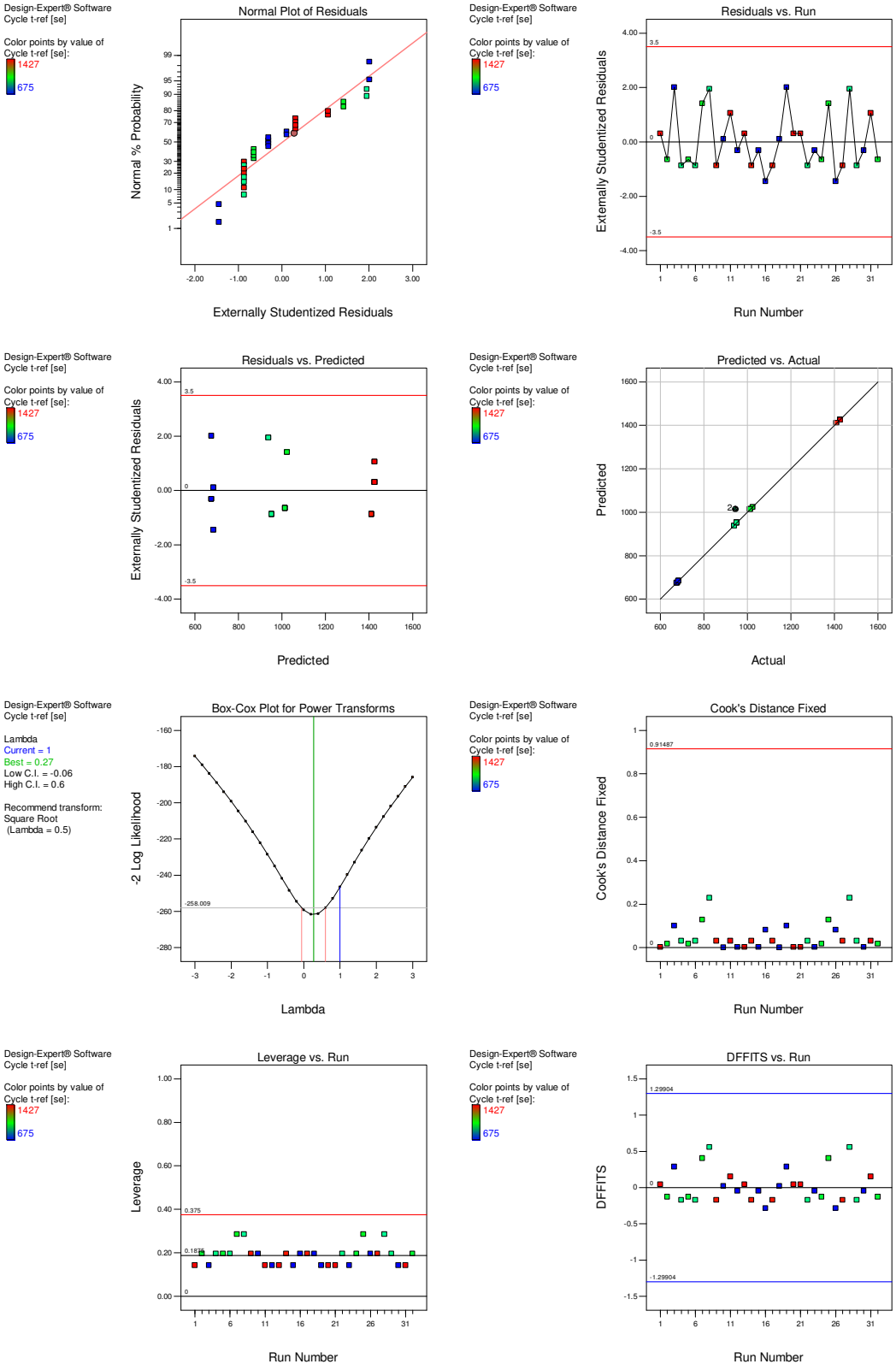

Addendum D Temperature profiles during DoE test

Excel plots of temperature profiles versus the cycle time as recorded during the DoE. The Profiles are distinguished by their run order (C- codes) and design identification (ID) number. Thus, they can be matched with corresponding settings and measured data in the DoE layout.

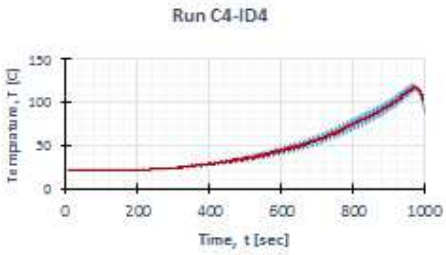

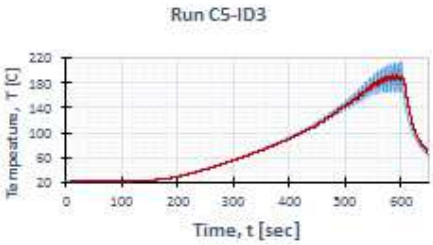

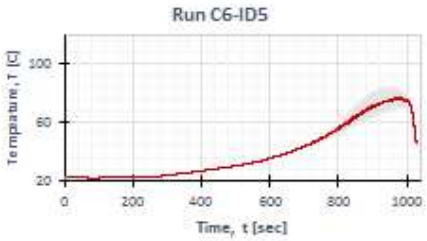

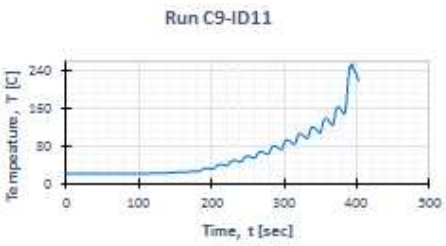

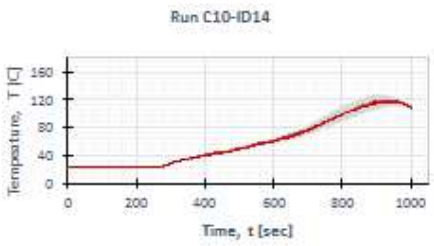

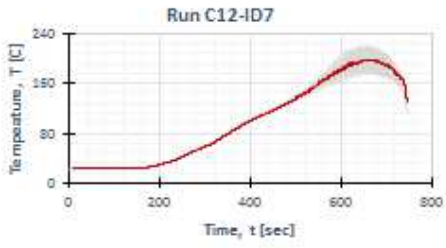

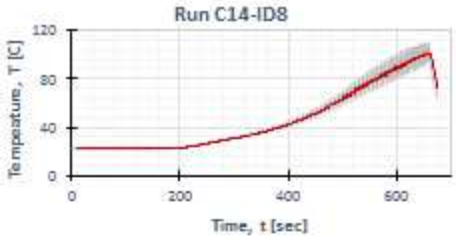

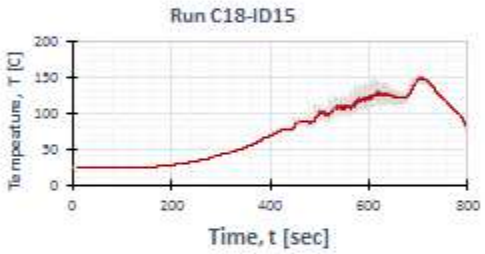

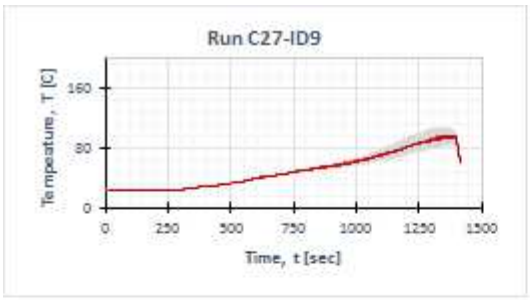

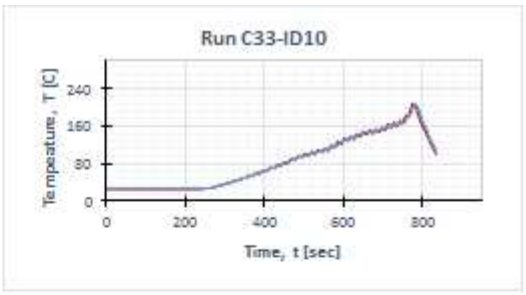

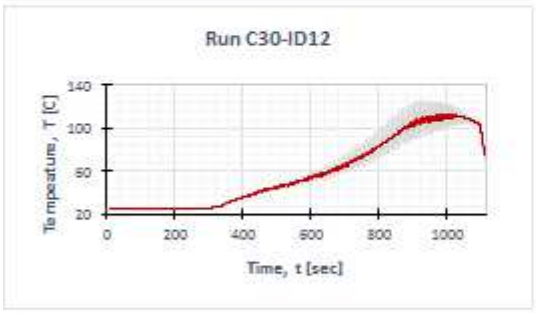

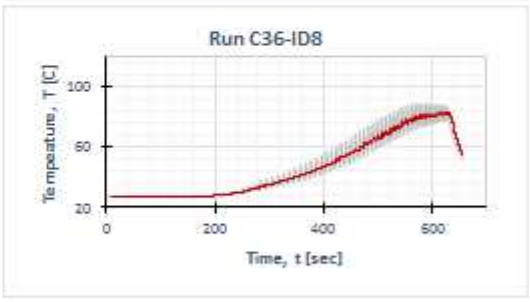

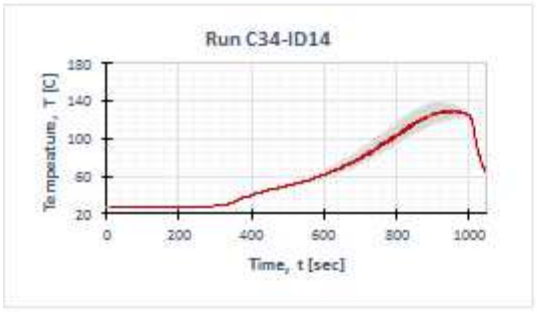

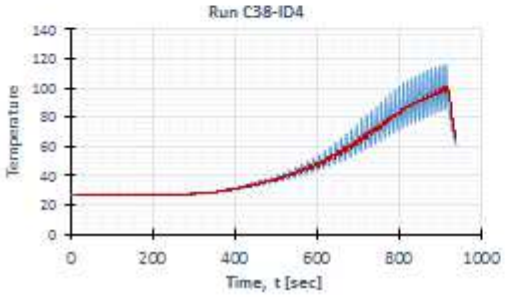

Addendum E Axial force profiles from the DoE test

Illustrations of axial forming force profiles versus the cycle time as obtained from the DoE